Scanning tunneling spectroscopy study of epitaxial graphene on superconducting rhenium

Charlène Tonnoir

UNIVERSITÉ DE GRENOBLE

THÈSE

Pour obtenir le grade de

DOCTEUR DE L'UNIVERSITÉ DE GRENOBLE

Spécialité : **Physique de la matière condensée et du rayonnement**

Arrêté ministériel : 7 août 2006

Présentée par

Charlène TONNOIR

Thèse dirigée par **Marc SANQUER**
et codirigée par **Claude CHAPELIER**

préparée au sein **du Laboratoire de transport électronique quantique et supraconductivité,**
de l'Institut nanosciences et cryogénie,
du CEA Grenoble
et de **l'Ecole doctorale de Physique de Grenoble**

Spectroscopie tunnel de graphène épitaxié sur du rhénium supraconducteur

Thèse soutenue publiquement le **20 décembre 2013**,
devant le jury composé de :

Hélène BOUCHIAT
Laboratoire de Physique des Solides, Examinatrice
Claude CHAPELIER
CEA Grenoble, Co-Directeur de thèse
Hervé COURTOIS
Professeur des Universités de l'Université Joseph Fourier, Institut Néel, Président
Andreas HÜTTEL
Institute for Experimental and Applied Physics, University of Regensburg, Rapporteur
Vincent REPAIN
Professeur des Universités, Laboratoire Matériaux et Phénomènes Quantiques / Université Paris Diderot-Paris 7, Rapporteur
Marc SANQUER
CEA Grenoble, Directeur de thèse
Markus TERNES
Max-Planck Institute for Solid State Physics, Stuttgart, Examinateur

Quand deux chemins s'ouvrent à toi, choisis toujours le plus difficile, celui qui exigera le meilleur de toi.

Proverbe tibétain

Contents

Acknowledgments

This work has been carried out at CEA-Grenoble in the Laboratoire de Transport Electronique Quantique et Supraconductivité (LaTEQS) of the Service de Physique Statistique Magnétisme et Supraconductivité (SPSMS). I would like to thank Jean-Pascal Brison, head of the SPSMS, and Marc Sanquer, head of the LaTEQS, for welcoming me in their laboratory.

I thank warmly Hélène Bouchiat, Claude Chapelier, Hervé Courtois, Andreas Hüttel, Vincent Repain, Marc Sanquer and Markus Ternes for being part of my thesis jury. I thank them for the interest they have shown in my work and the very stimulating questions session during my defense. They greatly contributed to make this day an extraordinary memory.

Je remercie mon directeur de thèse Marc Sanquer pour sa confiance et la liberté qu'il m'a accordée dans mes choix et mes orientations, notamment sur mon sujet de thèse et mon séjour en Espagne.

Claude, je te remercie du fond du coeur pour tous les moments qu'on a partagés, ton enthousiasme et ta curiosité inépuisables, ta pédagogie et ta passion de transmettre et surtout ta confiance et ton soutien dans tous mes projets, qu'ils aient été scientifiques ou personnels. Tu m'as fait découvrir et aimer la recherche fondamentale, ce fut un réel privilège de travailler à tes côtés pendant ces trois années et de partager ta passion pour la physique. Ta disponibilité et ta considération m'ont permis de surmonter les difficultés. Tu représentes pour moi le chercheur tel que je l'ai toujours imaginé depuis mon enfance, ouvert, curieux, désintéressé, ingénieux, exalté et je n'aurais pas pu souhaiter meilleur encadrant pour mon expérience dans la recherche. Merci pour la liberté et le soutien précieux que tu m'as accordés pour réaliser mes projets, quand bien même ils t'imposaient des sacrifices (mon séjour en Espagne, mes formations éclectiques, mon voyage aux États-Unis, etc). Nos "cafés littéraires", échanges d'idées et de points de vue vont me manquer, mais je sais que notre amitié perdurera malgré les kilomètres et les projets qui nous séparent.

Je remercie nos collaborateurs, et tout particulièrement Johann Coraux, Laurence Magaud, Amina Kimouche, Benjamin Delsol et Bruno Gilles pour leur investissement et leurs conseils dans notre projet commun. Grâce à eux, j'ai eu la chance de vivre une partie de ma thèse comme un travail en équipe en faisant avancer nos connaissances par des échanges constructifs. Notre manip commune au synchrotron de Trieste a constitué pour moi un moment fort de travail de groupe. Je les remercie sincèrement pour tous ces moments de partage.

Quiero dar las gracias al grupo de bajas temperaturas encabezado por Sebastián Vieira en la Universidad Autónoma de Madrid por su agradable acogida durante los dos meses de mi estancia. Fue una experiencia muy enriquecedora y durante la cual he apprendido mucho. Agradezco particularmente a José Gabriel Rodrigo sus explicaciones y el intercambio de conocimientos, así como el haberme facilitado el uso de su experimento.

Un immense merci à Benoit, cobureau de la P.309, qui a supporté mes débuts en tant que DJ amateur et dont la bonne humeur et le rire facile ont sauvé les jours les plus sombres de la période de rédaction. Merci (ou pas!) pour les discussions sur la syntaxe anglaise, nos premiers pas dans la chanson (promis à un grand avenir grâce à ses nombreux talents), le plaisir de voir grandir Némo bercée par le doux bruit de la pompe. Bref, merci pour tous nos délires et craquages qui ont illuminé ces trois années de cohabitation.

Merci aux thésards du SPSMS promo 2010 et en particulier à Mathieu mais aussi Benoit, Andi, Tristan, Caro et Driss pour avoir soutenu le lancement des Pipotages et contribué à leur succès. Merci également à tous les thésards et post-docs qui y ont activement participé. Ces rencontres d'échanges scientifiques entre jeunes du labo nous ont ouverts à d'autres thématiques et ont renforcé nos liens d'amitié, je les remercie pour ces moments de partage qui avaient beaucoup d'importance pour moi.

Je tiens à dire un grand merci à tous mes collègues qui ont fait du laboratoire un lieu de vie et d'échanges très agréable pendant ces trois années, Xavier, François, Vincent, Max, Christophe, Louis, Silvano, Fred G. et Jean-Claude mais aussi Georg, Alexandre, Bernard, Daniel, Dai, Jean-Michel et Iulian. Merci à Pierre et à Fred P. pour leurs nombreux coups de pouce en électronique et informatique. Merci à Jean-Luc pour veiller au bon fonctionnement du labo et pour ses abeilles et petits mots sur le tableau. Merci à Manuel pour son aide patiente sur mes questions théoriques.
Je remercie tous les thésards et post-docs du service avec qui j'ai passé de très bons moments, Alex (der Spitzbube), Andi (et son soutien moral les weekends de rédaction), Audrey et Benoît qui nous ont montré la voie comme Guillaume avant eux, Zoltan, Eduard, Mathieu, Toai, Alexandra, Mounir (et ses délicieux gâteaux), Jean-Eudes, Pol, Gaël, Yussei, Soumya, Eduardo (for sharing vodka in Poland), Natalia, Boris et les théoriciens Caro, Driss, Benoît G. et Vladimir. Un merci tout spécial à Julien pour nos discussions et ses conseils. Et bonne chance à la nouvelle relève de thésards, Alexandre A. (futur STMist professionnel), Andrea, Juan-Carlos et Patrick.

Je remercie sincèrement Stéphane Pignard, qui m'a suivie et soutenue pendant ma scolarité à Phelma et tout au long de ma thèse, sans jamais se lasser du foisonnement de mes projets "potentiels". Son ouverture d'esprit, son oreille attentive et son intérêt pour mes projets m'ont permis de progresser dans mes choix et de toujours garder une vision optimiste de l'avenir. Je le remercie pour sa confiance constante depuis notre rencontre.

C'est le moment de remercier ceux qui m'ont soutenue et ont contribué à mon équilibre mental en dehors du labo, et sans qui je n'aurais sans doute pas vu le bout du tunnel.

Tout d'abord les habitants passés et présents de Colocabel, en particulier Pat, Elo, Domi, Taylor et Hadrien. Merci pour les soirées autour d'un bon repas, pour les heures passées à refaire le monde, pour avoir partagé vos passions et ensoleillé mon quotidien.

L'ambiance ouverte et joyeuse de notre lieu de vie commune a pleinement contribué à mon épanouissement à Grenoble.

Un merci gargantuesque à la (sainte)ChartreuseTeam, Yannick, Fabrice, Isa, Aurel, Fabinou, Ln, Adri, Oliv, Michaël, Justine, François, Benoît, Jo, Emma, Alex (dit Teulle[2]), Gui. Merci pour nos soirées son & lumière jusqu'au bout de la nuit, pour nos débats enflammés, pour nos randos magiques car partagées, pour nos weekends colorés, pour nos voyages à l'autre bout du monde. Merci pour votre soutien sans faille, pour vos personnalités originales et généreuses et pour tous ces moments fantastiques passés ensemble et pour ceux qui viendront encore. Je vous aime fort les copaings.

Un autre merci zetsudai à Cédric, pour son amitié indéfectible et sa confiance qui a toujours été pour moi un socle sur lequel m'appuyer quand il m'en manquait. Merci pour avoir élargi mes horizons, pour m'avoir toujours encouragée à aller plus loin (au sens propre et figuré pour le coup) et m'avoir convaincue que rien n'est impossible pour peu qu'on le veuille vraiment (le plus dur étant de savoir ce que l'on veut!). Merci pour tout.

Pour terminer, ma dernière pensée va vers ma famille, pilier fondamental de mon existence. Je remercie du fond du coeur mes parents pour leur soutien, leurs encouragements et leur compréhension. Mon père pour sa curiosité intellectuelle et pour m'avoir intéressée au monde passionnant de la science. Ma mère pour son appui et son respect de mes choix, quand bien même ils me conduisent à des milliers de kilomètres d'eux. Je remercie aussi ma soeur Léa d'être venue de loin pour ma soutenance et lui souhaite bonne chance pour sa future thèse.

Introduction

Context

In 2010, Andre Geim and Konstantin Novoselov were jointly awarded the Nobel Prize in Physics "for groundbreaking experiments regarding the two-dimensional material graphene". This was only six years after their discovery of this extraordinary material. Since then, the number of publications and patents related to graphene has increased exponentially. Graphene is a one atom-thick carbon material, which achieved the feat to trigger the enthusiasm of numerous and incredibly various scientific communities: physicists, chemists, biologists, from the application and fundamental side of research, have all been won over by its exceptional properties.

On top of being the thinnest and strongest material ever measured, the best thermal conductor, the most impermeable matter, graphene is also an exceptional electrical conductor and can sustain current densities six order of magnitude higher than copper at room temperature. Highly transparent and flexible, it holds prodigious promises for future electronics. The foreseen fields of applications are as varied as numerous and focus the interests of technologists and industrial companies.

But graphene is also the center of attention of many fundamental science laboratories in the world. First of all, it is the first two-dimensional electrical conductor that is easy to produce and constitutes an autonomous nano-object. It is inert in air and easy to contact and study with local probes. But particularly, graphene exhibits a linear electronic dispersion, which implies that its charge carriers mimic massless relativistic particles, being described by the Dirac equation rather than the Schrödinger's one. This makes graphene a material at the frontiers between condensed matter physics and particle physics. This merging of two distinct faces promises new thrilling physical phenomena to uncover.

A current field of research is related to the interplay between graphene and superconductivity, which is a phenomenon occurring at low temperature, characterized by the repulsion of magnetic field and the circulation of dissipationless electrical currents. Although bare graphene itself does not exhibit intrinsic superconductivity, one can make it superconducting by doping or contacting it to a superconductor. The relativistic quantum description of graphene has been predicted to have important consequences on the physics of superconductivity.

The superconducting proximity effect in graphene underlies this work. Whereas a

Josephson super-current has been observed in graphene, thus attesting the presence of superconducting correlations, the superconducting proximity effect remains challenging. One reason is the difficulty to prepare a highly transparent interface between graphene and a superconducting metal, which is a prerequisite for the good transmission of superconducting correlations into graphene.
To solve this problem, we propose a new design of a graphene-superconductor hybrid system: the epitaxial growth of a graphene monolayer on top of superconducting rhenium. This thesis presents the first characterization and study of the local electronic properties of such a system by scanning tunneling microscopy (STM).

Content

The first chapter of this manuscript will be dedicated to the presentation of the scanning tunneling microscope operating at very low temperature (50 mK). We will describe the working principle and the experimental setup, with the control electronics and the cryogenics equipment.
In the second chapter, different techniques of scanning tunneling spectroscopy will be explained and illustrated by experimental works. A simple theoretical description of the classical tunneling spectroscopy technique will be given, followed by the model and experimental procedure used for point-contact Andreev spectroscopy. The last section will be related to tunneling spectroscopy with a superconducting STM tip. The interests and advantages of each method will be discussed.
An introduction to the physics of graphene and its peculiar physical properties will be provided in chapter 3. The transmission of superconducting properties to graphene (and more generally carbon-based compounds) described by theoretical proposals or previous experiments will be reviewed. The specific experimental constraints for its study with STM will be detailed in the last section.
The fourth chapter will present the epitaxial graphene grown on rhenium system. We will describe the fabrication of the mono-crystalline thin rhenium films and the graphene growth process, after a brief review on the graphene-metal systems already studied in the literature. Topographic analyses of our system, as well as density functional theory (DFT) calculations will be shown and interpreted with respect to the coupling strength between graphene and rhenium. A high-energy (few hundreds of meV) spectroscopy study will complete this description.
The superconducting properties of graphene grown on rhenium will be displayed in chapter 5. After presenting the bulk properties probed by transport measurements, we will investigate the local superconducting density of states (DOS) and its temperature evolution. Spatial evolution studies will be discussed and spectroscopic measurements in the superconducting mixed state under magnetic field will be exposed.

Introduction en français

Contexte

En 2010, le Prix Nobel de Physique récompense André Geim et Konstantin Novoselov "pour des expériences révolutionnaires concernant le graphène, matériau bidimensionnel". Cette reconnaissance arrive seulement six ans après leur découverte de ce matériau exceptionnel. Depuis lors, le nombre de publications et de brevets portant sur le graphène a augmenté de façon exponentielle. Le graphène est un matériau carboné épais d'un seul atome, qui a réussi l'exploit de déclencher l'enthousiasme de communautés scientifiques nombreuses et incroyablement diverses : physiciens, chimistes, biologistes, du côté appliqué ou fondamental de la recherche, tous ont été conquis par ses propriétés exceptionnelles.

En plus d'être le matériau le plus fin et le plus solide jamais mesuré, le meilleur conducteur thermique, la matière la plus imperméable, le graphène est également un conducteur électrique exceptionnel et peut supporter des densités de courant un million de fois plus élevées que le cuivre à température ambiante. Transparent et flexible, c'est un matériau d'avenir pour la microélectronique. Les champs d'application visés sont aussi variés que nombreux et concentrent les intérêts des technologues et des industriels.

Mais le graphène est aussi le centre d'attention de nombreux laboratoires de recherche de science fondamentale dans le monde. Tout d'abord, c'est le premier conducteur électrique bidimensionnel qu'il est facile de produire. Il est inerte à l'air et facile à contacter et à étudier avec des sondes locales. Mais particulièrement, le graphène présente une dispersion électronique linéaire, ce qui implique que ses porteurs de charge se comportent comme des particules relativistes sans masse, et sont décrits par l'équation de Dirac plutôt que par celle de Schrödinger. Cela fait du graphene un matériau à la frontière entre la physique de la matière condensée et la physique des particules. Cette fusion de deux facettes distinctes promet la découverte de phénomènes physiques passionnants.

Un thème de recherche actuel est lié à l'interaction entre le graphène et la supraconductivité. Cette dernière, qui apparait à basse température, est caractérisée par la répulsion du champ magnétique et la circulation de courants électriques non dissipatifs. Bien que le graphène seul ne présente pas de supraconductivité intrinsèque, on peut le rendre supraconducteur par dopage ou en le contactant à un supraconducteur. Des travaux théoriques ont prédit que la description quantique relativiste du graphène aurait d'importantes conséquences sur la physique de la supraconductivité.

L'effet de proximité supraconducteur dans le graphène définit le cadre de ce travail. Tandis qu'un super-courant Josephson a été mesuré dans le graphène, attestant par-là même la présence de corrélations supraconductrices, l'observation de l'effet de proximité supraconducteur représente encore un défi. L'une des raisons est la difficulté à préparer une interface hautement transparente entre le graphène et un métal supraconducteur, ce qui est un prérequis pour assurer une bonne transmission des corrélations supraconductrices dans le graphène. Pour résoudre ce problème, nous proposons un nouveau design d'un système hybride graphène-supraconducteur : une monocouche de graphène épitaxié sur du rhénium supraconducteur. Cette thèse présente la première caractérisation et étude des propriétés électroniques locales d'un tel système par microscopie tunnel à balayage (STM).

Contenu

Le premier chapitre de ce manuscrit sera dédié à la présentation du microscope à effet tunnel opérant à très basse température (50 mK). Nous décrirons le principe de fonctionnement et le montage expérimental, comprenant l'électronique de contrôle et les équipements cryogéniques.
Dans le second chapitre, différentes techniques de spectroscopie tunnel à balayage seront expliquées et illustrées par des travaux expérimentaux. Une description théorique simple de la technique de spectroscopie tunnel classique sera fournie, suivie d'un modèle et d'une procédure expérimentale utilisée pour la spectroscopie d'Andreev en mode point-contact. La dernière section introduira la spectroscopie tunnel avec une pointe STM supraconductrice. Les intérêts et avantages de chaque méthode seront discutés.
Une introduction à la physique du graphène et ses propriétés physiques particulières sera présentée au chapitre 3. La transmission des propriétés supraconductrices au graphène (et plus généralement aux composés carbonés) décrite par des propositions théoriques ou des expériences antérieures sera passée en revue. Les contraintes expérimentales spécifiques pour son étude avec un STM seront détaillées dans la dernière section.
Le quatrième chapitre présentera le système constitué d'une couche de graphène épitaxié sur du rhénium. Nous décrirons la fabrication des films minces de rhénium monocristallin et le procédé de croissance du graphène, après une brève revue des systèmes graphène-sur-métal préalablement étudiés dans la littérature. Des analyses topographiques de notre système, ainsi que des calculs utilisant la méthode de la théorie de la fonctionnelle de la densité (DFT) seront présentés et interprétés en terme de force de couplage entre le graphène et le rhénium. Une étude spectroscopique à haute énergie (quelques centaines de meV) complètera cette description.
Les propriétés supraconductrices du graphène épitaxié sur rhénium seront exposées au chapitre 5. Après avoir présenté les propriétés en volume sondées par des mesures de transport, nous examinerons la densité d'états (DOS) supraconductrice locale et son évolution avec la température. Nous discuterons également de l'évolution spatiale de la DOS et exposerons des mesures spectroscopiques dans l'état mixte supraconducteur sous champ magnétique. Enfin, une étude sur diverses morphologies de surface sera présentée, laquelle présente un effet de proximité supraconducteur latéral anormal, en apparente contradiction avec les modèles existants.

Chapter 1

Low temperature scanning tunneling microscope

Contents

Introduction

When Gerd Binnig and Heinrich Rohrer developed the first STM in 1981, they opened a door to the world of the infinitely small. Five years later, they won the Nobel Prize in Physics for their invention which gave the first impulsion for the development of numerous other local probe techniques like the atomic force microscope (AFM), the scanning near-field optical microscope (SNOM) and the magnetic force microscope (MFM). All these microscopes have in common that they use a very sharp and tiny *probe* to observe local properties of matter down to atomic resolution. Data are collected by *scanning* the probe on the surface and are then converted to an image representing the detected physical properties at each point of a grid. All these techniques are named scanning probe microscopes (SPM).

1.1 Working principle

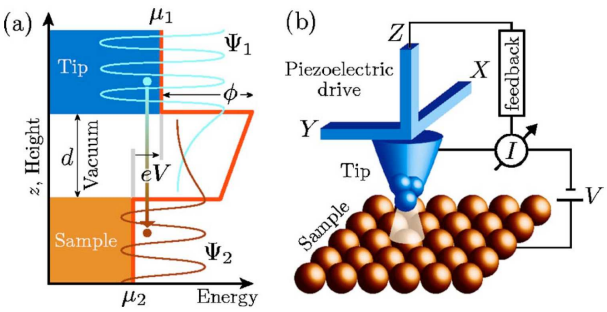

Figure 1.1 *(a) Tunneling process between the tip and sample across a vacuum barrier of width d and height ϕ (for simplicity, the tip and sample are assumed to have the same work function ϕ). The electron wave functions Ψ_1 and Ψ_2 of the tip and the sample respectively, decay exponentially into vacuum with a small overlap, allowing electrons to tunnel from one electrode to the other. With a positive bias voltage V applied to the sample, electrons tunnel preferentially from the tip into unoccupied sample states. (b) Schematic view of the scanning tunneling microscope. Reproduced from [54].*

The STM is based on the concept of quantum tunneling. The principle is to create a metal-insulator-metal junction between a metallic tip and a conducting sample separated by vacuum. At the surface of both metals, the exponential decrease of the electronic wave functions in vacuum leads to a non-zero overlap of them when the tip-sample distance is small enough (typically a few Angströms). The charge transfer from one electrode to the other happens by *tunnel effect* and depends exponentially on the tip-sample distance d:

$$I_t \sim e^{-2\kappa d} \quad , \quad \kappa = \sqrt{\frac{2m\phi}{\hbar^2}} \approx 0.5\sqrt{\phi}\,\text{Å}^{-1} \tag{1.1}$$

where ϕ is the electronic work function of the electrodes and m the free electron mass. In a metal, we have typically $\phi \approx 5\,\text{eV}$, i.e. $\kappa \sim \text{Å}^{-1}$: a variation in d of 1 Å results in an order of magnitude difference in the tunneling current. This explains the very good vertical resolution of the STM which allows to distinguish height differences of a few picometers [20]. The decisive technological element of the microscope is the scanning system, most of the time a piezoelectric tube, at the end of which the tip is positioned. Indeed, this one enables to control displacements down to the Angström scale in the three directions

of space, just by applying a voltage [19]. When the tip is few Angströms away from the sample surface, a potential difference across the junction induces a measurable tunneling current (typically 0.01 - 10 nA). This tunneling regime is then defined by three parameters: the tip-sample distance d, the tunneling current I_t and the polarisation voltage V_b. In a linear regime, the resistance of the junction $R_t = \frac{V_b}{I_t}$ is chosen big enough to guarantee a tunneling regime (typically $1 - 10^3\,M\Omega$). Nevertheless, varying I_t or V_b does not produce the same effect on the junction: the polarisation voltage sets the probed energy range, whereas a variation of the tunneling current simply translates into a variation of the tip-sample distance.

Feedback control The key element of the STM operating is undoubtedly the regulation system, i.e. the feedback loop that controls the tip height and the tunnel current. This is achieved by a *proportional-integral controller* (PI controller). A PI controller calculates an error value as the difference between a measured value and a desired set-point and attempts to minimize it by adjusting the process control inputs. For STM, the regulation is operated on the tunneling current I_t for which we define a set-point. On the electronics software interface (Nanonis, cf Sec.1.2.2), both the proportional and the integral gains are tuning parameters. The higher these values are set, the faster the controller reacts to deviations from the control signal to the set-point. Nevertheless, if the values are set too high, the controller starts to oscillate.

To get a topographic image of the sample surface, we apply voltages on the piezoelectric tube to make it scan the studied zone, line after line. Two imaging techniques are possible:

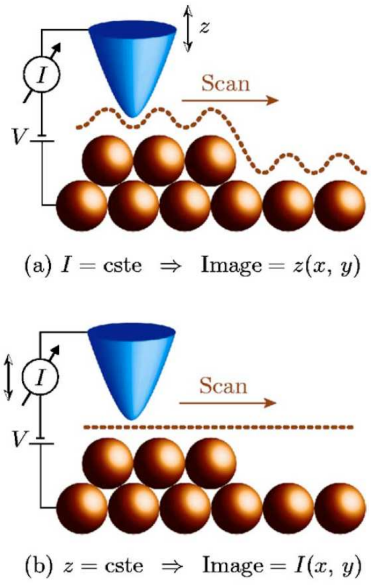

Figure 1.2 *Generic STM operating modes. Reproduced from [54].*

- **constant-current imaging mode (a)**: the tunnel current is kept constant thanks to a feedback loop controlling the elongation z of the tube, and thus the tip-sample distance.
- **constant-elongation imaging mode (b)**: the length of the tube is kept constant during scanning by freezing the feedback loop (in practice the feedback loop is not stopped but only slowed down with a very long response time and a small gain). This technique is preferentially used on atomically flat surfaces. In this case, the spatial variation of the electron density, i.e. the density of states (DOS), leads to strong current variations which allows to reconstitute a map of the electronic density in a given range of energy and down to the atomic resolution.

Thus, the tip moves above the surface with the current (resp. elongation) fixed and the coordinates $\{x, y, z\}$ (resp. $\{x, y, I\}$) of the tube enables to reconstitute an image of the studied zone.

The major interest of the STM lies in its spatial resolution. As the current is extremely sensitive to variations of d (cf Eq. 1.1), the tunnel current will necessary focus on the tip apex. One can thus obtain the atomic resolution, depending on the apex geometry and the electronic orbitals of the tip. Before the invention of the STM, the atomic lattice in solids was only obtained from indirect techniques of X-ray diffraction or with transmission electron microscopes. The scanning probe microscopy techniques henceforth allow to directly image the atoms arrangement at the surface of a sample and even to manipulate them. One can see the demonstration of such manipulations with STM on Fig. 1.3 which presents remarkable images of manipulated iron atoms physisorbed on a Cu(111) surface, obtained by Eigler's group in IBM Almaden.

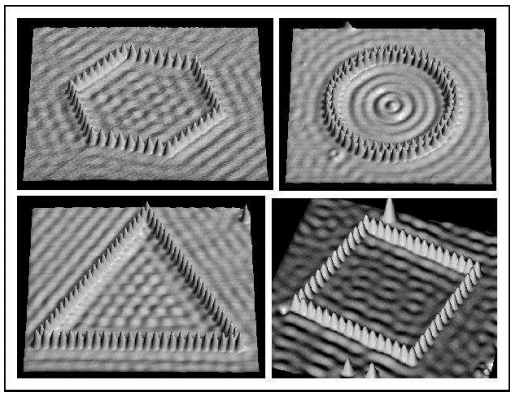

Figure 1.3 *Manipulation of iron atoms on a Cu(111) surface. Iron atoms are assembled in specific geometrical shape to form quantum corrals where the electronic wave functions are confined, thus forming well-defined quantum wave patterns [37].*

1.2 Description of the experimental setup

1.2.1 The microscope

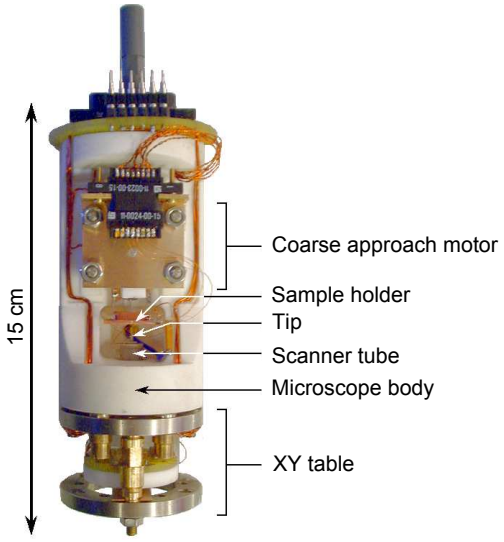

Figure 1.4 *Photography of the microscope.*

The microscope was entirely designed and assembled in the laboratory. In addition to the STM mode, it enables to perform transport measurement thanks to adapted cabling and to use the sample holder as a back gate if needed. The thermometer and the heater are mounted on the sample holder. We will describe here the principal components of our microscope. Other information is available in thesis previously defended in the laboratory [51, 115, 48].

1.2.1.1 Scanner: the piezoelectric tube

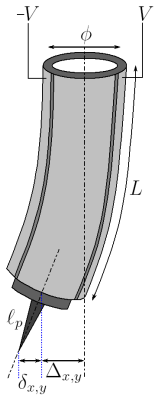

The piezoelectric tube is the central element of the microscope. It enables to make the tip scan the surface in the x,y plan as well as to adjust the tip-sample distance. The piezoelectric material is lead zirconate titanate ($PbTi_{1-x}Zr_xO_3$ with x close to 0.5), a widely used ceramic more commonly known as *PZT*, radially polarized [133]. The inside and outside walls of the tube are metallized, thus forming a capacitance of ~ 3 nF for a tube length of about 23 nm. The external electrode of the tube is divided into four sections, electrically isolated, to get two facing electrode pairs. By applying a potential difference between two opposite external electrodes, the tube bends along the directions $\pm x$ or $\pm y$. Line by line scanning can thus be achieved thanks to triangular bipolar voltage signals. When the voltage applied on the inner electrode varies, the tube extends or retracts depending on the polarization sign. The theoretical displacements of a tube are given by:

$$\Delta_{x,y} = \frac{0.9 V_{xy} d_{31} L^2}{Dt} \quad \text{and} \quad \Delta_z = \frac{d_{31} V_z L}{t} \tag{1.2}$$

where V_{xy} is the potential difference applied between two facing outer electrodes, V_z the applied voltage on the inner electrode, d_{31} the piezoelectric coefficient,L the tube length, D its diameter and t the wall thickness [123]. The characteristics of the tube we used are gathered in Table 1.1. By way of an example, the theoretical displacements with our tube are about 100 nm/V in the lateral direction and 5 nm/V in the vertical direction at room temperature. With a maximum polarization voltage of about ± 150 V, the maximum image size reachable is about $30\times30\,\mu m^2$ with a extension range of the tube along z of $1.5\,\mu$m. However, the temperature lowering decreases the piezoelectric coefficient of the ceramics we use, and thus reduces the size of the zone we can image to $3\times3\,\mu m^2$ below 4 K, with an extension range along z of about 480 nm.

Description	Symbol	Value
Tube length [mm]	L	23
Diameter [mm]	D	6
Wall thickness [mm]	t	0.38
Piezo. coeff. [mm/V]	d_{31}	$1.73\ 10^{-7}$

Table 1.1 *Physical characteristics of the piezoelectric tube.*

1.2.1.2 Coarse approach motor

The piezoelectric tube enables the displacement of the tip at some Angströms above the surface, but one first needs to approach the tip close enough to the sample surface to establish a "tunnel contact". For this purpose, one uses a coarse approach motor, which is composed of a sapphire prism and six piezoelectric legs. Four are glued on the microscope body and the last two are placed below a spring system composed of a copper-beryllium plate and an alumina marble that mechanically maintain the prism (cf Fig. 1.5). These legs are stacks of piezoelectric plates, metallized on each face and glued ones to the others

with a thin copper streamer contacting the electrodes. A final plate of polished alumina, glued on top of the stack, enables to reduce at the most the friction with the sapphire prism. Applying a voltage at the terminals of these piezoelectric ceramics will make them shear, which produces a lateral displacement of the whole prism. The sample holder being attached to one extremity of the prism, the coarse approach motor allows to approach the sample surface to the tip apex within a few nanometers.

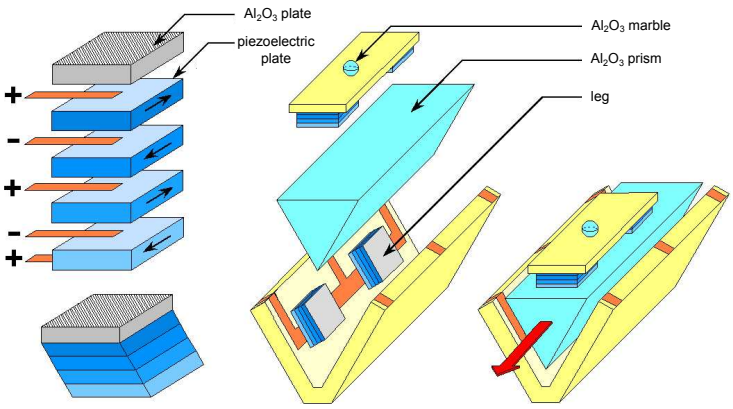

Figure 1.5 *Scheme of a piezoelectric leg and the coarse approach motor. The six piezoelectric legs are stuck on the microscope body, built in macor (a glass-ceramic). The prism is mechanically maintained against these legs thanks to a thin copper-beryllium plate with a small hole in the center, which presses on an alumina marble. This spring system allows on one hand to adjust the pressure on the legs, on the other to correct the parallelism defects.*

For such a mechanism to work, two methods can be considered:

- **the "Pan" method**: developed by S.H. Pan *et al.* [102], the working principle of this approach mechanism is briefly illustrated on the schematic drawing in Fig. 1.6 with four piezo legs. It consists in making slide each piezo leg successively while the prism is kept stationary by the friction with the five other piezo legs which remain inactive. After all legs have been independently slid backwards one after the other, the voltages on all legs are ramped down simultaneously, as shown in the drawing. Consequently, all the legs together carry the prism one step forward.
- **the inertial method**: it consists in gradually ramping up the voltage applied on the six legs so as to drag the prism into the desired direction, then make the six legs slide simultaneously back to their original position by a quick swing of the voltage polarity. The main merit of this method is to address all the piezo legs with only two wires, which is an advantage to work at low temperature.

The efficiency of the two methods is similar at room temperature, but although the Pan method enables a better control of the displacement of the prism, the inertial method is more adapted to avoid the piezo stacks to seize up at low temperature. Thus the Pan method is privileged for the tip coarse approach motor with a dedicated electronics developed in the laboratory to create the adequate signals, while the inertial method is often chosen to operate our lateral positioning motor (cf the paragraph below on the "XY Table"). It is important to notice that the reduction of the piezoelectric coefficient at low temperature affects the motor efficiency and implies to apply much higher voltage (up to 400 V instead 150 V at room temperature).

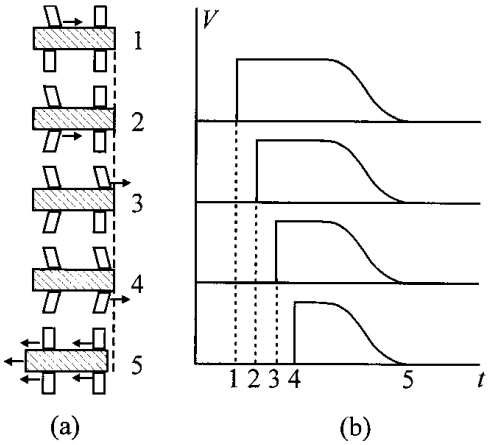

Figure 1.6 *Schematic illustration of the working principle of the piezo coarse approach motor with the "Pan' method. (a) The sequence of motions of shear piezo stacks and the sapphire prism. (b) The sequence of voltages applied to each piezo leg to produce the motions in (a). Reproduced from [102].*

1.2.1.3 XY Table

A lateral positioning motor is used to enlarge the field of observation of the STM. This XY Table is based on the same principle than the coarse approach motor for the Z direction described previously: six piezoelectric stacks hold a sapphire disk on which the piezoelectric scanner tube is glued (cf Fig. 1.7). The piezo legs pressure on the sapphire disk is adjusted just as for the Z coarse approach motor with a spring system composed of a copper-beryllium plate and an alumina marble. This positioning system over a surface of almost $2 \times 2\,\mathrm{mm}^2$ proves to be essential to study lithographed nanostructures or nano-objects scattered on a surface. In practice, we especially use it to move from a dirty or damaged zone of the sample.

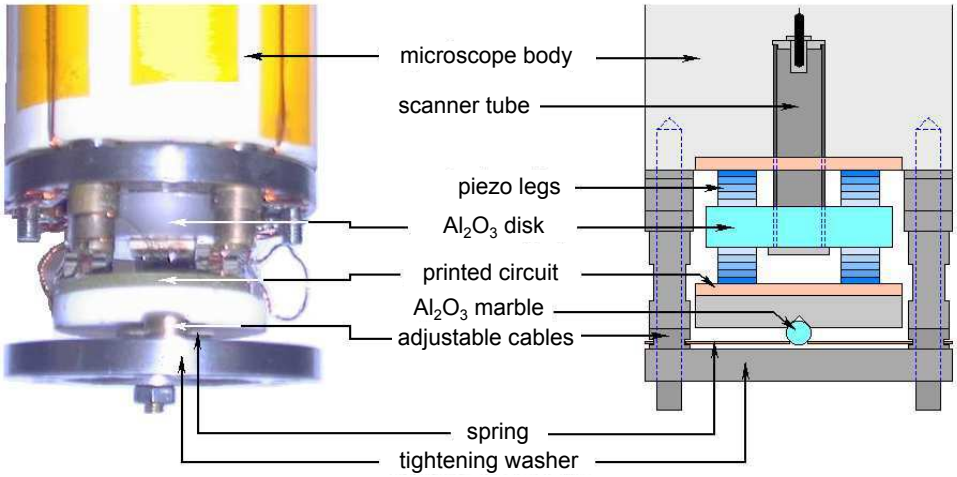

Figure 1.7 *Picture and scheme of the XY Table.*

1.2.1.4 Approach procedure

The tip-sample approach is a critical step in STM experiments as it can be decisive for the quality of the tunnel junction. This procedure must avoid the crash of the tip, while bringing it in tunnel regime in a reasonable time. We use two variants for the approach.

The first one is realized with our home-made electronics: we make forward steps with the coarse approach motor while keeping the feedback loop on the tunnel current active. As long as the measured tunnel current is zero, the electronic control unit (in this case Matrix, an Omicron product) keeps the length of the tube to its maximum. When the tunnel contact is established, the feedback loop keeps the tunnel current to its set point value by retracting the tube while the coarse approach motor finishes its last step. In this case, we have to make sure that the motor displacement is slow enough compared to the response time of the feedback loop. The other variant is directly operated by our second electronic control unit (Nanonis, a SPECS Zurich product), connected to the STM operated in the dilution refrigerator (see subsection 1.2.3 on cryogenics equipment). It alternates forward steps with the Z coarse approach motor and elongation of the tube to check if the tunnel contact is within reach. After each action of the coarse approach motor, the piezo tube is extended with the feedback loop on. If the tunnel current set point value cannot be reached while the tube is extended at its maximum length, the piezo tube is completely retracted and the coarse approach motor proceeds to another forward step. In this case, one must take care that the coarse approach step is always smaller than the total expansion of the tube. In both of these procedures, it is the detection of the tunnel current that automatically stops the coarse approach motor.

1.2.1.5 Tips

Most of the tips we use are obtained by cutting a Pt/Ir (90/10) wire of diameter 0.5 mm. The Pt/Ir alloy is stiffer than platinum, which guarantees high mechanical resonance frequencies, and besides remains stainless. These tips are embedded in a metallic tube with a slightly larger diameter glued on the piezoelectric tube. The apex of such tips is not controlled and can be very large (see Fig. 1.8), thus inducing multiple tip artifacts[1] on highly corrugated samples (such as lithographed nanostructures).

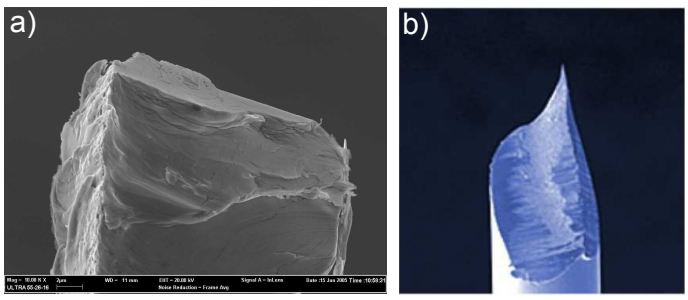

Figure 1.8 *(a) SEM image of the apex of a cut Pt/Ir tip. The image width is 30 µm. (b) SEM image of the apex of a 8 mm cut Platinum/Iridium wire sold by Bruker. Diameter: 0.25 mm, tip radius <50 nm.*

For such samples, where a very thin tip apex is required, we use commercial STM tips. These tips are prepared from a Platinum/Iridium wire cut at the end to form the tip. The wire is 0.25 mm in diameter and 8 mm in length, that we cut again to make it as short as possible to limit vibrations of the tip before gluing it on the piezoelectric tube with silver paste.

[1] While scanning, several bumps situated at the tip apex can tunnel successively on the same lump causing a multiple pattern of the relief on the image.

1.2.2 The electronics

1.2.2.1 Electronic control system

The control system realizes the following operations:

- Acquisition of the tunnel current signal.
- Generation of the junction polarization voltage.
- Generation of the five high voltage signals $\{x^+, x^-, y^+, y^-, z\}$ for the piezoelectric tube.
- Generation of the high voltage signals for the piezoelectric coarse approach motors.
- Regulation of the tunnel current.

During this research project, two commercial control systems were used. The first and older one is the Omicron NanoTechnolgy system, called Matrix, connected to the STM operated in the 4 K cryostat. Unfortunately, its software suffers from many bugs that caused the loss of many experimental data, probably linked to software stability problems. The newer control system was acquired during the first year of my project and is a SPECS Zurich product, called Nanonis, connected to the STM operated in the dilution fridge at 50 mK (cf the following subsection on cryogenics). It proved to be an excellent and very reliable tool for both imaging and spectroscopy. And even if some measurement procedures were not available, the possibility to implement our own procedures by coding them in the LabView programming language and calling them from the Nanonis interface allowed us to bypass this problem. This particularity offers a wide range of measurement possibilities.

1.2.2.2 Current-voltage converter

The measure of the tunnel current of an STM requires a current-voltage converter (or current amplifier) with a large gain and a bandwidth larger than 1 kHz. In our case, the gain is fixed to 10^8 V/A, which enables to work with currents between 0.05 and 50 nA. A negative feedback capacitance of the order of pF limits the bandwidth in order to reduce the noise at the exit and to stabilize the amplifier.
Moreover, to perform spectroscopic measurements in the *point-contact* mode, we modified this converter to get higher currents. For this purpose, we used a negative feedback resistance of $10^6\,\Omega$ enabling to work in the range 5 nA - 5 μA. This enables to pass continuously from the tunnel regime to the contact regime simply by increasing the current setpoint in the control system software. To keep the same bandwidth and limit the noise of the amplifier, we also used a negative feedback capacitance of 22 pF.

1.2.3 Cryogenics

During this project, I had the opportunity to work on three different cryostats, operating at different temperatures. In LaTEQS, we have two STM working in two different cooling systems: one is in a ^{4}He refrigerator that can operate down to 1.5 K if we pump on it, and the other one is an inverted dilution refrigerator working with a ^{3}He/^{4}He mixture at temperatures down to 50 mK. I used a third cooling system during my stay in Madrid, a ^{3}He refrigerator that could reach temperatures down to 300 mK. I will first briefly

present this latter one and then give a detailed description of our inverted dilution fridge (*sionludi*), in which most of our data have been acquired.

1.2.3.1 ^{3}He refrigerator

This system uses evaporating ^{3}He as a refrigerant. The one I used operates in 'single shot' mode, by pumping on a small charge of liquid ^{3}He condensed into the system. It allows to work for about a day before having to condense the ^{3}He again, depending of course on the temperature ramps made during the day.
Damping stage: There are two damping stages to isolate the microscope from external vibrations. The first one is linked to the way the microscope body is attached to the ^{3}He pot. A dozen of thin copper wires are bent to form a handle, the microscope being then fixed by two of these handles with a screw on a copper plate in contact with the ^{3}He pot. The copper wires ensure mechanical isolation as well as good thermal conduction to get the sample to the coldest temperature. The second stage of vibration isolation was realized by suspending the whole cryostat with springs (climbing ropes) to the ceiling. The combination of these two stages work pretty well and we could easily get the atomic resolution on the images (thanks also to a good design of the STM body).

1.2.3.2 Inverted dilution refrigerator

The inverted dilution fridge, also called *Sionludi*, is based on the same principle as a standard dilution fridge, namely the dilution of a ^{3}He/^{4}He mixture rich in ^{3}He in a phase rich in ^{4}He. Nevertheless, whereas the coldest stage is usually situated in the lower part of the cryogenic system in order to immerse this one in a liquid ^{4}He bath, the coldest point of the Sionludi is on top of the cryostat with the vacuum chamber at room temperature. Our cryostat includes five stages (100, 10, 4.2, 1, 0.05 K) held together by epoxy glass tubes providing both a good mechanical stiffness and a thermal decoupling. The radiation losses are limited by copper shields screwed on each stage (cf Fig. 1.9).

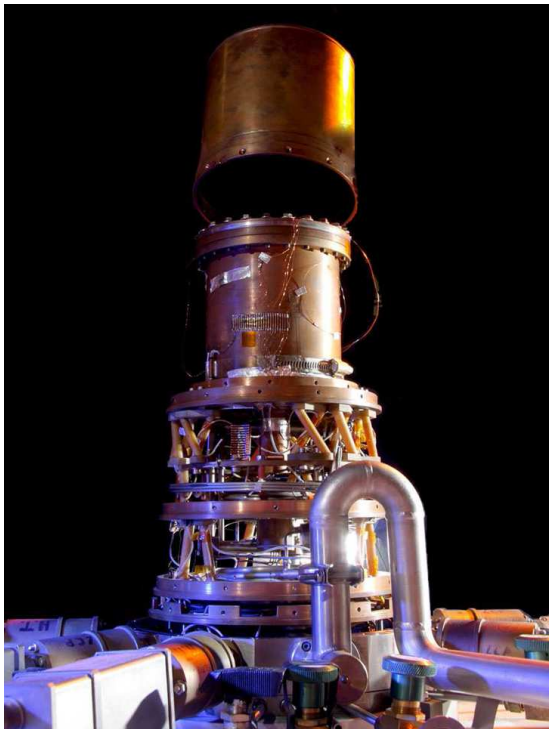

Figure 1.9 *Photography of the Sionludi cryostat.*

The absence of a 4.2 K bath required the integration of a specific pre-cooling circuit. A liquid ^{4}He dewar maintained under pressure (typically 50 mbar) fulfills this function by making the ^{4}He circulate up to the 4.2 K stage in a dedicated circuit, distinct from the dilution circuit. To cool down the upper stages from 300 K to 4.2 K, the ^{3}He/^{4}He mixture is injected at a high-flow rate in a fast injection circuit (i.e. without condensation impedance) and thermalized at 4.2 K thanks to a counter-current exchanger through which the ^{4}He vapors back flow. Two other injection circuits enable to reach 1 K for the first

one (by a Joule-Thomson expansion), and the dilution regime for the second one, that is to say a temperature of 50 mK. The cooling procedure is rather long:

- pumping on the vacuum chamber (high vacuum): one night
- cryopumping (ultra high vacuum): one day
- cooling down to 4.2 K: one night (fast injection circuit)
- cooling down to 1.5 K: $\sim$1 h (medium injection circuit)
- cooling down to 50 mK: $\sim$8 h (slow injection circuit)

which can long up to three days included the assembling of the STM in the dilution. During these steps, we should pay a particular attention to the microscope to prevent the tip to crash. Indeed, during the cooling the different parts of the microscope will retract. As different materials have different coefficients of thermal expansion, some parts of the microscope can actually get closer to each other, as it is the case for the sample and the tip. We must anticipate this by increasing the tip-sample distance before the cooling. After finding the tunnel regime at room temperature to check everything is well connected, we apply several hundreds steps at high voltage ($\sim$200 V) on the piezoelectric stacks of the coarse approach motor to withdraw the sample far from the tip. This implies to proceed again to an approach sequence of steps when we reach low temperatures, which can take some time as the piezoelectric coefficients also reduce with temperature. But we generally find back the tunneling regime after a few hundreds steps at 350 V.

Mechanical damping The cryostat is mounted on a massive table placed on pneumatic cylinders which damp the external mechanical vibrations. The significant accessible space provided by this type of inverted dilution cryostat allows to make a second mechanical damping system directly on the 50 mK stage at the microscope level.

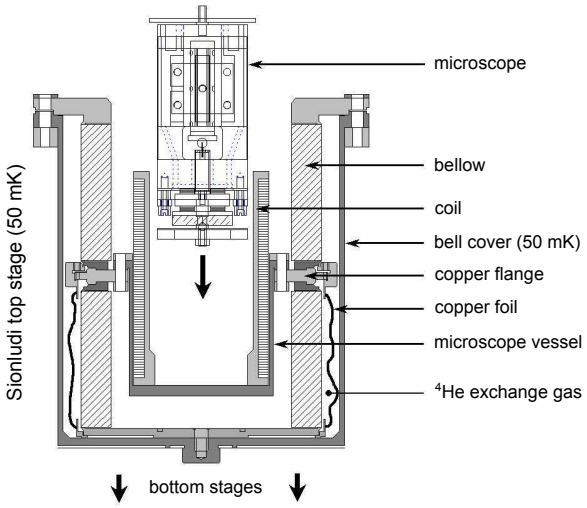

Figure 1.10 *Scheme of the microscope and coil setup on the 50 mK stage.*

In our case, the microscope is isolated from vibrations by a bellow system represented on Fig. 1.10. The whole is set up in a copper bell cover directly screwed on the mixing chamber. The space between the bellow and the bell cover contains one bar of helium gas at room temperature allowing the bellow thermalization. A fixation vessel welcoming the microscope is screwed on a copper flange soldered to the two bellows. Copper foils connect the flange to the bell cover base and enable to thermalize the microscope at the mixing chamber temperature. A superconducting coil[2] can be set in the vessel to apply a magnetic field perpendicular to the sample ($B_{max} \sim 0.1$ T).

[2]The magnetic field theoretically accessible with the used wire is 1.2 T. Nevertheless, the wire has been damaged during the winding, thus limiting the critical current to $I_c \simeq 350$ mA.

Cabling All the voltage-supply cables are 6-strand stainless steel cables insulated by a Teflon sheath inside a stainless steel shielding braid. This latter is thermalized at all the dilution stages. The strands connect directly the 300 K connectors to the kapton relays (polyimide foils) of the 50 mK stage. From there, 31 copper wires leave towards the microscope. The junction tunnel cables, voltage polarisation cable and tunnel current cable, require a peculiar attention. Indeed, assuming that the microscope is well mechanically isolated from the dilution thanks to the bellow, the mechanical vibrations due to the flow of the cryogenic fluids are mainly transmitted by the wires connecting the microscope. These latter must then be as thin and flexible as possible. Besides, these wires must ensure a good thermalization of the tip and the sample and must not be too fragile as we have to handle them every time we install or remove the microscope. Twisted pairs of copper wires of diameter 0.15 μm were used for this purpose and proved to be an efficient and perennial choice.

Chapter 2

Scanning tunneling spectroscopy

Contents

Introduction

One of the most fabulous potentials of the STM is to enable the acquisition of spectroscopic data with a spatial resolution better than the nanometre. As we will see, scanning tunneling spectroscopy (STS) is a very powerful tool to directly probe the local density of states (LDOS) of a sample. Different techniques to study the superconducting state of our sample with STS will be reviewed in this chapter. First of all, the most classical case with the use of a normal tip will be theoretically described and tunneling measurements on normal-insulator-superconductor (NIS) junctions will be interpreted and discussed. The second section will be dedicated to measurements in the *point-contact* mode, i.e. with a very low resistance of the junction, when the tip is in contact with the sample surface. This technique enables to transfer two charge carriers to the superconducting condensate by a process called Andreev reflection, and could give access to new energy scales. Finally, we will present a third spectroscopy technique based on the use of a superconducting tip and we will see what kind of new information we can extract from the collected data.

2.1 Tunneling spectroscopy

We present here a theoretical description of the tunnel effect based on the Fermi golden rule and explain why tunneling spectroscopy is an efficient tool to probe the LDOS. We also account for the influence of the energetic resolution of our set-up.

2.1.1 Theoretical description

The most successful theoretical method for understanding the electron tunneling between two metallic electrodes through an insulating barrier (NIN junction) has been introduced by Bardeen in 1960 [13]. This is a time-dependent perturbation approach, known as the "tunneling Hamiltonian" method. The main idea is to consider two separated subsystems first (the left and right electrodes) and solve the stationary Schrödinger equations to get the electronic states of both systems. The tunneling current is then calculated through the overlap of the wavefunctions of the two free systems using the Fermi golden rule.

The total tunneling rate from the left side electrode to the right side electrode $\overrightarrow{\Gamma}(V)$ is then given by the Fermi golden rule:

$$\begin{cases} \overrightarrow{\Gamma}(V) = \sum_{l,r} \Gamma_{l\to r} \left(1 - f_r(\epsilon_r)\right) f_l(\epsilon_l) \\ \\ \Gamma_{l\to r} = \dfrac{2\pi}{\hbar} \left|M(\epsilon_l, \epsilon_r)\right|^2 \delta(\epsilon_l - \epsilon_r - eV) \end{cases} \tag{2.1}$$

M is the tunneling matrix element, which represents the coupling between the electronic wavefunctions of the two electrodes. $\Gamma_{l\to r}$ is then explicitly the probability of an electron of energy ϵ_l in the left electrode to tunnel to a state of energy ϵ_r in the right electrode. $f_{l,r}(\epsilon)$ are the Fermi-Dirac distributions of the electrons of the left and right electrodes[1]

[1]The two distributions are shifted in energy by a factor eV. $f_{l,r}(E) = \dfrac{1}{1 + exp(\frac{E - E_{F_{l,r}}}{k_B T})}$ where $E_{F_r} = E_{F_l} + eV$

respectively, which give the occupation distribution of energy levels. $(1 - f_{l,r}(\epsilon_{l,r}))$ is therefore the distribution function for finding an empty space. V is the voltage applied to the junction (cf Fig. 1.1).
The total current $I(V) = e\Big(\overrightarrow{\Gamma}(V) + \overleftarrow{\Gamma}(V)\Big)$ through the tunnel barrier can be written:

$$I(V) = \frac{4\pi e}{\hbar} \sum_{l,r} |M(\epsilon_l, \epsilon_r)|^2 \, \delta(\epsilon_l - \epsilon_r) \Big[f_l(\epsilon_l) - f_r(\epsilon_r) \Big] \tag{2.2}$$

For a typical STM tunnel junction, the vacuum plays the role of the insulator with a relatively high barrier height. It is usually a reasonable approximation to neglect the variation of the tunnel transmission coefficient with energy and momentum [13]. We thus replace the matrix element $|M(\epsilon_l, \epsilon_r)|^2$ by its mean value $|M|^2$ that we suppose energy independent when the applied voltage V is very small compared to the Fermi energy E_F. Transforming the sum into an integral, the equation (2.2) becomes :

$$I(V) = \frac{4\pi e}{\hbar} |M|^2 \int d\epsilon \, N_l(\epsilon) \, N_r(\epsilon + eV) \Big[f_l(\epsilon) - f_r(\epsilon + eV) \Big] \tag{2.3}$$

where $N_l(\epsilon)$ and $N_r(\epsilon)$ are the density of states in the left and the right electrode respectively.

Case of a metal-insulator-metal junction For $eV << E_F$, the densities of states can be linearized and thus replaced by their value at the Fermi level $N_{l,r}$. The resulting integral in equation (2.3) is simply equal to the potential difference eV. This leads, in the case of two metallic electrodes, to a linear current-voltage relation:

$$I(V) = \frac{V}{R_T} \tag{2.4}$$

where $R_T = R_Q/(4\pi^2 N_l N_r |M|^2)$ is the tunneling resistance of the junction, with $\mathrm{R}_Q = h/e^2$ the quantum resistance.

2.1.2 Tunneling conductance

Unlike other scanning probe techniques, the STM has the fascinating ability to give access to the local density of states (LDOS) of the sample. We describe here the employed technique for spectroscopic data acquisition and their physical interpretation.
Deriving equation (2.3) with respect to the applied bias voltage V and identifying the left electrode to the grounded tip and the right one to the biased sample leads to:

$$\begin{aligned} \frac{dI}{dV} \propto \int_{-\infty}^{\infty} d\epsilon \Big[& N_t(\epsilon) N_s'(\epsilon + eV) f_t(\epsilon) \; - \; N_t(\epsilon) N_s'(\epsilon + eV) f_s(\epsilon + eV) \\ & - N_t(\epsilon) N_s(\epsilon + eV) f_s'(\epsilon + eV) \Big] \end{aligned} \tag{2.5}$$

where $N_s'(\epsilon)$ means the first derivative of the LDOS of the sample with respect to the energy, while $f'(\epsilon)$ is the first derivative of the Fermi-Dirac distribution function:

$$N_s'(\epsilon) = \frac{dN_s(\epsilon)}{d\epsilon}, \; f'(\epsilon) = \frac{\partial f(\epsilon)}{\partial \epsilon} = \frac{-exp(\epsilon/k_B T)}{k_B T (1 + exp(\epsilon/k_B T))^2} = \frac{-1}{4k_B T} \mathrm{ch}^{-2}\Big(\frac{\epsilon}{2k_B T}\Big) \tag{2.6}$$

As the tip is usually metallic, a common approximation consists in assuming a constant LDOS of the tip, i.e. $N_t' = 0$. The tunneling current derivative, also called differential conductance, thus gives access to the LDOS of the sample, convoluted with the Fermi-Dirac function derivative which describes the thermal distribution of the tip energy states. At a point $\mathbf{x}$ of the sample we get:

$$G(\mathbf{x}, V) = \frac{dI}{dV}(\mathbf{x}, V) \propto \int_{-\infty}^{+\infty} d\epsilon \, N_s(\mathbf{x}, \epsilon) f_t'(\epsilon - eV) \tag{2.7}$$

2.1.3 Tunneling conductance with NIS junction

In the case where only one of the two electrodes is metallic (e.g. the STM tip), the integral in equation (2.3) now only depends on the density of state of the second electrode (e.g. the sample). Therefore, the measurement of the current-voltage characteristics of such a junction enables to probe the density of states of any electronic system and thus gain access to the low energy electronic excitation spectrum.

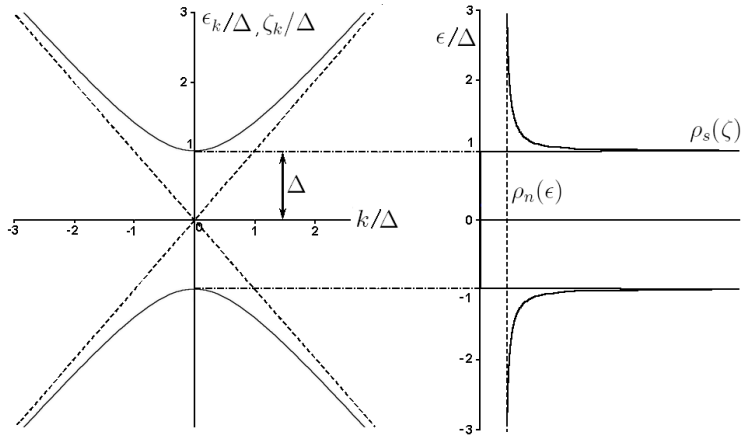

Figure 2.1 *Spectrum of elementary excitations and the corresponding single-particle density of states, in the BCS superconducting state (solid line) and in the normal state (dashed line).*

When the sample is superconducting for example, a forbidden band ("band gap") opens in the single-particle excitation spectrum (cf Fig.2.1). In the frame of the Bardeen-Cooper-Schrieffer (BCS) mean field theory, this spectrum equals to $E_k = \sqrt{\xi_k^2 + \Delta^2}$, where $\xi_k = \epsilon_k - E_F$ is the energy of one quasiparticle relative to the Fermi energy, and Δ is the BCS superconducting gap [57]. The single-particle density of states of the superconductor can be deduced from the relation between single-particle excitations in the superconductor and those in the normal state, i.e. $N_s(E)dE = N_n(\xi)d\xi$. As the density of states in the normal state varies little in the energy range of the superconducting gap (on the order of $10^{-3}eV$), it can be replaced by its value at the Fermi level $N(0)$. The density of states in the superconducting state $N_s(E)$ thus becomes:

$$\frac{N_s(E)}{N_n(0)} = \frac{d\xi}{dE} = \begin{cases} \dfrac{|E|}{\sqrt{E^2 - \Delta^2}} & (|E| > \Delta) \\ 0 & (|E| < \Delta) \end{cases} \tag{2.8}$$

It can be useful to add an imaginary part to the energy, called Γ in the literature: $\mathrm{E} \rightarrow \mathrm{E} + i\Gamma$. This phenomenological term was introduced by Dynes *et al.* [49] to take

into account the finite life-time of quasiparticle excitations. It corresponds to a pair-breaking term, which translates into non-zero subgap DOS. Nevertheless, its use was controversial as there was no convincing theoretical explanation behind this term. Much more recently, Pekola *et al.* showed that the subgap current in a high-quality opaque tunnel junction between a normal metal and a superconductor can be ascribed to photon-assisted tunneling [105]. They showed theoretically that this leads exactly to the Dynes DOS with an inverse lifetime of $\mathrm{e^2 k_B T_{env} R}/\hbar^2$, where $\mathrm{T_{env}}$ and R are the temperature and effective resistance of the environment.

2.1.4 Energetic resolution

Thermal broadening We will now take into account the influence of finite temperature on the differential conductance measurements. Combining Eq. 2.5 and 2.6 leads to:

$$\frac{dI}{dV} \propto N_t \int_{-\infty}^{+\infty} N_s(\epsilon)\, \mathrm{ch}^{-2}\left(\frac{\epsilon - eV}{k_B T}\right) d\epsilon \tag{2.9}$$

The LDOS of the sample is convoluted with a hyperbolic secant function, which smears out all electronic features. Our energetic resolution limit is thus defined by the full width at half maximum of this function, which is $\simeq 3.5\,\mathrm{k_B T}$. At ambient conditions of $\mathrm{T} = 300\,\mathrm{K}$, the energy resolution would be limited to $\Delta \mathrm{E} \approx 90\,\mathrm{meV}$, while at low-temperature the energy resolution is lower than the sub-meV range.

Finite modulation broadening To obtain spectroscopic data with high signal-to-noise ratio, we use a lock-in amplifier. This instrument employs a standard technique known as phase-sensitive detection to single out the component of the signal at a specific reference frequency and phase. Noise signals up to a certain level at frequencies other than the reference frequency are rejected and do not affect the measurement.
The tunneling voltage V is modulated with a small sinusoidal voltage $V_m sin(\omega_m t)$. The modulation frequency $f_m = \omega_m/2\pi$ is carefully chosen. For this purpose, we proceed to a fast Fourier transform (FFT) of the DC tunneling current signal to identify the frequencies exhibiting specific noise (e.g. electromagnetic noise at 50 Hz) and select a frequency that shows a low amplitude of noise. However, this modulation of the tunneling voltage limits our energy resolution. According to Ref. [131], we can define the *instrumental resolution function* $\mathrm{F}_m = \frac{2}{\pi}\frac{\sqrt{V_m^2 - E^2}}{V_m^2}$ of the lock-in. Put another way, our detected dI/dV signal can be written as a convolution of the sample LDOS N_s and the instrumental resolution function:

$$\frac{dI}{dV}(V) \propto (N_s * F_m)(V) = \frac{2}{\pi V_m}\int_{-V_m}^{+V_m} N_s(e(V+\epsilon))\sqrt{V_m^2 - \epsilon^2}\, d\epsilon \tag{2.10}$$

For a flat N_s with an only infinitely sharp feature at a given energy E, the broadening due to the lock-in modulation transforms the Dirac peak into a half-sphere of width $2\mathrm{eV}_m$ centered on E. To conclude, the broadening due to the lock-in measurement can be neglected as long as the modulation voltage is significantly smaller than the characteristic spectroscopic feature.

Definition of an effective temperature As seen in the previous paragraphs, both the temperature and the modulation voltage of the lock-in technique will limit our energetic resolution during a spectroscopic measurement. The measured dI/dV signal will thus be proportional to the sample LDOS convoluted with the thermal broadening function F_T=sech$^2(\epsilon/k_BT)$ and the instrumental resolution function F_m (eq.2.10):

$$\frac{dI}{dV}(V) \propto (N_s * F_T * F_m)(V) \tag{2.11}$$

Using the temperature as a fitting parameter is widely used for well known spectra, as for the BCS superconducting gap for example. The extracted temperature is a precise measurement of the electron gas temperature of the tip. Its discrepancy with the phonon bath temperature measured by the thermometer shows a problem of electronic thermalization. This can occur because of the poor efficiency at low temperature of the thermalization process involving phonons, or the presence of a voltage noise at the tunneling junction, originating from the power supply or the current-voltage converter. But as long as these noises are random, they can be included in Eq. 2.11 by using an effective temperature $T_{\text{eff}} = \sqrt{T^2 + T_n^2}$ with T_n the *noise temperature* originating from the electrical setup. The measured effective temperatures, typically between 230 - 300 mK, correspond to an energetic resolution of ∼70 - 90 μeV for our setup.

2.2 Andreev spectroscopy in point-contact mode on a superconductor

In this section, we will review how *point-contact* spectroscopy enables to probe a superconducting condensate. We will first describe the microscopic process of Andreev reflection and the electronic transport at an ideal N/S interface, then present the reference model of Blonder, Tinkham and Klapwijk (BTK) and some of its extensions. Finally, we will review the interests and advantages of this technique and present a set of experimental data acquired by point-contact spectroscopy.

2.2.1 Andreev reflection at a N/S interface

In a normal metal, electrons form a system of particles strongly interacting with each other via the Coulomb repulsion. Nevertheless, Landau showed it was possible to simplify this many-body system and describe this fermionic sea as a group of independent fermionic quasi-particles [9]. These quasi-particles correspond to an electron (when $\mathbf{k}>\mathbf{k}_F$) or a hole (when $\mathbf{k}<\mathbf{k}_F$) surrounded by their screening field. From now on, we will name electron (resp. hole) quasi-particles of electron (resp. hole) type.
In a superconducting metal described by the BCS theory, electrons closed to the Fermi level E_F are bound together in Cooper pairs below a critical temperature T_C. More precisely, an electron with a wave-vector $\mathbf{k}$ and a spin s is bound to an electron with opposite wave-vector and spin. This results in the apparition of an excitation gap Δ in the electronic density of states of the superconductor [14]. These Cooper pairs can carry a dissipationless electric current in the material.
We now consider a normal metal (N) brought in direct contact with a superconductor

(S), with no barrier at the N/S interface. Let apply to this junction a voltage V such as $eV < \Delta$. The transfer of quasi-particles of energy $\mid \varepsilon \mid < \Delta$ from the normal metal to the superconductor is forbidden as there are no available states in this latter in this energy range. This restriction only applies to single particle processes. Nevertheless, another type of transfer between N and S is possible at energies below Δ if we consider two-particles processes. Indeed, an electron can be transmitted into the superconductor if it goes along with a second electron, to form a Cooper pair in the superconducting metal. In terms of quasi-particle excitations, this process is equivalent to the reflection of the incident electron as a hole in the normal metal. Andreev described this process in 1964 [5]: an electron coming from the N side is reflected as a hole and a Cooper pair is transferred into S. Thus, for an incoming electron of energy $E_F+\varepsilon$, wave-vector $\mathbf{k}_F + \delta\mathbf{k}/2$ and spin s, the reflected hole will be characterized by an energy E_F-ε, a wave-vector $\mathbf{k}_F - \delta\mathbf{k}/2$ and a spin -s ([2]). This process turns out to double the conductance junction below the gap Δ.

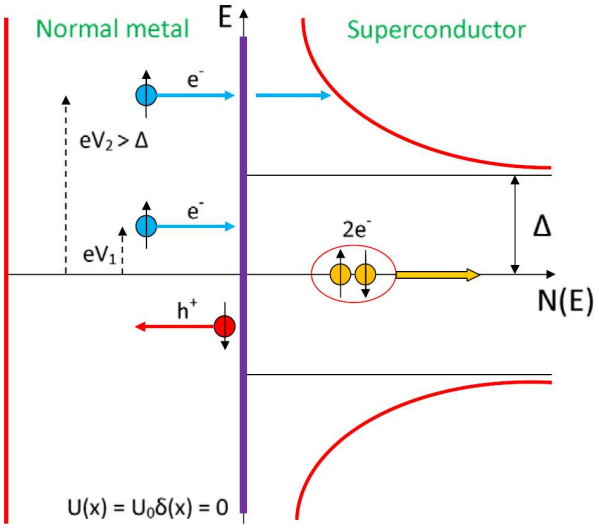

Figure 2.2 *Electrical transport at a transparent N/S interface. Incoming electrons with $eV_1 < \Delta$ are reflected as holes and induce Cooper pairs on the S side (Andreev reflection). Incoming electrons with $eV_2 >> \Delta$ are normally transmitted as electron-like quasiparticles. Reproduced from [38].*

If the applied voltage is now much greater than the gap ($eV \gg \Delta$), the current will have two contributions. The first one corresponds to the electrons whose energy is lower than the gap and still undergo *Andreev reflection* (AR), it thus does not depend on the applied voltage. The second contribution corresponds to the electrons with energy higher than the gap, which are simply transmitted through the interface (cf Fig.2.2) giving a voltage-dependent current. The total current for $eV \gg \Delta$ is:

$$I \propto ev_F(eV - \Delta) + 2ev_F\Delta \approx \frac{V}{R_N} + \frac{\alpha\Delta}{R_N} \tag{2.12}$$

where R_N is the contact resistance in the normal state and v_F the Fermi velocity in the superconducting metal. The first term simply refers to an ohmic behaviour whereas the second is an 'excess current', characteristic of the presence of a superconducting electrode. The numerical coefficient α takes into account the weakening of the order parameter at the interface, from Δ to 0. Its value is 1 if the gap drops from the bulk value to 0 over

[2] We here considered the case of an incoming electron with a normal incidence. For an ordinary incidence angle, the Andreev reflection transforms $\mathbf{k}$=$\mathbf{k}_\perp$+$\mathbf{k}_\parallel$ for the incoming electron into $\mathbf{k}$=$\mathbf{k}_\perp$-$\mathbf{k}_\parallel$ for the reflected hole.

a distance larger than the superconducting coherence length ξ and 4/3 in case of a sharp barrier [38].
The point-contact spectroscopic mode thus enables to probe the amplitude of the superconducting order parameter Δ via the Andreev reflection process. This technique is often referred to as point-contact Andreev-reflection spectroscopy (PCAR).

2.2.2 Blonder-Tinkham-Klapwijk model

We will now describe the phenomenon of Andreev reflection including the effect of a finite transparency of the interface. This model was introduced in 1982 by Blonder, Tinkham and Klapwijk and enables to calculate the current through a N/S junction from the metallic contact regime to the tunneling regime [23].

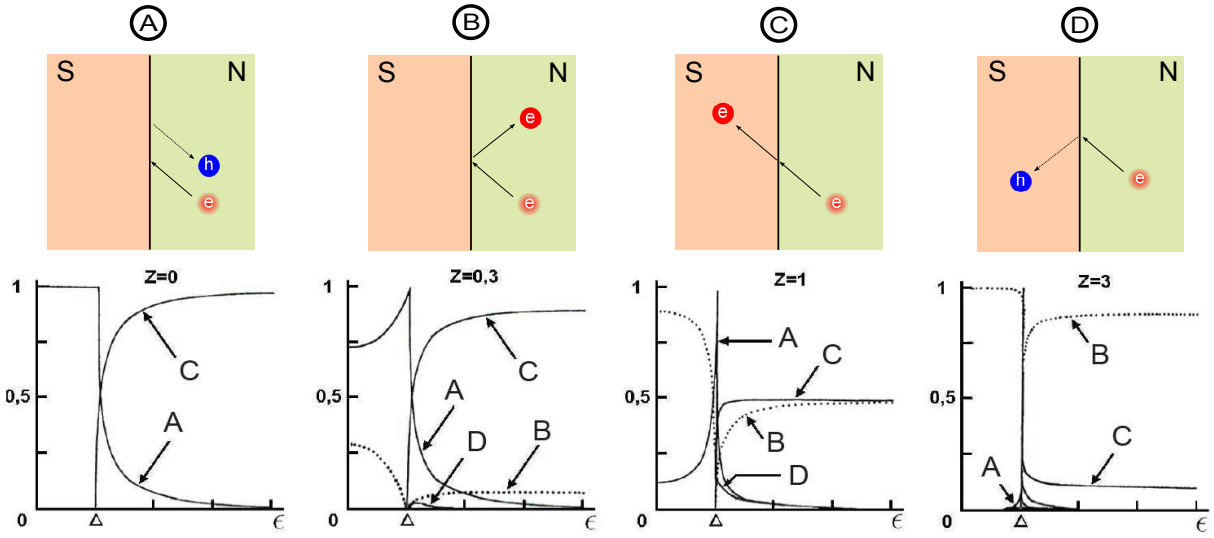

Figure 2.3 *Schemes showing the four elementary processes taken into account in the BTK model along with their associated probability in function of the interface transparency (Z) and the energy of the incoming particle. Adapted from [23].*

This is a ballistic 1D model (i.e. all the involved momenta are normal to the interface) which assumes a punctual contact involving only one conductance channel. The diffusion processes only happen at the interface, which is represented by a repulsive potential $U\delta(x)$, leading to the parameter $Z = U/\hbar v_F$. This dimensionless parameter corresponds to the *barrier transparency*. The smaller Z, the more transparent the barrier. In this way $Z = 0$ corresponds to a perfect transparency and $Z = \infty$ to a completely opaque barrier. This parameter is related to the reflection and transmission coefficients $\mathcal{R}$ and $\mathcal{T}$ of the interface through the following formula:

$$\mathcal{R} = \frac{Z^2}{1+Z^2} \quad , \quad \mathcal{T} = \frac{1}{1+Z^2} \tag{2.13}$$

An electron coming from the normal metal side N with an energy ε and meeting the interface with the superconductor S can undergo four different processes whose probabilities are:

A $\Longrightarrow$ probability of Andreev reflection: the electron is retro-reflected as a hole in N.

B $\Longrightarrow$ probability of normal specular reflection: the electron is reflected as an electron in N.

C $\Longrightarrow$ probability of transmission: the electron is transmitted in S as an electron.

D $\Longrightarrow$ probability of transmission with Fermi-surface crossing: the electron is transmitted in S as a hole.

Obviously, the sum of the four probabilities must be equal to 1. Solving the Bogoliubov-De Gennes equations enables to calculate the energy dependence of each parameter for every value of the Z parameter (cf Fig.2.3). We especially notice that the single particle transfer processes are impossible for energies below the superconducting gap, whatever the barrier transparency.
It can be shown that the expression of the total current across the junction, at T=0, is given by [23]

$$I_{NS} = 2N(0)ev_F\mathcal{A}\int_{-\infty}^{+\infty}[f(\varepsilon - eV) - f(\varepsilon)][1 + A(\varepsilon) - B(\varepsilon)]d\varepsilon \tag{2.14}$$

where f is the Fermi-Dirac distribution function, N(0) is the density of states at the Fermi energy and $\mathcal{A}$ refers to the contact area. The quantity $[1 + A(\varepsilon) - B(\varepsilon)]$ in Eq. 2.14 can be referred to as the *transmission coefficient for electrical current*. Its form highlights the competition between the specular reflection that contributes negatively to the current, and the Andreev reflection that increases it by transferring two transferred electrons (a Cooper pair) for one incident one. Besides, if both sides of the interface are normal metals, there is no Andreev reflection (A=0) and the transmission coefficient becomes $\mathcal{T} = (1 + Z^2)^{-1} = 1 - B(\varepsilon)$, so that Eq. 2.14 reduces to the simple form:

$$I_{NN} = \frac{2N(0)e^2v_F\mathcal{A}}{1 + Z^2}V \equiv \frac{V}{R_N} \tag{2.15}$$

Note that even in the absence of a barrier (Z=0), there is still a nonzero normal-state resistance. This is the resistance calculated by Sharvin in the ballistic regime, i.e. in the case of a point-contact geometry with a mean free path much larger than the contact radius [119].
The BTK model is thus a widely used and simple tool to understand the behavior of N/S junctions for different contact regimes. Nevertheless, it is based on a large number of approximations and simplifications. We present in the following two useful extensions of this model.

Finite temperature effects Taking in consideration the finite temperature effects in the BTK model is easily done by introducing the Fermi-Dirac distribution function at a finite temperature $f(\varepsilon, T)$ in Eq.2.14. The differential conductance can thus be written

$$G(V) = \frac{dI_{NS}}{dV} = 2N(0)ev_F\mathcal{A}\int_{-\infty}^{+\infty}[-f'(\varepsilon - eV)][1 + A(\varepsilon) - B(\varepsilon)]d\varepsilon \tag{2.16}$$

The evolution of the normalized conductance with parameters Z and T are plotted on Fig. 2.4. We notice for example that when T is increased, the two peaks typical of AR are smeared out, finally leaving a single maximum at the Fermi energy, with a reduced amplitude compared to the peaks' one at T=0.

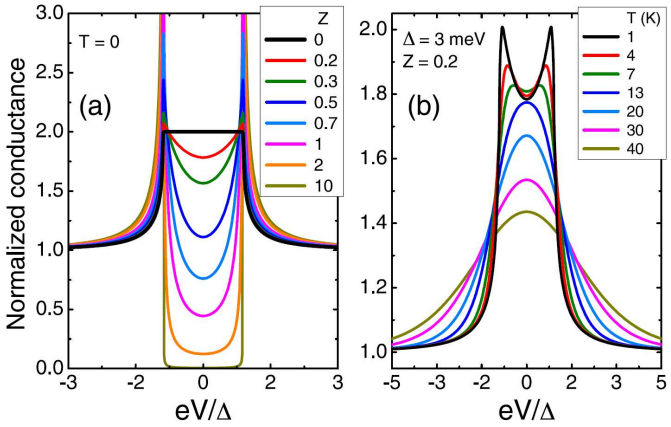

Figure 2.4 *Normalized conductance evolution. (a) At T=0 for different barrier parameter Z, from pure Andreev (Z=0) to pure tunneling (Z=10) regimes. (b) Effect of the thermal smearing on the normalized conductance with an intermediate barrier transparency (Z=0.2) and a fixed Δ = 3 meV. Reproduced from [38].*

Fermi velocity mismatch at the interface In a realistic system, when two materials are contacted, the Fermi velocity mismatch can give rise to charge carrier reflections at the interface even when no barrier is present. Blonder and Tinkham introduced this effect in the original BTK theory [22] by adopting an effective barrier parameter:

$$Z_{eff} = \sqrt{Z^2 + \frac{(1-r)^2}{4r}} \tag{2.17}$$

where the second term expresses the effect of the mismatch of the Fermi velocities between the S and the N sides in terms of their ratio r=v_{FS}/v_{FN}. A mismatch in the Fermi velocities leads to a renormalization of the Z parameter. On the experimental side, it is nevertheless impossible to distinguish these two contributions. Besides, PCAR spectroscopy measurements done on cuprates could be fitted with low Z values ($Z_{max} \simeq 0.3$) whereas the Fermi velocities a priori imposed a much higher limit Z_{min}, of the order of 2 by supposing the absence of any dielectric barrier [88]. Deutscher and Nozières explained this result asserting that the Fermi velocity of the quasi-particles undergoing AR was different from the one determined for a bulk sample, which is renormalized by taking into account the effects of many-body interactions [43].

In conclusion, though very simple, the BTK model proved to be a very useful tool to explain numerous experimental results on N/S junctions. The incorporation of additional effects, like for the 3D case, a finite width for the barrier or non spherical Fermi surfaces for example, thus only brings minor corrections to the original model.

2.2.3 Interests and advantages of PCAR spectroscopy

We have seen in the present chapter that tunneling and PCAR spectroscopy were two suitable techniques to probe the superconducting state. They are widely used to characterize numerous and various types of superconducting materials, like metals, doped semiconductors, high critical temperature superconductors or more recently disordered superconductors [42, 38]. We have also presented the BTK model, which enables to continuously describe the transition from the tunneling regime to the metallic regime by varying a unique parameter characterizing the interface between the normal metal and the superconductor. If this description is correct for many materials, it fails nonetheless for more complicated cases.

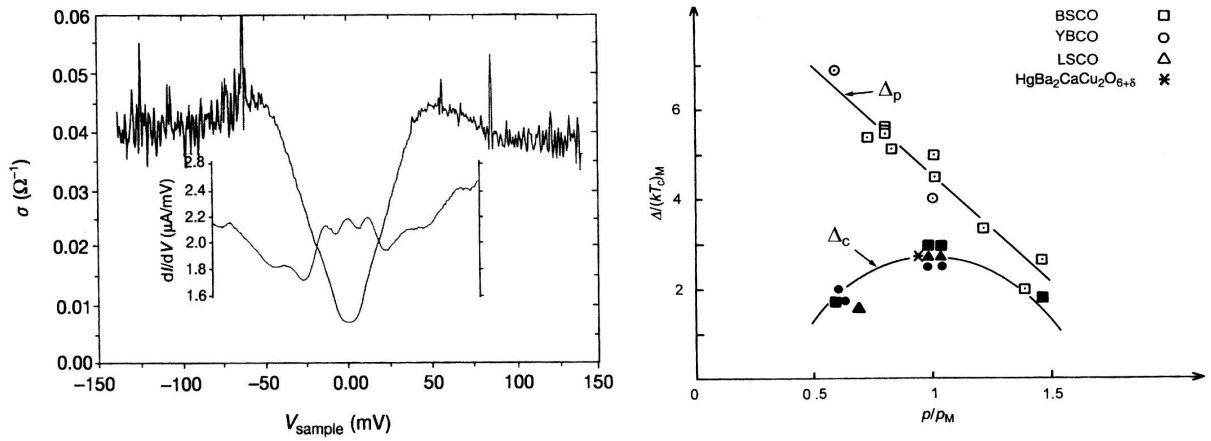

Figure 2.5 *Left: comparison between PCAR (inside graph) and tunneling spectroscopic measurements measured on similarly underdoped YBCO samples. Right: Behavior of PCAR and tunneling (or ARPES) energy scales as a function of doping in different cuprates. Reproduced from [41].*

Indeed, in 1999 Deutscher compared tunneling and PCAR spectroscopic measurements on different high-Tc superconducting cuprates and highlighted the presence of two different energy scales in these compounds (see Fig. 2.5). Surprisingly, the gap values obtained from conductance characteristics dominated by Andreev reflections are equal to or smaller than gap values obtained from single-particle tunneling. Although the origins of these two energy scales do not win unanimous support, many authors lean towards the thesis that connects the high temperature pseudogap with the pairing strength (i.e. the binding energy of the two electrons forming a Cooper pair) and the low energy scale with the superconducting condensation energy [69]. This theory supposes the pre-formation of Cooper pairs at a temperature $T^*>T_c$, which then later condense into a coherent superconducting state at the bulk transition temperature T_c.
This thesis has also been exploited in the case of strongly disordered superconductors, where a pseudogap-like feature was observed at $T>T_c$ and attributed to the localization of preformed Cooper pairs, which then condense into a single superconducting state at T_c [118]. A subsequent study by PCAR spectroscopy with an STM tip revealed the existence of two energy scales in the conductance spectra, the small one attributed to the condensation energy and the other to the pairing strength [47].

PCAR spectroscopic measurements performed on disordered superconducting thin films of NbSi are presented in the following section, to give an insight on these kind of experiments.

2.2.4 PCAR spectroscopy on NbSi disordered thin films

Superconductor-insulator transition in NbSi thin films During this thesis, I worked on two projects aiming at getting a better insight on the superconductor-to-insulator transition taking place in disordered superconducting thin films. STS study of amorphous Nb_xSi_{1-x} thin films has been one of these projects. These films present a quantum phase transition with an intermediate metallic phase that has been little explored.

Although transport measurements at low temperature have shown agreement with some theoretical predictions for a *Bose metal*[3] [36], no local study of the superconducting properties of amorphous Nb_xSi_{1-x} 2D systems has been reported so far.
We collaborated with Claire Marrache-Kikuchi at CSNSM[4] where the samples have been fabricated by an electron-beam co-evaporation technique. This method allows to control precisely the stoichiometry and the thickness of Nb_xSi_{1-x} thin films, which are made as homogeneous as possible. We will present STS data measured on a 10 nm-thick film of $Nb_{15}Si_{85}$. The STM study has been greatly complicated by the poor quality of the surface, due to a native oxide layer that grows when the films are exposed to ambient air, as well as by the very low transition temperature of the film (∼160 mK measured in transport in our STM set-up during the cooling down to 50 mK, see Fig. 2.6). Indeed, the energetic resolution of our set-up (∼250 mK) does not allow us to resolve the coherence peaks and a full gap when this latter is intrinsically small.

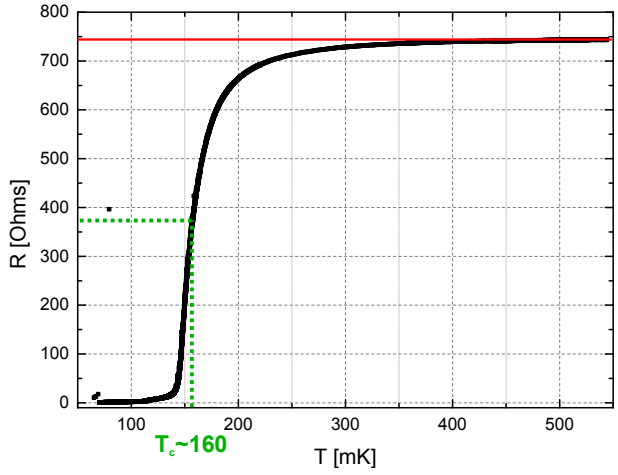

Figure 2.6 ***Transport measurement*** *- The superconducting transition temperature is taken at the middle point of the transition. This gives $T_c \sim 160$ mK.*

From the tunneling regime to the point-contact regime A scanning tunneling microscope offers the possibility to move continuously from a local tunneling spectroscopic measurement of the DOS to the measurement of the local conductance by Andreev spectroscopy. The gradual transition between the *tunneling regime* and the *contact regime* is controlled by the *contact resistance* R_c defined by $R_c = V_{bias}/I_t$ where (V_{bias}, I_t) is the working point of the microscope: the STM feedback-loop adjusts the tip-sample distance so as to get a tunnel current I_t when a potential difference V_{bias} is applied between the tip and the sample. The study of superconducting systems implies to work in an energy scale of the meV range, with a tunnel current such as $I_t \sim 0.1 - 1$ nA, which leads to a contact resistance $R_c \sim 1 - 10\,\mathrm{M\Omega}$. For a ballistic contact between two electrodes involving only one quantum channel, the tunneling regime is separated from the contact regime by the resistance quantum $R_q = h/2e^2 \sim 12.9\,\mathrm{k\Omega}$. In the case of Andreev spectroscopy, two electrons tunnel at once, and one should thus compare our contact resistance to $R_q \sim 6.5\,\mathrm{k\Omega}$. In practice, the "good" contact regime is obtained for typical values of $R_c \sim 5 - 10\,\mathrm{k\Omega}$.
To describe continuously the transition between the tunneling regime to the point-contact regime, we modified our current amplifier so as to work in a range of contact resistances

[3] A theoretically predicted 2D quantum metal formed of incoherent Cooper pairs [39].
[4] Centre de Sciences Nucléaires et de Sciences de la Matière, F-91405 Orsay.

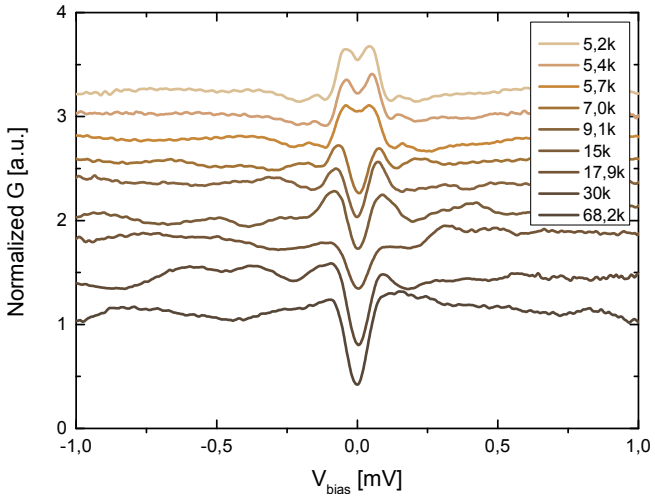

Figure 2.7 ***Evolution from tunnel regime to point-contact mode (1)*** - *STS measurements from tunnel regime (lowest curve) to point-contact mode (upper curve). The tunneling resistance is indicated in kΩ for each spectrum. The spectra have been shifted for clarity.*

such as $R_c \sim 0.5 - 500\,\mathrm{k\Omega}$. Starting from the tunneling regime, and fixing the lateral tip position over the sample surface, one then performs successive spectroscopic measurements while increasing the tunnel current set-point. The STM feedback-loop enables a precise control of the contact resistance as long as $R_c \gtrsim R_q$. For smaller values of R_c, the tunnel current does not show an exponential dependence with the tip-sample distance anymore and it is then more convenient to switch off the feedback-loop and act directly on the tip position: by gradually elongating the piezoelectric tube, one decreases R_c progressively until reaching the regime of best contact. A tunnel-to-contact regime evolution is presented on Fig. 2.7 for $R_c = 68.2\,\mathrm{k\Omega} \rightarrow 5.2\,\mathrm{k\Omega}$ (from the bottom to the top curve). In the tunneling regime, the coherence peaks of the spectra are hardly visible and the superconducting origin of the gap can be questioned. The advantage of the continuous evolution from the tunneling regime to the contact regime is to unveil this superconducting origin. Indeed, the increase of the conductance in the same energy range than the gap is qualitatively well described by the BTK model (see Fig. 2.4 a), with R_c playing the role of the barrier transparency.

Superconducting features in the tunneling regime In the tunneling regime ($\mathrm{R_{tunnel}} \sim 1\,\mathrm{M\Omega}$), the sample presents large inhomogeneities in the gap values, exhibiting very small gaps $\Delta_{small} \sim 100\,\mu eV$ without coherence peaks and a non-zero DOS at the Fermi energy (as seen on Fig. 2.7), as well as very large ones $\Delta_{large} \sim 400\,\mu eV$ with small but existing coherence peaks and a hard gap (DOS falling to zero). Surprisingly, no intermediate behavior has been observed. The small gaps measured in the tunneling regime close at various temperatures, we measured 600 mK and 1 K, which are much larger than the transition temperature estimated in transport ($\mathrm{T_c}$=160 mK at the middle point of the transition). For these gaps, we calculate Δ_{small}/T_c=7.25, which is in agreement with previous measurements performed on TiN [116] and InOx [118] disordered thin films. This corresponds to a so-called *pseudo-gap regime* characterized by the presence of pre-formed Cooper pairs above T_c that are more or less localized due to disorder. The effect of disorder is to add a contribution to the size of the gap (parity gap), leading to a Δ/T_c ratio much bigger than in the BCS case of 1.76 (more than 4 times larger in our case).

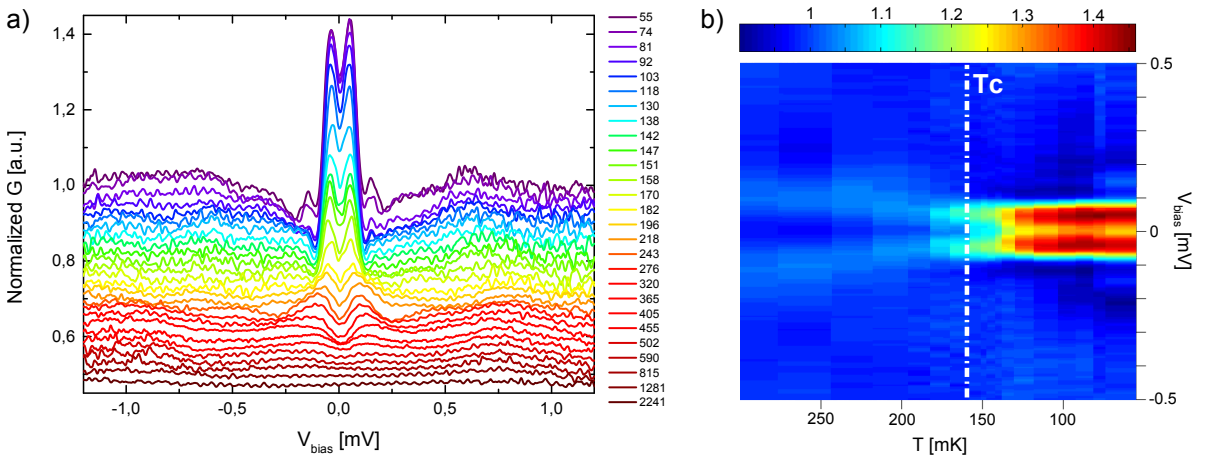

Figure 2.8 ***Temperature evolution in the contact regime (R_{tunnel}=5.4 kΩ) (1)*** *- (a) Temperature dependence of the conductance. The temperatures are indicated in mK. The spectra have been shifted for more clarity. (b) Normalized conductance map as a function of temperature and bias voltage.*

PCAR spectroscopy As already mentioned, Fig. 2.7 presents a tunnel-to-contact evolution for a small superconducting gap without coherence peaks. It is qualitatively well described by the BTK model with one energy scale corresponding to the gap border in the tunneling regime that transforms into two peaks in the contact regime. Once well stabilized in the regime of best contact ($R_c = 5.4\,\text{k}\Omega$), we carried out a temperature dependence spectroscopic measurement[5]. The data are plotted in Fig. 2.8, for T varying from 55 mK to 2.24 K. Here again, the temperature evolution presented in (a) is qualitatively well described by the BTK model (see Fig. 2.4 b), except that the conductance is not flat when we pass T_c ∼160 mK as expected in the BTK model, but becomes featureless at 450 mK. This is also clear on the conductance map (b). This could be explained in the framework of the superconducting fluctuations theory above T_c [81]. We notice that the peaks in the conductance spectra move at higher energies for T>T_c. This originates from the voltage drop at the tunnel junction due to the increase of the sample resistance. Indeed, as $V_{bias} = (R_c + R_{sample})I_t$, when R_{sample} increases for T>T_c the tunnel current decreases for a given voltage polarization set-point. Thus, the effective bias voltage at the tunnel junction $V_{\text{eff}} = R_c I_t$ decreases. In practice, one should then rescale the presented plot.

Another tunnel-to-contact evolution for a large superconducting gap is presented on Fig. 2.9, for $R_c = 100\,\text{k}\Omega \rightarrow 3.1\,\text{k}\Omega$ (from the bottom to the top curve). The evolution of the superconducting features seems complex and clearly beyond the simple BTK model. The temperature dependence of the conductance in the contact regime, plotted on Fig. 2.10 for T varying from 52 mK to 2.95 K, also presents various energy scales that behaves differently with temperature. If the two central peaks seem to disappear around

[5]Note that when the material will no longer be superconducting, the sample resistance will add to the contact resistance and the tunnel current will decrease for a fixed bias voltage. It is thus necessary to switch off the feedback-loop during the whole temperature dependence measurement to keep a constant tip-sample distance.

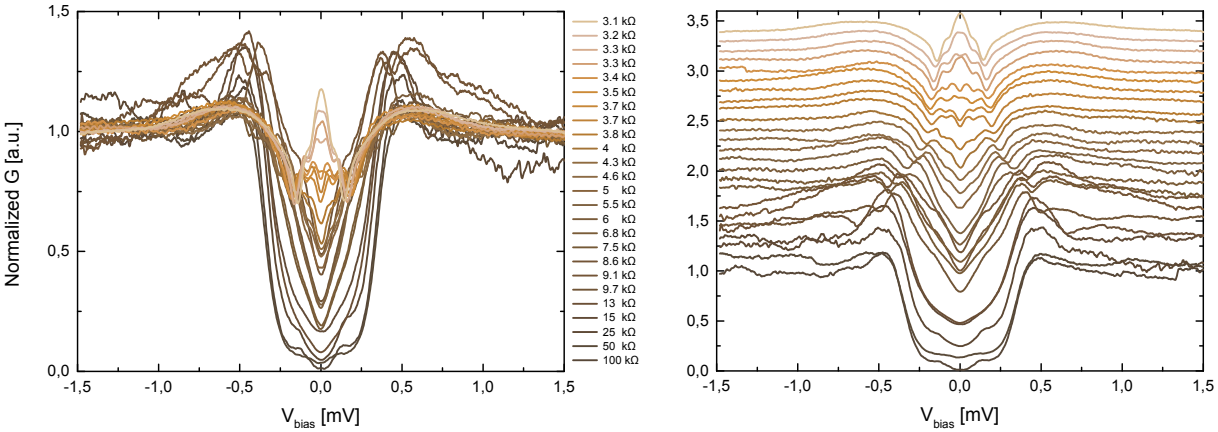

Figure 2.9 ***Evolution from tunnel regime to point-contact mode (2)*** *- STS measurements from tunnel regime (lowest curve) to point-contact mode (upper curve). The tunneling resistance is indicated in kΩ for each spectrum. Left: superimposed spectra. Right: shifted spectra for the sake of clarity.*

T_c, the external big bumps persist up to 2.5 K, as illustrated on panel (b). Previous works [48, 47] and theories [52] described the existence of different energy scales that could be revealed by PCAR spectroscopy on superconducting disordered systems. The spectral gap would be the sum of two components, a pairing energy term and a term linked to the superconducting coherence energy.

If the analysis of the presented data is beyond the scope of this thesis, clues for their interpretation should certainly be found in the cited works.

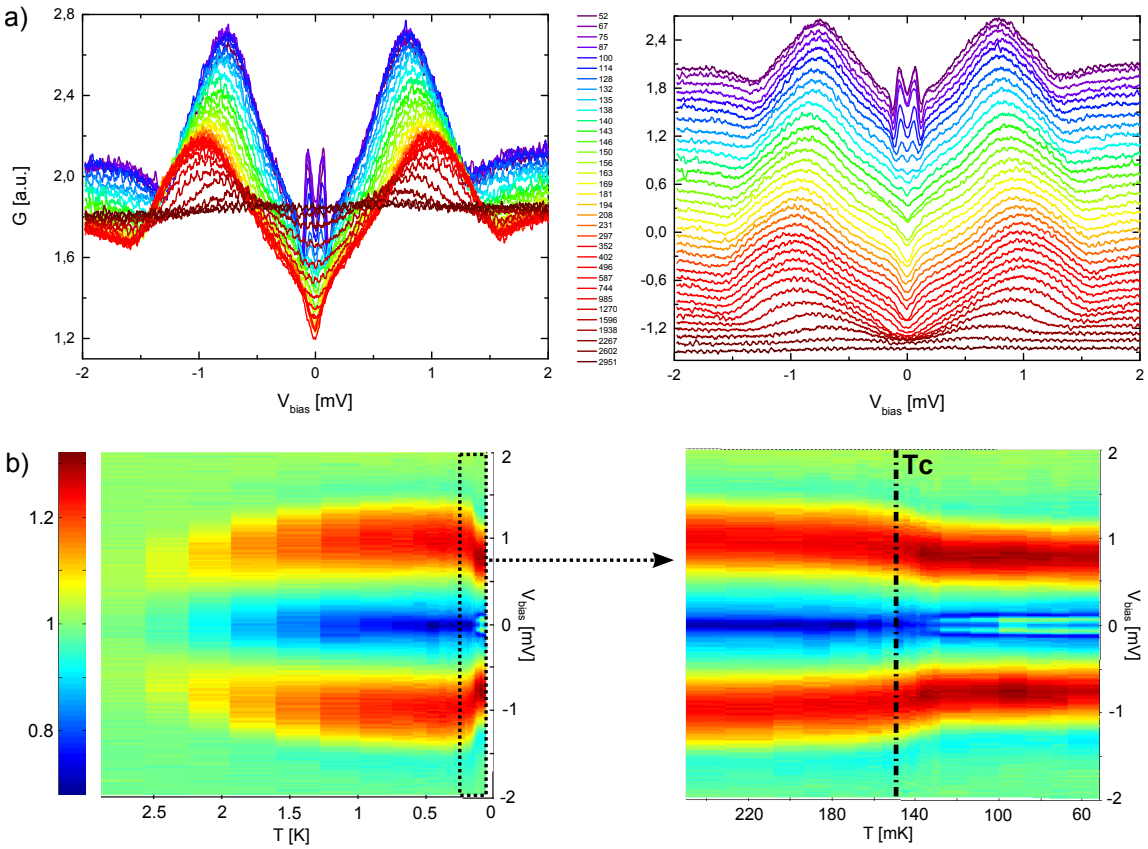

Figure 2.10 ***Temperature evolution in the contact regime (R_{tunnel}=4.3 kΩ) (2)*** - *(a) Temperature dependence of the conductance. The temperatures are indicated in mK. The spectra have been shifted on the right plot. (b) Normalized conductance maps as a function of bias voltage and temperature. The right map is a zoom between 50 and 250 mK.*

2.3 Tunneling spectroscopy with a SIS junction

If the STM has been widely used to study the local properties of superconducting samples since its early history, the first use of a superconducting tip was reported in 1998 [101]. Since then, several groups reported the use of superconducting tips as STS probes [94, 148, 113, 76]. Nevertheless, this technique encountered a limited enthusiasm in the scientific community that might be due to the difficulty to fabricate them. Yet, it enables to access new valuable information about the superconducting condensate and tremendously improves the spectroscopic resolution.

2.3.1 Improvements and new information accessed

Energetic resolution One of the key points for tunneling spectroscopy is the energetic resolution of our setup. As seen in details in section 2.1.4, there are several sources limiting our spectroscopic resolution, which can be gathered under two categories: the electronic noise and the temperature. For the first one, we try to reduce it by better filtering our signals and using low-noise cables and electronic apparatus. As for the second one, we are inevitably limited by the temperature of our refrigerator. Nevertheless, there is a way to get rid of this latter source of broadening. As it arises from the $\sim 3.5\,k_BT$ width of the Fermi edge, the idea is to use as a probe a material with a sharp spectroscopic feature (sharper than $3.5\,k_BT$). An obvious candidate is a superconductor, as it naturally presents two singularities at the gap edges (the coherence peaks). Indeed, as seen on Fig. 2.11, whereas the gap edge is broadened at finite temperature in the NIS case, it stays sharp and unbroadened in the SIS case, because of the crossing singularities in the DOS of the left and right electrodes.

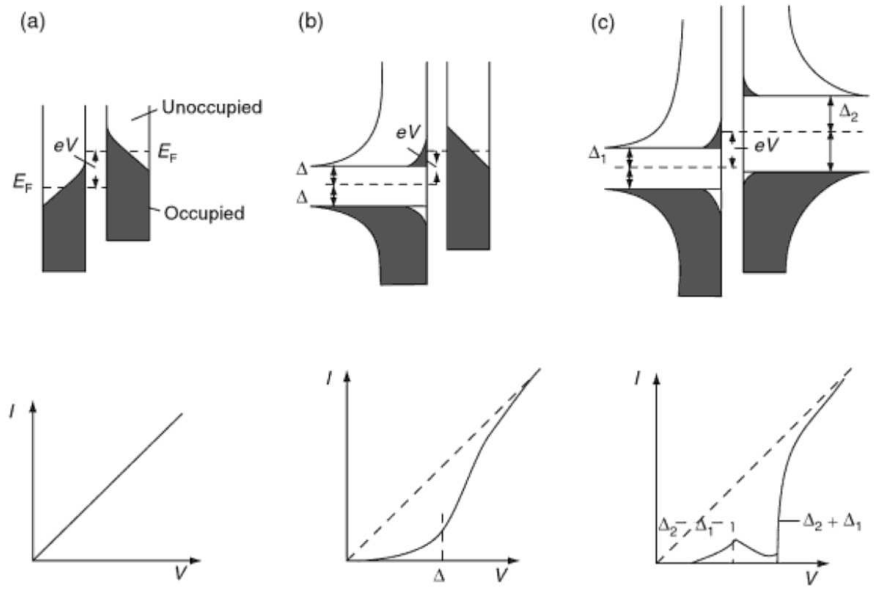

Figure 2.11 *Sketches indicating the quasiparticle current-voltage characteristics expected in three basic cases: (a) two normal metals, (b) a normal metal and a superconductor, and (c) two superconductors. Reproduced from [146].*

Josephson tunneling When we perform scanning tunneling spectroscopy with a normal tip, we probe the single-particle excitations spectrum. On superconductors, we thus access the gap structure, which is a consequence of superconductivity, but we don't directly probe the superconducting ground state itself. Yet, the properties of the condensate

on a local scale are largely unknown, for instance in high-T_C cuprate superconductors, which present the famous *pseudogap* in underdoped samples above T_C [84, 44, 110] or similar structures in the vortex cores [111, 103] and in disordered superconductors [117, 118]. The measurements used to characterize these samples (STS, ARPES,...) did not remove the ambiguity with respect to the existence of a finite superconducting pair amplitude. The STS performed with a superconducting tip has the ability to shed light on these interrogations, in measuring the contribution from **Josephson pair tunneling** to the total tunneling current. It thus gives access to the local superconducting pair amplitude with high spatial resolution.

2.3.2 Tip fabrication and characterization

The fabrication of an STM tip is a tricky process as it has to ensure that the obtained tip is of good quality for both topography and spectroscopy measurements. For measurements of the first kind, the tip must be atomically sharp to enable good spatial resolution during scanning. While for spectroscopy measurements, one needs to have an exact knowledge of the electronic properties of the superconducting tip, in order to be able to determine which spectroscopic features characterize the sample. This can actually be a problem when we notice the principal candidates to fabricate a superconducting tip (like Al, Pb, Nb) get easily oxidized in air. The interest of an STM installed in a UHV system becomes obvious here as it enables to fabricate the superconducting tip in a very clean environment just before using it [148, 109]. Nevertheless, if the UHV system is an advantage, it is not necessary. Indeed, some groups non equipped with UHV set-ups reported the controlled fabrication and use of superconducting tips as STS probes, among them the group of S. Vieira in Madrid. J.G. Rodrigo and S. Vieira reported their *in situ* fabrication process in their low temperature STM in several publications [113, 112, 114].

Preparations in air at room temperature A thin plate of pure lead (99.999% and about 1 mm thick) is used as based material to cut the superconducting tip. The apex is pyramid-shaped and must be as sharp as possible, with every face freshly cut to remove the accumulated lead oxide[6]. The tip is then positioned on the tip holder in the STM body. On the sample holder, besides the sample itself, we prepare a small lead sample (with a freshly cut surface) and a small gold sample. All these substrates are glued side by side. To position the tip over the different substrates, the microscope body is equipped with a capacitance bridge. It consists in two metallic plates glued opposite to each other, one on the microscope body, the other on the sample holder which can be shifted in the x direction. When the sample holder is moved, the overlapping surface of the two plates varies, inducing a capacitance variation measured with a lock-in technique[7]. The capacitance is at first measured at room temperature for different tip positioning that we can easily visualize thanks to a video-camera. This enables to realize a full calibration of the interesting zone covering the three substrates by establishing connection between the capacitance values and evolution and the position of the tip over the different samples. At low temperature (the set-up went down to 300 mK), the calibration will be slightly

[6] To obtain the desired tip geometry, it would be easier to begin from a lead wire but the easy oxidation of this material would prevent to get a fresh pure lead apex.

[7] Indeed the detected capacitance is very small (~ 0.5 pF) and thus hard to measure with precision.

different following the contraction of the gap between the two plates but the capacitance variation will stay linear along the samples alignment axis.

***In situ* tip modelling at low temperature** Once the low temperature regime has been reached, the tip is positioned on the lead substrate to process to the tip modelling. First, the tip is deeply indented into the lead sample, to form a strong contact between them, called connective neck, which can be elongated by means of a controlled pulling and pushing process. This results in the creation of a nanobridge between the tip and the sample, which can be broken apart leading to a clean sharp tip. As the mobility of the lead atoms are reduced at these very low temperatures, the tip apex won't change its shape over time. This *in situ* fabrication method at low temperature ensures the tip apex will be stable and clean, free from oxides or any type of external contamination.

Tip characterization

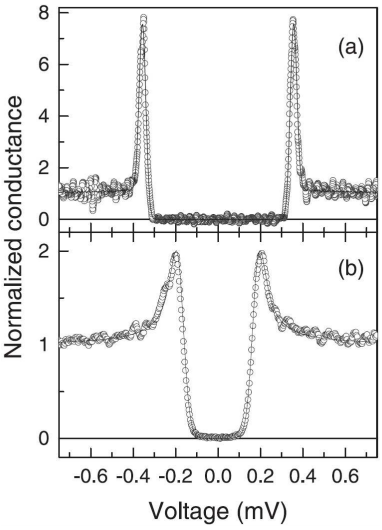

Figure 2.12 *Normalized conductance curves obtained in tunnelling regime when both tip and sample are made of Al (a), and when the Al tip is located over a gold sample (b). Reproduced from [114].*

Once a stable superconducting tip has been fabricated, one needs to characterize precisely its electronic properties. By measuring conductance curve on the gold sample we can get information on the superconducting gap of the tip Δ_{tip} and the temperature achieved in the junction region by fitting with the conventional BCS theory[8]. Fig. 2.12 shows an example of two spectra acquired with an aluminium tip on an aluminium (top) and a gold (down) sample, as found in the literature. The good agreement with the BCS fit in (b) shows that a nanoscopic superconducting tip presents the density of states predicted by theory for bulk superconductors, which is an important result in itself. The study is slightly more complicated with lead which is a strong coupling superconductor that presents an anisotropic gap. One must introduce a distribution of gap values and take the temperature (350 mK) and the energy resolution previously determined to extract the gap value. Once this latter is precisely known, it will be possible to extract relevant information on the sample parameters from the tunneling conductance which is a convolution of the two superconducting DOS (tip and sample).

2.3.3 Measurements on TiN thin films

The data presented in this section were collected in the *Laboratorio de Bajas Temperaturas* of the *Universidad Autónoma de Madrid* in the group of S. Vieira, on the set up of J.G. Rodrigo. The STM was cooled down to 300 mK in a He^3 refrigerator. TiN films were

[8]Note that this temperature can only be deduced after the determination of the spectroscopic resolution of the system extracted from spectra measured on the same superconductor sample [114].

chosen as they present a direct superconductor-to-insulator transition (SIT) close to the strong localization threshold.

Films characteristics The samples of titanium nitride were supplied by T. Baturina[9] and fabricated in IMEC[10]. Grown atomic layer per atomic layer, the films present an excellent crystallographic quality. Nevertheless, chlorine impurities are present as residues from the chemical reactions occurring during the growth. The films structure is polycrystalline with crystalline domains of about 5-10 nm diameter (see Fig. 2.13 middle). UV lithography enables to shape a Hall cross for transport measurements in four-terminal sensing (see Fig. 2.13 left). The STM tip will be positioned on a pad.

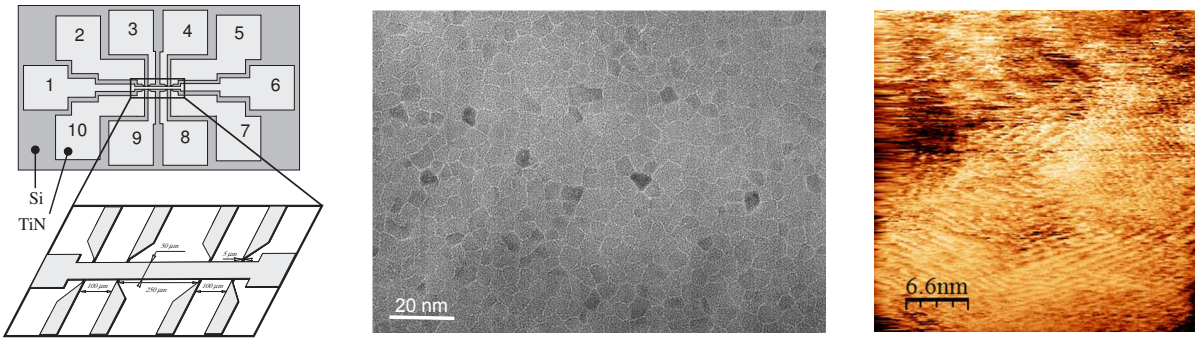

Figure 2.13 *Left: Scheme of the Hall cross. The pad surface is* $500 \times 500\,\mu m^2$*. Middle: TEM image of a TiN sample surface showing the polycrystalline structure of the film. Right: Low temperature STM topographic image.*

STM and STS measurements The measured film was 7 nm-thick and rather far from the SIT with a superconducting critical temperature of ~ 2 K. This was indeed a necessary preliminary step to well characterize the superconducting state before getting closer to the strong localization threshold. Atomic resolution could be achieved on topographic images showing areas with different atomic orientations, identified to crystallites (see Fig. 2.13 right). Analysing the topographic images by Fourier transform let us extract a lattice parameter of ~ 4.5 Å, which is consistent with the theoretical value of 4.2 Å (TiN is a face-centered cubic crystal system). A typical set of STS measurements can be seen on Fig. 2.14. They were acquired in the contact regime, i.e. with a tunneling resistance $R_T \sim 20\,k\Omega$, to reveal Josephson current and multiple Andreev reflections (MARs) features.

In this case, the differential conductance is not anymore proportional to the local density of states of the sample, as this simplification resulted from the assumption of a flat DOS of the tip. One must now deconvolve by the tip DOS if one wants to extract the sample DOS. In our case, we preferred to analyze the as-measured conductance spectra and extract the interesting quantities. As seen on Fig. 2.14, the conductance spectra present a gap with very sharp edges and non-zero conductance features inside this gap. The gap edge is at the energy $\Delta_1 + \Delta_2$ where $\Delta_{1,2}$ are the superconducting gaps of the

[9] Institute of Semiconductor Physics, Novosibirsk, 630090 Russia
[10] IMEC Kapeldreef 75, B-3001 Leuven, Belgium

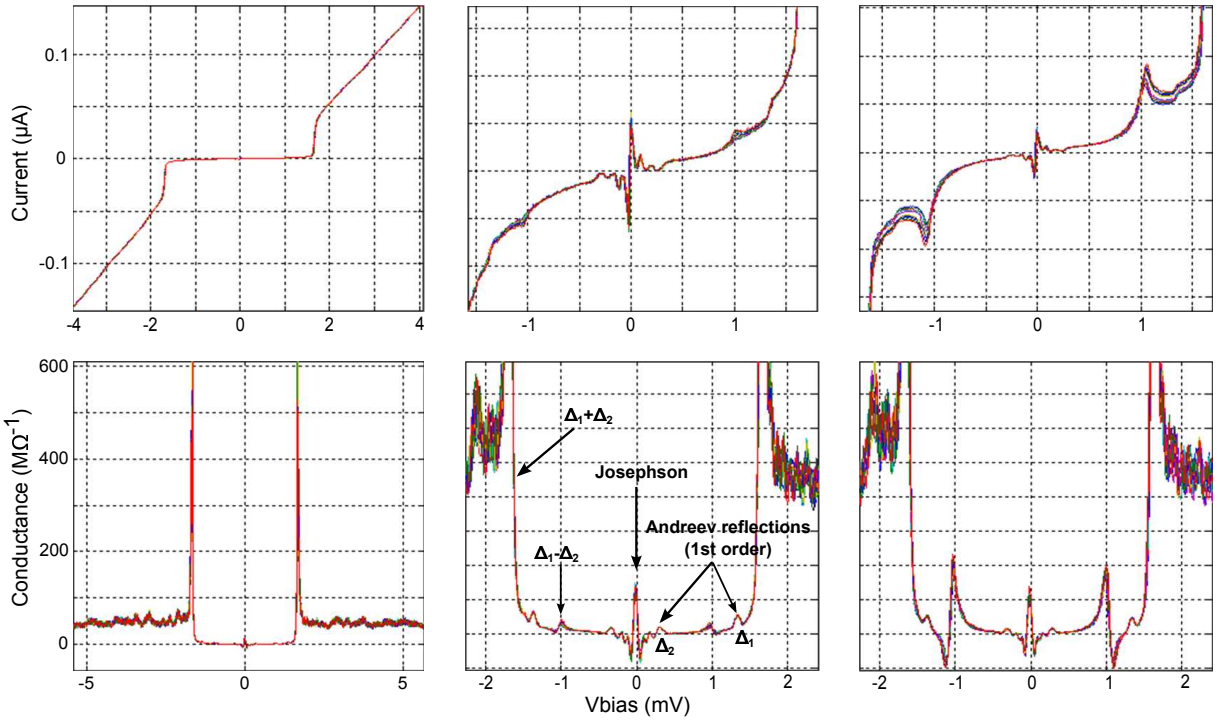

Figure 2.14 *Typical I-V characteristics (up) and conductance spectra (bottom) measured with a superconducting lead tip. The temperature is increased from left to right (T=0.60 K, 1.05 K, 1.50 K).*

tip and the sample. The two peaks at energies Δ_1 and Δ_2 are the hallmark of first order Andreev reflection processes. Indeed, in asymmetric superconducting tunnel junctions, MAR are predicted to occur at energies $\pm\Delta_1/m$, $\pm\Delta_2/m$ and $\pm(\Delta_1+\Delta_2)/(2m+1)$[11] [70]. Conductance peaks arising at $\pm \mid \Delta_1 - \Delta_2 \mid$ can have two different origins: either a thermal activated tunneling of single quasiparticles due to finite temperature in all kind of junctions at any junction resistances (see Fig. 2.11), or an enhancement of the probability of MAR that transfers three electron charges and involves two AR happening for asymmetric junctions at low junction resistances (see Fig. 2.15). Thanks to these subgap features, it is possible to estimate the gaps of the two superconductors (tip and sample) with good accuracy. In our case, we calculate $\Delta_{tip} = 1.35\,\text{mV}$ and $\Delta_{sample} = 0.33\,\text{mV}$, confirming a very asymmetric junction ($\Delta_{sample}/\Delta_{tip} \simeq 0.25$).

Also observed is the peak at V=0 corresponding to the Josephson current, i.e. the tunneling of Cooper pairs from the tip superconducting condensate to the sample superconducting condensate. Contrary to SIN junction spectroscopy measurements, where the gap structure is a consequence of superconductivity, the Josephson current is a *direct* probe of the superconducting ground state itself. Indeed, the critical current is determined by the Cooper pair density and the tunneling resistance of the junction [94]. The presence of a Josephson current peak at zero bias and Andreev reflection peaks at low tunneling resistance leaves no doubt on the existence of a finite superconducting pair

[11] This feature, which should appear around 0.56 mV, is not observed here. This is not surprising as its intensity is expected to be lower than the $\pm\Delta_1/m$ and $\pm\Delta_2/m$ peaks (which are not so pronounced here) and second, it is predicted to disappear for very asymmetric junctions (for $\Delta_2/\Delta_1 < 0.3$) [132]

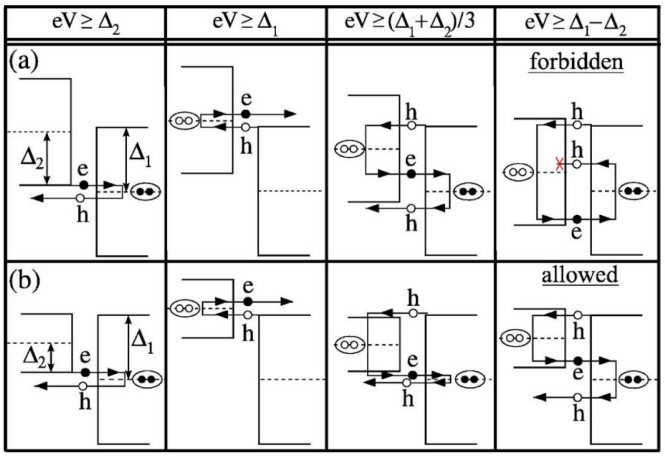

Figure 2.15 *Schematic representation of the most pronounced MARs in asymmetric SIS tunnel junctions. (a)* $\Delta_2/\Delta_1 \approx 0.8$*, (b)* $\Delta_2/\Delta_1 \approx 0.4$*. See more details in the text. Reproduced from [132].*

amplitude in the studied sample. This is a crucial information, which could contribute to close the debate on the origin of the pseudogap observed in high-T_c superconductors and disordered thin films.
In the experiment on TiN films presented hereabove, the sample was rather far from the SIT and no pseudogap regime was observed. This work was a preliminary step to characterize the "standard" superconducting state of TiN films, before studying samples closer to the SIT.

Conclusion

We have presented in this chapter different spectroscopy techniques accessible with an STM. The most common being the tunneling spectroscopy using a normal tip, which is easily set up and gives access to the local density of states of the sample. Nevertheless, it reaches limitations at very low temperature when one tries to access low energy scales ($<$ meV), due to the Fermi broadening of the tip DOS which smears out the features of the sample DOS. This could be problematic, particularly when the studied sample is a superconductor, as its features sharpness gives information about its superconducting state. In this case, it could be interesting to use one of the two other spectroscopy techniques. Point-contact Andreev reflection spectroscopy enables to access different energy scales when we consider superconductors that do not fit in the general frame of BCS theory (such as high-T_c or disordered superconductors). Another option is to do tunneling spectroscopy with a superconducting tip. In addition to tremendously increase the energetic resolution of the measurement due to the sharp features in the tip DOS, this last spectroscopy technique is a direct probe of the superconducting condensate. Indeed, the Cooper pair tunneling (or Josephson tunneling) gives access to the local superconducting pair amplitude with high spatial resolution.

Chapter 3

Superconductivity in graphene

Contents

Introduction

Graphene belongs to the family of the the carbon sp^2 allotropes, along with graphite, carbon nanotubes and fullerenes. It is conceptually considered as the 'mother structure' of these three other atomic arrangements, as it can be wrapped up into 0D fullerenes, rolled into 1D nanotubes or stacked into 3D graphite (cf Fig. 3.1). For this reason, graphene's electronic structure has been studied for more than 60 years [140] but no one knew if this form of carbon could exist. Indeed, it was believed that strictly 2D crystals were thermodynamically unstable and could not exist at any finite temperature, as demonstrated by Landau and Peierls in the 1930s. One had to wait until 2004 for this belief to be refuted by the isolation of a single sheet of graphene by Andre Geim and Konstantin Novoselov, who were awarded the Nobel Prize for their discovery.

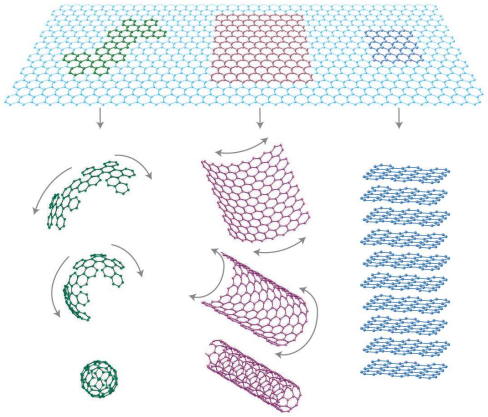

Figure 3.1 *The sp2 carbon allotropes: 0D fullerenes (left), 1D nanotubes (middle) and 3D graphite (right) can all be derived from a graphene sheet (top). Reproduced from [56].*

Graphene proved to be exceptional on numerous and various levels. First, it is a 2D material that can be grown on arbitrarily large surfaces with high-crystalline quality and is chemically stable in air with an easy accessible surface, unlike other 2D electron gases (2DEG). Graphene is also easy to physically or chemically functionnalize (adsorption, covalent grafting) in order to tailor its electronic properties. In addition to extraordinary electrical, thermal and mechanical properties [82, 11], its peculiar and unique band structure gives rise to exotic physical phenomena that triggered a considerable enthusiasm of the scientific community. The interplay between superconductivity and graphene is one of this recent fields of research.
If most of the theoretical activity has been focused on the ways of making graphene intrinsically superconducting, new features have also been predicted in the situation where the superconducting properties are induced by proximity effect. This latter case is a promising field of study since:

- graphene is self-passivated (no dangling bonds) and thus enables the realization of a clean Andreev interface (normal metal/superconductor interface)
- it presents a high electronic diffusion coefficient (D>100 cm^2/s) that is gate-tunable
- it shows low electronic density (compared to metals), which should result in a negligible inverse proximity effect.

In this chapter, we will first present a basic theoretical description of graphene's crystallographic structure and band structure and some of its most remarkable physical properties. In a second section, we will review the intrinsic superconducting properties of various carbon-based materials and present the theoretical predictions that have been made for

graphene as an intrinsic superconductor. We will then describe the superconducting proximity effect and its different characteristic length scales and see which consequences have been predicted and experimentally demonstrated for graphene-based hybrid systems. Finally, we will describe the specific experimental difficulties for studying this proximity effect in graphene with a scanning tunneling microscope.

3.1 Outstanding graphene physical properties

In this section, we will introduce graphene and some of its most peculiar characteristics. We will see that its crystallographic and band structure have important consequences on the physical properties of this unusual 2D material.

3.1.1 Crystallographic structure and band structure

Crystallographic structure Graphene is a 2D crystal of carbon atoms arranged in a honeycomb lattice (Fig. 3.2). This latter is not a Bravais lattice as two neighboring sites are not equivalent[1]. The crystal presents a triangular Bravais lattice described by the two vectors:

$$\mathbf{a_1} = \frac{a}{2}(3\mathbf{e_x} + \sqrt{3}\mathbf{e_y}) \ , \ \mathbf{a_2} = \frac{a}{2}(3\mathbf{e_x} - \sqrt{3}\mathbf{e_y}) \tag{3.1}$$

where $a = 1.42$ Å is the distance between nearest neighbors. Two atoms, named A and B, are contained in the unit cell and can define two sublattices generating the entire crystal lattice. The reciprocal lattice is defined by the basis vectors:

$$\mathbf{b_1} = \frac{2\pi}{3a}(\mathbf{k_x} + \sqrt{3}\mathbf{k_y}) \ , \ \mathbf{b_2} = \frac{2\pi}{3a}(\mathbf{k_x} - \sqrt{3}\mathbf{k_y}) \tag{3.2}$$

The first Brillouin zone is hexagonal (see Fig. 3.2b) and the high symmetry points are called Γ, M, K, K'. As in the real space atoms A and B can not be connected by a translation of the basis vectors, the same situation occurs in the reciprocal space: K and K' are non-equivalent consecutive corners of the first Brillouin zone. The wave vector associated to these points correspond to different physical situations. Their coordinates in momentum space are:

$$\mathbf{K} = \frac{2\pi}{3a}\left(1, \frac{1}{\sqrt{3}}\right) \ , \ \mathbf{K'} = \frac{2\pi}{3a}\left(1, -\frac{1}{\sqrt{3}}\right) \tag{3.3}$$

Band structure Carbon is the 6$^{\text{th}}$ element of the periodic table, built from 6 protons, 6 neutrons and 6 electrons. Its fundamental electronic configuration is $1s^2 2s^2 2p^2$. The two $1s$ electrons are core electrons, which are bound to the nucleus. The $2s$ and $2p$ orbitals get hybridized in the graphene lattice plane, giving rise to 3 sp^2 orbitals, which are linear combinations of $2s$, $2p_x$ and $2p_y$ states. Their geometrical shapes are presented on Fig. 3.3.

These orbitals are oriented in the xy-plane with mutual 120° angles and have a strong overlap, resulting in three σ bonds. This is the strongest type of covalent chemical bond,

[1] Indeed, a Bravais lattice is an infinite arrangement of points (or atoms) in space that looks exactly the same when viewed from any lattice point.

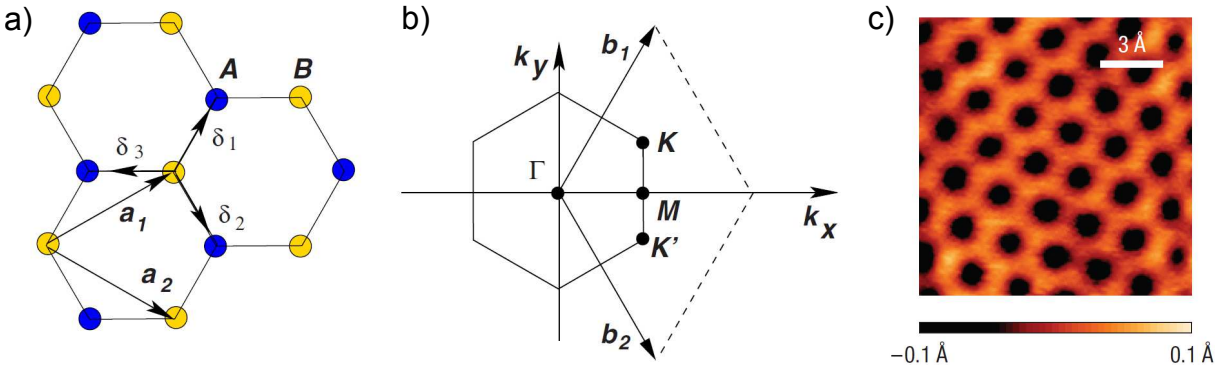

Figure 3.2 *Graphene crystallographic structure a) In the real space. The Bravais lattice is defined by the vectors* $\mathbf{a_1}$ *and* $\mathbf{a_2}$ *and two atoms (A and B). b) In the reciprocal space, representation of the first Brillouin zone with the two interesting points K and K'. Reproduced from [29]. c) STM topographic image of the graphene honeycomb lattice, reproduced from [152].*

responsible for the mechanical strength of the graphene structure. The remaining free $2p_z$ orbitals have a smaller overlap, creating out-of-plane π bonds, enabling highly mobile electrons throughout the carbon network.[2]
For both overlap configurations, the bonding of carbon atoms create so-called *bonding* and *anti-bonding* states, referred to as π, σ and $\pi*, \sigma*$ respectively. The bonding states have a lower energy than the anti-bonding ones. Carbon having four valence electrons with 8 energy bands to fill (6 $\sigma/\sigma*$ and 2 $\pi/\pi*$), only the bottom four bands (the bonding bands) will be filled. As the π and $\pi*$ bands touch at the K and K' points of the first Brillouin zone, the Fermi energy of *ideal* graphene crosses these so-called 'Dirac points'. In other words, the Fermi surface of electrically neutral graphene reduces to a set of points, which means the density of states at Fermi energy vanishes, without the existence of a bandgap. For that reason, graphene is called a *gapless semiconductor*.
The π and $\pi*$ bands are often referred to as the valence and conduction band respectively, while the σ and $\sigma*$ bands lie respectively far below and far above the Fermi energy, hence having a minor role in graphene electronic transport properties.

Dispersion relation The electronic band structure of graphene can be calculated within the tight-binding model, which applies to the case when overlap of neighboring orbitals is small. The interaction introduces a coupling between two non-modified levels in the form of a hopping parameter t between nearest-neighbors.[3] In the simplest case where hopping is considered between first neighbors only, the tight-binding Hamiltonian can be written as:

$$\mathcal{H} = -t \sum_{\langle i,j \rangle, \sigma} \left(a^{\dagger}_{\sigma,i} b_{\sigma,j} + H.c. \right) \tag{3.4}$$

where $a_{\sigma,i}$ ($a^{\dagger}_{\sigma,i}$) annihilates (creates) an electron with spin σ (σ=↑,↓) on site i of sublattice A (an equivalent definition is used for sublattice B) and t (≈2.8 eV) is the nearest-

[2]Note that the definition of σ and π bonds does not depend on the type of orbitals used in their creation. They refer to the location of the overlap region with respect to the bond axis.

[3]In simpler words, it assumes that the potential is so large that an electron spends most of its time tightly bound to its own ionic core, i.e. its state function is essentially that of an atomic orbital, uninfluenced by other atoms. From time to time, the electron will leak or tunnel to a neighbor ion.

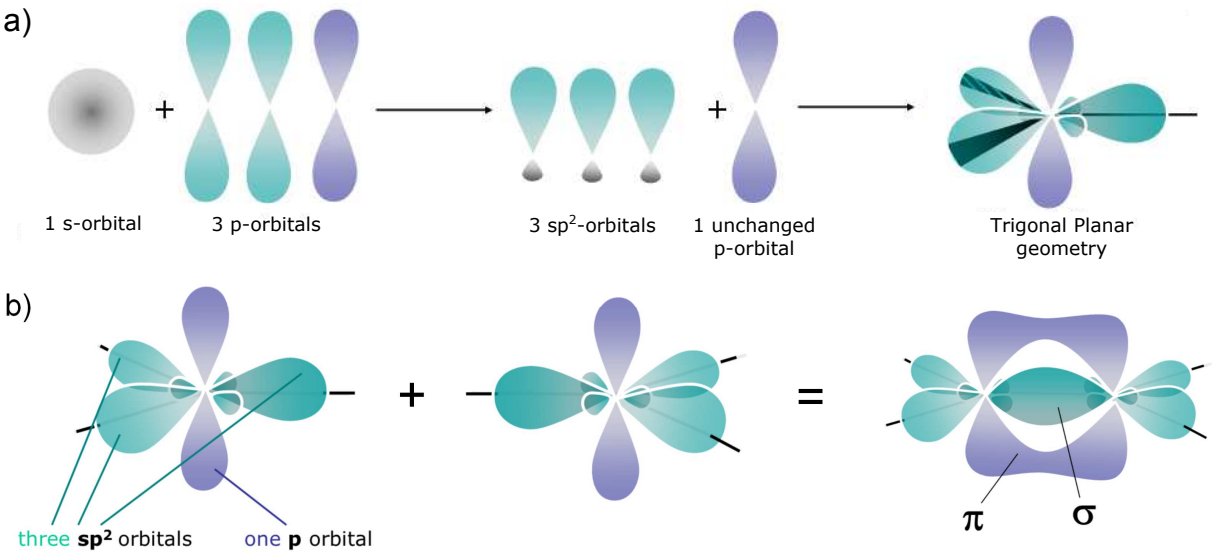

Figure 3.3 *a) Illustration of the hybridization process of carbon atomic orbitals, resulting into the formation of three equivalent sp^2-hybrid orbitals, which adopt a trigonal planar geometry, and one unchanged p-orbital that lies perpendicular to the plane. b) Bonding of two carbon atoms, creating σ and π bonds.*

neighbor hopping energy (between different sublattices). The energy bands derived from this Hamiltonian have the form:

$$E_{\pm}(k_x, k_y) = \pm t \sqrt{3 + 2\cos\left(\sqrt{3}k_y a\right) + 4\cos\left(\sqrt{3}\frac{k_y a}{2}\right)\cos\left(\frac{3k_x a}{2}\right)} \tag{3.5}$$

where the plus sign applies to the anti-bonding band ($\pi*$) and the minus sign to the bonding band (π). One obtains two symmetric bands, as plotted on Fig. 3.4, the conduction (red) and valence (blue) bands that meet at the so-called *Dirac points* (K,K') but do not overlap.

At low energy (E < 0.5 eV), the electronic states have wave vectors close to K/K'. We

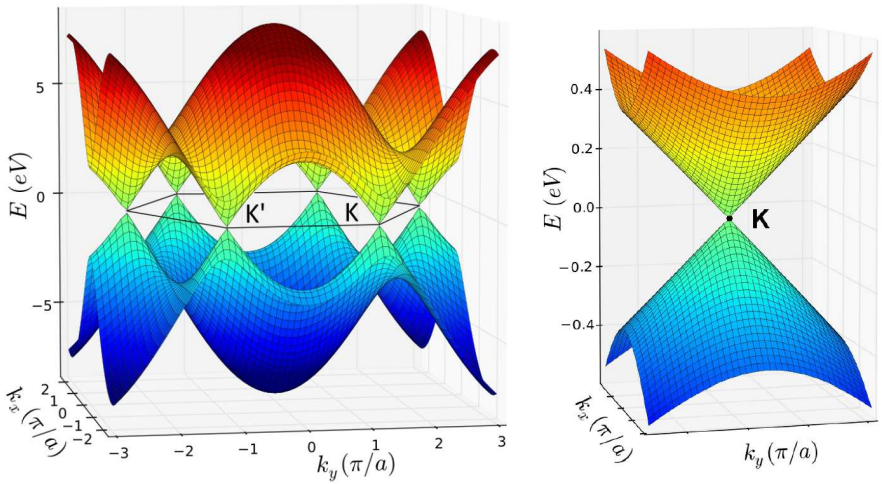

Figure 3.4 *Left: Graphene band structure (Eq. 3.4) obtained from tight-binding calculation. Right: Zoom at one K point. The band structure exhibits a conic shape, with a linear dispersion at low energies.*

can write $\mathbf{k} = \overrightarrow{\Gamma K} + \mathbf{q}$. As $\mathbf{q} \ll \overrightarrow{\Gamma K}$, the dispersion relation can be expanded to first order:

$$\epsilon_{\pm}(\mathbf{q}) \simeq \pm \hbar v_F \parallel \mathbf{q} \parallel \tag{3.6}$$

As a consequence, the Fermi velocity is written:

$$v_F = \frac{1}{\hbar} \frac{\partial \epsilon_{\pm}(\mathbf{q})}{\partial q} = t \frac{3a}{2\hbar} \approx 10^6 \, \mathrm{m.s^{-1}} \tag{3.7}$$

At low energy, the charge carriers velocity is thus constant (energy-independent) and the dispersion relation is isotropic and linear, defining a band structure with a conic shape. As mentioned above, there are only two non-equivalent points at the Brillouin zone corners in the reciprocal space. The bandstructure of graphene thus consists of two inequivalent cones or valleys at the corners of the first Brillouin zone[4], centered on K and K'. These cones are named *Dirac cones* and the intersection point between the conductance and valence bands is named the *Dirac point* (charge neutrality point). Finally, another consequence of the linear dispersion is a linear dependence with energy of the electronic density of states (per unit area):

$$\rho(\epsilon) = \frac{2}{\pi} \frac{|\epsilon|}{\hbar^2 v_F^2} \tag{3.8}$$

3.1.2 'Ultra-relativistic' massless particles

Dirac equation Quantum mechanics is usually described by the Schrödinger's equation, formulated in 1925 by the austrian physicist and focused on non-relativistic particles. Three years later, Dirac formulated a quantum description for relativistic fermions by way of the so-called Dirac equation. Due to the peculiar honeycomb lattice structure, graphene low energy carriers can also be described by an effective relativistic Dirac equation $E^2 = m^2c^4 + p^2c^2$, provided that we take $m = 0$, $c = v_F$ and $p = \hbar q$. This is the reason why electronic excitations in graphene are sometimes called *massless Dirac fermions*. Note however that the Fermi velocity in graphene $v_F = c/300$ is too low for electrons to be relativistic, they just mimic relativistic particles because of the peculiar symmetries of the Hamiltonian.

Chirality of charge carriers Let us now consider the symmetries of the system wavefunction. Each unit cell containing two atoms A and B with respective p_z orbitals $|\phi_A\rangle$ and $|\phi_B\rangle$, the system wavefunction can be decomposed on the basis formed by the Bloch functions of the two sublattices $\phi^{\mathbf{k}}_{A/B}(\mathbf{r})$:

$$\psi_{\mathbf{k}}(\mathbf{r}) = \begin{pmatrix} c_A(\mathbf{k}) \\ c_B(\mathbf{k}) \end{pmatrix} \tag{3.9}$$

As the local density of states of wavevector $\mathbf{k}$ equally originates from the A and B sites in graphene, for all $\mathbf{k}$ (i.e. for all energies) we have:

$$|c_A(\mathbf{k})| = |c_B(\mathbf{k})| \tag{3.10}$$

[4] This is referred to as the *valley degeneracy* of graphene.

At low energies, in the K and K' valleys, the system wavefunctions in the reciprocal space near K and K' points are:

$$\begin{aligned}\psi_{\pm,\mathrm{K}}(\mathbf{q}) &= \begin{pmatrix} c_A(\mathbf{q}) \\ c_B(\mathbf{q}) \end{pmatrix} = \frac{1}{\sqrt{2}} \begin{pmatrix} e^{i\theta_q/2} \\ \pm e^{-i\theta_q/2} \end{pmatrix} \\ \psi_{\pm,\mathrm{K'}}(\mathbf{q}) &= \begin{pmatrix} c_A(\mathbf{q}) \\ c_B(\mathbf{q}) \end{pmatrix} = \frac{1}{\sqrt{2}} \begin{pmatrix} e^{-i\theta_q/2} \\ \pm e^{i\theta_q/2} \end{pmatrix}\end{aligned} \tag{3.11}$$

where $\theta_q = \arctan(\frac{q_x}{q_y})$ and +/- refers to the conduction ($\pi*$) and valence (π) bands. In this way, the description of the wavefunction in terms of the two sublattices components brings up an additional phase factor θ_q, which reveals an analogy with a spin system[5]. For this reason, the vector is often referred to as a *pseudospin*. Note however that this terminology is due to the mathematical convenience we introduce to describe the wavefunctions symmetries and has nothing to do with the real spin of electrons.
The projection of the pseudospin on the direction of the kinetic momentum defines the *chirality* of the quasiparticules. In graphene, the direction of the quasiparticle pseudospin is parallel (positive chirality) or antiparallel (negative chirality) to their momentum. Electrons (holes) near the K point have positive (negative) chirality, whereas it is the opposite for charge carriers near the K' point[6]. In other words, electrons with opposite momentum within one valley travel in opposite direction with opposite pseudospin, thus have the same chirality. Chirality is a key feature having important consequences on transport properties, such as new quantum hall effect and weak anti-localization [99, 147]. STM has proved to be a relevant tool to probe the pseudospin and the chirality of epitaxial graphene quasiparticles at the nanometer scale, as reported in Ref. [25].

Klein tunneling The chiral nature of graphene quasiparticles leads to unusual transport properties. Indeed, while in quantum mechanics conventional tunneling is described by a probability of particles to travel through a potential barrier decreasing exponentially with the height of the barrier, a counter-intuitive process happens for relativistic particles, known as the *Klein paradox*: this probability rises in increasing the potential step, reaching unity for an infinitely high barrier. This effect can be attributed to the fact that while a potential is repulsive for electrons, it is at the same time attractive for positrons and results in positron states inside the barrier. Then, the greater the barrier height, the better the matching between electrons and positrons wavefunctions across the barrier, which leads to a high tunneling probability.

As seen on Fig. 3.5, the barrier remains perfectly transparent (T=1) for angles close to the normal incidence ($\phi = 0$). This perfect tunneling, due to the suppression of backscaterring, can be understood in terms of conservation of the pseudospin. Processes flipping the pseudospin are indeed rare as they require a short-range potential, acting differently on A and B sites of the graphene lattice. Looking at Fig. 3.5 schematic band diagrams, it means that a charge carrier on the 'red' branch can only be scattered to a charge carrier on the same 'red' branch but can not be transferred into any state on the 'green' branch., as this latter requires a pseudospin flip. In this way, an electron moving

[5] It corresponds to a degree of freedom of the orbital wavefunction

[6] We note that if the phase θ_q is rotated by 2π, the wavefunctions of the two valleys change their sign, indicating a phase-shift of π (referred to as a Berry's phase).

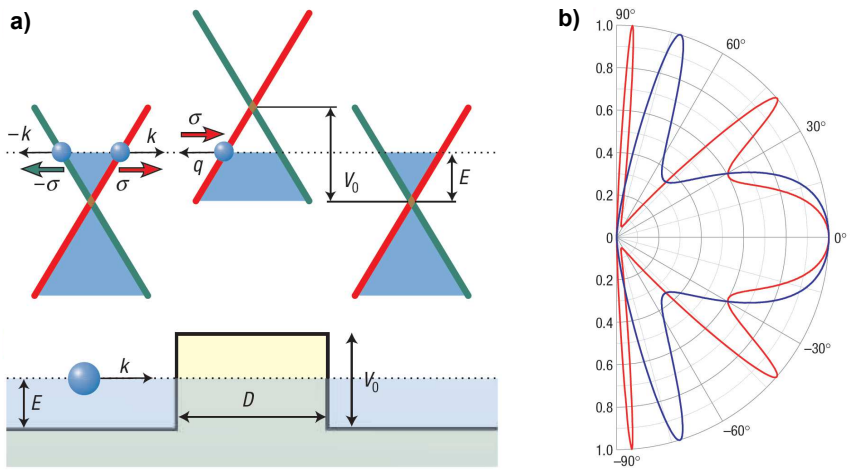

Figure 3.5 *a) Schematic diagram of the quasiparticles spectrum in graphene. When an electron meets a potential barrier, it can be transmitted as it exists available hole states in the barrier. The pseudospin σ is parallel (anti-parallel) to the motion of electrons (holes), i.e. σ keeps a fixed direction along the red and green branches of the electronic spectrum. b) Transmission probability through a 100 nm-wide barrier as a function of the incident angle. The blue curve corresponds to a higher barrier than the red curve. Reproduced from [72]*

to the right (of momentum $\mathbf{k}$) can only be scattered to a right-moving electron state or a left-moving hole state (of momentum $\mathbf{q}$): backscattering is thus prohibited. The Klein-tunneling effect has been experimentally observed in 2009 by two groups [120, 149].

3.1.3 Transport properties of graphene

3.1.3.1 Ambipolar electric field effect

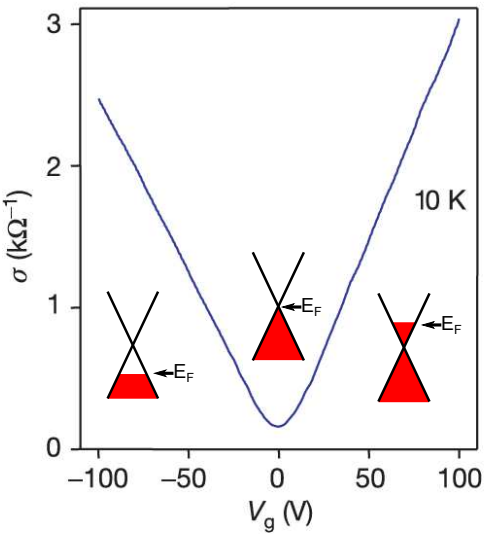

Figure 3.6 *Conductivity versus gate voltage characteristic of a monolayer graphene exfoliated on $Si0_2$ and measured in a Hall bar geometry. Adapted from [99].*

Most of the graphene samples measured in mesoscale experiments are reported on Si/SiO_2 substrates. The silicon is usually heavily doped to allow to apply an electric field to the sample (the Si substrate is then used as a gate). This enables to tune the chemical potential of graphene. Owing to its peculiar band structure, one can change the carriers type from electrons to holes by sweeping the gate voltage. A measurement of this so-called ambipolar field effect is presented on Fig. 3.6. The conductivity curves often present a linear dependence on the gate voltage close to the charge neutrality point (Dirac point). The number of charge carriers n is also proportional to the gate voltage V_g with $n = \alpha V_g$, where $\alpha = \epsilon_0 \epsilon_r / ed$ (with ϵ_r the dielectric constant and d the oxide thickness). One can thus write the conductivity $\sigma = ne\mu = \alpha e V_g \mu$ where μ is the mobility of the charge carriers. This latter can then be estimated with the slope $\partial\sigma/\partial V_g$

close to the Dirac point. It reaches 15 000 $cm^2V^{-1}s^{-1}$ in the case of Fig. 3.6 and is little affected by the temperature. For suspended graphene, the mobility can be as high as 10^5 $cm^2V^{-1}s^{-1}$ [24]. Its value allows to evaluate the disorder in the sample, in particular the substrate-induced disorder.

3.1.3.2 Finite conductivity minimum and electron/hole puddles

Fig. 3.6 also presents a counter-intuitive result: the conductivity does not go to zero at the charge neutrality point. So even though the density of states vanishes at the Dirac point, i.e. no charge can participate to the transport, the conductivity shows a finite minimum value $\sigma_{min} \sim 4e^2/h$. This value is actually non-universal and depends on the disorder of the sample [128]. This non-zero value of the conductance at the Dirac point is an effect of charge inhomogeneities, which modify spatially the position of the Dirac point with respect to the Fermi energy, giving rise to puddles of electron-doped regions and hole-doped regions near the charge neutrality point [30, 87] (see Fig. 3.7). An STM study showed that the charge puddles have an average length scale of 20 nm and originate from charge-impurities trapped between graphene and the SiO_2 substrate [151]. Recent experiments on double-layer graphene heterostructures have showed that these electron–hole puddles indeed disallow localization, but as soon as the charge inhomogeneities were screened graphene becomes insulating at the Dirac point [106].

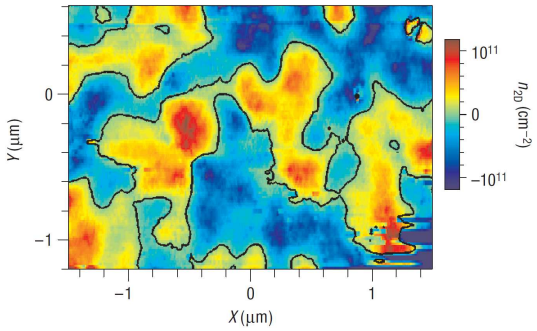

Figure 3.7 ***Electron/hole puddles*** *Local charge inhomogeneities measured near the charge neutrality point in graphene reported on SiO_2. Reproduced from [87].*

3.1.3.3 Fractional Quantum Hall Effect

In the presence of a perpendicular magnetic field, a two-dimensional electron system cooled down to low temperature presents the so-called Quantum Hall Effect (QHE). The electrons follow quantized circular cyclotron orbits, of energy $E_n = \pm\hbar\omega_c(n+1/2)$, where $\omega_s = eB/m$ is the cyclotron frequency, B the magnetic field, m the electron mass and n an integer. These orbitals are known as *Landau levels*. Due to its linear (and not parabolic) energy dispersion relation, the graphene's electronic spectrum quantization in magnetic field is different. In graphene, the Landau level energy is given by $E_n = \pm v_F\sqrt{2e\hbar Bn}$ (see Fig. 3.8 a). Thus it exists a quantized level at zero energy, which is shared by electrons and holes.
The experimental signature of the QHE in graphene has been first demonstrated in 2005 by two groups from Columbia [153] and Manchester [99]. They measured an abnormal quantization of the transverse conductivity σ_{xy} as a function of the carrier density (see Fig. 3.8 b). Indeed, for a conventional 2D electron gas, σ_{xy} presents plateaux at multiples of the conductance quantum $\sigma_{xy} = \pm nge^2/h$, where g is the system degeneracy ($g = 2$

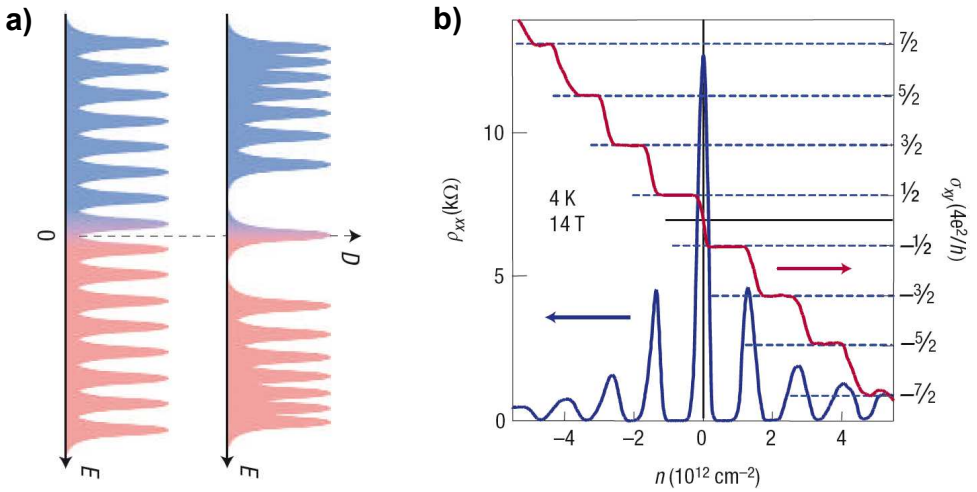

Figure 3.8 *(a) Sketches of Landau levels spectrum for a conventional 2D electron system (left) and graphene (right). (b) Fractionnal quantum hall effect observed on exfoliated graphene at T=4 K and B=14 T. The transverse conductivity σ_{xy} presents plateaux at half-integer values of $4e^2/h$ in function of the carrier density n. Reproduced from [56].*

for the spin degeneracy). For graphene, the plateaux sequence is shifted by $1/2$, so that $\sigma_{xy} = \pm(n + 1/2)ge^2/h$, where $g = 4$ due to double valley and spin degeneracy. The conductance plateaux are thus twice as much spaced out as for a conventional 2D system.

3.2 Intrinsic superconducting properties of graphene

If graphene itself never proved to be superconducting, the superconductivity in carbon-based compounds has been discovered and studied for half a century. If most of them have been made superconducting by doping, some, like carbon nanotubes, exhibit an intrinsic superconductivity. In the recent years, many theories have studied different options to make graphene intrinsically superconducting and analyzed the physics of the interactions that would be involved in the process.

3.2.1 Superconductivity in carbon-based materials

Carbon-based materials makes a broad category, which actually focused the efforts of a wide community of scientists for 50 years in order to reveal their intrinsic superconducting properties. Classified herebelow according to their general structure, we briefly review these properties listed by discovery date.

– *Graphite intercalated compounds (GICs)*: superconductivity in carbon-based materials was first discovered in 1965 in intercalation compounds of graphite with alkali metals [64]. Their structure is graphitic-like, with alkali-metal atoms lying in layers alternating with the graphite carbon layers. The first reported superconducting compound was C_8K, which has a transition temperature of 0.15 K. More recently, in 2005, a research work carried on the C_6Ca and C_6Yb compounds reported a superconducting transition at 11.5 K and 6.5 K, respectively [144]. Shortly after, a

theoretical paper demonstrated that superconductivity in GICs could not be interpreted simply as doping of a graphene layer but the full GIC's full structure had to be considered [28]. In the case of C_6Ca, they identified that the electron-phonon coupling responsible for superconductivity mostly involve C vibrations perpendicular and Ca vibrations parallel to the graphite layers.

– *Fullerene-based compounds*: in the beginning of the nineties, the observation of superconductivity in alkali-doped C_{60} compounds (fullerides) at 18 K in K_3C_{60} [65] and 33 K in $Cs_xRb_yC_{60}$ [130] has triggered much enthusiasm in the community for research on the superconducting properties of these compounds.

– *Carbon nanotubes*: predicted in 1995 [18], the intrinsic superconductivity of single-walled carbon nanotubes was experimentally verified in 2001, with an estimated transition temperature of 15 K [129]. Superconductivity in ropes of single-walled carbon nanotubes was also simultaneously observed below 0.55 K [75].

– *Diamond*: for the first time in 2004, boron-doped diamond was found to exhibit superconductivity below 4 K [50].

All these materials belong to the broader category of *superconducting covalent systems*, which carry high expectations for exhibiting high-temperature superconductivity [21]. Indeed, the combination of a low atomic mass, which is known to lead to high-frequency phonon modes, and strong covalent bonding that leads to large electron-phonon coupling potential, should contribute to the increase of the superconducting transition temperature.

3.2.2 Theoretical predictions in graphene

Although graphene exhibits numerous remarkable properties, superconductivity is notably absent from the list. This is due to the vanishing density of states at the Fermi energy. However, a shift of the graphene chemical potential away from the Dirac point should enable electrons to form Cooper pairs. This can be achieved by doping graphene with a metal coating. Several theoretical works have studied the possible mechanisms for superconductivity arising from this system.

One of the earliest theoretical papers was written by Uchoa and Castro-Neto [136] in 2007, where they study the superconducting states of pure and doped graphene. They identify possible phonon and plasmon mediated superconductivity in chemically modified, metal coated graphene, by deposition of alkaline metal atoms on top of the graphene crystal. The electrostatic equilibrium is then established by the migration of s electrons to the π-band to compensate the strong difference in electronegativities, thereby raising up graphene chemical potential from Dirac points. They point out that the electron-phonon mechanism tends to favor superconductivity at *high* electronic densities, whereas the electron-plasmon mechanism, in which the attractive electron-electron interaction is mediated by a screened acoustic plasmon of the metal, is favorable to superconductivity at *low* electronic densities.

In 2008, Kopnin and Sonin proposed a model where they analyzed possible superconductivity of graphene in the frame of the BCS model, calculating the critical temperature,

the superconducting energy gap and the supercurrent as functions of the doping level and the pairing interaction strength [79].

Phonon-mediated superconductivity was further explored in Profeta, Calandra and Mauri's paper in early 2012 [107]. The starting point of their reasoning is the electron-phonon coupling constant λ, which is written:

$$\lambda = \frac{N(0)D^2}{M\omega_{ph}^2} \tag{3.12}$$

where N(0) is the DOS at Fermi level, D the deformation potential, M the effective atomic mass and ω_{ph}^2 the phonon frequency. Assessing phonon-mediated superconductivity does not occur in undoped graphene due to its small number of carriers (and thus small DOS at the Fermi level) and pointing out the negative implications resulting from a simple doping of the carbon π-states, they promote the necessity to enhance the electron-phonon coupling by a different approach. Inspired by what happens in GICs, they show the onset of superconductivity is possible by doping the graphene surface with alkaline metal adatoms thanks to the appearance of an interlayer band at the Fermi level that increases the λ value, on the condition that this interlayer state is localized as close as possible to the graphene plane. Using DFT calculations, they predict one LiC_6 monolayer to be superconducting with a superconducting critical temperature up to 8.1 K, although bulk LiC_6 is not superconducting itself due to strong confinement in the z direction that prevents the occupation of the interlayer state. On the other hand, metal-covered graphene with other chemical species (such as Ca) should present a reduced superconducting critical temperature with respect to the corresponding GIC (for example, for CaC_6 Tc(bulk)=11.5 K and Tc(monolayer)=1.4 K).

Another type of superconductivity was predicted in 2010 by McChesney *et al.* on the basis of their measurements of the band structure of highly doped graphene determined by angle-resolved photoemission spectroscopy (ARPES) [91]. They achieved a strong doping by intercalating Ca atoms between graphene and the SiC substrate and adsorbing additional Ca or K atoms on top of the graphene layer. By this method, they could bring the Fermi energy to the saddle point (M points of the Brillouin zone, see Fig. 3.2b), where the DOS has a Van Hove singularity[7] (vHS). By implementing their experimental Fermi surface into calculations of the screened Coulomb interactions, they predicted an instability of the system towards superconductivity, with electron-electron interactions being responsible for the superconducting pairing. In 2012, a theoretical paper by Nandkishore, Levitov and Chubukov corroborated this proposal [95]. Their renormalization group analysis indeed indicated the presence of a superconducting order (referred to as "chiral superconductivity"), wherein repulsive interactions give rise to a pairing attraction in a d-wave channel.

[7] By definition, a Van Hove singularity is a divergence in the DOS of a crystalline solid.

3.3 Extrinsic superconductivity: the proximity effect

Another way to make graphene acquire superconducting properties is to make use of the superconducting proximity effect. The superconducting proximity effect is the transmission of superconducting properties to a normal metal (N) placed in electrical contact with a superconductor. This effect was first highlighted in the sixties, when it was understood that superconducting correlations could extend over a large length scale in a normal metal, even in the absence of electron-electron interactions. First studied on thin films, the later development of nano-fabrication technologies in the nineties made possible to fabricate small enough devices so as to make the electrons coherent over the sample size. The superconducting proximity effect thus knew a resurgence of popularity and many experiments successfully clarified its basic mechanism. In this section, we will first make a general description of the superconducting proximity effect and present a few models solving this problem. We will then present measurements of the superconducting proximity effect observed on various carbon-based materials. The last part will be focused on the manifestation of the superconducting proximity in graphene and the peculiar features predicted by theories due to the ballistic and relativistic character of its fermions. We will end this section by presenting the first experimental evidences, mainly via transport measurements, of the superconducting proximity effect in graphene that have been published along the last five years.

3.3.1 The proximity effect: theory and length scales

3.3.1.1 Andreev reflection and characteristic length scales

What happens when one contacts a normal metal (N) to a superconductor (S)? Because of the existence of an energy gap Δ at the Fermi energy in the density of states of the superconductor, the transfer of single quasiparticles with an energy $\varepsilon < \Delta$ is forbidden. The transfer of charges occurs at the S/N interface via a two-particles process described by Andreev in 1964 [5], and referred to as **Andreev reflection**: an incoming electron in N is retro-reflected as a hole with opposite **k** vector, opposite spin and opposite energy with respect to the Fermi level. The outcome of this process is a charge transfer of $2e$, an energy transfer of $2E_F$, a zero momentum transfer[8] and a zero spin transfer. This is equivalent to the transmission of a Cooper pair in S[9]. The incident electron and the reflected hole travel along time-reversed paths, which means the Andreev reflection correlates the electron-hole pair in N. They are referred to as "Andreev pairs" as their existence is not due to an intrinsic attractive interaction in N as for Cooper pairs, but to a remote effect at the N/S interface. Nevertheless, they are often seen as the *diffusion* of Cooper pairs in the normal metal. Andreev reflection is thus a crucial ingredient of the superconducting proximity effect.

The second ingredient is the **phase coherence** of the process, or how the electron-hole pair will loose its correlated properties in N. Indeed, we stated hereabove that the electron and the hole form a phase-conjugated pair, traveling along time-reversed paths.

[8] This is an approximation only valid when $\Delta \ll E_F$, i.e. the kinetic energy of the incident electron is not significantly affected.

[9] For a more detailed description, see Section 2.2.1.

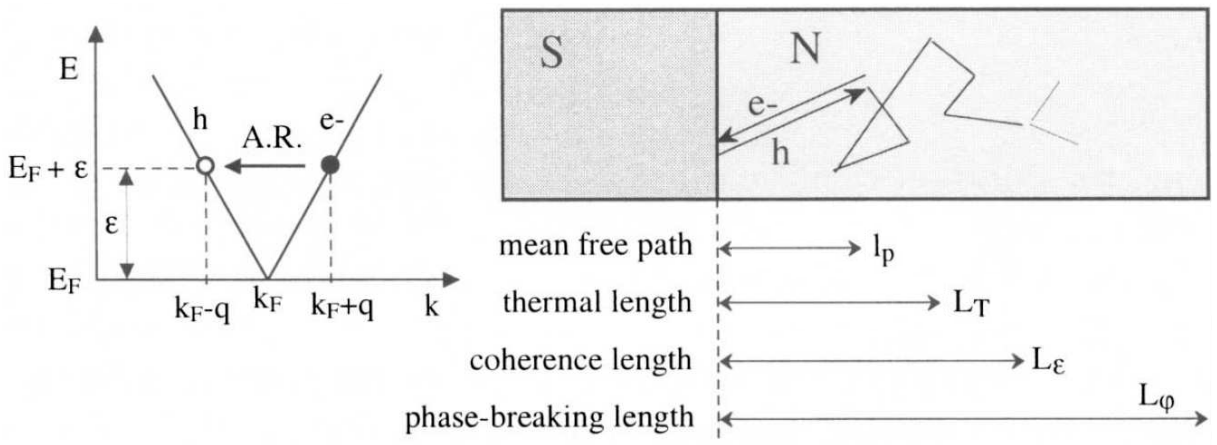

Figure 3.9 ***Coherence of the Andreev pairs in a normal metal.*** *Left: schematic of the Andreev process. The incident electron and the reflected hole have a slight wave-vector mismatch* $2q$*. Right: Relevant length scales in the normal metal (not to scale). The energy-dependent coherence length* L_ϵ *is the length over which the electron and hole of an Andreev pair acquire a phase difference of order* π*. Adapted from [35].*

This statement is valid in the approximation that they have exactly opposite wave-vector $\mathbf{k}$, which happens only at the Fermi energy (see Fig. 3.9 left). Otherwise, they present a wave-vector mismatch, which results in a *phase shift* between the two particles that will eventually breaks the Andreev pair when its value reaches π. This happens at a distance L_ϵ from the interface, called the *energy-dependent coherence length*:

$$L_\epsilon = \sqrt{\frac{\hbar D}{\epsilon}} \tag{3.13}$$

with D the diffusion coefficient in N. L_ϵ plays the role of the coherence length of Andreev pairs. Said differently, the Andreev pair looses its coherence when the influence of the superconductor can not be felt anymore, i.e. when the electrons have an energy ϵ bigger than the Thouless energy[10]:

$$E_{Th} = \frac{\hbar D}{L^2} \tag{3.14}$$

If one considers the whole electron distribution at thermal equilibrium, the relevant energy scale is the thermal energy and the decoherence length is the *thermal length*:

$$L_T = \sqrt{\frac{\hbar D}{2\pi k_B T}} \tag{3.15}$$

At high energy ($\epsilon \sim k_B T$), L_T corresponds to the lower limit of the coherence length of an Andreev pair, whereas the upper limit is given at low energy ($\epsilon \sim 0$) by the phase-breaking length L_φ of a single-electron. Fig. 3.9 (right) summarizes the relevant length scales for the superconducting proximity effect.

[10]The Thouless energy is a correlation energy expressing the sensitivity to the boundary conditions of the system.

3.3.1.2 McMillan's tunneling model of the superconducting proximity effect

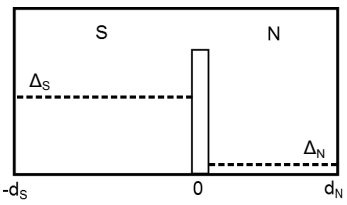

A theoretical model of the superconducting proximity effect between a normal metal (N) and a superconductor (S) was proposed by McMillan in 1968 [92]. In this model, the electrical contact between N and S is replaced by tunneling of electrons through a potential barrier. It enables to calculate the tunneling DOS in each film of "clean" NS sandwiches, i.e. for which the mean free path l is approximately equal to the film thickness. For the model to be valid, the thickness of each film must be smaller than the corresponding coherence length, so that the superconducting properties of each film may be considered uniform across its thickness. The BCS potential Δ (dashed lines on the sketch here above) is constant in each metal.

For a given SN sandwich, this model has two parameters, Γ_N and Γ_S, and one relationship $\Gamma_N/\Gamma_S = N_S d_S/N_N d_N$, which leaves one free parameter. The parameters are defined as followed: d_N and d_S are the thicknesses of the normal metal and the superconductor respectively, N_N and N_S their bulk DOS (per unit volume), $\Gamma_{N,S} = \hbar/\tau_{N,S}$ where τ_N is the relaxation time for tunneling from N to S, i.e. the average time an electron spends in N before penetrating the barrier and escaping into S (and vice versa for τ_S). Thus the bigger Γ_N, the shorter the relaxation time τ_N, the more transparent the barrier[11].

Noat *et al.* have simulated the DOS of proximity layers using the McMillan model [98] with parameters values that could mimic the system we propose to study in the following chapters. Indeed, they have made the computations for $N_S d_S/N_N d_N = 20$, i.e. in the case of a very thin normal film as compared to the superconductor. This corresponds to our system with a monolayer of graphene on a 50 nm-thick rhenium film. Their results for different values of the coupling parameter Γ_N are presented in Fig. 3.10. The coupling strength increases from left to right.

For a small coupling (a), the superconducting DOS remains unchanged in S while N exhibits a very small induced gap. For an intermediate coupling (b), the superconducting gap is reduced in S (due to inverse proximity effect) and a comparable gap is induced in N. They both exhibit a strong departure from BCS. For a strong coupling (c), the same BCS-like DOS is recovered in both N and S. This model gives us a good element of comparison for our studies of the superconducting proximity effect induced on the graphene layer grown on top of a superconducting rhenium film.

3.3.1.3 De Gennes-Saint James resonant states in ballistic SN systems

In 1963, De Gennes and Saint James applied the BCS theory generalized by Bogoliubov to the case of a SN bilayer, where N is a ballistic medium [40]. They predicted the existence of quantum bound states, which give rise to peaks in the normal DOS at energies $E_k < \Delta$. Their model is based on a ballistic normal metal with finite thickness d_N and a zero pair potential, and a perfectly transparent and ballistic interface. In other words, there is no

[11] In the normal state, $\tau_N = L_N/(v_{F,N}\sigma)$ where L_N is the average path length for an electron between two reflections with the barrier and where σ is the transmission probability of the barrier. This gives $\Gamma_N = \hbar v_{F,N}\sigma/L_N$.

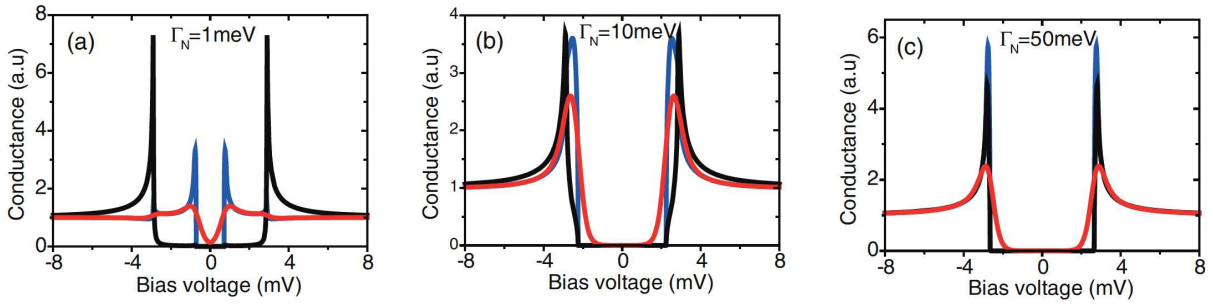

Figure 3.10 ***McMillan's model of the superconducting proximity effect*** *- DOS of the SN sandwich for $N_S d_S / N_N d_N = 20$ (thick S as compared to N) and different values of the coupling parameter Γ_N. Black curves: DOS in the superconductor. Blue: DOS in the normal metal. Red: simulated tunneling conductance in N for T=2.3 K. Reproduced from [98].*

potential barrier and the direction of the reflected particle is totally determined by the incident angle. In this framework, the calculated DOS presents discontinuities at energies E_k smaller than the superconducting gap such as:

$$tan\left(\frac{2E_k d_N}{\hbar v_F}\right) = \frac{\sqrt{\Delta^2 - E_k^2}}{E_k} \tag{3.16}$$

Therefore, there is no gap in the excitation spectrum for any finite thickness d_N of the normal metal (see Fig. 3.11). This arises from the fact that all the incidence angles with respect to the interface are considered. The quasi-particles that cross the normal metal thus have trajectories of lengths that vary from d_N (for a zero incident angle) to infinite (if the incident angle approaches $\pi/2$). We then observe a continuum of excitations from the Fermi energy. One should note that the SN geometry of this system is equivalent to a SNS geometry for a normal metal of thickness $2d_N$.

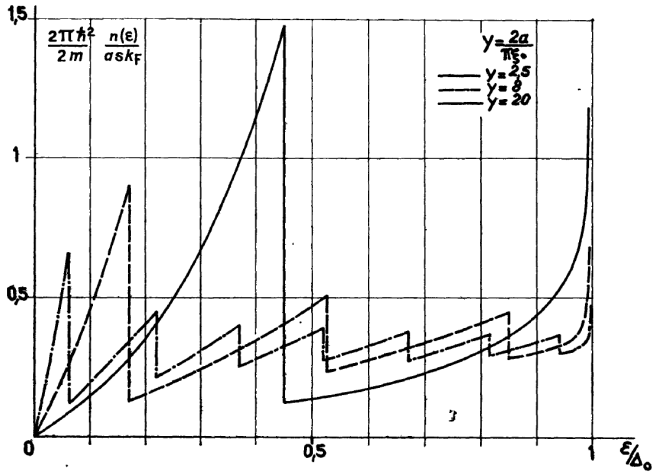

Figure 3.11 ***De Gennes-Saint James resonant states.*** *DOS in a ballistic normal metal (N) calculated for different thicknesses of N. Reproduced from [40].*

In conclusion, the thicker the normal metal, the more discontinuities in the energy spectrum. And reverse-wise, for a thin metal, the resonant state peak comes on top of the coherence peak at the superconducting gap energy.

3.3.2 Superconducting proximity effect in graphene

3.3.2.1 Proximity effect in carbon-based compounds

In 1999, a superconducting proximity effect was revealed in carbon-based compounds for the first time. Kasumov *et al.* measured supercurrents in single-walled carbon nanotubes (SWCNT) suspended between two superconducting electrodes [71]. The superconducting properties of such samples exhibit unusual features due to their strong one-dimensional character. To induce a proximity effect, they used superconducting bilayer electrodes made of Re/Au or Ta/Au. Indeed, a good electrical contact between the SWCNT and the metallic electrodes is a prerequisite to induce superconducting properties in the SWCNT. In this work, this has been obtained by laser welding to solder the SWCNT to the metallic contacts. Gold was chosen as an ideal solder as it does not react with carbon nor oxidizes. Although the gold layer decreases the expected superconducting temperature because of the inverse proximity effect they could still achieve reasonable transition temperatures (1.1 K and 0.4 K instead of 1.7 K for Re and 4.5 K for Ta).

3.3.2.2 Theoretical predictions in graphene

Because of its unique electronic properties, graphene makes possible to explore the superconductivity of relativistic massless carriers. Several theoretical papers have been reporting the unusual features that arise from the combination of the Dirac equation of relativistic quantum mechanics and the Bogoliubov-de Gennes equation of superconductivity [16, 135]. As seen previously, the superconducting proximity effect arises from Andreev reflection processes occurring at the normal metal-superconductor interface. An electron excitation at energy $E_F + \epsilon$ in graphene will thus be converted into a hole excitation at energy $E_F - \epsilon$ for $0 < \epsilon < \Delta$ (the superconducting gap) and a Cooper pair

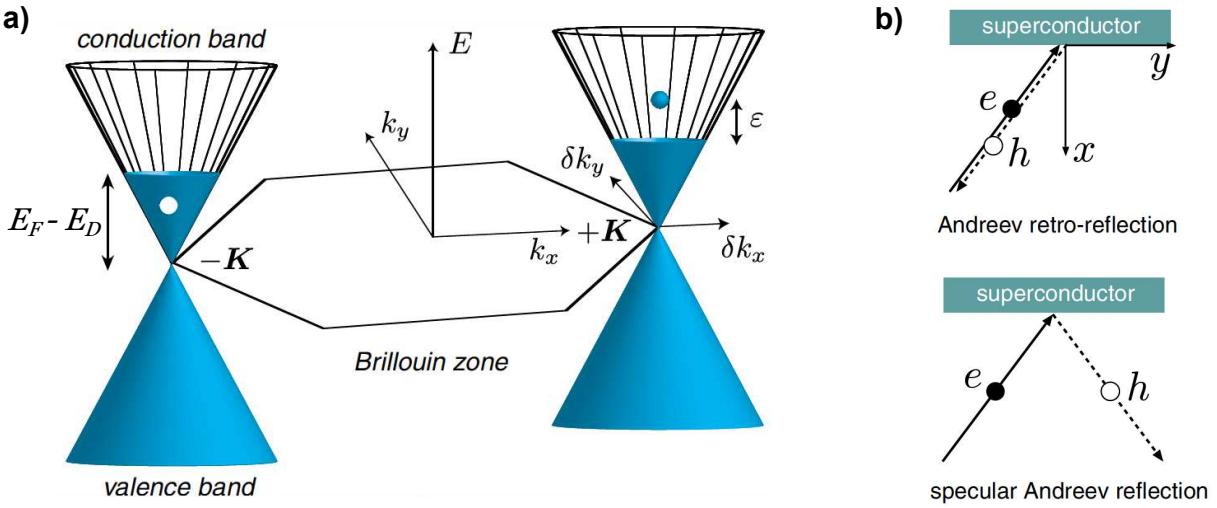

Figure 3.12 ***Andreev reflection in graphene (1)*** *(a) Band structure of (electron-doped) graphene illustrating how an electron and a hole excitations (filled and empty circles at energies $E_F - E_D \pm \epsilon$) are converted into each other by the (classical) Andreev reflection. (b) Top: Andreev retro-reflection at a normal metal-superconductor interface. Bottom: specular Andreev reflection at the interface between undoped graphene and a superconductor. Reproduced from [17].*

will be transmitted into the superconductor. As a Cooper pair carries zero total momentum at equilibrium, the electron and hole excitations in graphene must be taken from opposite corners $\pm\mathbf{K}$ of the Brillouin zone (see Fig 3.12 a). Consequently, Andreev reflection switches the valleys in graphene. If we go further in this description, we notice that for heavily doped graphene the Andreev process illustrated for the n-doped case in Fig 3.12 a) couples an electron and a hole both from the conduction band: this corresponds to *intraband* Andreev reflection.

When the graphene is in the low doping regime, i.e. for $\Delta > |E_D - E_F|$, a new kind of Andreev reflection occurs. If the electron energy $\epsilon < |E_D - E_F|$, the electron undergoes a classical Andreev reflection. But when its energy verifies $|E_D - E_F| < \epsilon < \Delta$, the Andreev reflection becomes *interband*: an electron in the conduction band is converted into a hole in the valence band. This unusual process was first highlighted by C.W.J. Beenakker in 2006 and corresponds to a **specular Andreev reflection**, illustrated on Fig 3.13. Here, in contrast to usual Andreev retro-reflection where all components of velocity change sign, only the component perpendicular to the interface changes sign in low-doped graphene (Fig. 3.13 a). Indeed, for both types of reflection, since the hole is reflected into graphene, its velocity along x ($v_x = dE/dk_x$) must be positive, whereas the sign of v_y will be opposite for the two reflections in virtue of the conservation of k_y.
When graphene is undoped, i.e. E_F=E_D, Andreev reflection is then *interband* at all energies. Beenakker further demonstrated that the specular Andreev reflection has a drastic impact on the conductance of a NS junction made of graphene and predicted a clear experimental signature [16].

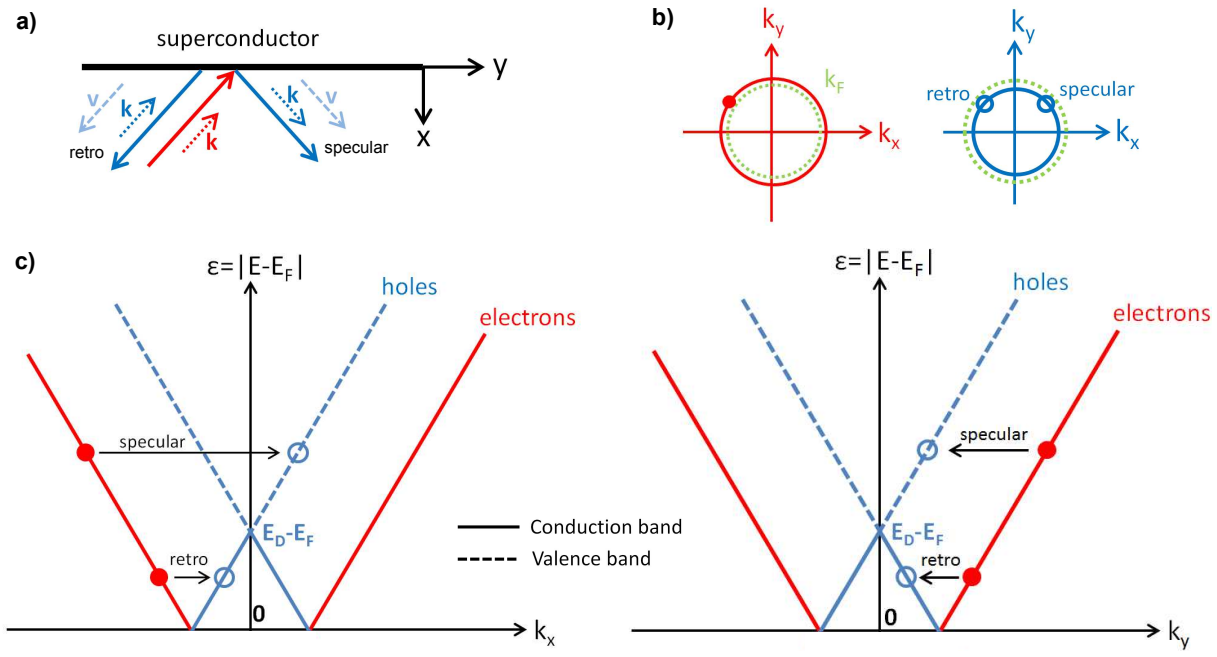

Figure 3.13 ***Andreev reflection in graphene (2)*** *Red/blue lines: electron/hole excitations. (a) Andreev retro-reflection and specular reflection showing the directions of the wave-vector* $\boldsymbol{k}$ *and the group velocity* $\boldsymbol{v}$*. (b) Schematics in* $\boldsymbol{k}$*-space. Green circle = Fermi surface. (c) 2D energy diagram sketching the two types of Andreev reflection occurring in low-doped graphene (i.e. for* $\Delta > |E_D - E_F|$*). Solid/dotted line: conduction/valence band.*

Soon after, the case of a long superconductor-graphene-superconductor junction[12] was investigated by Titov *et al.* [135]. They demonstrated that specular Andreev reflection creates charge-neutral modes propagating along the superconducting boundaries in the undoped graphene channel. These *Andreev modes* are a coherent superposition of electron states from the conduction band and hole states from the valence band, coupled by specular Andreev reflection at the NS interface (see Fig. 3.14).

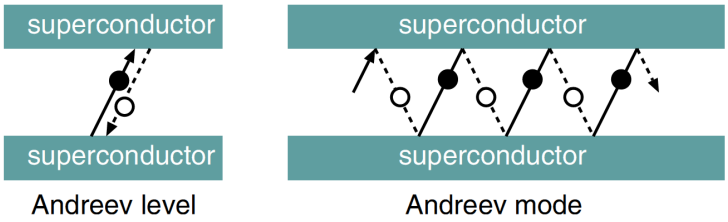

Figure 3.14 ***Trajectories of Andreev pairs in the real space.*** *Left: localized level in case of retroreflection. Right: propagating mode in case of specular Andreev reflection. Reproduced from [17].*

The authors predict a transition from a gapless excitation spectrum for $E_F \gg E_T = \hbar v/d$ (high-doping regime) to an excitation spectrum exhibiting a gap E_0 for $E_F \lesssim E_T$ (low-doping regime), with $E_0 = (\pi - \mid \phi \mid)E_T/2$ where ϕ is the phase difference between the two superconductors (see Fig. 3.15 a and b). In the high-doping regime, the lowest resonance is at the same energy E_0 as the gap edge in the low-doping regime, but the density of states is gapless, vanishing linearly at small excitation energies. The peaks are then analogous to the De Gennes–Saint James resonances in conventional SNS junctions [40] (see Sec.3.3.1.3).

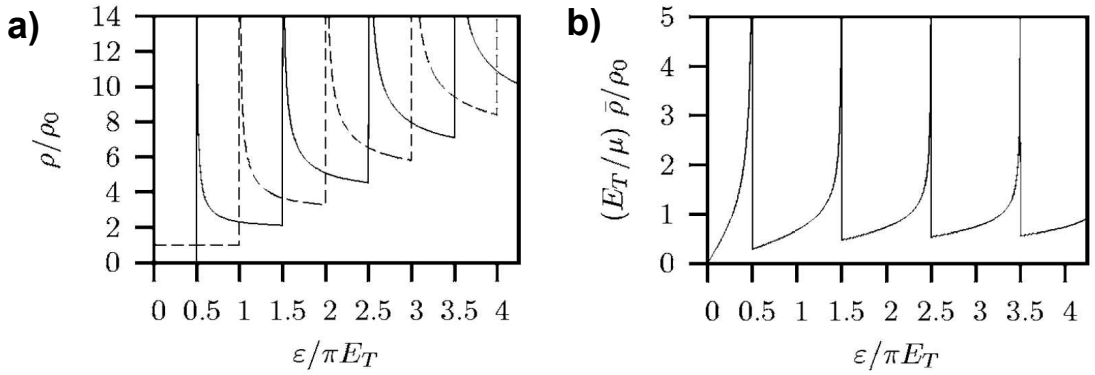

Figure 3.15 *(a) DOS of the SNS junction in the low-doping regime, for superconducting phase difference ϕ=0 (solid curves) and $\phi = \Pi$ (dashed curves). (b) DOS of the SNS junction in the high-doping regime for ϕ=0. Reproduced from [135].*

[12] When the superconducting gap Δ is much larger than the Thouless energy $E_T = \hbar v/d$, where v is the carrier velocity in graphene and d the separation of the NS boundaries.

3.3.2.3 Experimental results in transport

Graphene contacted to superconducting nanostructures The first evidence of a superconducting proximity effect in graphene was reported in 2007 by Heersche *et al.* [66]. They transferred an exfoliated graphene sheet onto an oxidized Si substrate and contacted it with superconducting bilayers made of Ti(10nm)/Al(70nm), as seen on Fig. 3.16 a. Titanium was used to ensure a good electrical contact to graphene. They observed multiple Andreev reflections (Fig. 3.16 b) and demonstrated the existence of a gate-tunable and bipolar supercurrent flowing through graphene (Fig. 3.16 c), which stays nonzero even if the Fermi level is tuned to the point of zero carrier concentration. As the critical current is correlated to the normal state resistance by the relation $I_c R_n \approx 2\Delta/e$, corresponding to the short junction limit, one can vary its value in graphene by changing R_n with the gate voltage.

These results were reproduced by Du *et al.* [45] by the same device fabrication technique, with Ti(2nm)/Al(30nm) superconducting electrodes. The authors show that the evolution of the critical current as a function of the gate voltage is well described by the Usadel equations for a diffusive junction and is inconsistent with the predictions of the ballistic model established for graphene by Titov *et al.* [134]. The diffusive transport in these junctions is stated to be a consequence of the short mean free path and smearing of the Dirac point caused by scattering from substrate-induced charge inhomogeneities.

Several other teams have then realized superconducting-graphene-superconducting (SGS) junctions with different superconductors but the observation of a supercurrent is not systematic. Ojeda *et al.* had to proceed to an in-situ annealing treatement of graphene by applying a strong current in the junction [100]. In long SGS junctions, Komatsu *et al.* reported an anomalous suppression of the supercurrent in the vicinity of the Dirac point, attributed to specular Andreev reflections occurring at boundaries between electron-doped and hole-doped regions in globally neutral graphene [77]. These results highlight the possibility to fabricate SGS junctions with transparent enough interfaces to observe multiple Andreev reflections and the Josephson effect.

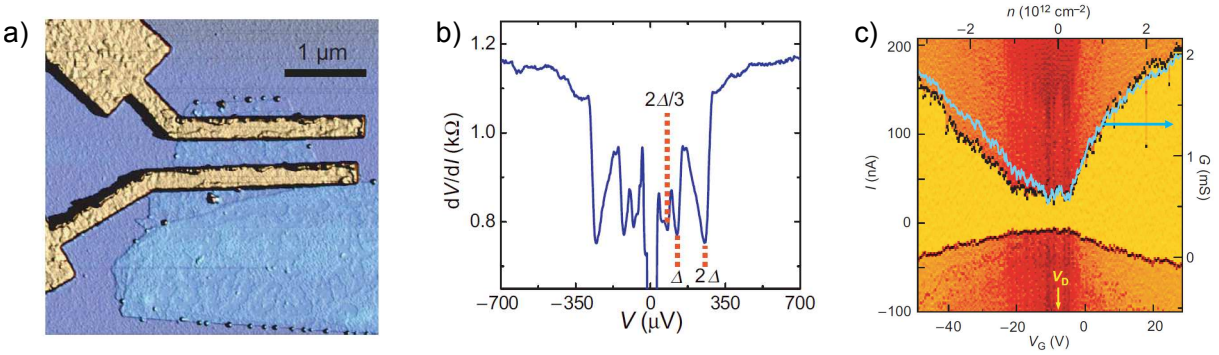

Figure 3.16 *(a) Atomic force microscope of the monolayer graphene device contacted by two superconducting electrodes. (b) Differential resistance (dV/dI) versus V, exhibiting a drop for a bias voltage smaller than $2\Delta_{Al}$=300 µV. We also observe multiple Andreev reflection dips occurring at fractional values of the gap V=2Δ/n. (c) Differential resistance map versus the gate voltage and the polarisation current. The yellow central part corresponds to the Josephson current. The blue curve depicts the normal state conductance. Reproduced from [66].*

Nevertheless, they do not reveal phenomena intrinsic to graphene and the physics stays limited to the frame of diffusive SNS junctions, with the additional possibility to tune the critical current of the junction by a field effect. This property was exploited by Girit et al. to realize a tunable SQUID based on SGS junctions [58].

Graphene decorated with superconducting droplets Another original way to induce superconductivity in graphene was proposed by Feigel'man *et al.* [53] and realized by Kessler *et al.* in 2010 [73] and Allain *et al.* in 2012 [3]. It consists in decorating graphene with a nonpercolating network of nanoscale superconducting clusters. They took advantage of the poor wettability of graphite and deposit tin nanoparticles by thermal evaporation on pristine graphene reported on an oxidized silicon substrate (see Fig. 3.17 a). The resulting nominal thickness of tin is 10 nm, forming islands with 80 nm diameter and separated by about 13 nm to 25 nm (see Fig. 3.17 b).

Using mechanically exfoliated graphene sheets, Kessler *et al.* have shown that this hybrid system can exhibit a gate-tunable Berezinski-Kosterlitz-Thouless (BTK) transition towards a two-dimensional homogeneous superconducting state. Whereas in the case of a more disordered graphene (CVD grown on copper foils) with a more dense tin islands network, Allain *et al.* demonstrated than the same hybrid system displays a gate tunable superconductor-to-insulator transition (see Fig. 3.17 c).

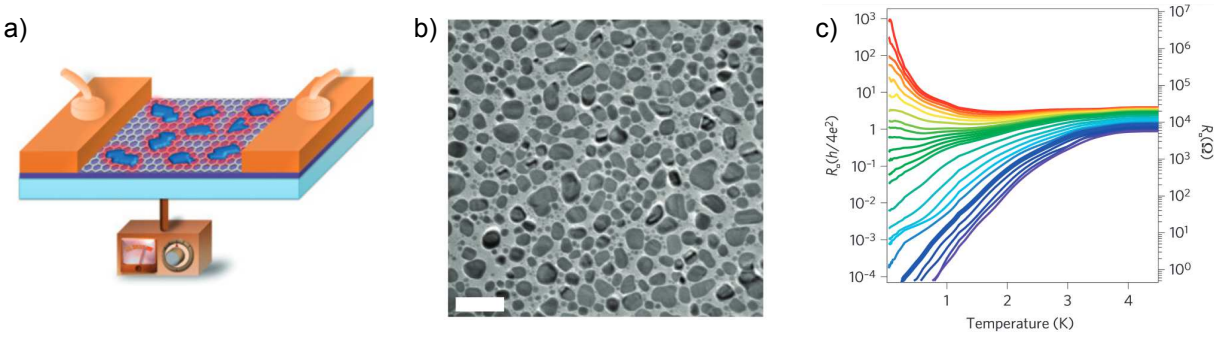

Figure 3.17 *(a) Sketch of the device. (b) Transmission electron micrograph of the graphene sample decorated by tin droplets (scale bar: 200 nm). (c) Sheet resistance as a function of temperature for different gate voltages, showing a superconductor-to-insulator transition of the device. Reproduced from [3].*

These experiments demonstrate that graphene can convey superconducting correlations when coupled to a superconductor, either by a lateral contact or by partially covering its surface with a superconducting islands array, and at the same time conserve some of its exceptional properties, such as the tunability of its carriers density by a field effect.

However, several points need improvements or remain unresolved:

- a **good electronic coupling between graphene and a superconductor** is difficult to achieve.
- the **Dirac point physics** remains uncovered and concealed by the graphene-substrate interaction, which induces random doping of the graphene layer.
- the **ballistic regime** is still challenging.
- the **local superconducting properties of graphene** have never been probed (all the reported experiments were carried out at the meso- or macro-scale).

These remarks defined the framework of our project.

3.4 Local study of the induced superconducting properties of graphene

The goal of our project is to study the **local superconducting correlations in graphene** by STM and STS. By cooling our microscope down to 50 mK, we can map the superconducting density of states and see how it evolves when one goes away from the graphene/superconductor interface. During this project, we studied different sample geometries, detailed hereinafter.

3.4.1 STM on graphene contacted to a superconducting reservoir

The first attempt to study locally induced superconductivity in graphene was conducted by Zoltán Osváth[13], a former post-doc in our laboratory. He has been focused on the elaboration of a sample constituted of an exfoliated graphene sheet reported on a Si/SiO_2 substrate and contacted all around by a superconductor. However, the use of STM implies many constraints and requirements. First of all, one needs to be able to find the graphene/supercondutor interface once the STM tip is in contact. As one can not aim a sample area with a better accuracy than half a millimeter, it requires the presence of markers easily identifiable by scanning the STM tip. The elaboration procedure of the sample was the following:

- an exfoliated graphene flake was deposited on a Si/SiO_2 substrate previously prepared with gold markers separated by $\sim$60 μm.
- a superconducting trilayer of Ti/Nb/Au (5/40/10 nm) was sputtered covering a large area over the sample and overlapping slightly it on its edges (see Fig. 3.18 a).
- accurate Au marks (of few microns size) were further realized close to the sample in order to allow an accurate location with the STM.

In this way, it was possible to find the interface after the approach. Atomic resolution was obtained on the graphene layer, corroborating the cleanliness of the surface. The following difficulty which Z. Osváth was confronted to was the interface profile smoothness. Indeed, the lift-off process that removes the protective resist from the graphene flake after the deposition of Nb/Au can result in rough patches right at the interface position, which would damage the tip during the scan. The problem could be solved by using another resist and a smooth Nb profile could be obtained at the interface (see Fig. 3.18 c,b). Unfortunately, the superconductivity was already destroyed in the Ti/Nb/Au trilayer before reaching graphene (see Fig. 3.18 c,d,e), probably due to a chemical reaction between niobium and PMMA. This sample geometry is now further investigated using a mechanical mask (silica marbles) to avoid using resist.

[13]Now at Institute for Technical Physics and Materials Science (MFA), Research Centre for Natural Sciences, Hungary.

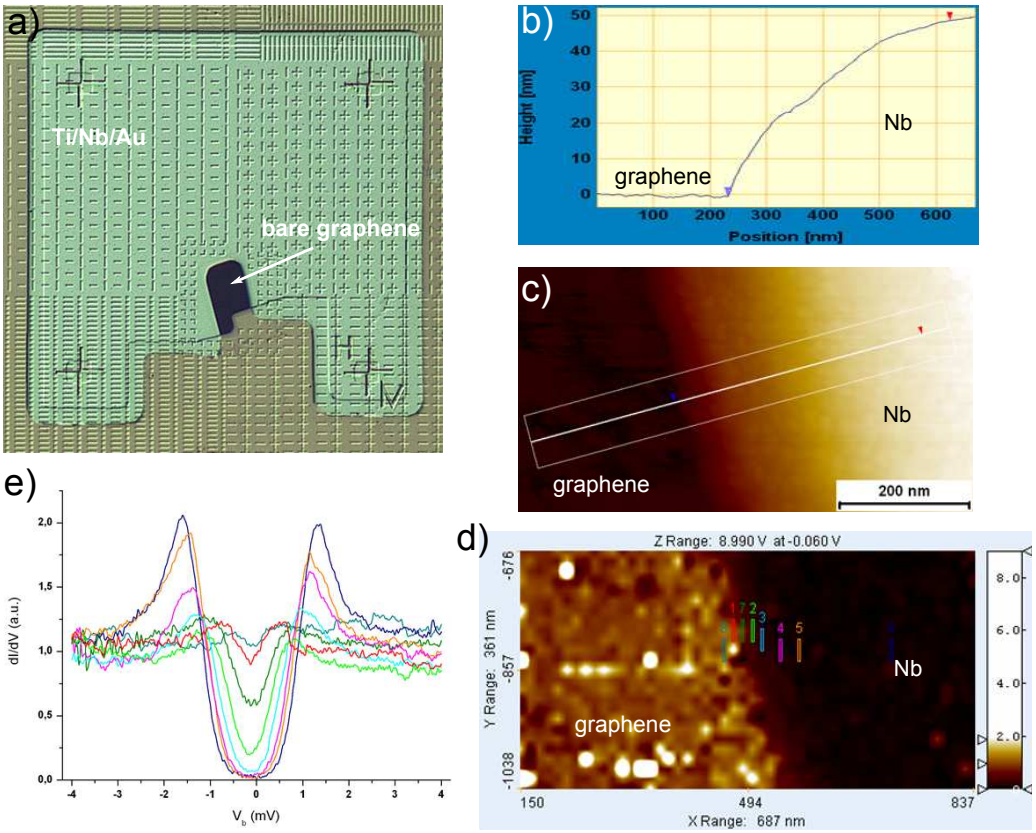

Figure 3.18 *(a) SEM image of the exfoliated graphene sheet reported on a Si/SiO_2 substrate, contacted all around by a Ti/Nb/Au trilayer. (b) Profile line at the bare graphene/superconductor interface imaged in (c) STM topography of the interface. (d) Differential conductance map of the interface at the Fermi energy. (e) Differential conductance spectra averaged on different zones at the interface. Colors correspond to the small rectangles in (d). Courtesy of Zoltán Osváth.*

3.4.2 STM on graphene decorated with superconducting nano-islands

Tin superconducting clusters We collaborated with Vincent Bouchiat's team at Institut Néel[14] to study their decorated graphene samples by STM. To avoid further lithography steps and at the same time get rid of detrimental graphene-substrate interactions, a new type of substrate has been imagined: a graphene sheet has been reported on a transmission electron microscope (TEM) perforated Si_3N_4 membrane. These membranes have a size of about $500\times500\,\mu m^2$, which makes them visible to the naked eye and allows a tip approach. The $2\,\mu$m diameter holes of the membrane are spaced by $2\,\mu$m. These holes are small enough to be identifiable by STM even at low temperature and they support free-standing graphene. Once the graphene had been reported on the upper face of a TEM membrane, one proceeded to the evaporation of tin droplets on the other face to create the superconducting clusters network described in the previous section. TEM images of the sample are presented on Fig. 3.19. The STM study was then carried out on the upper face of the membrane, free from Sn droplets that would have prevented the

[14]Institut Néel, 25 Rue des Martyrs, F-38042 Grenoble.

STM tip apex to reach the graphene layer. The topographic imaging of the free-standing graphene in the holes proved to be impossible as it leaded to the loss of the tunnel current, as if the membrane was buckling under the weight of the tin clusters. Most of the time, even on the Si_3N_4 membrane, the tunneling junction was very unstable, making think of a polluted surface, and resulted in a rapid deterioration of the tip. We did not reiterate this experience for now, but the availability of a higher quality graphene than the one used previously and a better control of the Sn nano-clusters coverage could increase our chances in the future to study such a sample with STM.

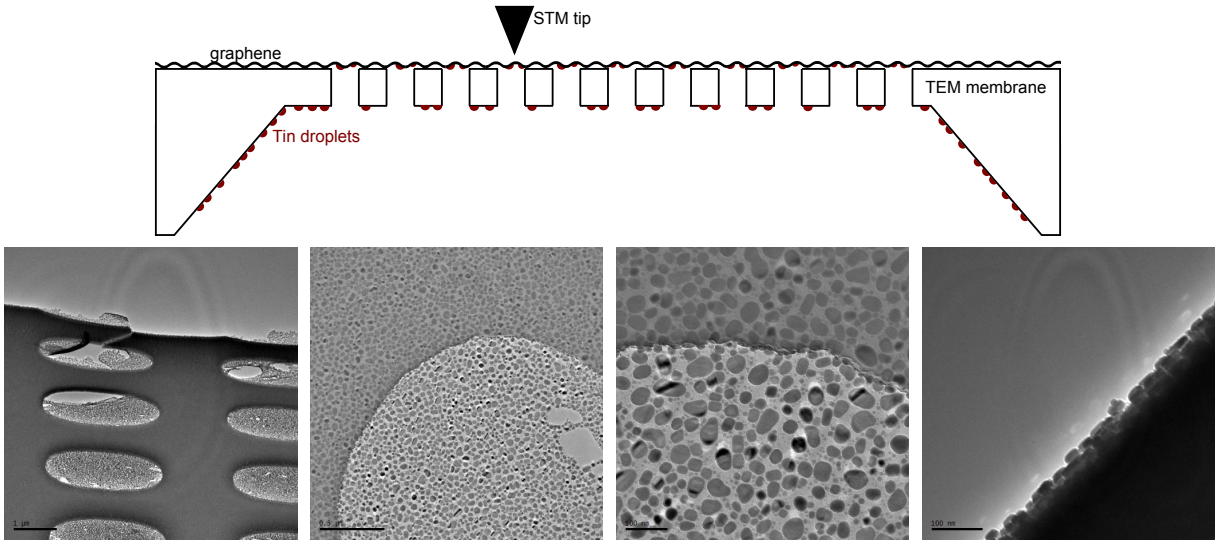

Figure 3.19 *Top: sketch of the STM experiment. Bottom: TEM images of graphene reported on a TEM membrane. The tin nano-islands evaporated at the back of the graphene sheet are visible through the Si_3N_4 membrane. The right image is a cross-section view of the tin nano-islands. Courtesy of Zheng Han.*

Indium superconducting nano-droplets We also collaborated with Hélène Bouchiat's group at LPS[15] for the study of a graphite sample covered by superconducting indium nano-particles of ∼10-20 nm of diameter (see SEM images in Fig. 3.20), deposited by sputtering process. As seen on the STM images presented in Fig. 3.20, we did not achieve to image the indium nano-particles by STM. The surface presents some graphite atomic steps (top right image) and a very rough texture, on which it is not possible to identify metallic nano-particles. Our guess is that the nano-particles are being easily swept by the STM tip. The bottom right SEM image seems to corroborate this hypothesis: we can see a clear limit between a zone with indium marbles and a "clean" zone, where some nano-islands are piled up in places. Nevertheless, the roughness of the surface is very unusual for graphite, which is normally easily imaged by STM. This might come from a contamination of the surface during the sputtering process, or by the fact that the scan is disturbed by the indium nano-particles swept by the tip. To overcome this difficulty, we are designing an STM experiment with *in situ* deposition of indium or tin nano-particles.

[15]Laboratoire de Physique des Solides, UMR 8502 Université Paris sud, F-91405 Orsay.

With this new set-up, it will be possible to evaporate tin in cryogenic vacuum, with the help of a heated tungsten filament placed close to the sample surface. This is a side-project we are trying to develop at room temperature in a first phase, in order to study its feasibility.

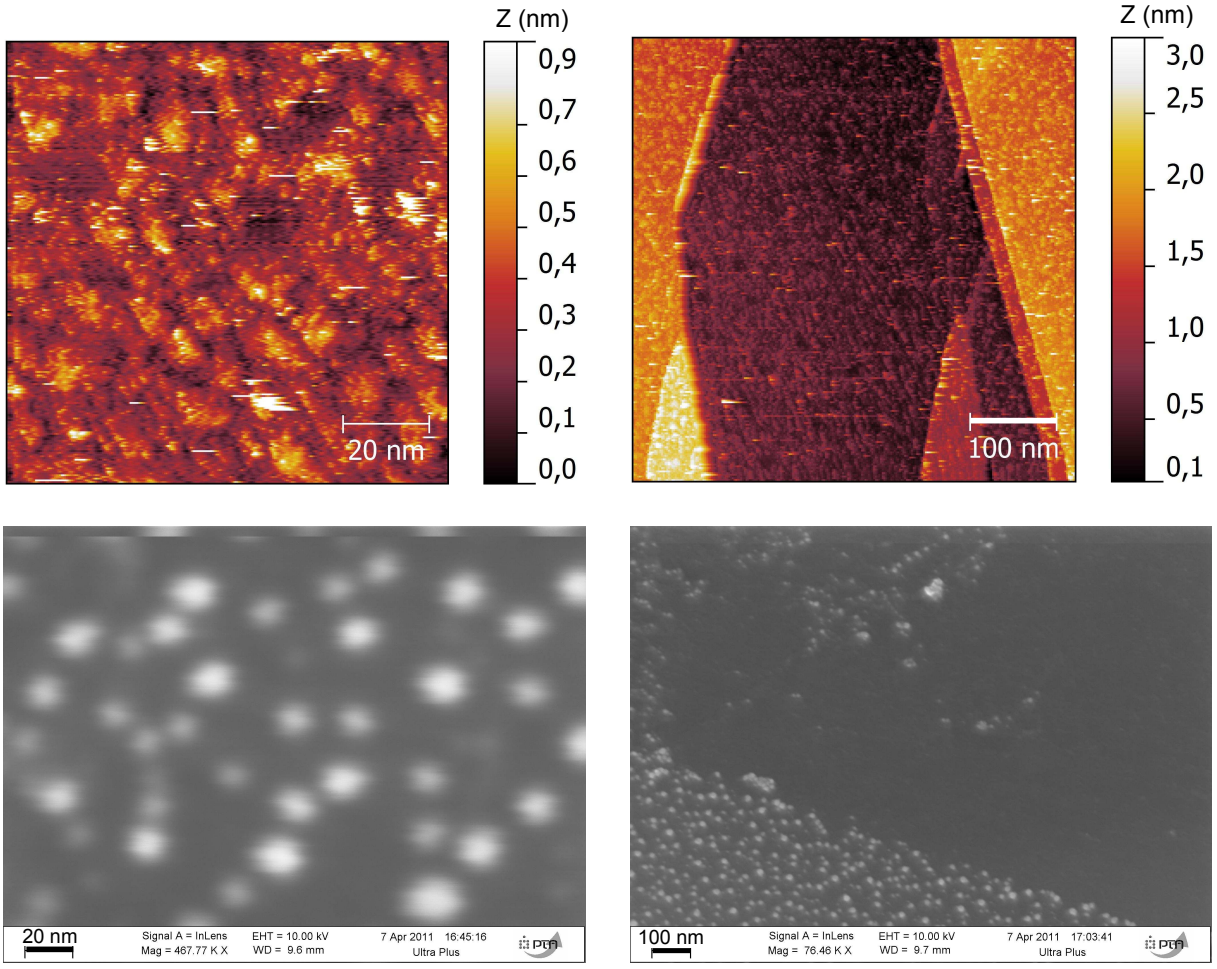

Figure 3.20 ***Graphite decorated with indium marbles*** *- Top: STM topographic images at 300 K, where no indium marbles are clearly identifiable. Right topography exhibits graphite atomic steps. Bottom: SEM images taken after the STM study, showing indium marbles of diameter $\leq$20 nm, separated by $\sim$40 nm. Right image presents a zone where indium marbles are absent, potentially moved away by the STM tip.*

3.4.3 A new design

All these unsuccessful attempts made us think about the conception of a different sample design, enabling to study the induced superconducting properties of graphene at low temperature, but more adapted to a local STM study.
The requirements are the following:

- a clean surface easy to reach with a STM tip
- a graphene sheet with high-crystallographic quality
- a good electronic coupling between graphene and the superconductor

To verify simultaneously all these criteria, we proposed the **growth of an epitaxial layer of graphene directly on top of a superconductor** by chemical vapor deposition (CVD) method.
In this way, the first criterion is indubitably guaranteed. The second one implies the choice of an adequate substrate, itself exhibiting high-crystallographic quality, and steps of optimization of the growth parameters to reach a satisfying quality. The third criterion will need to be verified as the graphene-on-metal systems are known to present various interaction strengths.

From our collaboration with Bruno Gilles[16], who can prepare rhenium thin films with very high crystallographic quality, and Johann Coraux[17], who masters the CVD growth of grahene on various metallic substrates, arises our new system: **a graphene monolayer epitaxially grown on a rhenium thin film**.

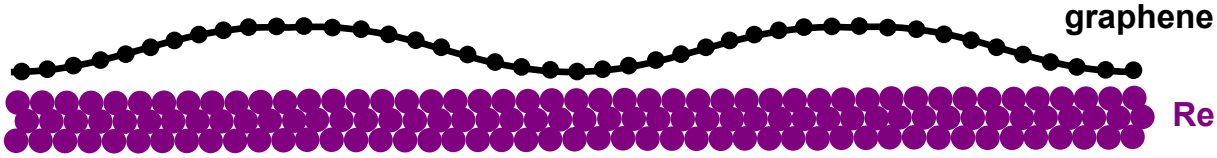

The next chapters of this manuscript present the characterization and very low temperature study of this system by scanning tunneling microscopy and spectroscopy.

[16]SIMAP, 1130 rue de la Piscine, BP 75, F-38402 Saint Martin d'Hères.
[17]Institut Néel, 25 Rue des Martyrs, F-38042 Grenoble.

Chapter 4

Epitaxial graphene grown on rhenium

Contents

Introduction

This chapter is dedicated to the presentation of the graphene-rhenium system. In a first section, we review the properties of rhenium and the superconducting mono-crystalline thin films fabricated by Bruno Gilles and his team. We then describe the growth of graphene on metallic substrates by chemical vapor deposition methods and make a synthetic presentation of the graphene-metal systems already studied in the literature. In particular, we see that the metal substrates can be sorted in two categories according to their coupling strength with graphene. After describing our growth process, we present STM topographic analyses of our graphene-rhenium system and the study of the resulting moiré superstructure. We show that our observations are in agreement with DFT calculations simulating our system. Finally, we present a spectroscopic study at high-energy (several hundreds of meV). These different approaches allow us to conclude as for the type of coupling that characterizes our graphene-rhenium system.

4.1 Rhenium thin films

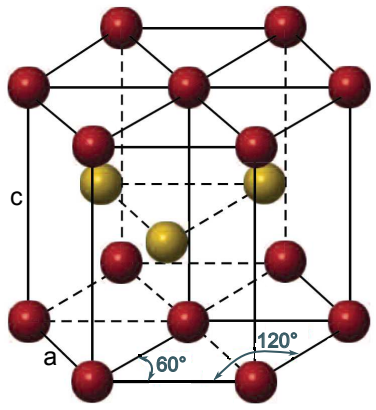

Figure 4.1 *Hexagonal close-packed (hcp) structure of Rhenium.*

Properties of Rhenium Rhenium is a refractory metal, with atomic number 75, having a hexagonal close-packed crystallographic structure with lattice parameters a=2.76 Å and c=4.45 Å, leading to an interplane distance of 2.23 Å (cf Fig. 4.1). It is known for its good resistance to heat, has the second highest melting point of all metals with T= 3185°C, and excellent wear properties. Despite its high price (which can reach up to 14 k€/Kg), Rhenium is widely used for aerospace applications, mainly as an alloying element, due to its excellent mechanical strength and resistance to creep at high temperatures. Its high resistance to corrosion also makes him an attractive material for coating. Of primary importance for us, Rhenium does not form carbide compounds at ambient pressure. Nevertheless, the solubility of carbon in Re is relatively high along with the wettability between these two elements, which yields to excellent bond strength between Re and C atoms[1]. Finally, bulk Rhenium is a type I superconductor with T_c=1.697 K and its mono-crystalline form does not easily oxidize.

4.1.1 Rhenium thin films fabrication process

The rhenium thin films were prepared by molecular beam epitaxy (MBE) on commercial sapphire substrates by Bruno Gilles and coworkers at SIMAP[2]. Sapphire is a suitable substrate for epitaxial growth of Re, as the two materials present the following epitaxial

[1] Rhenium is indeed widely used as an erosion-resistant coating element on carbon surfaces, for example in high-temperature rocket engines and hot gas valves [96].

[2] SIMAP, Grenoble INP, 1130 rue de la Piscine, BP 75, F-38402 Saint-Martin-d'Hères, France

relation: $(0001)Al_2O_3//(0001)Re$ with $\langle 2\bar{1}\bar{1}0\rangle Al_2O_3//\langle 01\bar{1}0\rangle Re$. In this configuration, the metallic atomic sites (Al and Re) coincide.

Preparation of the sapphire substrate To eliminate the impurities and smooth the surface, the sapphire substrates require a cleaning in a peroxymonosulfuric acid bath and an annealing process of 1 h at T=1130°C under Ar(80%) and O_2(20%) atmosphere. X-ray photoelectron spectroscopy (XPS) analysis and atomic force microscope (AFM) images confirm the good surface conditions before proceeding to the Re growth. To grow a mono-crystalline Re film, one needs to ensure a good mobility of the Re atoms on the surface by heating the surface at a sufficiently high temperature. Given the high melting temperature of Rhenium, the substrate base temperature must be around 730°C. The heating is provided by a furnace block with a tungsten filament placed 10 mm below the sapphire substrate, which is fixed on a sample holder hollowed in its center. As photon radiation alone does not enable to reach a temperature higher than 730°C, one can combine it with electron beam heating by applying a potential difference between the tungsten filament and the substrate. To optimize these two heating processes, a tungsten film is sputtered on the back side of the sapphire substrate (about 300 nm thickness), which allows a more efficient radiative absorption and charge evacuation during the electronic beam heating.

Epitaxial growth of Re The MBE process takes place in an ultra-high vacuum (UHV) chamber where ultra-pure Re cylinders (purity 99.95%) are heated in a separate effusion cell until they begin to slowly sublime. The gaseous elements will then condense on the sapphire substrate, previously thermalized around 730°C. The Re evaporated atoms do not interact with each other or residual vacuum chamber gases until they reach the wafer, due to their long mean free paths. The monolayer deposition time can be long and is limited to 6 Å/min for the films presented here[3]. During operation, the crystal layers growth is controlled by reflection high energy electron diffraction (RHEED).

4.1.2 Selection of rhenium films

To select rhenium films better suited to our system, we benefited from the extensive study made by Bruno Gilles and his team at SIMAP, where they examined the influence of the different parameters, such as the substrate temperature during the growth or the film thickness, on the film morphology and its superconducting properties.
As Re grows in the form of grains, an important point for us was to have the larger terraces (or grains) as possible. This is obtained with higher growth temperature (>730°C) and bigger film thickness (>25 nm). This is a rather intuitive result, as a higher temperature means a higher mobility of the Re atoms on the surface during growth, letting them organize more easily to minimize the constraints due to the epitaxy with the sapphire substrate. Following the same idea, increasing the thickness enables Re to release the constraints and creates dislocations. After a critical thickness (around 30 nm), the influence on the grain size is reduced though.
Concerning the superconducting properties, in which we are highly interested, they also

[3]The deposition rate is measured with a quartz crystal microbalance placed near the substrate.

vary with the growth temperature and the film thickness. For a given thickness, the superconducting transition temperature T_c decreases with increasing the growth temperature. In the same way, T_c decreases with increasing the film thickness. This seems to lead to the conclusion that accumulating constraints in the film increases the critical temperature.

4.2 Epitaxial graphene on rhenium

Although the formation of graphitic carbon layers on metals was first reported in the sixties [12], sometimes even identified as "monolayer of graphite" (from LEED[4] patterns analyses [90]), and further studied by surface scientists (see for example the first analysis of the structure of single-layer graphene on metallic single crystals in [80]), one had to wait after 2005 for these systems to be center stage and become the third main field in graphene research [145]. The renewed interest in the preparation of graphene on metallic single crystals arises from the possibility to grow high quality graphene flakes and then transfer them to whatever support by chemically etching the metal, thus making possible an industrial production of graphene films [83, 74, 10].

4.2.1 Graphene growth on metal substrates

There are two common ways to grow graphene on metals, known as the segregation and the deposition method, both described hereinafter.

Deposition method Graphene can be grown by catalytic thermal decomposition of carbon precursors such as ethylene, a process often referred to as chemical vapor deposition (CVD). The counterpart process with a carbon atom flux instead of hydrocarbon molecules is called physical vapor deposition (PVD). As this latter does not involve catalytic processes, it can be performed on various substrates, including semiconductors and insulators (e.g. Si, hexagonal boron nitride, mica). For metals however, CVD is often preferred and two methods can be distinguished: either the metallic substrate is first annealed and the carbon precursor is further introduced, so that the molecules are adsorbed on the hot sample, or one first proceeds to the room temperature adsorption of the precursor followed by a temperature flash to decompose the molecules and desorb the hydrogen[5]. The islands morphology is then very much dependent on the flash temperature, their size decreasing with temperature. As for the graphene coverage, it depends on the ethylene dose (roughly ethylene pressure $\times$ exposure time). The growth stages are more related to the interaction strength between graphene and the metal atoms, as will be briefly mentioned later on.

Segregation method For metals with significant carbon solubility, graphene layers can be prepared by segregation to the surface of bulk-dissolved carbon. As seen in Fig. 4.2 a, rhenium belongs to this category. For this kind of growth, one can use a substrate with residual carbon impurities or a high-purity sample, in which carbon is formerly dissolved.

[4] LEED stands for low-energy electron diffraction.

[5] This method is often referred to as temperature programmed growth (TPG) to distinguish it from the CVD process in the strict sense.

In this latter case, the first step consists in heating up the metal substrate at a high temperature in a UHV chamber and proceed to carbon dissolution by introducing hydrocarbon gases in the chamber as the source of carbon: the hydrocarbon molecules dehydrogenate at the metal surface and carbon atoms diffuse into the bulk. Then, decreasing the temperature lowers the interstitial carbon solubility in the metal and drives carbon atoms towards the surface. The temperature ramp is a decisive parameter for the graphene growth. As illustrated on Fig. 4.2 b, an extremely fast cooling acts as a quench, the solute carbon atoms losing their mobility before being able to diffuse, resulting in a strong carbon concentration close to the surface. At the other limit, a very slow cooling rate enables the atoms to diffuse into the bulk over a long time, thus decreasing the amount of carbon that will segregate on the surface. However, an intermediate cooling rate results in a finite amount of carbon segregating which turns into graphene growth. The number of graphene layers and the amount of defects are very much dependent on this cooling rate. This method enables a good control of the growth process, with precise monitoring of the number of graphene layers and of its structural quality.

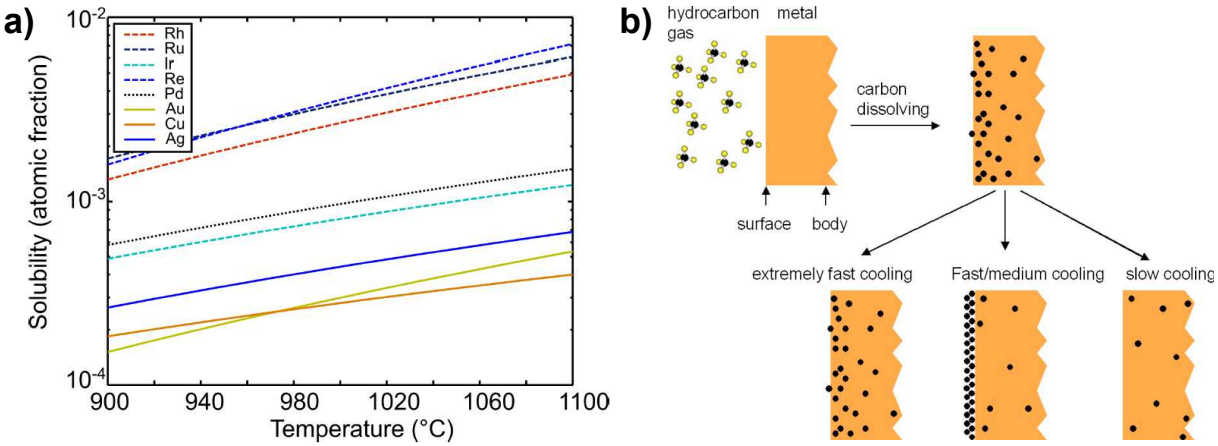

Figure 4.2 *(a) Solubility of carbon in various metals in function of the temperature. From [8]. (b) Illustration of graphene growth by segregation on Ni surfaces. Reproduced from [150].*

It is important to notice that the graphene growth is always performed at high temperatures (600-1500°C) to ensure enhanced catalytic activity of the metal surface and high carbon adatom[6] mobility (the diffusion length is bigger than 1 μm at 850°C and 10^{-9}mbar [32]).
Nevertheless, the growth proceeding highly depends on the metal element properties, such as its melting point[7], the carbon solubility in its bulk and the carbon-metal interaction, which will have strong impact on the growth type. In this regard, metals can be divided into **two binding classes**: the ones that present a weak interaction with graphene (Cu, Ir, Pt) and those that strongly interact with graphene (Co, Ni, Ru, Rh). Fig. 4.3 presents a summary of the interaction strength between graphene and the transition metals. Relying on two review articles [145, 15], we will now present some characteristics of the graphene layer grown on top of these two classes of metals.

[6] An adatom is an atom adsorbed on a surface.

[7] For instance, the melting points of the different metallic elements are: Cu: 1085°C, Ni: 1455°C, Ru: 2250°C, Ir: 2443°C, Re: 3185°C.

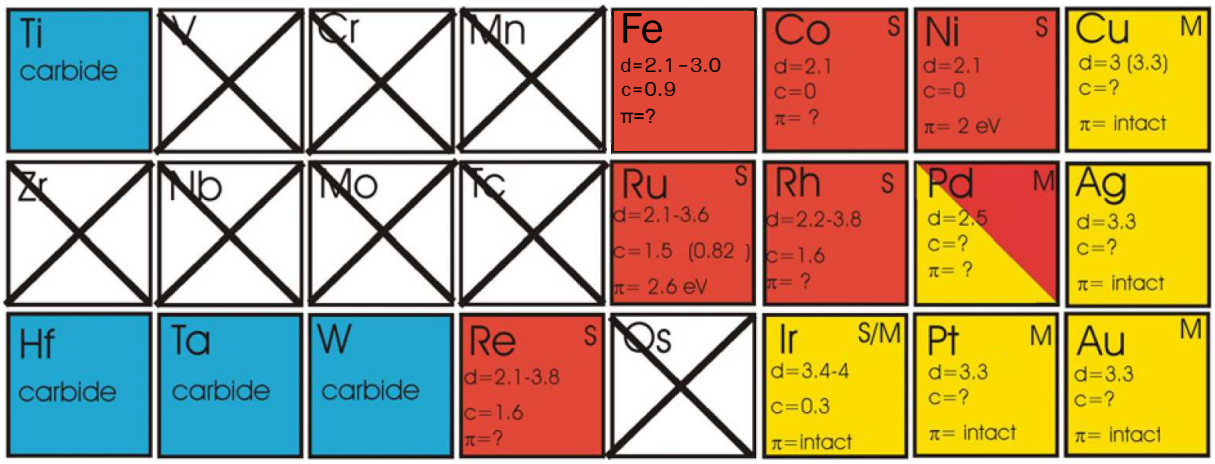

Figure 4.3 ***Summary of the interactions between transition metals and graphene.*** *Blue: graphene may grow from these elements bulk-carbide. Red: metals interacting strongly with graphene (data reported on Fe [139] have been added to the original table). Yellow: metals interacting weakly with graphene. Crosses: no graphene growth reported yet. 'S/M' in the upper-right corner indicates if graphene form single/multiple rotational domains. 'd' is the graphene-metal separation in Å, 'c' the buckling or corrugation of the graphene sheet in Å and 'π' the downward shift of the π-band ('Intact' means that a linear dispersion at the Dirac point is still observed). Adapted from [15].*

4.2.2 Graphene-metal systems

Weakly interacting systems

The metals that interact weakly with the graphene overlayer are represented in the yellow boxes on Fig. 4.3, the best-studied being copper [55], iridium [33, 34, 27] and platinum [80, 127]. They present a very large metal-graphene distance (up to 4Å for Ir(111)), that implies small corrugation of the graphene sheet (0.3Å). The mismatch of the lattice parameters of the graphene (2.46Å) and the metals (Cu(111): 2.56Å, Ir(111): 2.72Å, Pt(111): 2.77Å) leads to superstructures with large lattice constants, the so-called *moiré structures*. On Ir(111) for example, graphene forms an incommensurate moiré structure with a periodicity of 9.32 Ir lattice constants (∼2.5 nm) and domains with different orientations of the C atomic rows compared to the Ir atomic rows (see Fig. 4.4). However, several graphene phases coexist on Pt(111) and Cu(111): at least three have been reported on Pt (rotational angle/moiré periodicity: non-rotated/2.2 nm, 1.5°/2.0 nm, 90°/9.0 nm [80]) and several on Cu (the most often observed being non-rotated/6.6 nm and 7°/2.0 nm [55]).

Strongly interacting systems

The metals that interact strongly with the graphene overlayer are represented in the red boxes on Fig. 4.3. They all present small graphene-metal distances (down to 2.1Å for Ru(0001)), that imply strong corrugation of the graphene sheet (up to 1.6Å). This separation is much shorter than expected for a physisorbed layer[8], indicating the formation

[8] If the graphene is physisorbed, one would expect graphene-metal distance comparable to the layer spacing in bulk graphite (3.35Å).

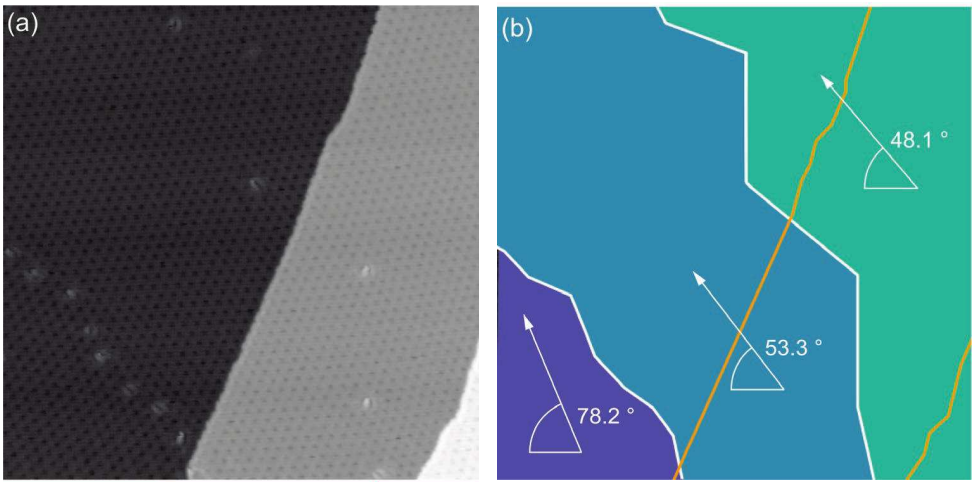

Figure 4.4 ***Graphene-Ir(111) system*** *(a) STM image of a graphene monolayer grown on Ir(111) at 1120 K (108 nm×108 nm). (b) Colored-map delimiting the three moiré domains in (a) with different rotational angles. Reproduced from [33].*

of genuine chemical bonds between the C and metal atoms. Owing to the close lattice match for Ni(111) (a_{Ni}=2.49Å) and Co(0001) (a_{Co}=2.51Å), graphene growth leads to a commensurate (1×1) structure. On the other hand, for Rh(111) (a_{Rh}=2.69Å) and Ru(0001) (a_{Ru}=2.71Å), like for weakly-interacting metals, the graphene overlayer outlines a moiré pattern. Fig. 4.5 a shows this moiré pattern for a Ru(0001) substrate, with a periodicity of 3.0 nm, corresponding to twelve carbon rings matching eleven Ru atoms. The graphene layer is strongly buckled, as confirmed by DFT calculations presented in Fig. 4.5 b. The atomic resolved image in (c) shows that the atomically contrast varies in the unit cell of the moiré structure: one resolves all the six C atoms on the bright hills but only one over two in the dark valleys. This can be explained considering the different positions occupied by the C atoms compared to the underneath Ru atoms, as illustrated on the simulated figures (b) and (d). This point will be discuss further in the following sections for the graphene-rhenium system.

The growth stages have also been found to be quite different regarding the binding class to which the metal belongs. On Ir(111) for example, graphene has been reported to grow continuously across step edges, both in the downhill and the uphill directions (Fig. 4.6 a-c), whereas the uphill growth is blocked in the case of Ru(0001) (Fig. 4.6 d-e). Furthermore, graphene growth occurs through C-monomers attachment on Ir(111) but cluster attachments on Ru(0001), as illustrated on Fig. 4.6 f. This was first understood by analyzing the graphene growth rate regarding the C-monomer concentration: the clearly non-linear behavior could be explained by pentamers attachment to the graphene growing sheet.

It should be noted that no qualitative explanation has been given relatively to the strong differences observed in the binding of graphene with various transition metals. The so-called *d-band model*, which predicts a stronger binding with decreasing occupation of the d band (i.e. following a line from right to left in the periodic table), and a stronger binding from the 5d to the 3d metals, is consistent with previous observations but does not account for the large distance variations between the metal-graphene systems. Any-

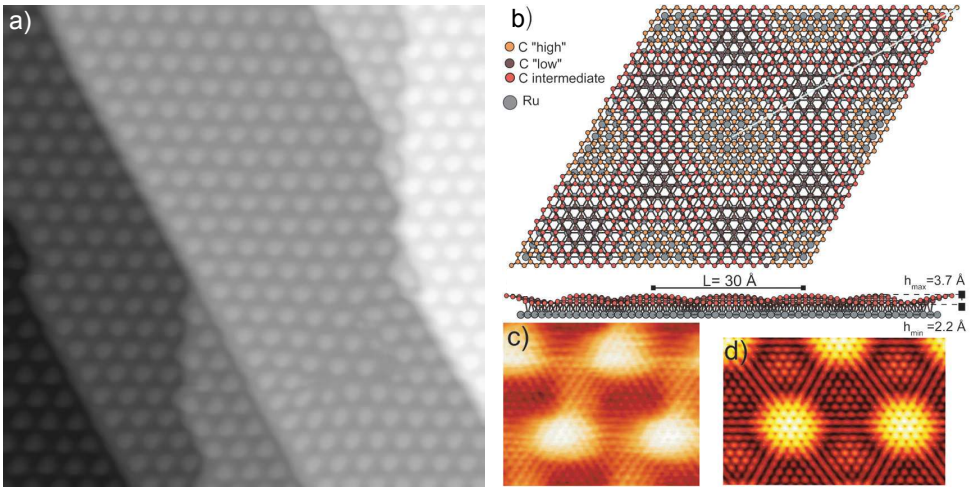

Figure 4.5 ***Graphene-Ru(0001) system*** *(a) STM image of a graphene monolayer grown on Ru(0001) at 1200° C showing substrate steps (50 nm×50 nm). (b) DFT model of the moiré structure of graphene on Ru(0001), calculated for a (12×12) graphene cell over a (11×11) Ru cell. The underneath side view shows the buckling of the graphene layer. (c) Atomically resolved STM image showing three different levels of apparent heights, high, intermediate and low, identifiable on the calculated figure (b) (5nm×4nm). (d) Computed constant current STM image using the Tersoff-Hamman approximation. Reproduced from [145].*

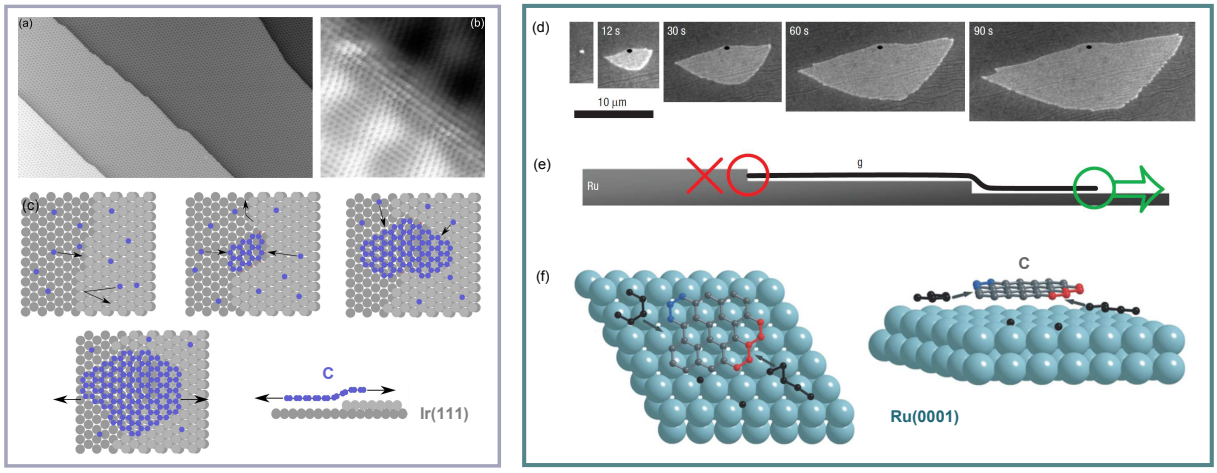

Figure 4.6 ***Left panel: graphene-Ir(111) system****. (a) STM image of graphene crossing several Ir steps (125 nm×250 nm). (b) Continuous atomic arrangement in graphene across a step edge (5 nm×5 nm). Reproduced from [33]. (c) Growth model of graphene on Ir(111): C adatoms first nucleate at the lower side of a step edge in the energetically most favorable configuration (regarding the preferential lattice orientations of graphene relatively to Ir) and the uphill growth is delayed until the C atoms of the upper terrace edge have enough energy to break the C-Ir bond and form σ bond with the C atoms below. Reproduced from [32].* ***Right panel: graphene-Ru(0001) system****. (d,e) Low-energy electron microscopy (LEEM) data and schematic view of graphene growth on Ru(0001) showing the downhill carpet-like expansion of the graphene sheet, whereas uphill growth is blocked. Reproduced from [126]. (f) Schematic views of the cluster attachment mechanism responsible for graphene growth on Ru(0001). Reproduced from [15].*

how, the two binding classes seem to distinguish between a situation where graphene is physisorbed on the surface (with Cu, Ir, Pt), bringing into place weak interacting forces (van der Waals), and one where it is chemisorbed, forming covalent or ionic bonds with the underneath metal (Ni, Co, Ru, Rh).

4.2.3 Graphene-rhenium system

As presented in 4.2.1, two methods are possible to grow epitaxial graphene on a metal substrate. Given the high solubility of carbon in rhenium and the better monitoring and structural quality of the graphene layer offered by the segregation process, we opted for this one.

Preparation of the Re films surface After the Re growth, the samples were transferred into another UHV system equipped for chemical vapor deposition (CVD). The graphene growth was carried out by Amina Kimouche and Johann Coraux in Institut Néel[9]. As the Re/sapphire samples were exposed to air during the transfer, they all went through a cleaning process after their installation in the CVD chamber, performed in three successive steps:

- annealing at 900°C during 30 mn
- O_2 exposure during 5 - 10 mn with $P_{O_2} \simeq 10^{-8}$ mbar (optional)
- flash at 1200°C

Afterwards, the surface was checked in situ by RHEED and STM (Fig. 4.7 a) to ensure its cleanness (absence of impurities) and its smoothness (flat Rhenium terraces).

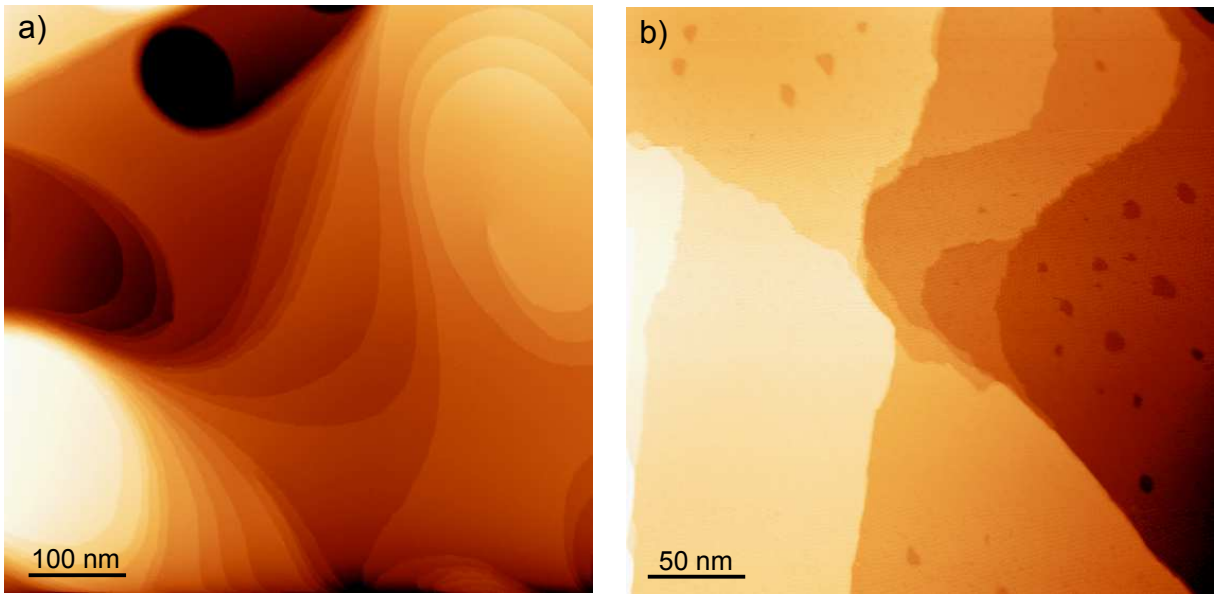

Figure 4.7 ***STM topographic images in UHV*** *(a) Before graphene growth (V_{bias}=1.5 V, I_t=1.8 nA). (b) After graphene growth (V_{bias}=0.5 V, I_t=20 nA). Courtesy of Amina Kimouche.*

[9]Institut Néel, CNRS/UJF, 25 rue des Martyrs, F-38042 Grenoble cedex 9, France

Graphene growth Graphene was then grown on the Re(0001) surface following the segregation method:

- annealing at 1000°C under ethylene exposure (10^{-7}-10^{-8} mbar during several minutes)
- ethylene flux is turned off and the temperature is slowly decreased from 1000°C to 600°C (several tens of minutes)
- heating is stopped, resulting in fast cooling of the sample down to room temperature

A summary of the different growth conditions is presented on Tab. 4.1. The samples written in bold characters have been studied in the low-temperature STM, their topographic aspect is indicated in the last column.

The surface was then checked by RHEED or STM to ensure the graphene growth was completed. Fig. 4.7 b presents a $300\times300\,nm^2$ topographic image acquired with the UHV STM just after a successful growth. What is striking is the presence of holes on the Re terraces, that were absent before carbon introduction. Although the scale is too large to conclude, we will see later that they correspond to holes in the Re film and not in the graphene layer. The fact that they can not be observed on the pristine Re surface indicates that these features appear during the growth. Studying their formation could thus be a good lead to understand the growth process of graphene on Re(0001) thin films.

What's next

A fundamental question for our study is: to which binding class does Rhenium belong? Is it weakly interacting with graphene, like other studied 5d metals (Ir, Pt), or strongly interacting with it, as other low-filled d band metals (Fe,Ru)? We have seen in Chapter 3 the importance of the interface quality between graphene and the coupled superconductor for the efficiency of the superconducting proximity effect. Our goal is to create a graphene-superconductor system with a highly transparent interface to study how the superconducting properties are transferred and survive into graphene. A characterization of our system regarding the coupling strength between graphene and rhenium is thus essential before going further in the analyses of the superconducting properties.

Sample	Re thickness (nm)	Ethylene dose (mbar)	Exposure time (min)	Temperature ramp (min)	STM observations @LT
AK 23	30	10^-8	10	60	Moiré
AK 27	50	5.10^-8	10	60	Moiré (but dirty sample)
AK 37	50	10^-7	25	60	
AK 43	50	10^-7	40	60	Moiré + amorphous C
AK 44	50	10^-7	1	10	
		10^-8	1	10	
		10^-8	5	10	
		10^-8	10	10	
AK 48	50	10^-7	1	10	
AK 49	50	10^-7	2	30	Moiré + disordered regions
AK 50	50	10^-8	10	20	No moiré
AK 51	50	10^-8	5	20	

Table 4.1 *List and growth conditions of the different graphene-Re(0001) samples.*

4.3 Topographic analyses

After the graphene growth, the samples were taken out from UHV and set up in our STM, where they were cooled down to 50 mK. Although they had been exposed to air, we did not observe excessive contamination of the surface that could disturb the STM study. As our system does not enable us to perform annealing before cooling down the sample, we made do with a slight heating before cryopumping. All the images were acquired at low temperatures with Pt/Ir tips, hand-cut or commercial ones (described in Chapter 1).

4.3.1 Large scale morphology

Large scale STM images show numerous flat Re monocrystalline grains, with sizes varying from 50 to 200 nm, as seen on Fig. 4.8 a. The bright spots are dusts or impurities. Zooming on terraces reveal a superstructure, the so-called *moiré pattern*, characteristic of graphene grown on mismatched substrates (see Fig. 4.8 b-d). The difference between the graphene and Re lattice parameters (a_C=2.46Å, a_{Re}=2.76Å) induces strain in graphene that is relaxed by the mean of a periodic rippling of the graphene sheet[10]. The graphene layer is thus lying at a varying distance from the Re surface, resulting in a series of 'valleys' and 'hills' defining the moiré structure. During the growth, a full coverage of monolayer graphene[11] was achieved over the Re surface, as attested by the presence of the moiré on every Re mount. At the bottom of image (b), Re grains are covered by graphene with irregular borders. This feature is nevertheless rarely observed and will therefore not be further discussed. Some defects can also be observed in the regular pattern of the moiré on the terraces, better seen on images (c) and (d). On these latter images, we can clearly distinguish several 'holes' (in the sense of missing 'hills') in the moiré structure. These defects will be addressed later on in this manuscript. Image (e) is a 3D-plot of a 8×8 nm^2 surface exhibiting a perfectly regular moiré pattern. The apparent moiré corrugation (height difference between hills and valleys) is estimated here around 1.5 Å but is actually very tip-dependent.

An interesting feature recurrently observed is presented on Fig. 4.9. (a) is a topography image showing three Re atomic steps and several holes in the Re films, the biggest one having a length of about 45 nm and measures 10 nm at its largest point. From this picture, we can deduce with certainty that these holes are associated with a step in the Re film and do not correspond to holes in the graphene layer. Indeed, we can clearly see the presence of a moiré pattern inside the hole, attesting the presence of graphene, but at an underlying level. Line profile (Fig. 4.9 c) over the three Re step edges (red) allows to measure a step height of about 2.2 Å, which is consistent with the Re interplane distance of 2.25 Å[12]. Another line profile (violet) shows the hole depth matches the Re step height, confirming the hypothesis of a hole in the first Re layer. One can notice that the hole edges follow the moiré directions, which is not surprising as these latter are

[10] This is the smoothest way to relax the strain due to the epitaxial growth. A more drastic one being the creation of dislocations in the graphene layer.

[11] Several experimental observations indicate that we are indeed in presence of a single layer of graphene, as well as comparison to DFT calculations of the observed moiré supercell. We will come back to the justification later on.

[12] and thus confirms the good calibration of the STM piezoelectric tube.

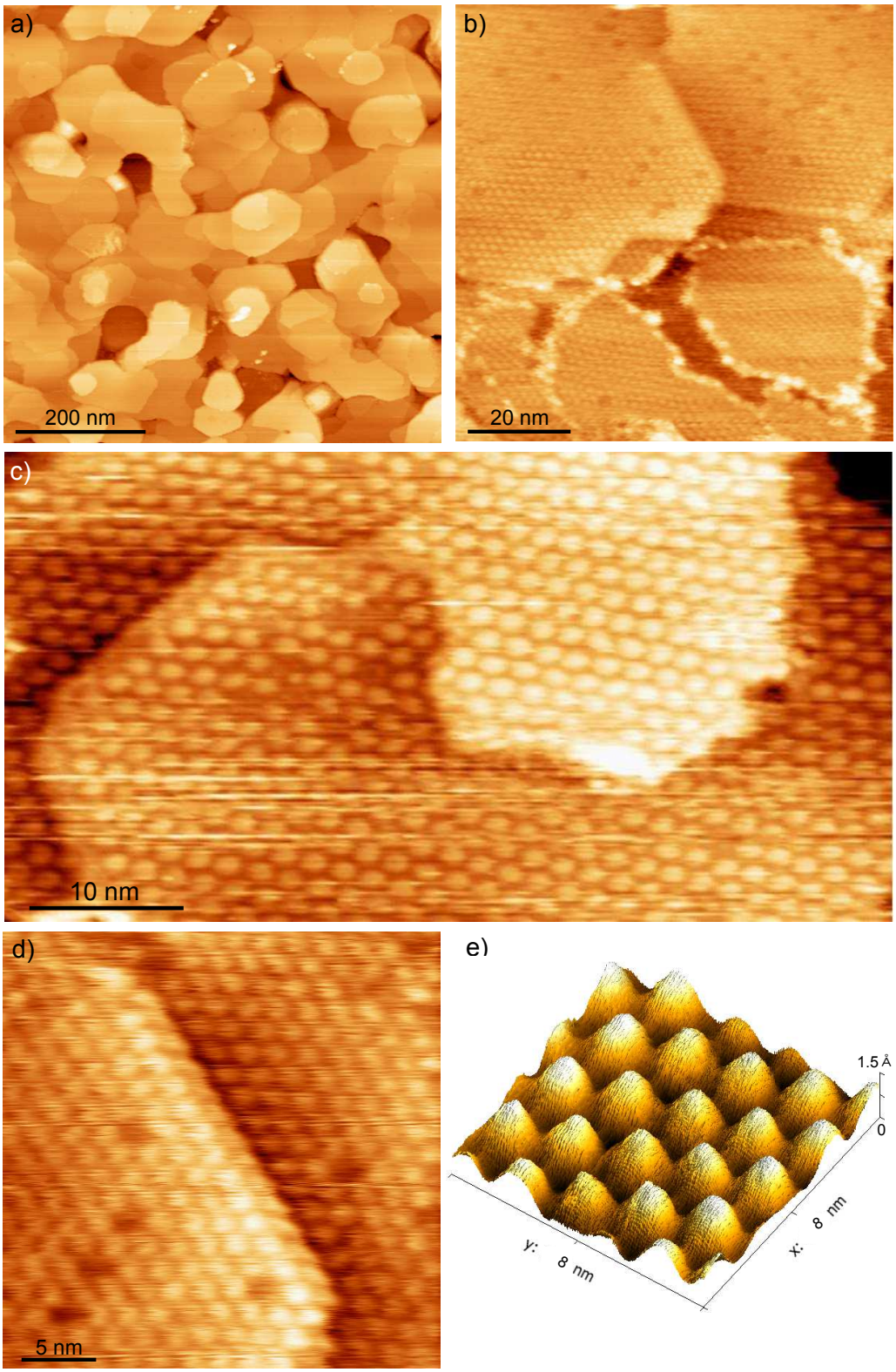

Figure 4.8 ***STM topographic images of a graphene-Re(0001) sample surface at different scales.*** *(a) Large scale image showing Re grains (V_{bias}=260 μV,I_t=50 pA). (b) Middle scale image showing the moiré superstructure, attesting the full coverage of graphene on Re terraces (V_{bias}=20 mV,I_t=200 pA). (c) Re steps and moiré hole-type defects (V_{bias}=500 mV,I_t=500 pA). (d) Zoom of image (b) on a Re dislocation step showing defects in the moiré pattern. (e) 3D plot of the moiré structure (V_{bias}=100 mV,I_t=100 pA).*

directly correlated to Re(0001) in-plane crystallographic directions. On this image, the moiré corrugations were measured as high as 1.4 Å. Fig. 4.9 b is an enlargement of the black frame in image (a) showing a dislocation in the moiré pattern (insertion of a hill row [green] between two others [black]) originating from a moiré hole (missing hill). This implies some rearrangement of the carbon layer at the atomic level, we unfortunately can not explore further here as it would require atomically resolved images we do not have for such features. One should notice that these moiré holes are not necessarily associated with 'moiré dislocations' as seen here. Most of the time, they just appear as a missing hill in an otherwise regular moiré pattern over the surface.

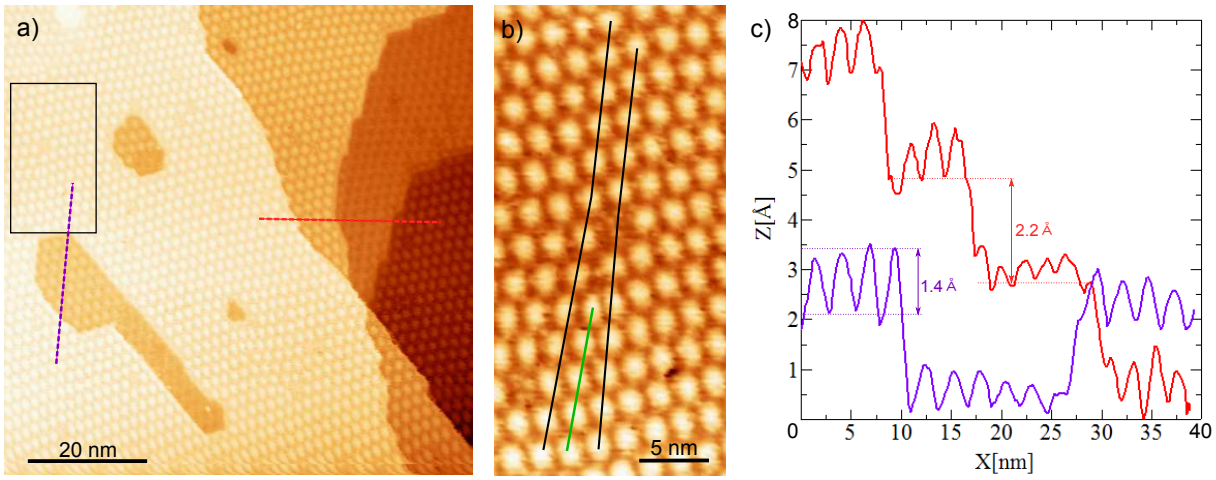

Figure 4.9 *(a) UHV STM topographic image showing holes in the Re film (V_b=500 mV, I_t=30 nA). Courtesy of Amina Kimouche. (b) Enlargement of the left-corner frame in (b) showing a 'moiré dislocation' originating from a moiré 'hole'. (c) Profiles along lines in image (a) - red: profile over 3 Re step edges, violet: profile over a hole.*

4.3.2 Moiré structure

The moiré is a superstructure resulting from the superimposition of two identical rotated lattices or two mismatched lattices (see Fig. 4.10). The analysis of our moiré pattern, and in particular of its periodicity and its angle with the carbon atomic rows, enables to determine the arrangements of carbon atoms on the rhenium ones and the rotational angle between the C and Re lattices. We present two STM topographic images with atomic resolution, Fig. 4.12 and 4.13, acquired in UHV and at 1.5 K respectively. We plot their fast Fourier transform images and several profile lines, which will enable to study in details the atoms arrangement of the structure. The three-fold periodicity of the moiré pattern is clearly visible both in the direct (hills/valleys hexagons) and reciprocal spaces. We will extract the moiré periodicity knowing the carbon atoms periodicity b_{GR}=2.46Å. We chose to calibrate our piezo with this theoretical value to increase our measurement precision at small scales.

STM image of Fig. 4.12 presents an almost perfect alignment of the carbon atomic rows (green line) with the moiré direction (violet line). Only a tiny misalignment <3° can be estimated. Indeed we can distinguish parallel lines that correspond to rows of atoms

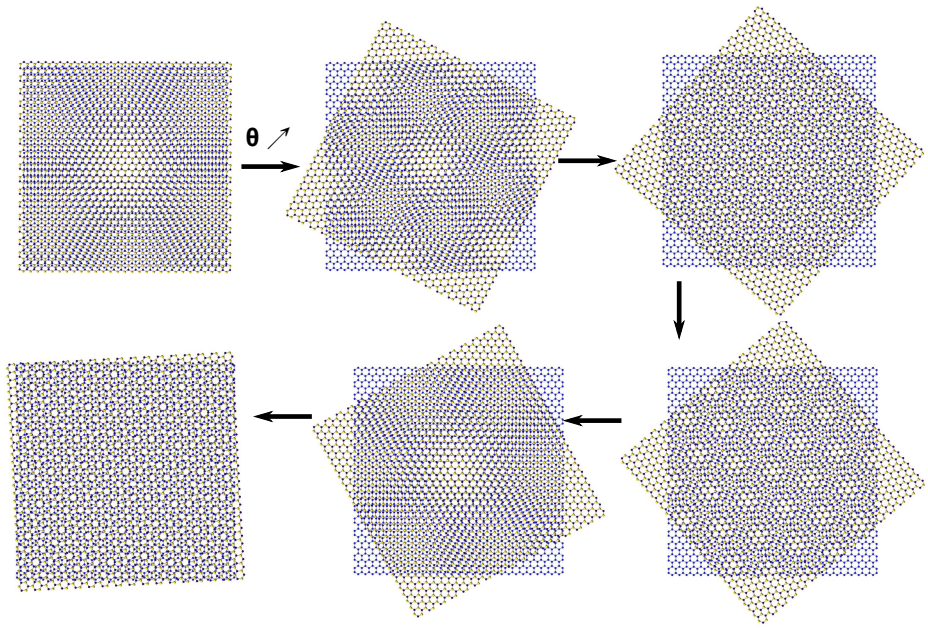

Figure 4.10 *Moiré patterns appearing when two periodic lattices are overlaid. The superstructure periodicity changes when the two lattices are rotated relatively to each other (angle θ). In the case presented here, it corresponds to graphene and boron nitride lattices. Credits: Columbia University.*

belonging to a same sublattice. These rows are schematized on Fig. 4.11 a by green doted lines and are separated by a distance $c_{\text{graphene}} = \frac{3}{2}a_{\text{graphene}} = 2.13$Å. These rows eventually transform into dots at some places, enabling to resolve one atom over two of the graphene lattice, that are separated by a distance $b_{\text{graphene}} = a_{\text{graphene}}\sqrt{3} = 2.46$Å. This distance corresponds to the periodicity of one sublattice. For rhenium one has $b_{\text{rhenium}} = 2.76$Å.

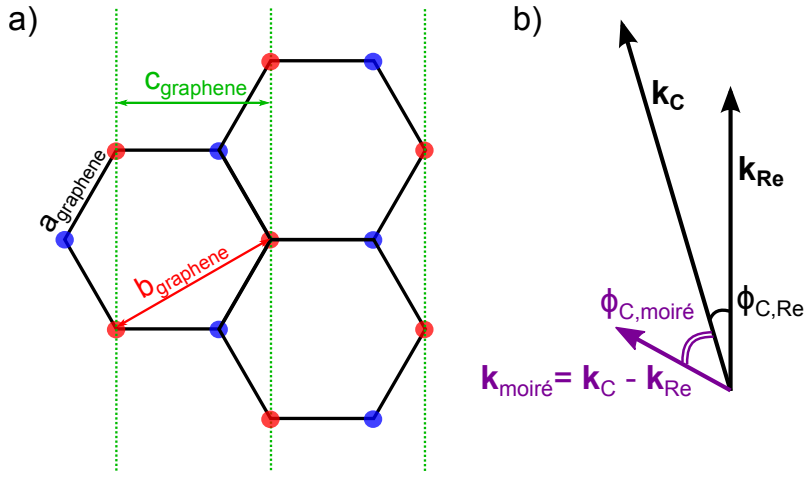

Figure 4.11 *(a) Schematics of graphene non-equivalent sublattices (red and blue) with characteristics distances. (b) Sketch in the reciprocal space of the **k**-vectors defining the moiré structure.*

The good alignment of carbon atomic rows with the moiré direction is confirmed on the FFT image where we can draw a line profile passing both by peaks representing the moiré periodicity (in the center of the image) and by peaks representing the carbon atoms periodicity (on the outside), as seen on Fig. 4.12. We can deduce $a_{\text{moiré}} = 1.9\,\text{nm} \pm 0.05\,\text{nm}$

by averaging the ratios in the different directions of the hexagon.

Fig. 4.13 presents an STM topographic image acquired at 1.5 K where the moiré direction (violet line) is rotated as compared to the carbon atomic rows (green line). The rotational angle, measured to be $\phi_{\text{C,moiré}} \simeq 14.6°$, is due to a misalignment between the rhenium substrate's and the graphene's atomic rows. As the moiré acts as a magnification effect, one can trace back to the tilt of the two lattices with respect to each other $\phi_{\text{C,Re}}$. Indeed, as illustrated on Fig. 4.11 b, the moiré can be defined by a reciprocal lattice vector expressed as the difference: $\mathbf{k}_{\text{moiré}} = \mathbf{k}_{\text{C}} - \mathbf{k}_{\text{Re}}$, where $\mathbf{k}_i = \frac{2\pi}{b_i}$. One can then derive [97]:

$$\sin(\phi_{\text{C,Re}}) = \left(\cos(\phi_{\text{C,Re}}) - \frac{k_{\text{C}}}{k_{\text{Re}}}\right) \tan(\phi_{\text{C,moiré}}) \tag{4.1}$$

For small angles $\phi_{\text{C,Re}}$ and $\phi_{\text{C,moiré}}$, this simplifies into

$$\phi_{\text{C,Re}} = \frac{k_{\text{Re}} - k_{\text{C}}}{k_{\text{Re}}} . \phi_{\text{C,moiré}} \tag{4.2}$$

with the constant factor $\left|\frac{k_{\text{Re}} - k_{\text{C}}}{k_{\text{Re}}}\right|^{-1} \approx 8.2$ being the angular magnification. Thus, on this image one can estimate $\phi_{\text{C,Re}} \approx \frac{14.6}{8.2} \approx 1.8°$. Note that we never observed boundaries between different rotational domains (with different $\phi_{\text{C,Re}}$). This may be due to the limited size of the rhenium grains.
To determine the moiré periodicity, we proceeded the same way as for the previous image, i.e. by ratios on FFT and topographic profiles. As this time the carbon atomic rows are misaligned with respect to the moiré direction, we drew two line profiles on the FFT, one passing by peaks representing the moiré periodicity (violet) and another slightly tilted passing by peaks representing the graphene periodicity (green), as seen on Fig. 4.13. We can deduce $a_{\text{moiré}} = 2.1\,\text{nm} \pm 0.1\,\text{nm}$ by averaging the ratios in the different directions of the hexagon. We find the same estimation from topographic profiles.

To describe further more the superstructure, we counted the number of carbon atomic rows in one moiré period on the image of Fig. 4.12: we found $\text{R} = \frac{b_{\text{moiré}}}{b_{\text{graphene}}} = 8$. From this ratio, one can trace back to $\text{r} = \frac{b_{\text{graphene}}}{b_{\text{Re}}}$ and thus to the real graphene lattice parameter, by a simple geometric reasoning based on Fig. 4.11 b, which is a schematic representing the reciprocal lattice vectors of the Re, C and the resulting moiré. One can derive in order:

$$k_{\text{moiré}} = \sqrt{(k_{\text{C}} \sin(\phi_{\text{C,Re}}))^2 + (k_{\text{C}} \cos(\phi_{\text{C,Re}}) - k_{\text{Re}})^2} \tag{4.3}$$

$$\text{R} = \left(\sqrt{1 + \text{r}^2 - 2\text{r}\cos(\phi_{\text{C,Re}})}\right)^{-1} \tag{4.4}$$

and using Eq. 4.2, one follows:

$$\text{r}^3 + (\phi^2_{\text{C,moiré}} - 2)\,\text{r}^2 + (1 - \frac{1}{\text{R}^2} - 2\phi^2_{\text{C,moiré}})\text{r} + \phi^2_{\text{C,moiré}} = 0 \tag{4.5}$$

which is a polynomial equation of third degree with real coefficients that can be easily numerically solved using *Mathematica* for example. In the simpler case of Fig. 4.12

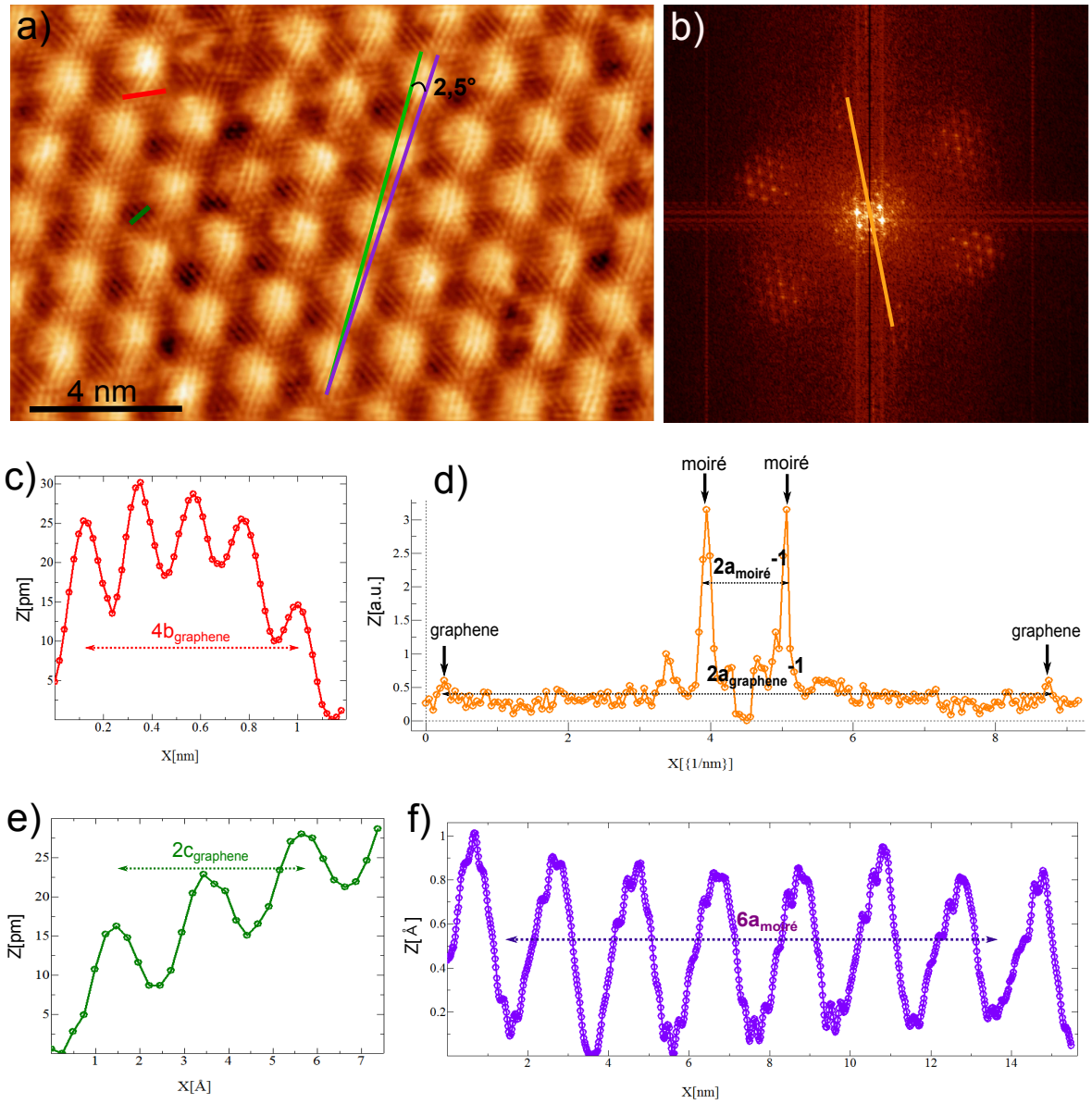

Figure 4.12 ***Graphene-Re(0001) in UHV*** *(a) STM topographic image of the moiré pattern, presenting an almost perfect alignment of the carbon atomic rows (green line) with the moiré direction (violet line). Measured with* $V_{\mathrm{bias}} = 224\,mV$ *and* $I_{\mathrm{t}} = 31\,nA$*. Courtesy of Amina Kimouche. (b) FFT of image (a). (c) Profile along the red line on the topographic image exhibiting the graphene atoms periodicity. (d) Profile along the orange line in the FFT image exhibiting the moiré and graphene periodicities. (e) Profile across carbon atomic rows (small dark green line). (f) Profile along a moiré row. The dots in the profiles represent single measurement points.*

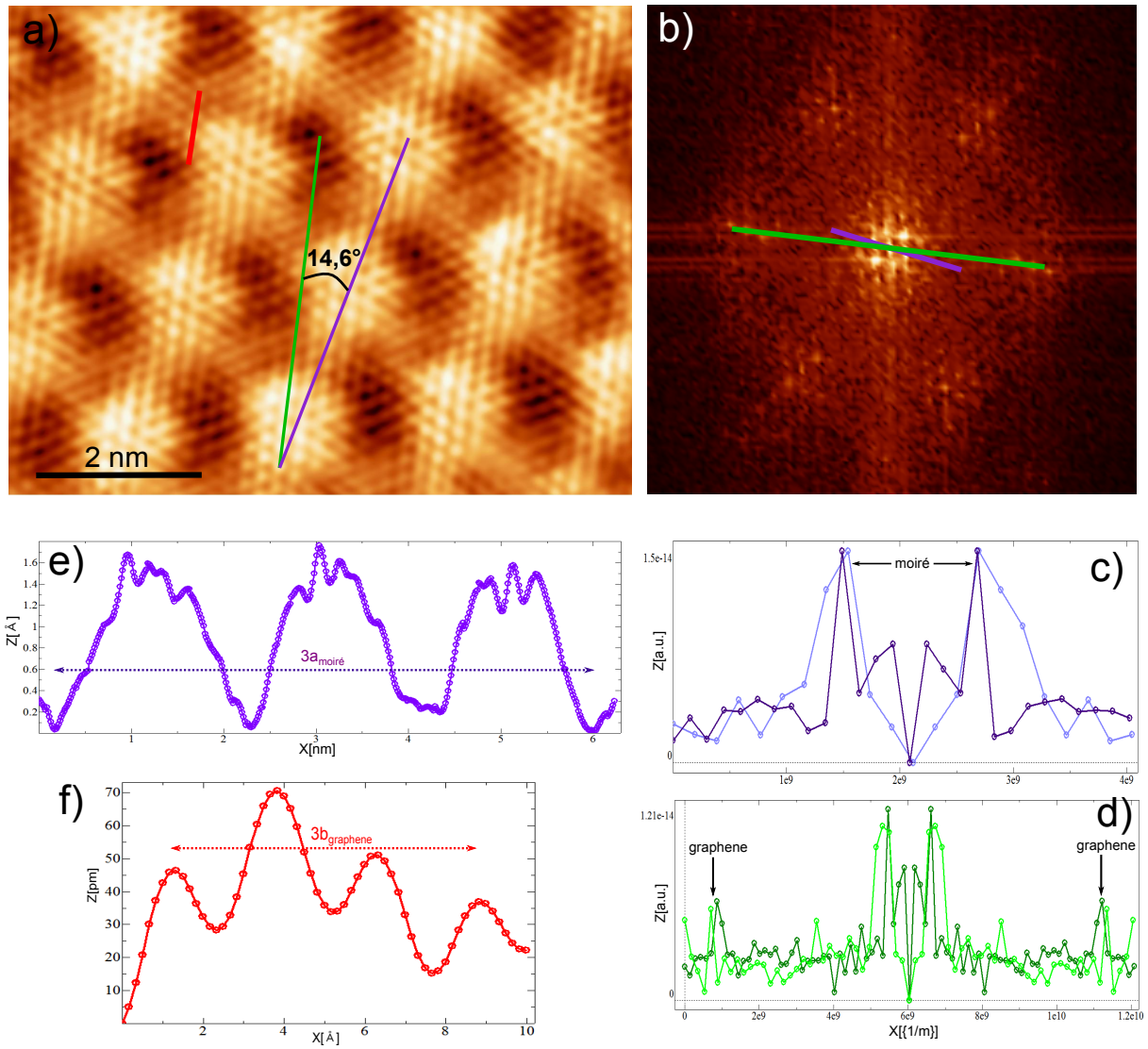

Figure 4.13 ***Graphene-Re(0001) at 1.5 K*** *(a) STM topographic image of the atomically resolved moiré pattern presenting a misoriented carbon lattice with respect to the moiré direction. Measured with* $V_{\mathrm{bias}} = 10\,mV$ *and* $I_{\mathrm{t}} = 10\,nA$*. (b) FFT of image (a). (c,d) Profiles along the purple (moiré) and green (carbon atoms) lines in the FFT image. (e) Profile along a moiré row (violet line) in the topographic image. (f) Profile along the red line on the topographic image exhibiting the graphene atoms periodicity. The dots in the profiles represent single measurement points.*

where $\phi_{\text{C,moiré}} = \phi_{\text{C,Re}} \simeq 0$, Eq. 4.4 turns into $r=\frac{R-1}{R}$ i.e. $r=\frac{7}{8} = 0.875$. Written differently, $7\, b_{\text{Re}} = 8\, b_{\text{C}}$: **the moiré superstructure is composed of eight carbon rings matching seven Re atoms**. The notation (7:8) will be used to refer to this structure in the following. If these numbers are exact, i.e. if the numbers of atomic rhenium and graphene sites per moiré cell are integer, the graphene on Re(0001) is said to be a *commensurate* system. In this case, the graphene lattice is slightly distorted to fit the Re lattice and one can estimate $b^{real}_{\text{graphene}} = r{*}b_{\text{Re}} = 0.875{*}2.76 = 2.42$Å, corresponding to a compression of the graphene cell of 1.8%. In the case of Fig. 4.13 where $\phi_{\text{C,moiré}} \approx 14.6°$, one calculated $r\simeq 0.879$, which gives $b^{real}_{\text{graphene}} = 2.43$Å, corresponding to a compression of the graphene cell of 1.3%. We see here that our decision to calibrate our lateral displacements with the theoretical value of the graphene atomic periodicity is only valid at first order and eventually induces imprecision on the moiré periodicity value.
The moiré periodicity can be calculated by $b_{\text{moiré}}=8b_{\text{Re}}=1.93$nm, which is consistent with our previous calculations from FFT and topographic profiles.
RHEED patterns acquired just after the graphene growth on two different samples (i.e. grown with different graphene growth parameters) enabled to conclude to the presence of a (7:8) superstructure in one case and a (9:10) superstructure in the other case. This latter had already been observed in the reciprocal space in a low energy electron diffraction (LEED) experiment carried on by Miniussi and coworkers [93]. We did not observe this structure on the samples we measured by STM.
The moiré will be further explored in more details in section 4.4 where we will present DFT calculations of the (7:8) superstructure that corroborate our STM observations.

What can be deduced concerning the coupling strength between graphene and rhenium from the observation of the moiré?
We saw in section 4.2.2 that strong interacting graphene-metal systems present small carbon-rhenium atoms distance (down to 2.1Å for Ru) and strong corrugations of the graphene layer (up to 1.6Å). From the two profiles over the moiré hills presented on Fig. 4.12 and 4.13, we extract corrugations of the graphene layer of 0.9Å and 1.6Å. These numbers can vary strongly as STM is sensitive to both the electronic wavefunctions of the sample surface and of the tip. Thus, they reflect the combination of the topographic corrugation of the moiré and an electronic component that can be responsible for more than 50% of the observed corrugations. It is impossible to disentangle between these two components with STM. Nevertheless, the observation of high corrugation values seems to indicate that rhenium can be placed in the category of metals that strongly interact with graphene, such as Ru, Rh, Ni, Co and Fe.

By looking closer at an atomically resolved image, such as in Fig. 4.14, one can resolve six atoms on the hills of the moiré (marked by an hexagon) but only three in the valleys (marked by a triangle). This different atomic periodicity suggests that the graphene layer is overall less strongly coupled to the Re substrate on the hills than on the valleys. This is the same electronic effect as observed on graphite for example, where only one atom over two is resolved by STM due to the AB stacking of the last two graphene layers: the atoms of one sublattice are all positioned on top of carbon atoms of the underneath graphene layer and form van der Waals bonds while the atoms of the other sublattice lie above the center of the underneath carbon hexagon. Therefore, these latter atoms exhibit localized dangling bonds that strongly enhance the tunnel current. Applying the same reasoning

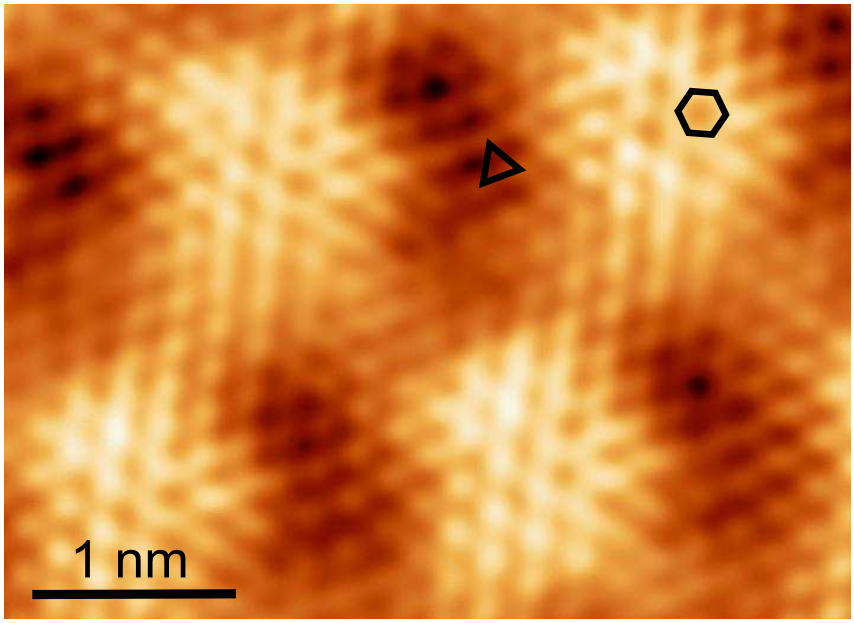

Figure 4.14 *Zoom on a moiré supercell in STM topographic image presented in Fig. 4.13. One identifies zones with three-fold (atoms marked by a triangle) or six-fold atomic periodicity (atoms marked by an hexagon).*

in our case leads to the interpretation that one atom over two in the valleys is strongly coupled to the Re substrate, while atoms positioned on the hills are less strongly bonded due to their higher position with respect to the underlying metallic substrate.

Moiré hole-type defect

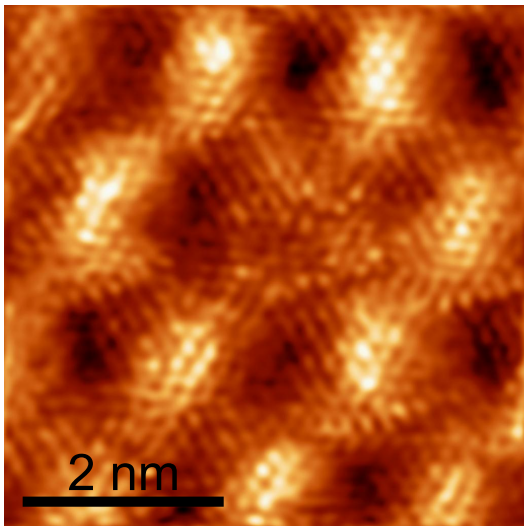

Figure 4.15 *Moiré hole-type defect (V_{bias}=-10 mV,I_t=25 nA).*

Like already mentioned before and seen on Fig. 4.8 and 4.9, the regular moiré pattern sometimes exhibits defects, characterized by a 'missing hill', and referred to as moiré hole-type defect. An atomically resolved STM topographic image shows such a defect on Fig. 4.15. The central missing hill is replaced by a valley-like region, where we can see the presence of an 'atoms ring' in the center. The exact atomic configuration of the graphene sheet in this region is difficult to analyze as we do not resolve all the atoms in our image. If it would have been the case, we could have followed the carbon atomic rows to deduce if this defect geometry was the result of a dislocation or atomic defect in the graphene sheet.

4.4 DFT calculations of the moiré structure

What is DFT? Density functional theory (DFT) is one of the most popular and successful approach to compute the electronic structure of matter. The main idea of DFT is to describe an interacting system of fermions by using the electron density as the central quantity, instead of its many-body wave-function, thus drastically reducing the number of variables of the problem and then the computational effort. The name of this theory originates from the fact that the properties of the system can be determined by using functionals of the spatially dependent electron density. The energy of the system is computed using a variational principle, which is nevertheless limited to the ground state. Hence, this strategy can not be easily transferred to the problem of excited states.

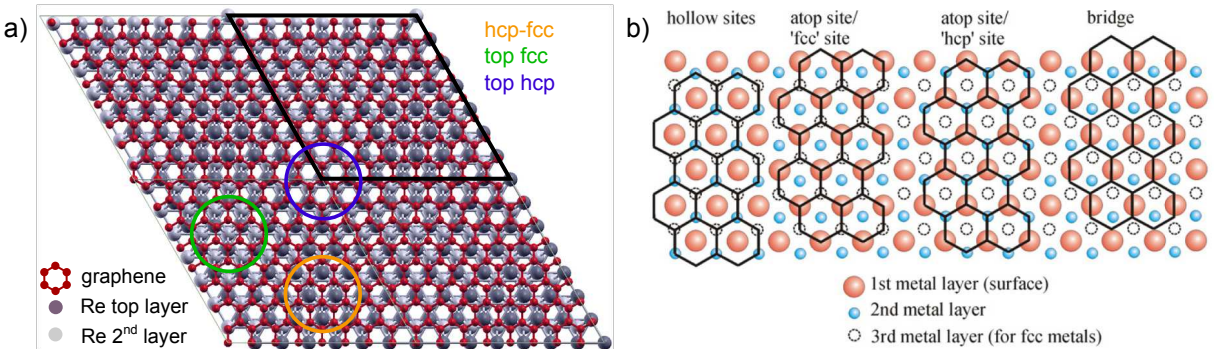

Figure 4.16 *(a) Schematic view from the top of the (7:8) graphene-rhenium superstructure. One indicated by colored circles the different high-symmetry stacking positions of carbon atoms on Re(0001). (b) Four basic adsorption arrangements for non-rotated graphene on hexagonal (fcc(111) or hcp(0001)) metal surfaces (see text for details). Reproduced from [15].*

Simulation results The DFT calculations have been carried out by Laurence Magaud[13] with a slab containing five Re layers, one graphene layer and a 10 Å-thick vacuum space on top. The Re plane in the middle (third plane) of the slab was fixed while all the other atoms were allowed to relax[14]. The lateral size of the supercell corresponds to a (7×7) cell for rhenium and a (8×8) cell for graphene, to match the geometry we observed experimentally by STM. Fig. 4.16 a shows a schematic view from the top, the black diamond delimiting a single moiré supercell. The colored circles identify different high-symmetry stacking positions of carbon atoms on Re(0001) that are schematically clarified in (b). One spotted three main regions, described here-after in a nomenclature where the adsorption structure is labeled by the sites of the carbon atoms with respect to the underlying metal surface:

- **hcp-fcp region**, or "hollow sites" (orange circle): carbon atoms surround the top layer atoms of the metal, i.e. are located in three-fold hollow sites of the surface (i.e. on top of the Re second layer atoms in our case)
- **top fcc region** (green circle): carbon atoms are alternately occupying metal-atop sites and the 'fcc' hollow sites. They surround the metal atom of the second layer.
- **top hcp region** (blue circle): carbon atoms are alternately occupying metal-atop sites and the 'hcp' hollow sites (on top of the Re second layer atoms).

[13] Institut Néel, 25 Rue des Martyrs, F-38042 Grenoble.
[14] For more details on the DFT calculations, see [1].

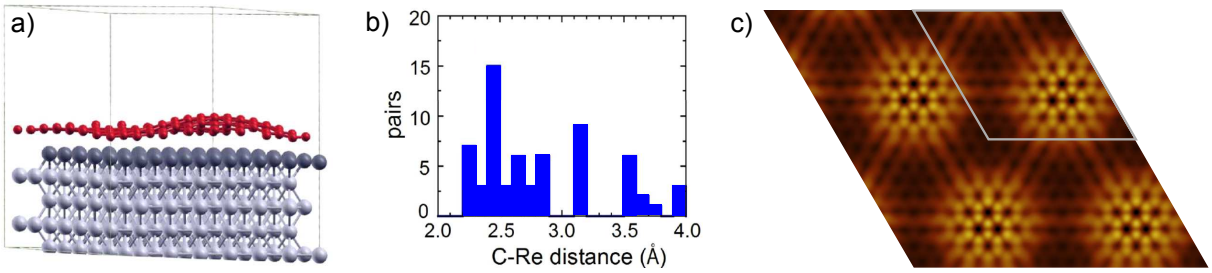

Figure 4.17 ***Results of DFT calculations on graphene-Re(0001).*** *(a) Schematic view of the slab from the side to show the graphene buckling. (b) Number of C-Re pairs as a function of distance. (c) Cross section of the square modulus of the wave-function integrated between E_F and E_F +0.5 eV. The cut has been done on the same superstructure as presented in Fig. 4.16.*

The last configuration presented in Fig. 4.16 b that we did not identify on our representation of the graphene-rhenium system is called "bridge position" and corresponds to a situation where the carbon atoms are bridged by the metal-atop sites.

Results of DFT calculations are summed up on Fig. 4.17. They show that the graphene layer is buckled with regions where the C atoms are close to Re ones, the so-called valleys, and regions where they lay much higher, the so-called hills. The first regions correspond to strong graphene-Re interaction (top hcp and top fcc), the second to much weaker interaction (hcp-fcc). The buckling of the graphene layer has been calculated to be 1.6Å and the C-Re first neighbor distances range from 2.24 to 3.97Å, which puts Re in the category of strong interacting metals. The Re layers below graphene are also slightly buckled, with corrugation height of 0.15Å in the first Re layer just below the graphene and 0.13Å in the second Re layer. The higher Re atoms lie below the higher C atoms. Fig. 4.17 c shows the square modulus of the wave-function integrated between the Fermi level (E_F) and E_F+0.5 eV, which corresponds to the quantity mapped by STM in the constant z-height mode (current image). This cross section is taken just above the highest graphene atom, the grey diamond delimits a single moiré supercell. It shows bright protuberances that correspond to hcp-fcc stacking regions described in Fig. 4.16 and to hills regions in STM images of Fig. 4.12 and 4.13, being in good agreement with them. Moreover, the hexagonal symmetry of the carbon atoms on the hills and the triangular symmetry in the valleys are also visible in this computed image.

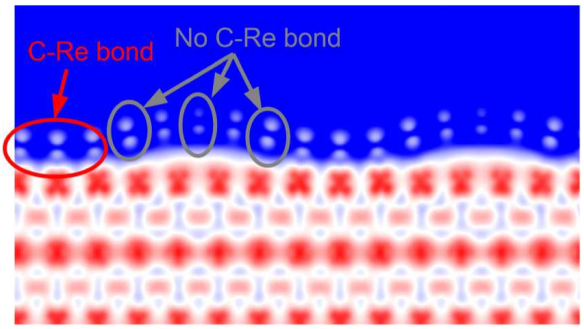

Figure 4.18 *Cross section of the square modulus of the wave-function integrated between E_F-0.5 eV and E_F. The cross section line is parallel to the x supercell axis and goes through the hcp-fcc site. Color scale: blue/white/red correspond to low/intermediate/strong intensity respectively.*

Another cross-section parallel to the x supercell axis presented in Fig. 4.18 illustrates the formation of covalent bonds between graphene and Re atoms except in the hcp-fcc

region, thus corroborating that the moiré hills are less strongly coupled to Re than the valleys. Band structure calculations have shown no trace of graphene linear dispersion (Dirac cone), which is another evidence of the strong graphene-Re interaction. In addition, carbon related states (at the Γ point) were found at an energy lower than in graphene indicating an electron transfer from Re to C.

4.5 High energy DOS

Before focusing on the superconducting properties of the system, we investigated the density of states of graphene on rhenium at high energy (several hundreds of meV) by tunneling spectroscopy. Indeed, this quantity gives us information on the coupling strength between graphene and Re, as we can compare with spectroscopic features obtained for graphene coupled to other metals or for free-standing graphene.

Although graphene on metal systems have been widely studied by STM, spectroscopic data on such systems are not so abundant in the literature. This can be explained by the difficulty to interpret them, as the measured conductance is always a convolution of the DOS of the sample and the DOS of the tip, which is most often unknown. As the tip is different between two experiments and even often within a same experimental run[15], it is difficult to compare spectroscopic data if one can not dissociate the influence of the tip in the measured features. If the general behavior can be extracted and discussed, one should pay attention not to compare spectroscopic data of two different experiments too hastily.

Spectroscopic spectra measured over the moiré pattern are presented on Fig. 4.19. We performed current-imaging tunneling spectroscopy (CITS) measurements: the tip is scanned in the constant current mode and at each point of a grid the feedback loop is disabled and a spectroscopic measurement is performed. The top left image is a topographic image where we distinguish moiré valleys (dark) and hills (bright). The top right image is a simultaneously recorded map of the differential conductance G=dI/dV measured at E_F (i.e. at zero tip-sample bias). The spectroscopic signal was obtained by a lock-in technique with an *rms* modulation voltage of 5 mV. On this spectroscopy map we observe enhanced conductance on the moiré hills. This contrast can be understood by looking at the full spectra recorded on hills and on valleys (bottom panel): an enhancement of the conductance is reported on moiré hills with respect to valleys around the Fermi energy, between -400 meV and +200 meV in the presented graph. This evidences strong electronic effects which are likely to play a central role in the observed moiré. The inset in the graph presents a curiosity: spectra acquired on different hills display a maximum at different energies. These spectroscopic variations between different hills are not well understood, as it would mean that different hills are non-equivalent. We ventured the hypothesis that it could originate from a slight misalignment between the crystallographic directions of the graphene and the Re (as seen on Fig. 4.13). The resulting incommensurability in the moiré would then lead to non-equivalent hills, first in term of adsorption arrangements

[15] It is common that the tip changes randomly during a scan, which means that the tip apex changes its atomic configuration and thus its electronic wave-function. Nevertheless, these changes are rather easily detectable by lines jump, a change of contrast or even a change of spot in the scanned image.

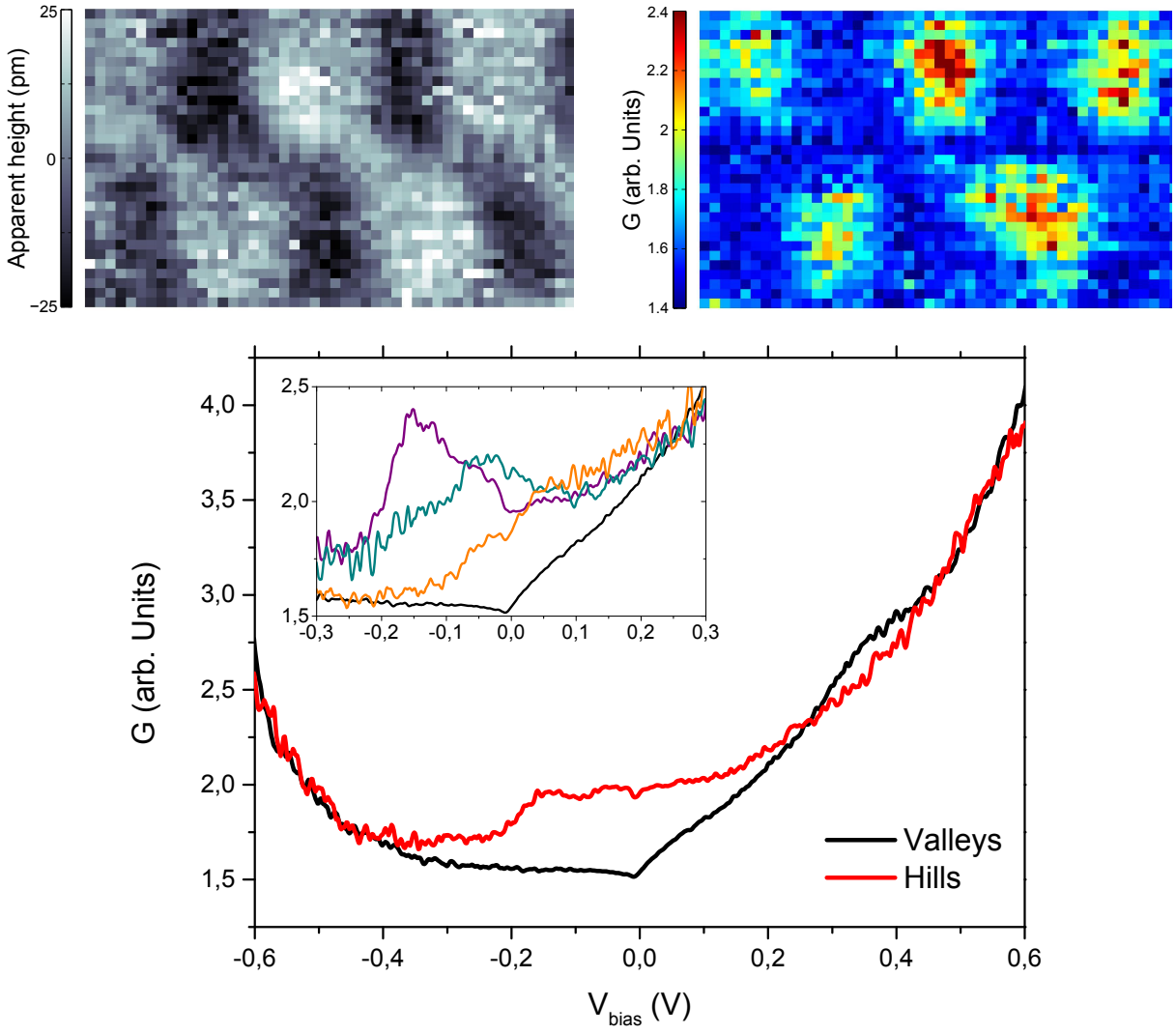

Figure 4.19 ***High-energy spectroscopy on graphene-Re (1).*** *Top panel: Left: topographic image ($5\times3\,nm^2$) measured at V_{bias}=800 mV and I=5 nA. Right: conductance map at the Fermi energy. Bottom panel: spectra averaged over the hills (red) and valleys (black). Inset: zoom in energy of spectra averaged on individual hills (colors) and the spectrum averaged in the valleys (black).*

of the carbon atoms on the Re ones, and then regarding their electronic properties. To validate this scenario, one would need to study in details the atomic arrangement of this specific moiré superstructure, which naturally requires atomically resolved images. Unfortunately, such high-resolved images were not acquired during these measurements and we can not therefore conclude in this case.

The general shape of the tunneling spectra thus reminds a 'semi-metal' behavior, similar to what was obtained for the strongly coupled system graphene/Ru(0001) [86, 137, 104, 63], and in contrast to the V-shaped DOS of a decoupled graphene layer [6].

By studying the literature on the graphene-Ru(0001) system, we note a huge dispersion in the experimental spectroscopic data, despite that some of them are reported by the same group. Fig. 4.20 presents data reported in a selection of three papers on this system. First, if we look at the right column presenting spectroscopic data, we notice that the spectra reported in distinct papers are very different from each other. The STM images in (a) illustrate the contrast inversion they measure on this system, the same effect is also observable in conductance maps in (b) and (c). The latter experiments present spectroscopic data acquired at different positions on the moiré pattern, confirming the idea that the occupied DOS is always larger in the hills regions, while the empty DOS is larger in the valleys. But whereas distinct peaks are visible in (c), spectra presented in (a) and (b) look rather smooth. This sampling of spectroscopic data collected on the graphene-Ru system shows that it can be difficult to compare data from different experiments. The interpretations of the spectroscopic features are as much diversified, making reference to Ru d-states, phonon excitations [63] or periodic modulation of the potential [137].

In the case of our graphene-Re(0001) system, we never observed such a contrast inversion on the topographic or conductance maps, whatever the considered energy. Indeed, looking at the averaged spectra on Fig. 4.19, the DOS on the moiré hills is always equal to or greater than the DOS on the valleys[16]. On the other hand, a systematic enhancement of the conductance around the Fermi energy is observed on moiré hills with respect to valleys, as shown in Fig. 4.21. These data were acquired on a same sample during the same experimental run but at different positions.

The three panels correspond to three different sets of CITS measurement. All these measurements are centered on a moiré hole defect. In each panel is presented an STM topographic image of the scanned region (top left). To study the DOS evolution with respect to the topographic height (i.e. hills or valleys positions), we sorted the spectra of the CITS map into n slices corresponding to n height ranges of the topographic image. For the top panel for example, we chose 8 slices corresponding to the following height ranges:

$$\text{-15 pm} \xrightarrow{1} \text{-11.3 pm} \xrightarrow{2} \text{-7.5 pm} \xrightarrow{3} \text{-3.8 pm} \xrightarrow{4} 0 \xrightarrow{5} \text{3.8 pm} \xrightarrow{6} \text{7.5 pm} \xrightarrow{7} \text{11.3 pm} \xrightarrow{8} \text{15 pm}$$

The pixels belonging to the same slice are plotted in the same color on the discretized topographic map (bottom left). The histogram of the height distribution is plotted for each measurement, on which we superimposed the corresponding slices. We can thus

[16] the slight inversion around 400 meV is too subtle to be seen on the conductance maps, being drowned in the spectra noise.

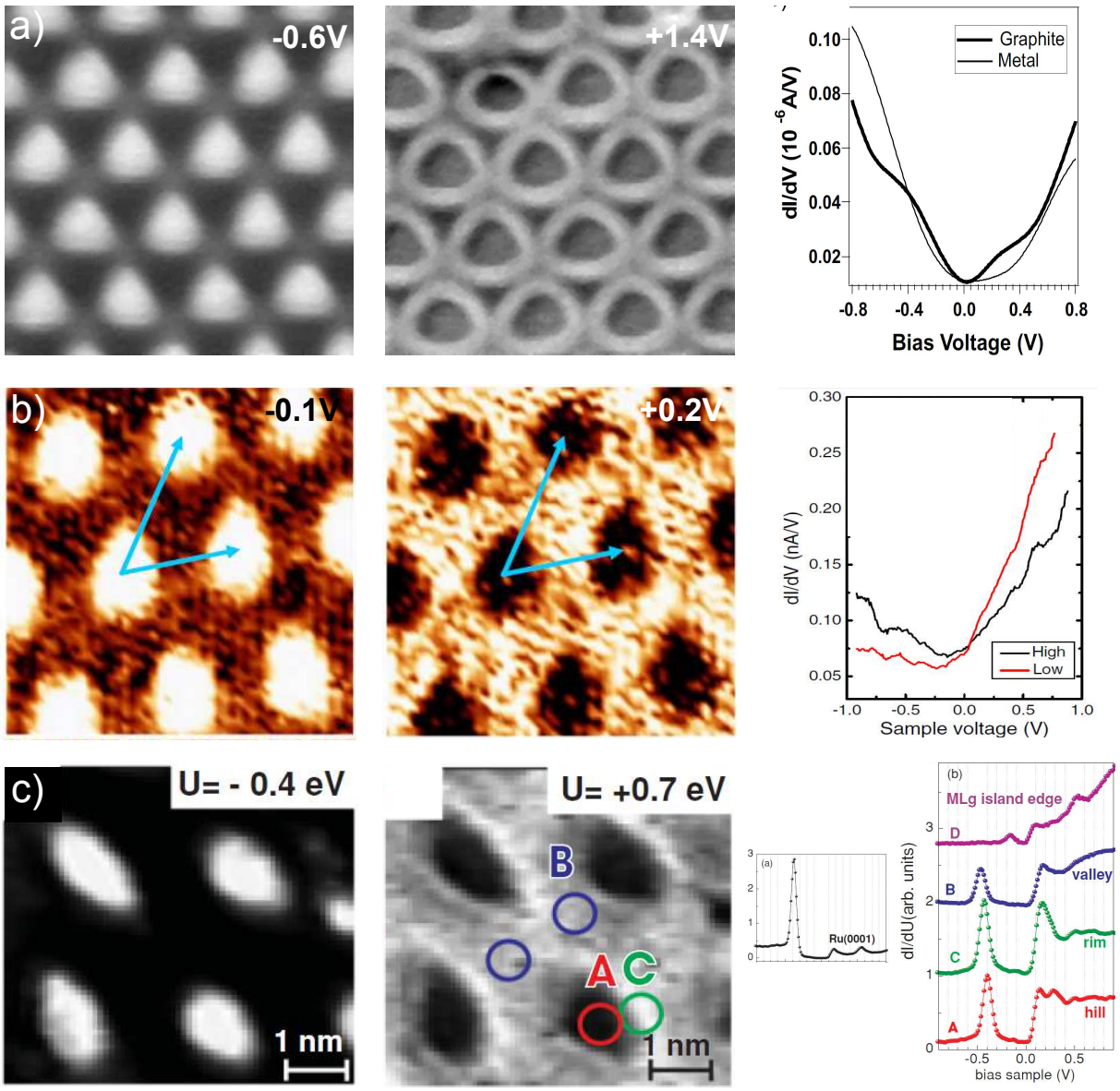

Figure 4.20 ***Graphene-Ru(0001) system*** - *Left and middle columns: (a) STM topographic images for different V_{bias}, (b and c) Spatial maps of the tunneling conductance for different bias voltages. Right column: spectroscopic data measured on different positions on the moiré cell. Data reproduced from (a) Marchini et al. [86] (b) Vazquez et al. [137] (c) Gyamfi et al. [63].*

ensure that a significant number of pixels are gathered in each slice. Finally, we plot on the same graph (on the right) the averaged spectra for each slice. The spectrum Z=i corresponds to the ith slice. In addition, we plot for comparison a spectrum averaged independently on the moiré hole-type defects (pink spectrum).

First, looking syncreticly at the plots of averaged spectra (one should note that the energy ranges differ between the three experiments), one can notice that:

- There are several **common features** for the three sets of measurements.
  First, the differential conductance, and thus the LDOS, is enhanced around the Fermi energy in the high regions of the moiré with respect to the low regions. Second, the spectrum averaged on the moiré hole defect always corresponds to the lowest DOS around the Fermi energy. And third, distinctive peaks grow when we go from low regions to high regions of the moiré.
- Nevertheless, we also observe **pronounced differences** between the three sets.
  Mainly, the peaks develop at different energies: -340 mV, -150 mV, and -100 mV and +320 mV for each set respectively (from top to bottom panel). In addition, the spectra seem to sometimes present inversions of the DOS amplitude, from higher on the hills to higher on the valleys. However, if these inversions are detectable (at +250 mV on the first set, +400 mV and -250 mV on the third set and none on the second set), they are too weak and therefore are not visible on conductance maps plotted at different energies (contrary to the case of graphene-Ru(0001) where the inversion is very strong). If this effect is indeed real, it highlights strong electronic effects. Nevertheless, it rather seems to be in the noise level of our experiments and will thus not be further commented later on.

In summary we have: a **systematic enhancement of the DOS amplitude around the Fermi energy**, from about -250 mV to +250 mV, and **peaks growing in the DOS of the low to the high moiré regions at certain energies that differ from experiment to experiment**.

To explain these features, we went back to the abundant literature published on the graphene-Ru(0001) system, which has many similarities with our own one, starting with a strong coupling between the metal and the graphene layer. As already seen previously, the experimental spectroscopic data reported on graphene-Ru present strong discrepancies and thus do not offer a solid basis for comparison with graphene-Re. We rather opted for looking at theoretical papers presenting simulated DOS, most of the time by DFT calculations, similar to the ones performed on our system by Laurence Magaud. The main active groups in this topic are leaded by M-L. Bocquet[17] [142, 141, 26, 143] and F. Martin and R. Miranda[18] [137, 138, 121, 122]. Their different publications, though sometimes in contradiction, are complementary and offer a very deep study of the graphene-Ru system, with DOS and band structure calculations. To date, they reach agreements on several points listed below:

- graphene is strongly coupled to the Ru(0001) substrate, the interaction being mediated by covalent bonds
- this results in a strong buckling of the graphene sheet (>1Å)

[17] Laboratoire de Chimie, Ecole Normale Supérieure de Lyon, CNRS, 69007 Lyon, France.
[18] Instituto Madrileño de Estudios Avanzados en Nanociencia, Cantoblanco, 28049 Madrid, Spain.

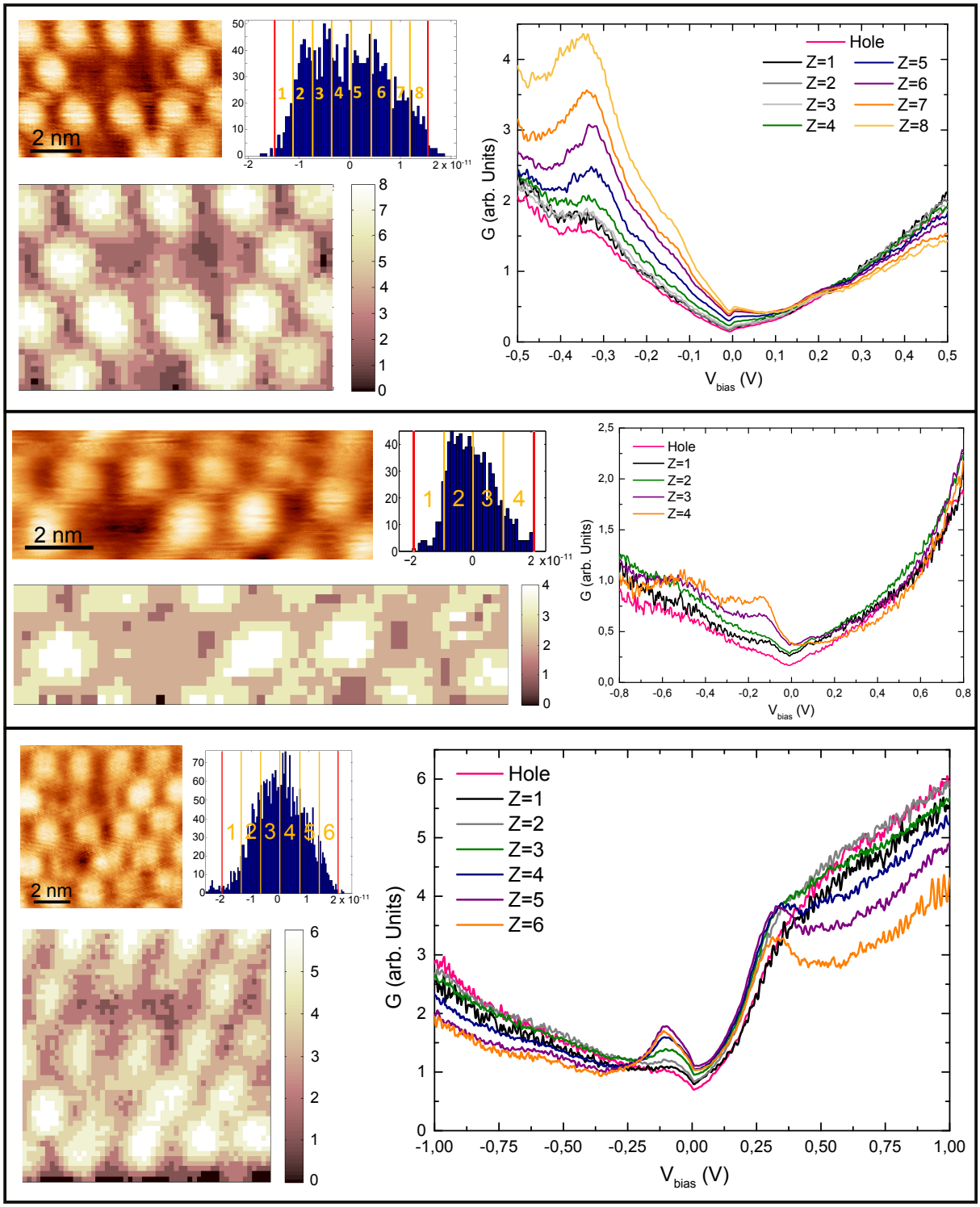

Figure 4.21 ***High-energy spectroscopy on graphene-Re (2).*** *Data collected on three different CITS measurements. For each panel is presented: Top left: STM topographic image. Bottom left: discretized topography of the spectroscopic map. The pixels are divided up in n slices (with n=8,6,4 from top to bottom) according to their topographic height. Top middle: Histogram of the pixels height with the slices distribution. Right: spectra averaged over the the pixels belonging to the same topographic slice. The pink curve represents the spectrum averaged over the moiré hole-type defects.*

– the bonding of graphene with Ru is non-uniform over the moiré structure, with a stronger graphene-Ru interaction in valleys than in hills

These properties are also shared by our graphene-Re(0001) system and make the graphene-Ru a good element of comparison.
In Ref.[142], Bocquet's group demonstrates that valleys display a hybridization of graphene states with Ru states, whereas graphene hardly couples to Ru on the hills. They have computed DOS calculations on fictitious epitaxial Ru/(1×1) graphene structures, in which the C-Ru distances were kept fixed at their optimized values in the moiré supercell while the horizontal position of the graphene overlayer was varied to imitate hill and valley regions. These models provide prototype electronic structures for the complex (12×12)C/(11×11)Ru interface. Their results show that the graphene electronic structure is only a little altered in the high regions as compared to the case of freestanding graphene, with a recognizable V-shape-like structure and a vanishing DOS at the Dirac point (shifted by -0.4 eV). The computations on the low regions of the moiré show strong alterations of the DOS, due to a large band opening (of 2 eV) in the graphene energy bands, with resonances arising at energies well below the Fermi level (∼-3.5 eV). These results do not reproduce our experimental observations on the graphene-Re(0001) system, even qualitatively. Indeed, we do not observe a V-shape DOS on the hills of the moiré. On the contrary, we usually measure a lowest DOS in the valleys and a clearly higher DOS in the hills around E_F. This disagreement may arise from the simplification they made by choosing epitaxial (1×1) cells to compute the DOS. Although necessary to calculate such complicated band structures, their model might be over-simplified by treating low and high regions independently. DFT calculations performed by L. Magaud for a graphene-SiC system on similar (1×1) cells proved to show huge discrepancies as compared to results obtained with a non-reduced cell [85].

The joint spanish teams published a paper in 2012 where they performed DFT calculations that include van der Waals interactions on a large (11×11) unit cell of the graphene-Ru(0001) system [122]. They propose a theoretical description of the electronic structure of graphene-Ru that reproduces the features they observe in new STS measurements presented in the paper. Their results are presented on Fig. 4.22. They show that the recorded dI/dV spectra on the moiré hills and valleys show marked differences: while the hill spectrum presents a well-defined series of peaks both at negative and positive voltages, these structures are much less pronounced on the valley spectrum. Their calculations show some similarities with the experimental data. They attribute these peaks to the localization of electronic states below the hills due to electron doping from the Ru substrate. Qualitatively, these localized states around the Fermi level arise from the opening of the graphene Dirac cone resulting from the interaction with the metallic substrate.

A paper from Armbrust *et al.* [7] with a different experimental approach (angle-resolved two-photon photoemission) also suggests the existence of an unoccupied Ru/graphene interface state (+0.91 eV above the Fermi level). According to these authors, dissimilar graphene-Ru distances in the valleys and the hills regions lead to different confinement and energy shifts of the Ru(0001) surface resonance. These localized states are thus similar to quantum dots below the hills.

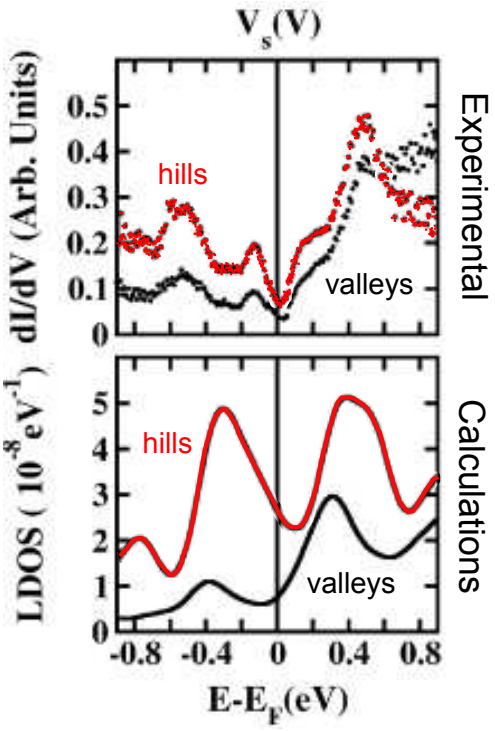

Figure 4.22 ***Graphene-Ru(0001) system.*** *Top: experimental STS spectra, measured over the valleys (black) and the hills (red) of the graphene moiré. Bottom: calculated DOS on the valleys (black) and the hills (red). Adapted from [122].*

If we compare qualitatively our differential conductance curves with the ones presented in Fig. 4.22 we note many similarities. First of all, their spectra, both experimental and theoretical, also show an enhancement of DOS on the hills as compared to the valleys. Second, the peaks at -550 meV, -150 meV and +500 meV, if visible on the valleys spectrum, get much more pronounced on the hills spectrum. This is indeed the very same behavior we observe, although the structures appear at different energies. This analysis suggests that the peaks we observe in our graphene-Re system would also be linked to localized electronic states below the hills. However, we could then reasonably ask why these peaks appear at different energies for a same sample at different positions. As the confinement arises from the modulation of graphene-Re distances, the different energies of these resonances can be interpreted by a dissimilar corrugation of the graphene layer on the rhenium substrate. This is possible as our measurements were performed on areas with distinct topographies: no defects on Fig. 4.19 and between one and three moiré holes on Fig. 4.21. The C-Re atoms distances could thus differ between the different areas for a considered high or low moiré zone. This thesis seems to be corroborated by the observations we made on the spectra presented in the inset of Fig. 4.19. We interpreted the shift in the peak energy for different hills as due to a misalignment between graphene and Re crystallographic directions, which results in different adsorption arrangements of the C atoms on the Re ones. The different hills could indeed be characterized by slightly different C-Re atoms distances. Nevertheless, we do not know to which extend this interpretation is plausible. To answer this question, we would need to investigate the quantitative effect of C-Re atoms distances on the localized states energies. This would require complex DFT calculations with different supercell geometries (crystallographic misalignment or moiré

cells with/without defects) we are not able to provide yet.

In conclusion, our spectroscopic data validate the scenario of a **graphene layer strongly coupled to the Re(0001) substrate**. They also show qualitative agreement with the thesis indicating the presence of several **localized electronic states near the Fermi energy below the moiré hills**, which appear as peaks in the LDOS. The energy of these resonances are found to vary between different spots, which could be related to variations in C-Re atoms distances possibly due to crystallographic misalignment between the Re and the graphene lattices or to the presence of moiré hole-type defects.

Conclusion

In this chapter, we have introduced the system we designed to locally study the superconducting proximity effect in graphene. We described the segregation process, which results in the growth of a graphene monolayer covering entirely the surface of the superconducting mono-crystalline rhenium thin film we use as a substrate. STM topographic analyses have shown the surface displays a superstructure called a moiré pattern, resulting from the lattice mismatch between graphene and rhenium. This moiré has a periodicity of about 2 nm and its supercell consists in eight carbon rings matching seven rhenium atoms. The analysis of the atomically resolved topographic images goes in favor of a strong coupling strength between the graphene sheet and the metal substrate, interpretation corroborated by DFT calculations. High-energy spectroscopic studies revealed a modulation of the DOS at the Fermi energy on the moiré scale. Indeed, a systematic increase of the differential conductance is measured on the moiré hills as compared to the valleys. This highlights strong electronic effect, also attested by various features (peaks for instance) present in the conductance spectra at energies varying with the scanned zone. They could be interpreted as the result of the localization of electronic states below the moiré hills.

Chapter 5

Superconducting properties of graphene grown on rhenium

Contents

Introduction

Now that we have established the strong coupling between graphene and rhenium, we will explore in this chapter the superconducting properties of the graphene-Re(0001) system. In the first part, we will present the superconducting properties probed by transport measurements (T_c, ξ_s) and compare them with previous measurements made on a bare Re films. The second part will be dedicated to the superconducting DOS measured on this system by scanning tunneling spectroscopy (STS) and its evolution with temperature. We will also compare our results with the case of bare rhenium. Then, a spatial study on the homogeneity of the superconducting properties at the moiré scale will be presented. Some spectroscopic data measured under magnetic field revealing magnetic vortices will be displayed. Finally, we will discuss a spectroscopic study carried out on a graphene-rhenium sample presenting disordered regions, possibly composed of amorphous carbon, which display a strong abnormal lateral superconducting proximity effect.

5.1 Bulk superconducting properties probed by transport measurements

We probed the superconducting properties of the bulk graphene-rhenium system by transport measurements. The data are presented on Fig. 5.1 for a 30 nm thick film. On the left panel, the resistance versus temperature curve was acquired by a four-terminal sensing method to eliminate contact resistances. The resistance of the film (between the voltage probes) at room temperature is about 8 Ω and decreases linearly with temperature until it reaches a plateau at 5 Ω around 30 K, when the high-energy phonons are not excited and do not contribute to scattering processes anymore. Then, the film transits into its superconducting state at $\mathbf{T_c \sim 2\,K}$, defined as the temperature for which R becomes zero. The transition is rather large ($\Delta T_c \sim 0.4$ K) with a tail at the foot of the transition. This tail, which has also been observed in bare rhenium films, still needs to be understood. The study of the superconducting transition under different magnetic fields gives access to the superconducting coherence length. Indeed, from the graph Hc_2=f(T) on the right of Fig. 5.1, we can use the formula $\xi_S = \Phi_0/2\pi T_c \left|\frac{\partial H_{c_2}}{\partial T}\right|$ to extract $\boldsymbol{\xi_S = 18\,nm}$. Note that in this case the temperatures reported on the abscissa axis correspond to a transition temperature T_c^* defined in the middle of the transition (ΔR/R=50%) for convenience.

To understand the influence of the carbon atoms dissolved in the rhenium matrix, consequence of the segregation growth process of graphene, we wanted to compare our values to the ones measured on bare rhenium films. As seen in Sec. 4.1.2, the transition temperature of thin Re(0001) films depends on their thickness (the thinner the film, the higher its T_c). This is related to the accumulation of constraints that can not be released for small thicknesses and have shown to increase the transition temperature [78]. The only available data for a rhenium film of similar thickness (25 nm) gives $T_c \sim 2.1K$[1], which is consistent with our values. It has also been previously shown that a small addition

[1]This film was inhomogenous with a superconducting transition in two steps: 92% of the sample had transited at 2.10 K (foot of the first transition step) and the transition was then complete at 1.83 K. These transport measurements were carried out by Benjamin Delsol at Institut Néel.

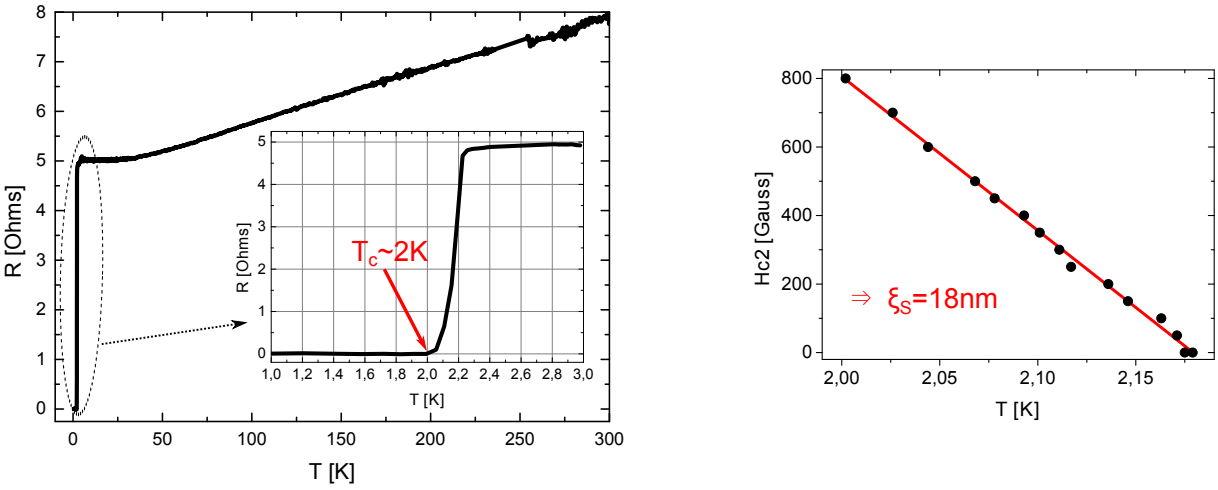

Figure 5.1 ***Transport measurements on graphene-Re*** *- Left: resistance versus temperature curves showing a superconducting transition at T_c ∼2.0 K. Right: critical field versus temperature curve from which we extract $\xi_S = 18\,nm$.*

of impurities in rhenium increases its T_c [31]. It has been explained in terms of band-structure smearing due to impurity scattering near a singularity in the DOS of rhenium located just below the Fermi energy [89]: impurity scattering is expected to smear out this singularity and increase the density of states at the Fermi level, and thus enhance the transition temperature[2]. In our case, it seems that the thickness effect dominates the doping one.
The superconducting coherence length of the 25 nm-thick bare rhenium film was also measured and estimated at ξ_S=38.5 nm. This value is twice as large as the one we measured on our 30 nm-thick graphene-rhenium film whereas it is expected to increase for thicker films. This behavior is likely related to the reduction of the mean free path due to the introduction of carbon impurities in the rhenium matrix during the graphene growth that act as scattering centers.

5.2 Superconducting DOS and temperature evolution

In order to measure the superconducting DOS of our graphene-rhenium system, we cooled it down to 50 mK and performed tunneling spectroscopy at low bias voltage. We directly extracted the differential conductance by using a lock-in measurement, with an *rms* modulation voltage of 40 μV. The normalized conductance G versus the bias voltage V_{bias} is plotted in Fig. 5.2. Assuming a flat DOS for the tip, this spectrum can be directly interpreted as the LDOS of the sample. This is clearly the DOS of a superconducting material, which is in addition very well fitted with the standard BCS theory. The fitting parameters are the superconducting gap $\mathbf{\Delta = 330 \pm 10\,\mu eV}$ and the effective temperature T_{eff}=284 mK. This measurement was performed on the sample named 'AK23' (cf Tab. 4.1)

[2]According to the BCS formula $T_c \sim \Theta_D \exp[-1/N_d(E_F)V]$ leads to $\frac{\Delta T_c}{T_c} \sim \frac{\Delta N}{N} \ln(\Theta_D/T_c)$.

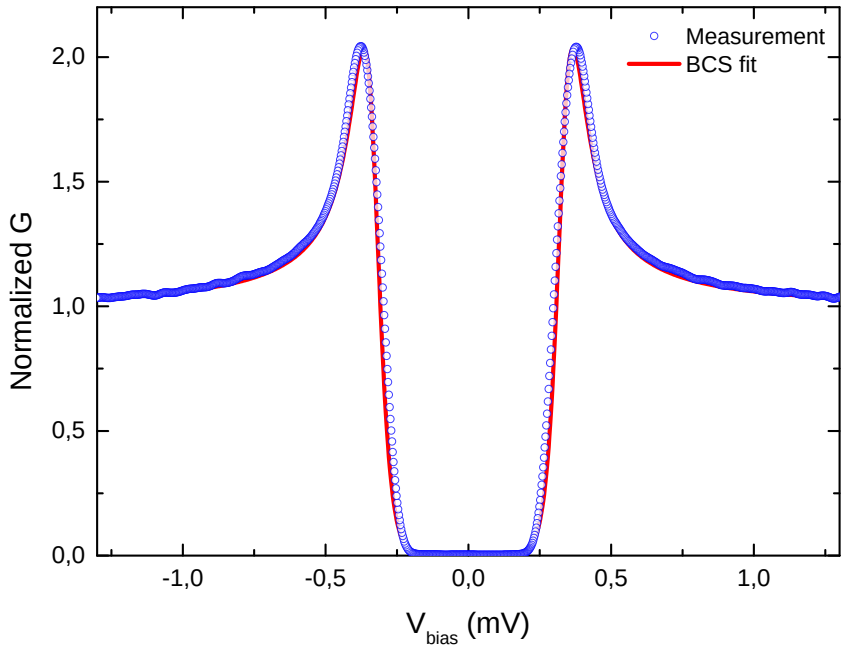

Figure 5.2 *Normalized differential conductance G measured at 50 mK. BCS fit with* Δ*=330* μeV *and* T_{eff}*=284 mK .*

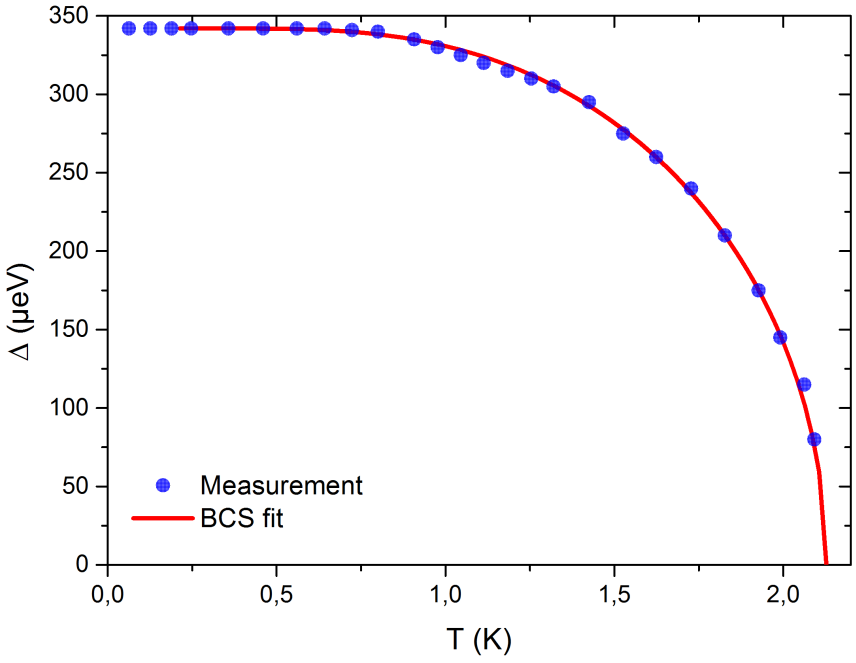

Figure 5.3 *Temperature evolution of the superconducting gap. BCS fit with* $\Delta/k_B T_c$*=1.88.*

and the gap value was found uniform across the sample. Other spectroscopic measurements performed on different samples ('AK43','AK49','AK50') gave the same value of the superconducting gap for comparable T_c. The thermal dependence of the gap, plotted on Fig. 5.3, also follows very accurately the BCS model. It should be noticed that the BCS fit was plotted for $\mathbf{\Delta/k_BT=1.88}$, instead of 1.76 for conventional BCS. This indicates a slightly larger electron-phonon coupling than for the BCS standard, which is not surprising as this constant is material-dependent. From this second plot we can extract a superconducting transition temperature of $\mathbf{T_c \simeq 2.1\,K}$. This value corresponds to the tail of the resistive transition measured in transport and is therefore slightly higher than T_c defined by the zero resistance state.

As seen in Chapter 3, this spectroscopic measurement is a very sensitive probe to the quality of the interface between the normal "metal" (N), here graphene, and the superconductor (S). Indeed, the size of the gap induced by proximity effect in N depends on the barrier height between N and S. In absence of this barrier, the superconducting gap in S and the induced one in N are equal, the latter being reduced for a less transparent interface (see Sec. 3.3.1.2). To get quantitative information about this interface, one should compare our spectroscopic data with spectra acquired on a rhenium surface without graphene. This would be ideally achievable if the surface of our sample was only partially covered by graphene, a situation referred to as *sub-monolayer graphene*. In this case, we would have zones covered by graphene and graphene-free areas next to each other and would be able to compare the superconducting gaps in both area and extract the interface transparency between graphene and rhenium. Unfortunately, we could not reach this regime during our growth attempts.

Nevertheless, we could compare our data with previous spectroscopic measurements performed on 80 nm-thick bare Rhenium films. As the film thickness has a strong impact on its superconducting properties, we will limit ourselves to a qualitative comparison. The temperature evolution of the DOS and superconducting gap of these bare

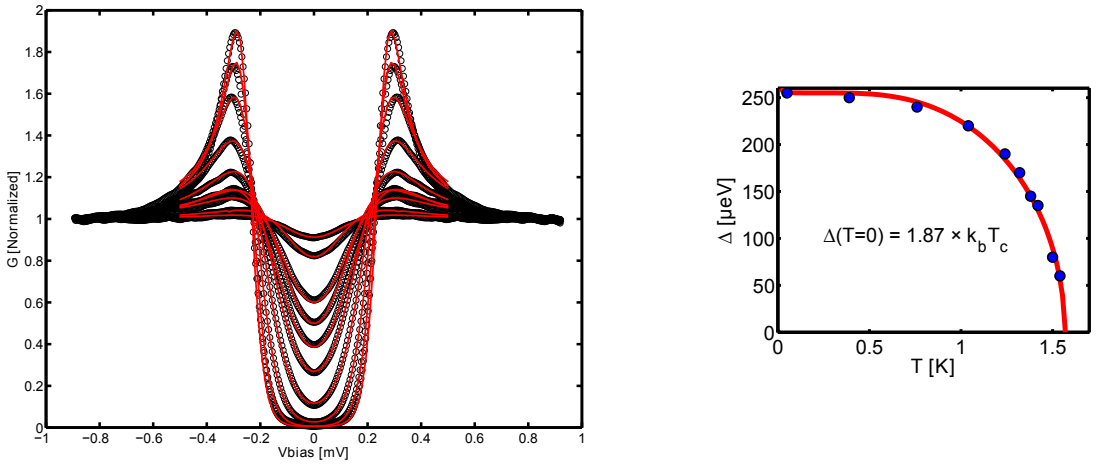

Figure 5.4 ***Spectroscopic measurements on bare Rhenium*** *- Left: temperature evolution of the DOS between 45 mK and $T_c = 1.6$ K (black dots) with BCS fits (red lines). Right: temperature evolution of the superconducting gap. The red line corresponds to a BCS fit with Δ/k_BT=1.87. Adapted from [48].*

films are presented on Fig. 5.4. One can extract $\Delta_{Re} = 255\,\mu eV$ and $T_c(Re) \simeq 1.6\,K$, with $\Delta_{Re}/k_B T_c$=1.87. As expected for thicker rhenium films, the T_c is smaller than in our films. The superconducting gap has also been consequently modified but with very similar $\Delta/k_B T_c$ ratio. Since it is very unlikely that the electron-phonon coupling has been drastically changed by the dissolved carbon atoms, we expect a comparable $\Delta/k_B T_c$ ratio in the graphene-rhenium system. However, according to McMillan's model, the measured Δ on graphene could be reduced because of an imperfect interface with rhenium (see Sec. 3.3.1.2). This is not what we observe since on our graphene-rhenium sample $\Delta/k_B T_c$=1.88. We can therefore conclude that the interface between graphene and rhenium is highly transparent with an Andreev reflection probability close to one.

The experience that would have enabled to validate this hypothesis indisputably is the measurement of the superconducting parameters (Δ,T_c,$\Delta/k_B T$) on the same sample after removal of the graphene layer. We have actually tried to do so by a reactive-ion etching (RIE) method (an oxygen plasma is generated and chemically reacts with the graphene layer), as it had been shown to be efficient to remove a graphene layer on SiC substrate. In our case, the result was difficult to interpret. After the RIE etching, the STM images showed a granular surface, with a typical grain size of 30 nm, and did not exhibit the recognizable rhenium mounts or steps. Nevertheless, we can not draw a conclusion as our sample was "old" when we performed this experiment and already presented a "dirty surface". This aging effect seems to be visible to the naked eye: after few months, the dark color of the surface brightens up in the edges, this zone extending progressively to the center, and small bright spots appear, which origin is still unknown (see Fig. 5.5). To conclude, the etching process should be repeated on a "fresh" sample, previously characterized by STM to enable comparison.

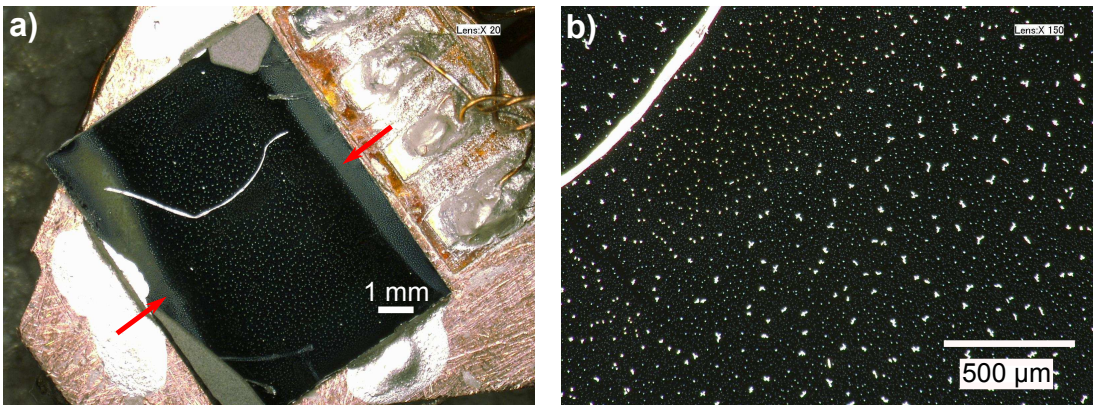

Figure 5.5 ***Sample aging*** *- Pictures at various scales showing the presence of impurities and bright spots of different sizes that seem to diffuse from the edges to the center of the samples. (a) Two edges covered by packed bright spots, giving this light grey color (red arrow). (b) Zoom in the middle zone of (a), showing different sizes of bright spots.*

The superconducting properties have also been measured on other samples, grown with various parameters, i.e. with different ethylene doses (roughly estimated by $P_{ethylene}$ x exposure time) and different temperature ramps for the cooling process (see Sec. 4.2.3). We have always found a superconducting gap on the order of $\Delta = 330 \pm 10\,\mu eV$ and a

transition temperature of $\sim 2.1\,\mathrm{K} \pm 0.1\,\mathrm{K}$ (deduced from the extrapolation of the BCS fit). It seems to mean that the actual carbon dose dissolved into the rhenium films does not vary much from film to film despite the maximum variation of one order of magnitude in the ethylene dose. This leads to the conclusion that the fraction of the ethylene molecules that actually dissolve into rhenium should be always sufficient to saturate our rhenium films with carbon. This was indeed corroborated by a simple calculation using the value of the carbon solubility in rhenium at 990°C found in the literature (2.10^{-3} atomic fraction [8]). Nevertheless, this does not explain why we observe very different surface morphology on samples grown with an *a priori* identical temperature ramp but different ethylene dose. This contradiction could only be dispelled by a precise study of the growth process and by achieving the regime of sub-monolayer graphene growth.

5.3 Superconducting DOS spatial homogeneity

We have seen in Sec. 4.5 that the high-energy LDOS presents a spatial variation at the moiré scale, probably due to the variation of C-Re atoms distances in a moiré supercell, which result in a locally different coupling of the graphene layer with the rhenium substrate. Regarding the superconducting properties, the Usadel formalism, which extends the BCS theory to the diffusive limit in the frame of the quasiclassical approximation[3], state on their variations on a scale of the superconducting coherence length ξ_S. In our system, we estimate the coherence length in carbon doped rhenium to be on the order of 18 nm from transport measurement, which means we do not expect strong variations of the superconducting properties on a smaller scale. The moiré periodicity is $\sim 2\,\mathrm{nm}$, i.e. about 9 times smaller than ξ_S. Variations of the superconducting properties should be very small, probably less than 5%. Nevertheless, if we adopt a framework beyond the quasiclassical approximation, by considering for example that the surface wavefunctions differ locally due to different C-Re coupling and therefore can not be averaged on the scale of λ_F, modification of the superconducting properties are possible on distances smaller than ξ_S. Indeed, modulation of the superconducting gap of 2H-$NbSe_2$ at the atomic-scale has been revealed by STS and attributed to multiband superconductivity [61] (this compound has a complex Fermi surface, with different Fermi sheets exhibiting different superconducting gaps). It is thus legitimate to wonder if we can see a modulation of the superconducting LDOS on the moiré scale.
To answer this question, we performed CITS measurements at very low temperature and low energy to extract the superconducting LDOS on moiré topographic maps. Like in the high-energy study, we divided the moiré zones in slices of different height ranges and averaged the spectra belonging to the same slice to smooth the noise. For each slice, we have two distinct averaged spectra as in each point of the spectroscopic grid the differential conductance was measured by sweeping the bias voltage from positive to negative voltage (forward spectrum) and back to the polarization bias (backward spectrum). A variation in the superconducting properties would appear as a modification of the gap value and/or a modification in the coherence peaks height. These latter are a much more

[3]The quasiclassical approximation is based on the observation that the transport properties of Cooper pairs, which are non-local objects, do not vary strongly on the scale of the Fermi wavelength λ_F. In this approach, it is thus assumed that all relevant variations occur on a length scale larger than λ_F.

sensitive probe when we try to detect possible tiny variations of the superconducting properties. Our analysis will thus be focused on these ones (indeed, no dispersion of the gap value could be detected). The relevant plot will represent the coherence peaks height of the averaged spectra versus the corresponding slice. There are four coherence peaks, referred to as $\mathrm{Lpeak}_{\mathrm{fwd/bwd}}$ and $\mathrm{Rpeak}_{\mathrm{fwd/bwd}}$ for the left and right coherence peaks of the forward/backward spectrum respectively.

We performed a dozen of CITS measurements centered on a moiré supercell. Nevertheless, some **qualitative criteria** have been fixed to select the relevant data:

- First, to enable to conclude as for possible spatial variations of the superconducting properties, one must clearly identify different spatial zones of the moiré, i.e. the moiré corrugations (hills and valleys) should be clearly visible in the simultaneously recorded topographic map.
- Second, CITS presenting "exotic" conductance spectra, likely due to tip effects, have been eliminated straight away (see Fig. 5.6).
- Third, one ensured that no obvious tip changes were detectable in the data. This would usually lead to disruptions in the topographic image with sudden jumps of the scanned area, changes in the topographic corrugation amplitude or in the spectra shape. If such changes were detected during a CITS measurement, the data set would be truncated to select an area free of visible tip changes.

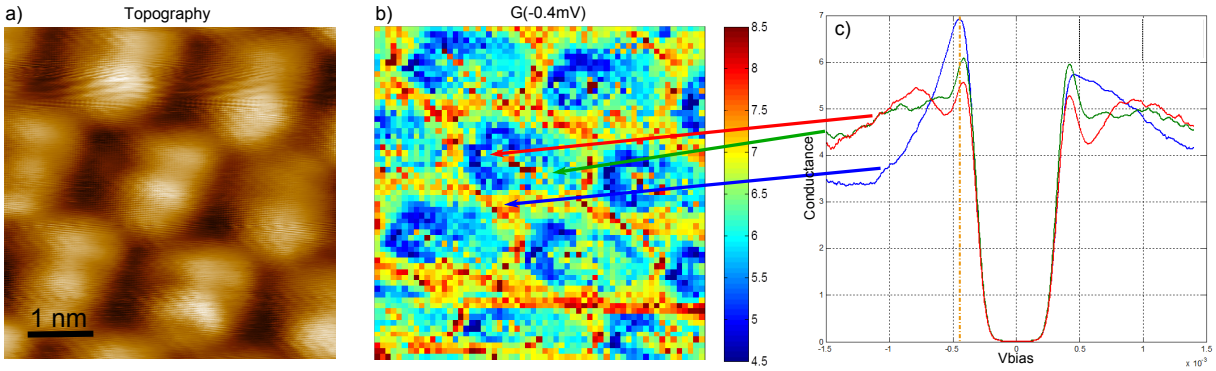

Figure 5.6 ***CITS presenting "exotic" spectra*** *- (a) Topographic image showing a deformed moiré pattern. (b) Conductance map at the energy of the left coherence peak (-0.4 mV). (c) Average conductance spectra representative of three different zones indicated by the colored arrows. Their shape is not understood. After cleaning the tip by field emission, we recovered usual superconducting spectra.*

In addition to these three qualitative "objective" criteria, we added **quantitative ones** to avoid counting individual noisy spectra that could disturb the signal:

- Criterion 1 : the first quantitative criterion eliminates noisy or tilted spectra via a normalization procedure: we normalize the spectra by dividing them by the average value of the DOS measured for the N first points (negative bias). Usually, N=100-200 over 1000 registered points for a whole spectrum. Then, we select a spectrum only if the average value of its N last points (positive bias) is between 0.9 and 1.1, which corresponds to a tilt tolerance of 10%.

– Criterion 2 : the second quantitative criterion eliminates spectra that present an asymmetry in the height of the left and right coherence peaks. For example, we keep spectra for which the height difference between the right and the left coherence peaks does not exceed 5%.

These two quantitative criteria are **subjective** and **arbitrary**. They are empirical in the sense they were chosen to get rid of specific observed sources of noise.

Fig. 5.7 presents an analysis carried out on a truncated CITS measurement. On the simultaneously recorded topographic map shown on the left, we can identify 3 moiré hills and 2.5 valleys. The (a) panel discloses the discretized topographic map, for which one color corresponds to one slice (slice 1: bottom valleys → slice 4: top hills). The black dots (slice 0) correspond to the spectra eliminated with the first quantitative criterion, i.e. by the normalization procedure. We thus verify than the number of averaged spectra is still representative (relatively few black dots). On the right, we plotted the four coherence peaks heights of the forward and backward average spectrum of each slice. The overall maximum difference of peak height is of 0.04 for an average peak height of 1.96, which makes a difference of the order of 2%. Beside being extremely small, this variation is not linked to a clear trend and we can thus conclude that the height variations are in the noise level of our experiment.
Looking at individual spectra, we noticed an asymmetry in the coherence peak heights: the right peak is sometimes higher than the left one. As the graphene is strongly coupled to the rhenium substrate, it is similar to a metallic system and we do not expect an asymmetry between electrons and holes. As this asymmetry could not be linked to an obvious physical interpretation, we chose to apply an additional filter which corresponds to the second quantitative criterion. The (b) panel shows the data resulting from the addition of this second quantitative criterion, i.e. eliminating asymmetric spectra with respect to the height of the right and left coherence peaks with a tolerance of 5 %. We can see on the corresponding discretized topographic map that many more spectra have been eliminated. Although this criterion is strict, the number of remaining spectra seems acceptable to define a representative average. On the right plot, we extract a maximum difference of peak height of 0.1, which makes a difference of the order of 5%. This time we observe a clear upward trend of the coherence peak amplitude with respect to the height on the moiré: the higher the position on the moiré, the higher the coherence peak. If we plot the corresponding spectra for each slice for the backward measurement for example (see panel (c)), the trend is clear. We are thus inclined to conclude that the coherence peak amplitude is correlated to the moiré position, these correlations being apparent when we remove the "bad" spectra from the sampling. To check the validity of this statement, we proceeded to many other CITS measurements and present here another one verifying the three first qualitative "objective" criteria.

Fig. 5.8 illustrates this latter measurement. On the topographic map on the right, we can clearly identify moiré hills and valleys. The (b) panel shows data extracted with the first quantitative criterion. We discretized the topography in five slices and the number of averaged spectra for each slice is important (few eliminated spectra ∼ "black dots"). This time, after the first selection, we surprisingly observe a downward trend of the coherence peak amplitude with respect to the height on the moiré. The overall difference is on the

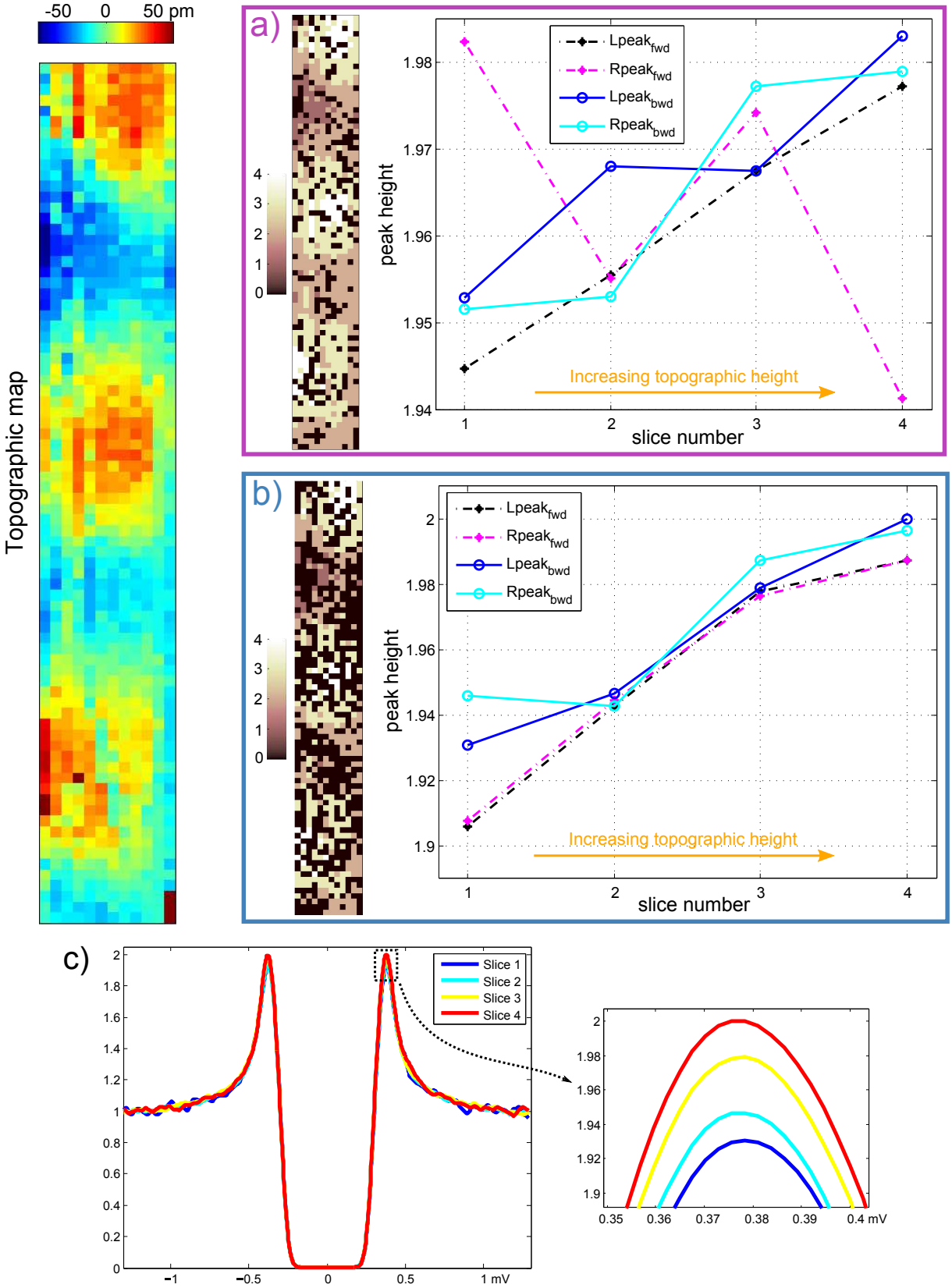

Figure 5.7 ***Peak height study on the moiré scale - Measurement 1*** *- (a) Spectra filtered according to criterion 1 (plateaux ∈[0.9,1.1]). (b) Spectra filtered according to criterion 1 and 2 (plateaux ∈[0.9,1.1] and left/right peak height difference <5%). (c) Average spectra for each slice corresponding to b). Slice 1: -60<z<-30 pm, slice 2: -30<z<0 pm, slice 3: 0<z<30 pm , slice 4: 30<z<60 pm.*

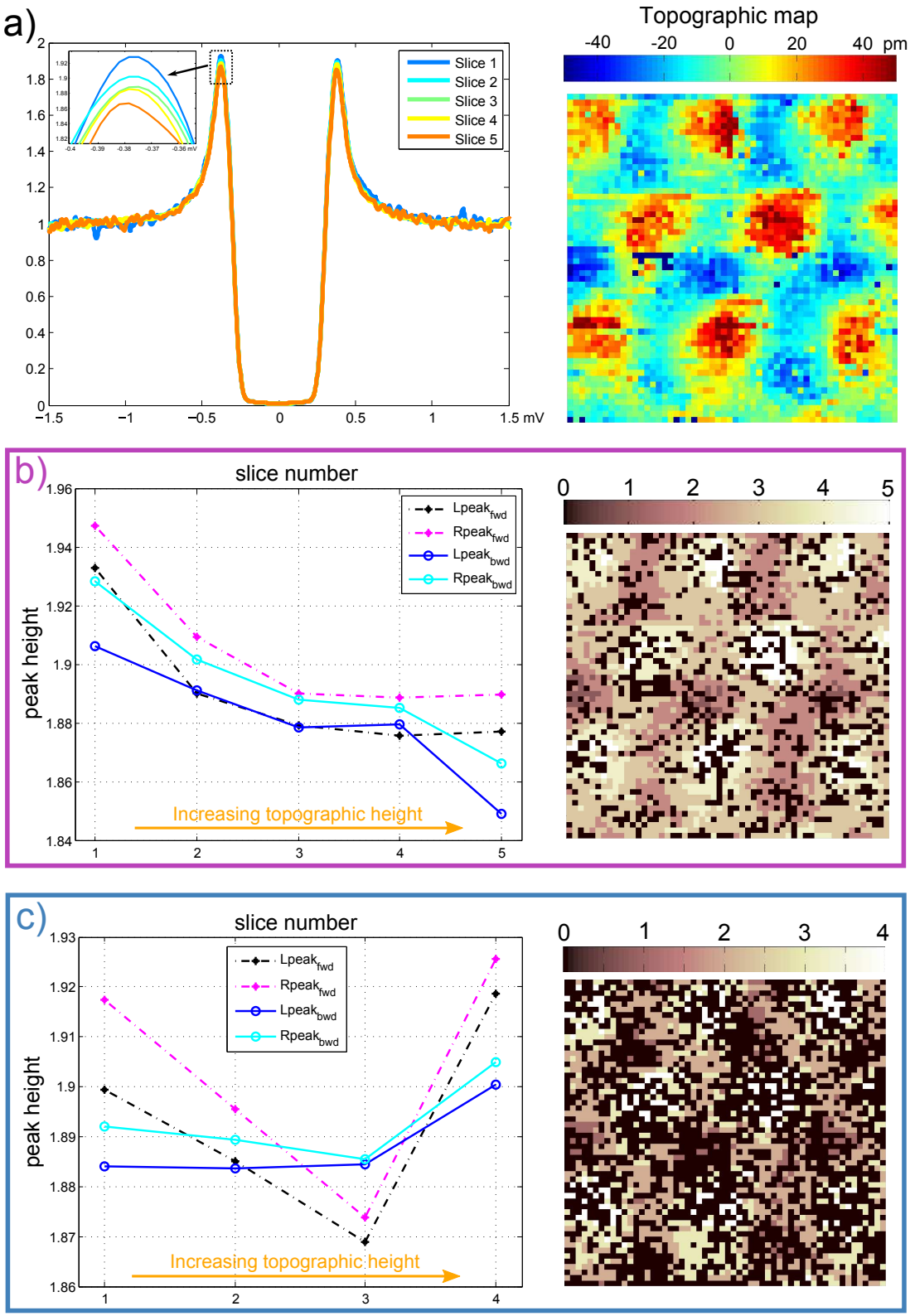

Figure 5.8 ***Peak height study on the moiré scale - Measurement 2 (1/2)*** *- (a) Average spectra for each slice corresponding to b). (b) Spectra filtered according to criterion 1 (plateaux ∈[0.9,1.1]). Slice 1: -50<z<-30 pm, slice 2: -30<z<-10 pm, slice 3: -10<z<10 pm, slice 4: 10<z<30 pm , slice 5: 30<z<50 pm. (c) Spectra filtered according to criterion 1 and 2 (plateaux ∈[0.9,1.1] and left/right peak height difference <5%). Slice 1: -40<z<-20 pm, slice 2: -20<z<0 pm, slice 3: 0<z<20 pm , slice 4: 20<z<40 pm.*

order of 0.06, which makes a difference of $\sim 3\%$. The backward spectra are presented on panel (a) and illustrate clearly the downward trend: the higher the position on the moiré, the lower the coherence peak amplitude.
To evaluate if this evolution is related to the peak height asymmetry, we then applied another filter corresponding to the second quantitative criterion. The results are given on panel (c) for a selection of four slices. Again, we see on the discretized topographic map that many spectra have been eliminated. Looking at the plot of the peak amplitudes, no clear trend emerges this time. Indeed, while we removed the "bad" spectra with a filter validated by the results of the first CITS measurement, we do not only loose the negative correlations obtained after the application of the first filter but we do not even recover the positive correlations we extracted from the first CITS.
To analyze more deeply the relevance of the statistic average that gives the value of the peaks amplitude per slice, we plot the histograms representing the peak height distribution for each peak of each slice (see Fig.5.9 a). The standard deviation of the mean can be estimated by fitting an histogram by a Gaussian. The error will thus be $\sigma/\sqrt{n}$ where σ is the Gaussian standard deviation and n the total number of averaged points for the corresponding peak and slice. An example is given for the fifth slice, where we superimposed the histogram and the corresponding Gaussian fit. This slice presents the larger dispersion of peak height values, but the $\sigma/\sqrt{n}$ value obtained by the fit never exceeded 0.015 in the worst case (with $\sigma = 0.17$ and $n = 130$). However, the position of the center of the Gaussian fit, which is theoretically the average value, presents a much higher deviation. We estimate the incertitude on the Gaussian center to be ± 0.03 for slices 1,5 and ± 0.02 for slices 2,3,4. This incertitude dominates the error characterized by the Gaussian width. We plot on Fig. 5.9 b the graph of the second CITS measurement with the estimated error bars. This shows the downward trend is actually in the noise level of our statistic distribution.

Finally, we can not conclude as for the variations of the coherence peak amplitude with the position on the moiré. If such correlations do exist, they could not be revealed by the statistic analysis of our STS measurements. This study shows one should be careful with the interpretation of "representative" spectra obtained by data averaging. One can also call into question the arbitrary and "subjective" criteria chosen to filter noise and select "physical" data. The second criterion, for instance, could be possibly overrun if one imagines the case of a doped graphene layer. The Dirac point would thus be shifted from the Fermi level, which would result in a shift of the V-shape DOS that could create an asymmetry in the DOS of filled and empty states. In our case, we ruled out this hypothesis based on our high-energy study, where no graphene-like DOS (V-shape) could be observed due to the strong coupling with the rhenium substrate.

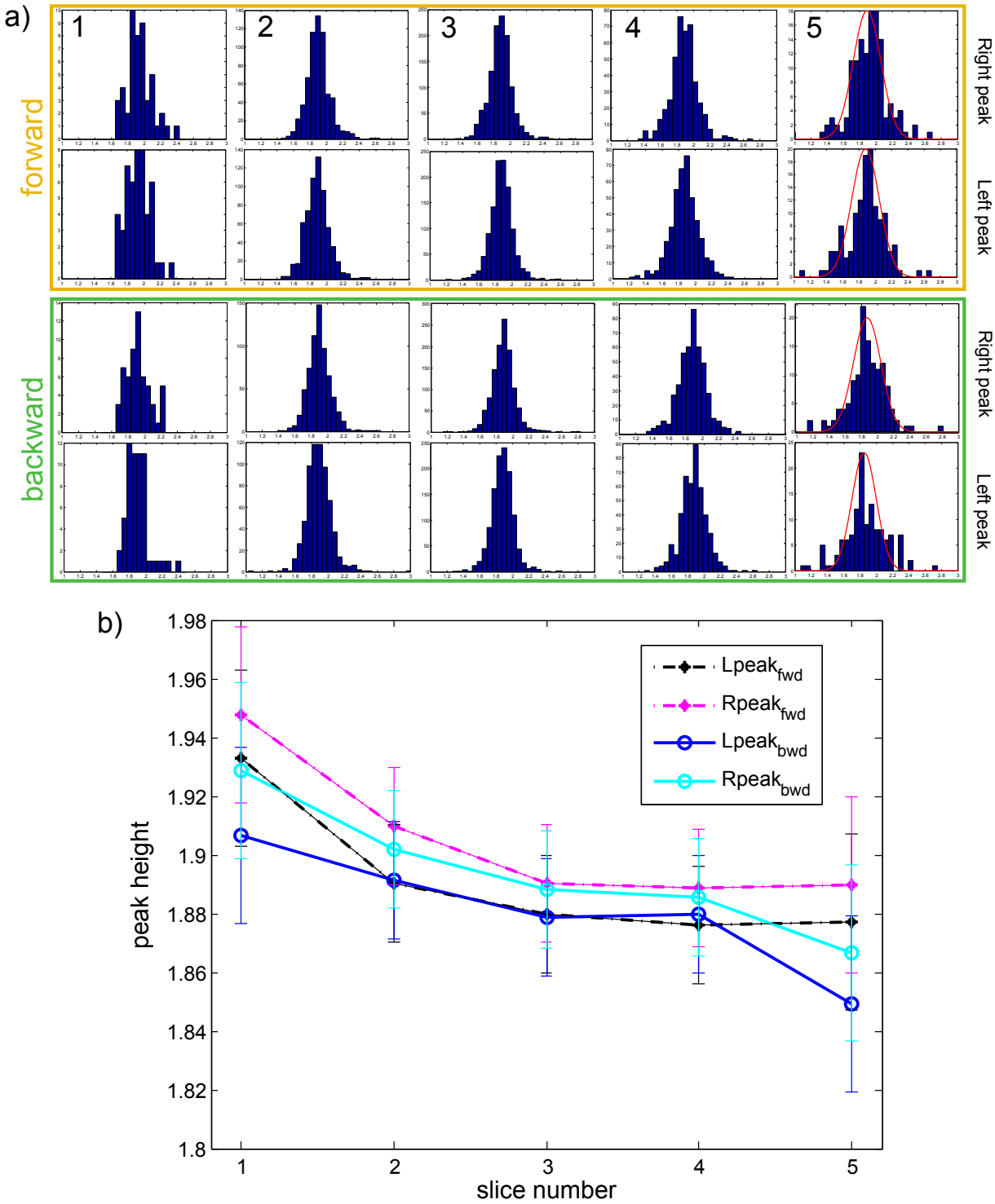

Figure 5.9 ***Peak height study on the moiré scale - Measurement 2 (2/2)*** *- (a) Histograms of the peak amplitude per slice for the right and left coherence peaks of the forward and backward spectra selected by the first criterion (plateaux ∈[0.9,1.1]). The fifth column, corresponding to the fifth (highest) slice, presents a Gaussian fit used to estimate the error bars. (b) Error bars resulting from the Gaussian center imprecision.*

5.4 Magnetic vortices in the superconducting mixed state

Type II superconductor While bulk rhenium is a type I superconductor, rhenium thin films exhibit a type II superconductivity, which is characterized by two critical magnetic fields H_{c_1} and H_{c_2}. When $H > H_{c_1}$, the magnetic field starts to penetrate into the sample as an array of normal cores called magnetic vortices, each vortex carrying a quantum of superconducting flux $\Phi_0 = h/2e$. This mixed state lingers on up to H_{c_2} when the whole material transits into its normal state.

STM imaging In 1989, H.F. Hess *et al.* have reported for the first time the use of STM to observe the Abrikosov vortex-lattice [2] in the mixed state of $NbSe_2$ [67]. The imaging method relies on the peculiar spectral properties of vortices. Indeed, in first approximation, the vortex core is a non-superconducting metallic zone surrounded by supercurrents that screen the magnetic field crossing the core. Thus, the DOS of a

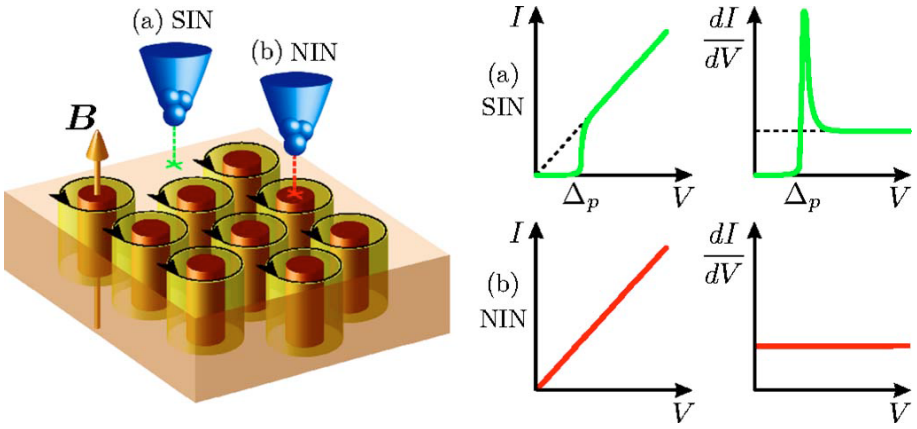

Figure 5.10 ***Illustration of the vortex-lattice imaging by STM*** *- (a) Local SIN junction with typical BCS DOS when the tip is between vortices. (b) Local NIN junction when the tip is positioned over a vortex core. The differential conductance is constant, energy-independent. Reproduced from [54].*

vortex core is metallic[4], i.e. energy-independent, whereas the DOS measured between vortices presents superconducting features (see Fig. 5.10). The vortex arrangement can thus be easily imaged by combining topography and spectroscopy measurements when a magnetic field is applied perpendicularly to the sample. The sample-tip bias voltage needs to be set close to the BCS coherence peak value, where the DOS contrast between a superconducting and a normal zone is maximum. Then, the presence of a vortex is revealed by a decrease of the dI/dV signal (simultaneously acquired by a lock-in technique for instance), which gives a dark spot in the differential conductance map (see Fig. 5.11). This method enables to map rather quickly[5] the spatial organization of the vortex-lattice. Afterwards, one proceeds to a CITS measurement on a specific zone to make a complete cartography of the DOS and get information on the vortex core electronic states.

[4]This approximation is valid in superconductors in the dirty limit, when $\xi >> l_e$ where l_e is the elastic mean free path.

[5]Although it greatly relies on the quality of the lock-in signal and thus on the tunnel junction stability.

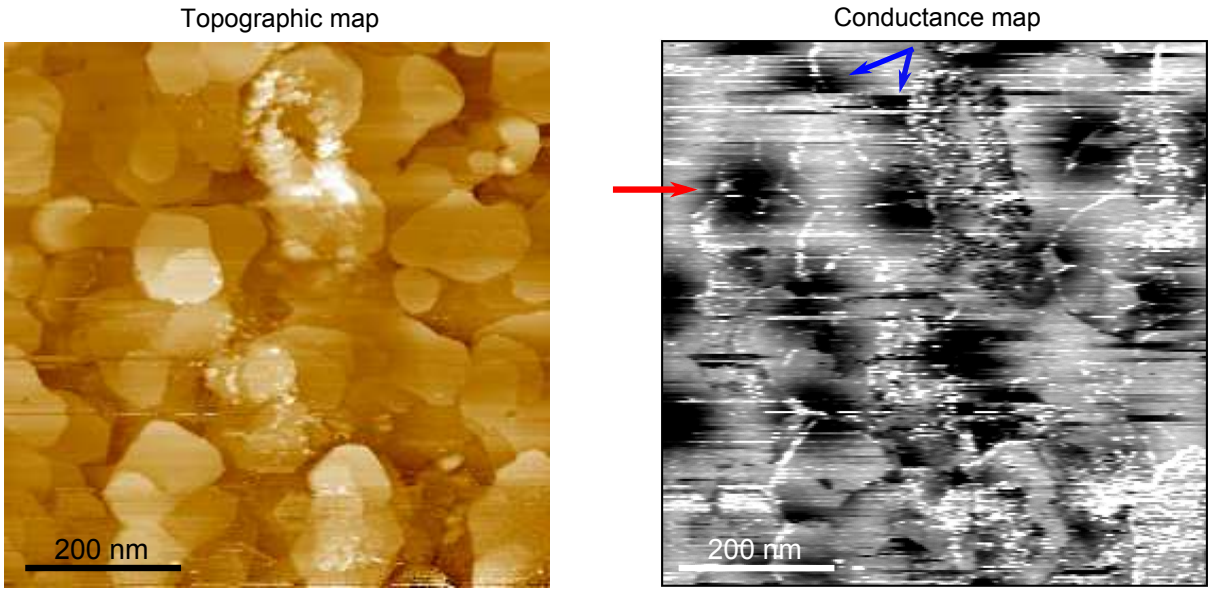

Figure 5.11 ***STM imaging of vortices in the graphene-rhenium system*** *- Simultaneous topographic and spectroscopic measurement at the energy of the coherence peak. The vortices are visible as black spots on the conductance map. The red arrow points out the vortex studied in more details in Fig. 5.12. The blue arrows point our a split vortex (see text).*

Vortices in the graphene-rhenium system We performed this kind of measurements on one of our graphene-rhenium films. We applied a perpendicular magnetic field of 575 Gauss (i.e. 57.5 mT) and simultaneously registered a topographic map and a differential conductance map (the output of the lock-in) with the bias voltage fixed at the energy of the coherence peak $V_{bias} = 260\,\mu$eV. The maps are presented on Fig. 5.11. On the topographic image (left), we see rhenium grains of about 100 nm, sometimes separated by deeper furrows. The white misty features are dust present on the surface and possibly moved by the tip during the scan. The conductance map (right) exhibits a distorted hexagonal Abrikosov vortex-lattice, corresponding to the black dots. The disorder is inherent to the film morphology, as vortices are always preferentially pinned in defect sites. On the upper extremity of the image, one has the feeling that a vortex is cut into two pieces (blue arrows). It actually corresponds to the displacement of a single vortex by the STM tip during the scan. This is a well known effect due to the metastability of the vortex between two pinning centers [46, 68]. To get a detailed cartography of the vortices core electronic states we need to carry out a CITS measurement on a more limited zone. We chose to focus on a vortex on the top-left part of the conductance image, indicated by a red arrow.
The data are presented in Fig. 5.12. A highly resolved topographic image of the studied zone is given in (d), which shows a full graphene coverage of the surface (moiré pattern visible everywhere). Only the shell-shaped central grain presents a different morphology with a possible disordered carbon layer. The CITS simultaneously recorded topographic map is given in (a), where the concentric circles indicate the vortex position and extension, that we can clearly visualize on the conductance map at the Fermi energy given in (b). The inner core of the vortex is located on the lowest rhenium grain visible on the topographic image, in a hole-like part of the rhenium film, possibly a preferential pin-

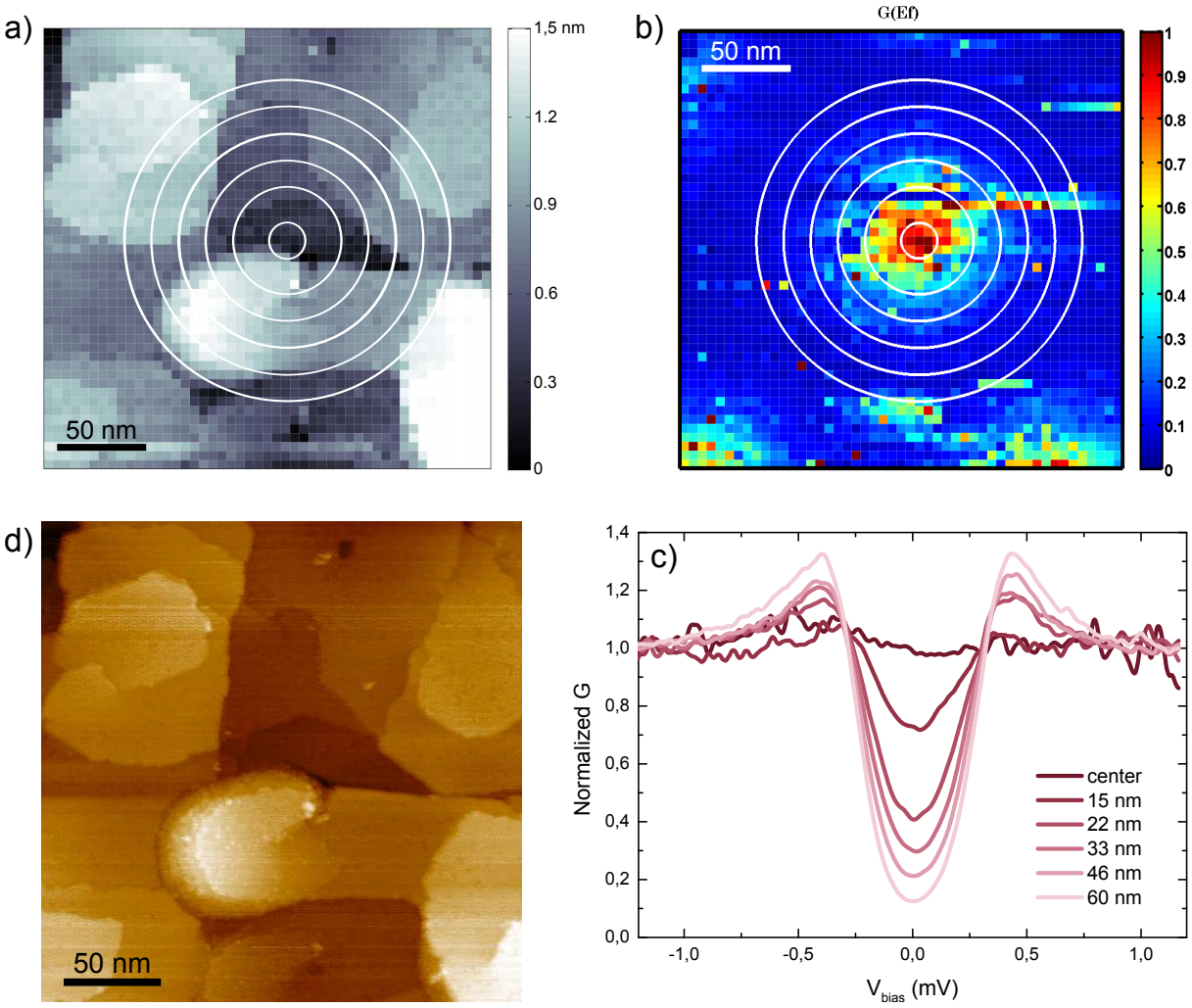

Figure 5.12 ***STM study of a vortex core*** - *(a) Topographic image recorded during the spectroscopic measurement. (b) Conductance map at the Fermi energy centered on a vortex core. (c) Closing of the superconducting gap in the vortex core region. (d) Topographic image after the CITS measurement.*

ning site. Nevertheless, we notice again on the conductance image that a line of spectra crossing the vortex core is shifted from the rest of the vortex core, which indicates its displacement between two pinning centers. The spatial evolution of the conductance spectra as a function of the distance to the vortex center is displayed in (c). Each spectrum is the result of an average of the spectra included in the different crowns drawn on (b). The vortex inner core presents in this case a constant, metallic-like DOS. This is a classical evolution of the DOS in a vortex core for a superconductor in the dirty limit[6] [60].
It is difficult to give a quantitative description of this vortex, as this one is not isolated. Indeed, we can see on the bottom part of image (b) that two other vortex cores are nearby (these latter can also be identified on Fig. 5.11). As can be seen on the spectra evolution (c), the spectra averaged on the crown the most remote from the center present a non-zero DOS at the Fermi energy and reduced coherence peaks. This is due to the influence of the surrounding vortices, whose screening supercurrents act as pair-breaking scatterers.

[6] When $l \ll \xi_0$, where l is the electron mean free path and ξ_0 the superconducting coherence length.

The measurement of an isolated magnetic vortex core radius would also have enabled to add an argument in favor of the strong coupling between rhenium and the graphene layer. Indeed, for a standard SN proximity junction, the vortex core radius measured in N is expected to increase with a decreasing interface transparency [59]. By comparing the radius measured on graphene and on the bare rhenium film for the same magnetic field, one could have concluded as for the interface quality. This might be possible by achieving the graphene sub-monolayer growth regime if the zones with and without graphene are large enough and well separated.

5.5 Lateral superconducting proximity effect

We have demonstrated, by growing graphene epitaxially on top of superconducting rhenium, that we succeed to make a hybrid system where the graphene layer is very well coupled to the rhenium substrate and acquires its superconducting properties. Nevertheless, our system presents a major drawback, which results from its most desired characteristic: graphene is so strongly bond to rhenium that it looses its peculiar intrinsic properties. Indeed, the crystallized carbon monolayer we grew on top of rhenium does not exhibit the electronic structure of graphene, with the characteristic V-shape DOS, even in the less-coupled regions (hills of the moiré). To overcome this problem while keeping our highly transparent interface between graphene and the superconductor, we need to **locally decouple** the graphene layer from the rhenium substrate.

A first way to do it, proposed by Sutter *et al.* on graphene-Ru(0001) [126], consists in growing a second graphene layer on top of the first one. Indeed, it has been shown that whereas the first graphene layer interacts strongly with the metal substrate, the second layer shows very weak electronic coupling to the metal, and hence retains the electronic structure inherent to graphene. This was revealed by four-probe transport measurements in UHV and Raman measurements, where the characteristic G and 2D peaks of graphene Raman signal was recovered on the bilayer whereas these peaks are absent on the first layer[7] [126]. Further STM measurements on bilayer graphene on ruthenium resolved the six-fold periodicity of the honeycomb lattice and micro-ARPES[8] spectra showed a linear band dispersion near K, with a Dirac point about 500 meV below the Fermi level [124]. These results confirm that the top sheet of the bilayer behaves like free-standing monolayer graphene except for a down-shift of the Dirac point, indicating an electron doping of the top graphene layer.

Inspired by these results on ruthenium, we tried to grow a bilayer graphene on our rhenium thin films, preferably stopping the growth in a mixed state with monolayer and bilayer areas. If the CVD growth of multi-layers graphene depends on the metallic substrate[9], it is easier to achieve by the segregation method. In the case of ruthenium,

[7] Our attempts to make Raman spectroscopy on our samples have always been unsuccessful as no signal related to graphene could be extracted. The signal was always clearly dominated by the metal fluorescence.

[8] ARPES stands for angle-resolved photo-emission spectroscopy.

[9] On Ir(111) for example, the graphene growth is self-limited: graphene can only grow in the presence of bare metal [32].

the second layer growth begins after the completion of the first graphene layer if the slow temperature ramp is continued [124]. By increasing the ethylene dose and cooling down our sample with a very slow temperature ramp, we fabricated a sample with a new morphology (sample 'AK 43'). Fig. 5.13 presents STM images showing various topographic features on AK 43. The sample surface exhibits two main different areas: zones covered with moiré, characteristic of graphene on rhenium (pointed out by blue arrows in image

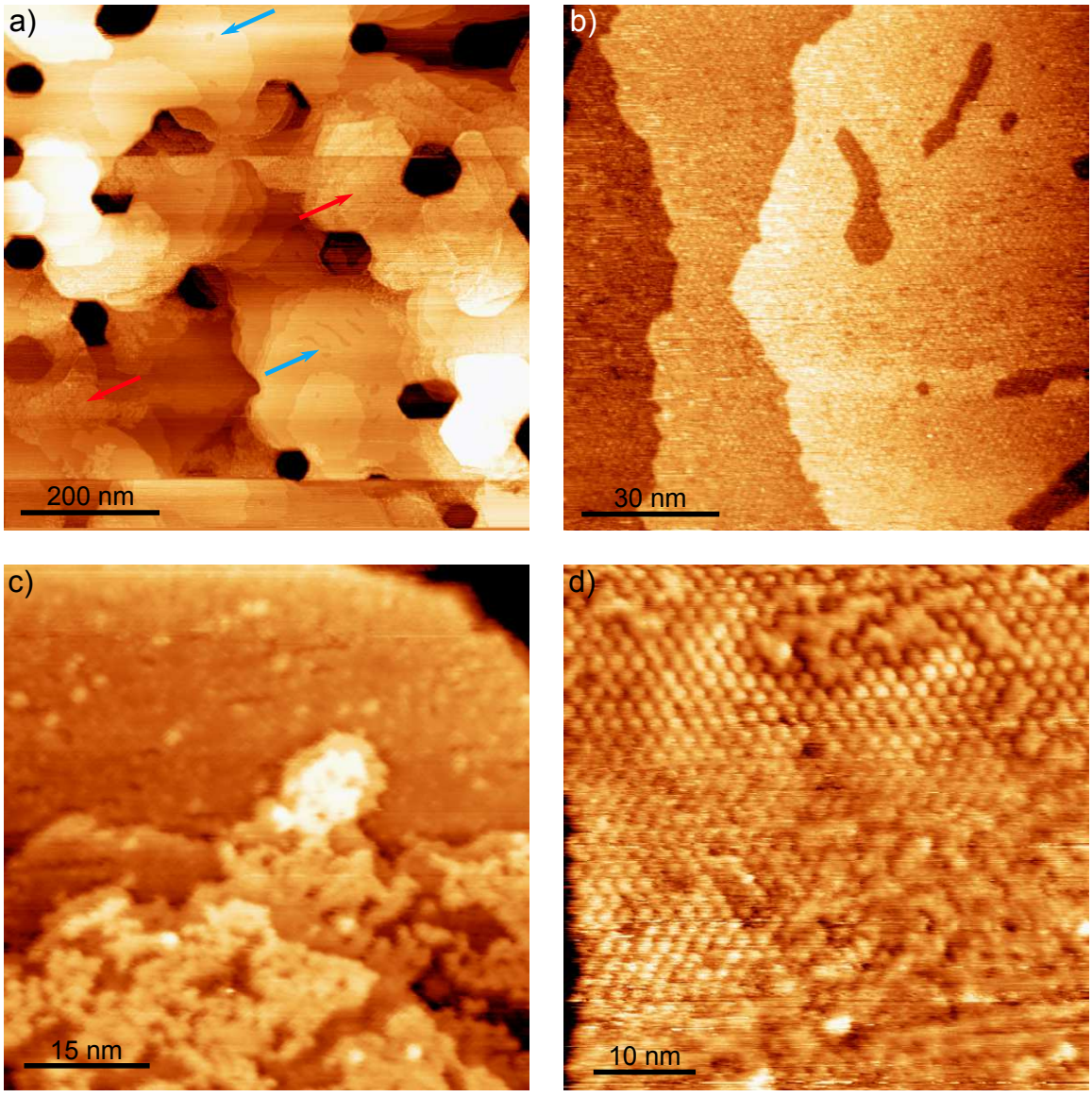

Figure 5.13 ***STM topographic images of 'AK43'*** *- (a) Large scale image showing Re grains separated by deep hexagonal holes. The blue arrows point out moiré areas with holes in the Re top layer. The red ones point out unsual topographic features, attributed to an additional amorphous carbon layer. (V_{bias}=5 mV,I_t=1 nA). (b) Zoom showing several Re steps covered by graphene, as attested by the presence of the characteristic moiré, and holes in the Re top layer. (V_{bias}=200 mV,I_t=300 pA). (c) Zoom on an amorphous carbon layer presenting a 'dendritic' geometry. (V_{bias}=1.5 mV,I_t=800 pA). (d) Moiré exhibiting irregularities, looking as premises of graphene 'bubbles'. (V_{bias}=5 mV,I_t=1 nA).*

(a)), and ones presenting what seems to be an additional amorphous carbon layer (pointed out by red arrows in image (a)). Images (b) and (c) are zooms on a moiré area and on an amorphous carbon layer respectively. One can also notice that the upper part of image (c) does not exhibit the moiré attesting the periodic arrangement of the graphene atoms on the rhenium ones. It could be a not-yet fully crystallized carbon layer, like it has been reported on the graphene-ruthenium system [62]. Image (d) shows another peculiarity of the sample surface. The regular moiré pattern seems to be lifted up from rhenium at some places, as if several moiré hills were merging together, leading to graphene 'bubbles' suspended over the Re substrate. This morphology will be referred to as *detached moiré* later on. Although these features are not completely understood, we seized the opportunity to study the influence of these surface geometries on the superconducting proximity effect.

Superconducting properties of detached moiré

Fig. 5.14 a shows a topographic STM images several areas, with amorphous carbon (right of the image) and zones with moiré and detached moiré (left). We carrieds out a CITS measurement on a mixed zone (image b) exhibiting regular moiré (right) and detached moiré (left). The regular moiré zone also presents several hole-type defects. Image (c) is a topographic map of the CITS and (d) is a conductance map at the Fermi energy. We note that $G(E_F)$ is lower in the regular moiré area than in the detached moiré area. In this latter, we also remark the presence of smaller zones where $G(E_F)$ is significantly higher, referred to as "bumps". The averaged conductance spectrum for each of the three zones: regular moiré, detached moiré and bumps, is presented on image (e). The overall shape of the spectra is the same, with a slight asymmetry in the coherence peaks height and a non-zero DOS in the superconducting gap. The main difference stands in the value of the DOS at the Fermi energy, as already seen on the conductance map. This non-zero $DOS(E_F)$ seems to be the manifestation of a pair-breaking phenomenon, also attested by the low amplitude of the coherence peaks. Despite small differences between moiré zones and detached moiré ones, there is no drastic differences in the superconducting properties.

Lateral superconducting proximity effect

We performed a spectroscopic measurement (CITS 1) on a sample area where the three different types of surface morphology were present (see Fig. 5.15 a). We focused on a limited rectangular zone presenting these three different aspects (image c): moiré (left), detached moiré (middle) and amorphous carbon (right). Image (e) presents a conductance map at the energy of the gap edge (at an energy just below the energy of the coherence peak). Thus, the higher the conductance value, the smaller the gap. Whereas we observe a small evolution between the moiré area and the detached moiré one, in agreement with the previous observation, there is a strong lateral proximity effect when approaching the more disordered zone: the superconducting gap is closing when we go from the moiré region to the region of amorphous carbon. The full averaged spectra plotted on image (f) confirm this trend and exhibit another unexpected feature: **while the superconducting gap decreases, the coherence peaks height increases**. This effect, visible on a large scale ($\sim$60 nm), is the total opposite of what should be observed in a standard superconducting proximity effect (the coherence peak height amplitude decreases when the gap closes). This unusual effect can not be attributed to a tip effect as it has been reproduced on different spots with different STM tips.

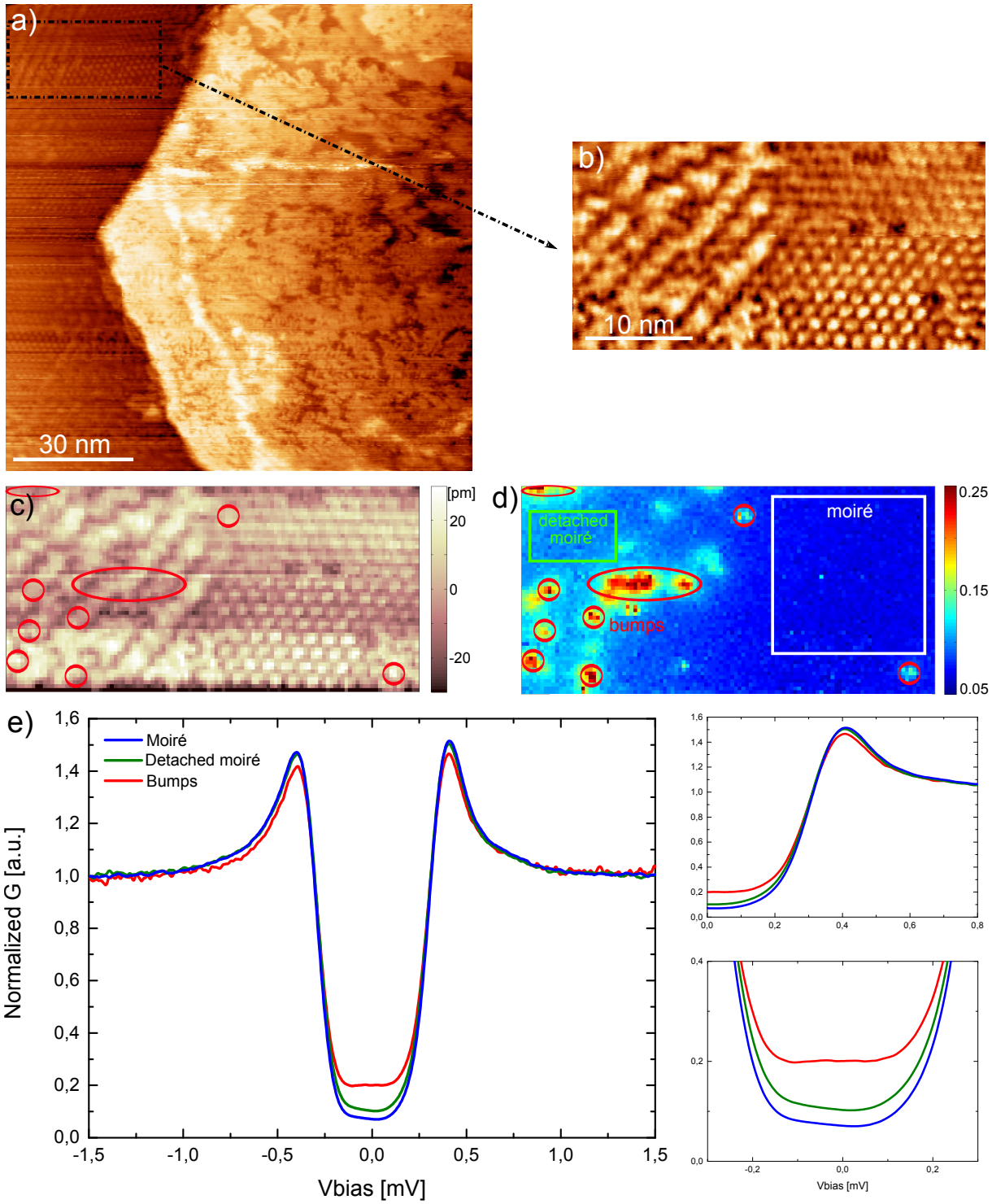

Figure 5.14 ***Comparison moiré/detached moiré*** - *(a) Topographic image (V_{bias}=5 mV, I_t=1 nA). (b) Topographic image recorded during the spectroscopic measurement (V_{bias}=1.8 mV, I_t=1.25 nA). (c) Topographic map of the CITS. (d) Conductance map at the Fermi energy. (e) Normalized conductance spectra averaged on various zones of the conductance map (d) and zooms on the gap edge and the DOS at the Fermi energy.*

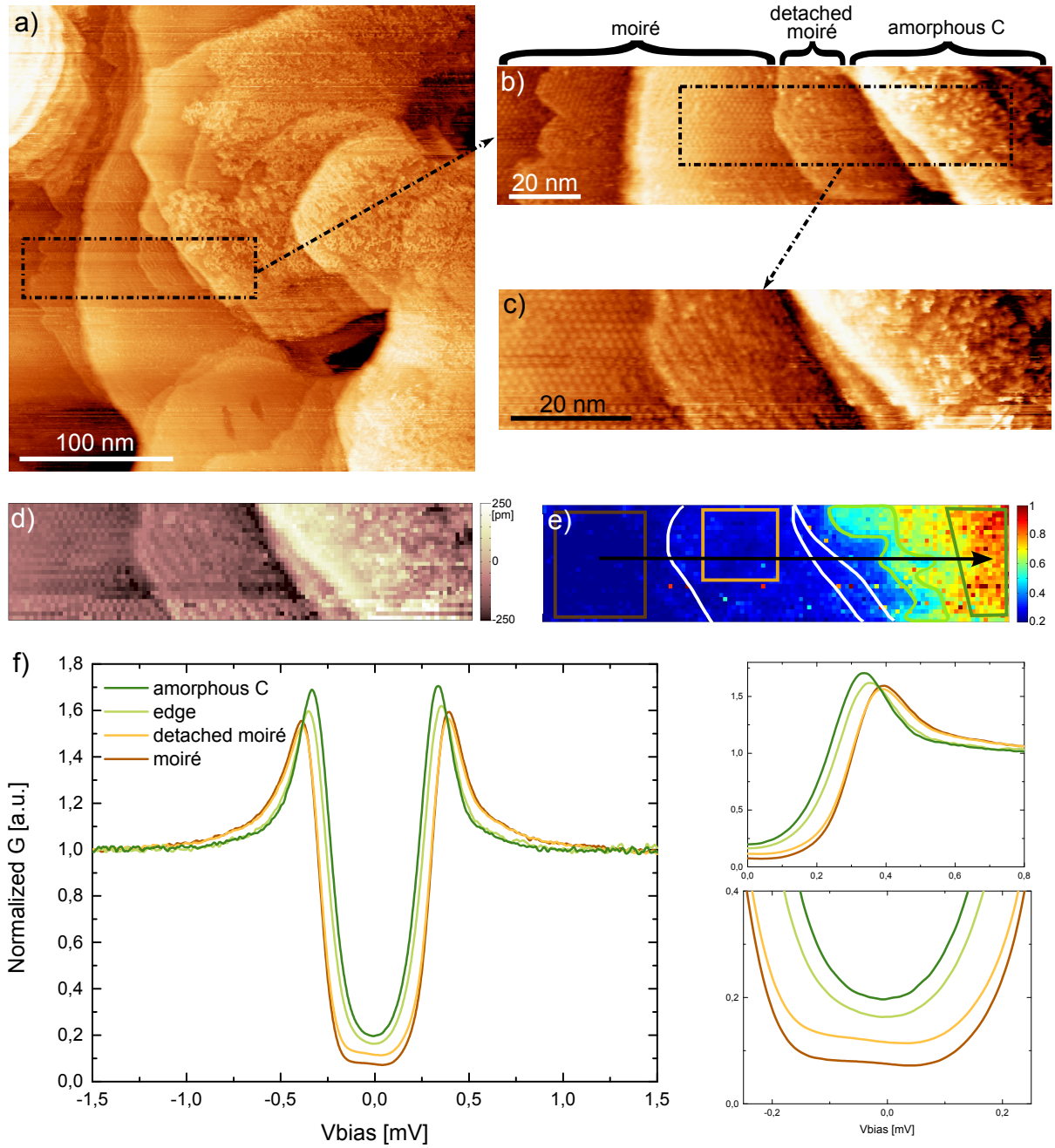

Figure 5.15 ***Lateral proximity effect (CITS 1)*** - *(a) Topographic image (V_{bias}=5 mV,I_t=1 nA). (b) Zoom exhibiting three distinct topographic zones. (c) Topographic image recorded during the spectroscopic measurement (V_{bias}=1.5 mV,I_t=1 nA). (d) Topographic map of the CITS. (e) Conductance map at the energy of the gap edge (-0.2 mV). (f) Normalized conductance spectra averaged on various zones of the conductance map (e) and zooms on the gap edge and the DOS at the Fermi energy.*

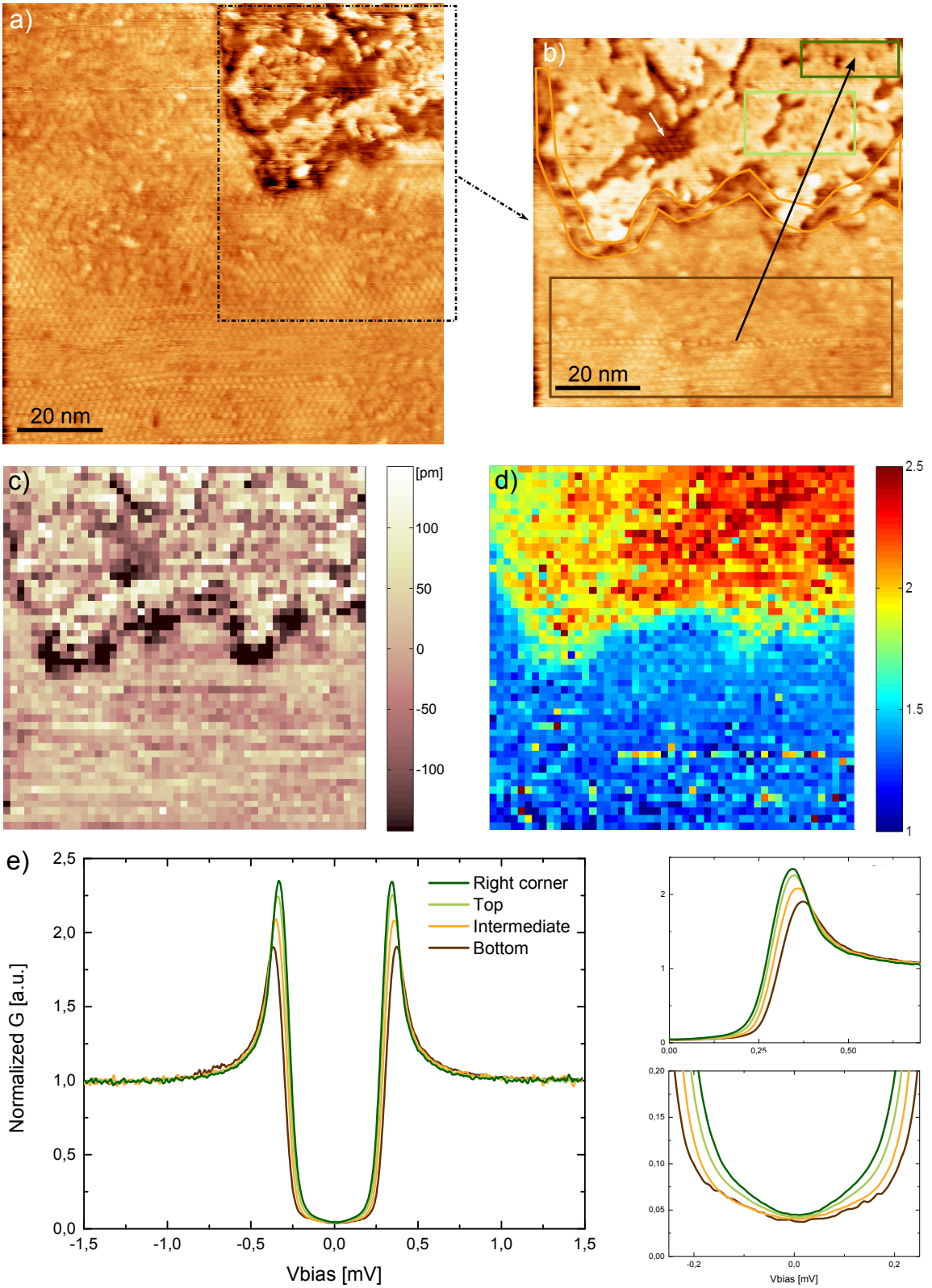

Figure 5.16 ***Lateral proximity effect (CITS 2)*** *- (a) Topographic image (V_{bias}=5 mV,I_t=1 nA). (b) Zoom in the measured area (V_{bias}=20 mV,I_t=500 pA). (c) Topographic map of the CITS. (d) Conductance map at the energy of the gap edge (-0.3 mV). (e) Normalized conductance spectra averaged on various zones of the topographic image (a) and zooms on the gap edge and the DOS at the Fermi energy.*

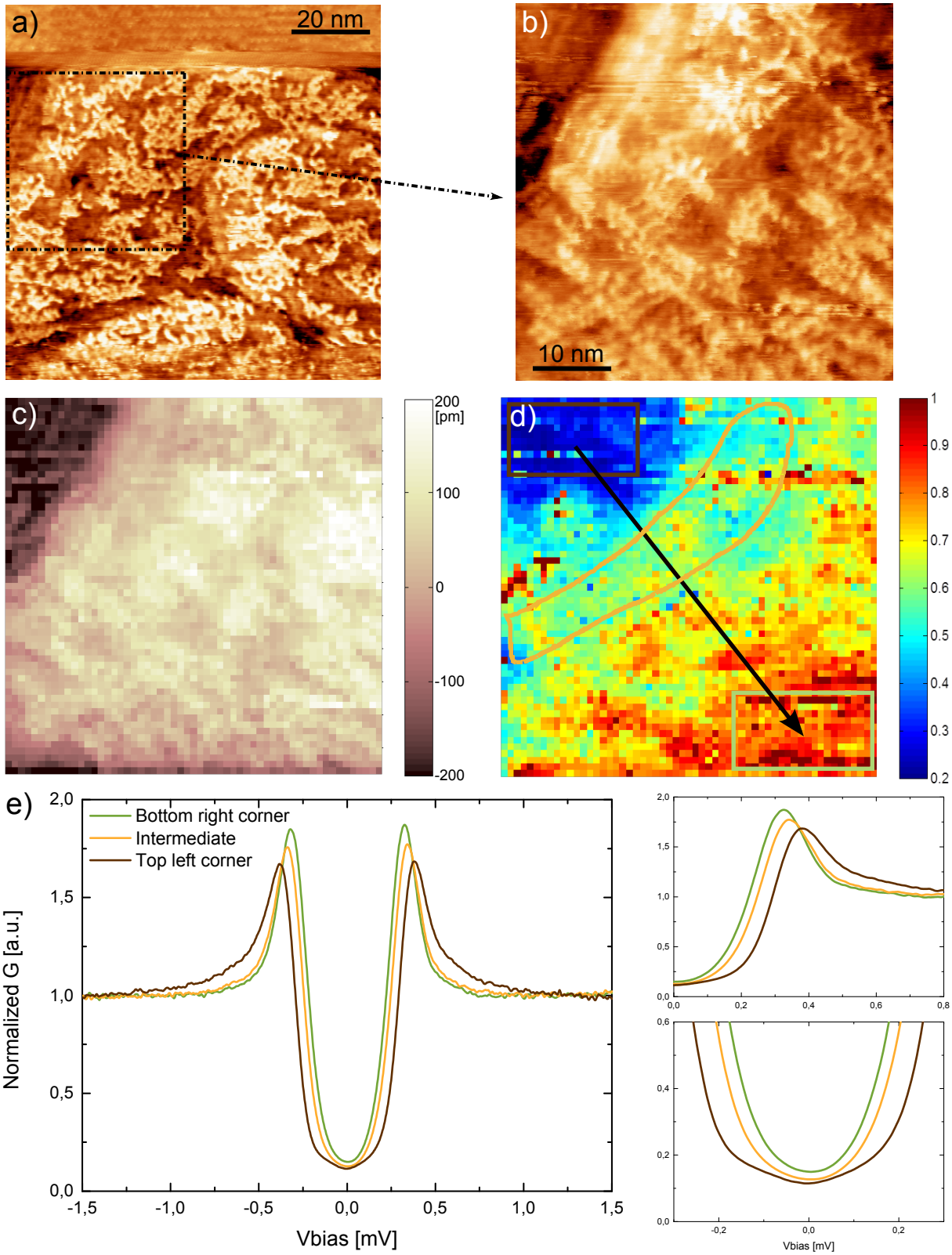

Figure 5.17 ***Lateral proximity effect (CITS 3)*** *- (a) Topographic image (V_{bias}=1.5 mV,I_t=1 nA). (b) Topographic image recorded during the spectroscopic measurement (V_{bias}=1.5 mV,I_t=1 nA). (c) Topographic map of the CITS. (d) Conductance map at the energy of the gap edge (-0.2 mV). (e) Normalized conductance spectra averaged on various zones of the conductance map (d) and zooms on the gap edge and the DOS at the Fermi energy.*

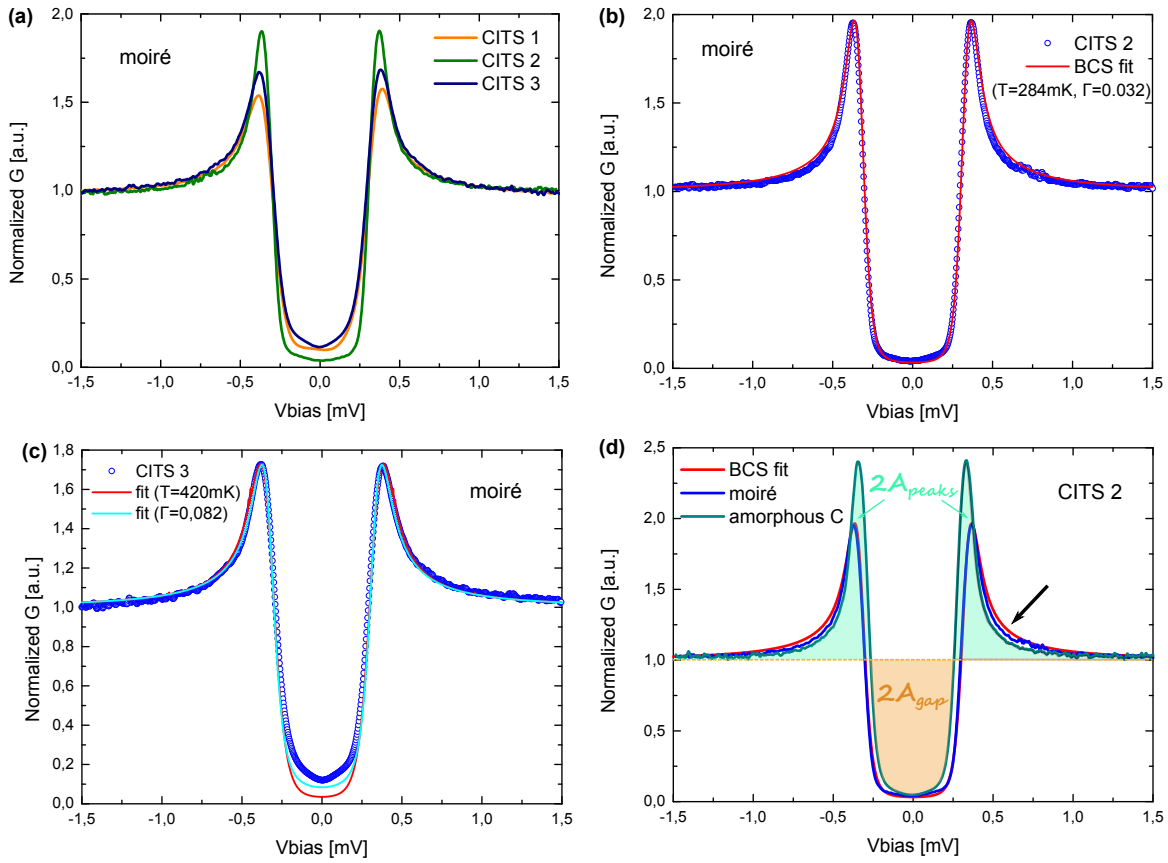

Figure 5.18 ***Spectroscopic analysis*** *- (a) Superposition of the spectra averaged on the moiré regions of the three CITS. (b) BCS fit of the moiré spectrum of CITS 2 with* $\Delta = 330\mu eV$*,* T_{eff}*=284 mK,* Γ*=0.032 (in* Δ*-unit). (c) BCS fit of the moiré spectrum of CITS 3 with* $\Delta = 330\mu eV$*,* T_{eff}*=480 mK,* Γ*=0.032 (red) and* $\Delta = 330\mu eV$*,* T_{eff}*=284 mK,* Γ*=0.082 (cyan). (d) Superposition of spectra averaged on CITS 2 on moiré and amorphous C with the BCS fit of (b).*

Fig. 5.16 and Fig. 5.17 show two other CITS measurements that exhibit the same abnormal superconducting proximity effect. CITS 2 has been carried out on an area presenting moiré and an amorphous carbon layer (respectively bottom and top part of Fig. 5.16 b). The moiré is not so clearly visible and one can wonder if it disappears in the bottom area due to a tip change or due to a real change in the surface morphology. Actually, Fig. 5.16 a, which is a larger scale image of the same area, helps us conclude that moiré is indeed present, with some detached moiré zones, until the edge of the amorphous carbon zone. Its disappearance in Fig. 5.16 b is therefore a tip effect. The white arrow in the image points out a hole in the amorphous carbon layer, where we can clearly identify a moiré pattern. The averaged spectra for the different zones, presented in Fig. 5.16 e, show the same anomalous superconducting proximity effect as previously reported. Note that the spectrum averaged in the hole region (not shown) is very similar to the one averaged on the surrounding amorphous carbon zone. Finally, Fig. 5.17 (CITS 3) presents another measurement of this effect carried out on a mostly amorphous surface with a small moiré zone on the top left part of the topographic image (b). The anomalous superconducting effect is thus visible on the three CITS on a similar length scale (∼60 nm).

If we now superimpose the three spectra corresponding to moiré areas of each CITS (Fig. 5.18 a), we see the spectra present the same superconducting gap but various coherence peaks height and DOS(E_F). The moiré spectrum of CITS 2 is well fitted by the BCS theory with $\Delta = 330\,\mu$eV, T_{eff}=284 mK and a Dynes parameter Γ=0.032 in Δ-unit (Fig. 5.18 b), whereas we could not reach a satisfying fit for the moiré spectrum of CITS 3 (Fig. 5.18 c) due to a too large number of sub-gap states and a V-shape of the DOS at low energy. The spectrum of CITS 1 presents an equivalent amount of sub-gap states but significantly lower coherence peaks, which also make it difficult to fit (the better fit was obtained for a very high Dynes parameter Γ=0.09, not shown). In conclusion, we find again a superconducting gap of 330 μeV in all the moiré areas like for our previous samples, but we observe a significant amount of sub-gap states that can vary from place to place.

To quantify the differences observed between the spectra averaged on moiré zones and amorphous C zones for the three CITS, we chose to look at three peculiar superconducting features: the DOS at Fermi energy, the 'gap'[10] size at G=0.5 and the coherence peaks amplitude. These three quantities are plotted on Fig. 5.19 with respect to the distance from the moiré zone (each dot represents an averaged spectrum in the respective CITS). Although the variations present different amplitudes for the three CITS, a general behavior can be extracted from this plot. From a moiré area to the most remote amorphous carbon area, the superconducting DOS systematically presents:

- an increase of the DOS at the Fermi energy
- a decrease of the 'gap' value at G=0.5
- an increase of the coherence peaks height.

In the following, we will retain and analyze the main effect, which is the gap size decrease

[10]Note that this convenient definition does not correspond to the effective superconducting gap Δ that we estimated at 330μeV by a BCS fit, but to the energy value when the conductance is equal to 0.5 in the spectra.

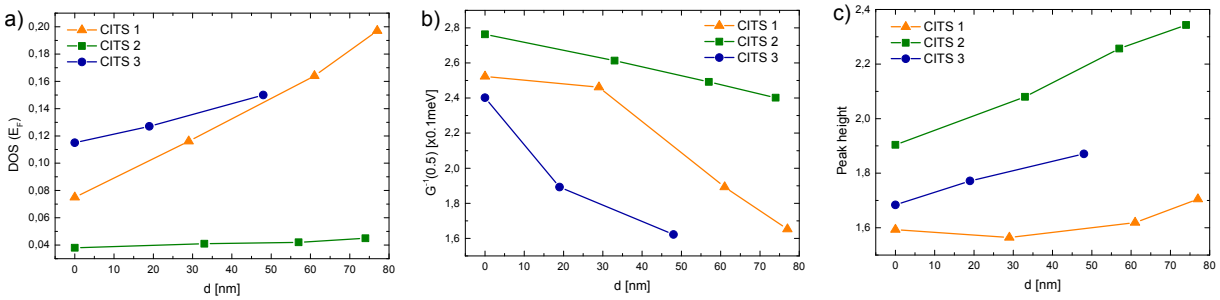

Figure 5.19 *(a) DOS at Fermi energy as a function of d, the distance of the average spectra from the moiré spectra for each CITS (d = 0 corresponds to the moiré zone itself). (b) Energy value when the conductance is 0.5 as a function of d. (c) Coherence peak height as a function of d.*

going along with an increase in the coherence peaks amplitude when we go from a regular moiré region to an amorphous C area. We will first focus on the CITS 2 measurement as it is the best fitted by the well-known BCS theory. We superimpose on Fig. 5.18 d the moiré spectrum with its BCS fit and the spectrum of the amorphous C region. The amorphous C spectrum can not be fitted by a BCS spectrum, as it will be demonstrated below.
In BCS theory, the DOS taken between $-\infty$ and $+\infty$ should always be conserved through the superconducting transition. In other words, the electronic states lost by the opening of the superconducting gap are pushed into the gap edges and form the so-called coherence peaks, leading to the conservation of the area under the curve. To check this law with our data, we calculated the area between the spectroscopic curves and the line G=1 in the coherence peaks region ($\mathcal{A}_{peaks}$ = half the blue area in Fig. 5.18 d) and in the gap region ($\mathcal{A}_{gap}$ = half the orange area in Fig. 5.18 d). The results are summed up in Tab. 5.1.

	BCS fit	moiré	amorphous C
$\mathcal{A}_{peaks}$	2.16	1.93	2.33
$\mathcal{A}_{gap}$	2.53	2.52	2.12
$(\mathcal{A}_{peaks}$-$\mathcal{A}_{gap})/\mathcal{A}_{gap}$	-15%	-23%	+10%

Table 5.1 *Areas under the different curves plotted on Fig. 5.18 d in unit [0.1 mV]. The last line shows the relative variations. The amorphous carbon layer presents a clear opposite variation.*

For the BCS fit, we see that $\mathcal{A}_{gap} \gtrsim \mathcal{A}_{peaks}$. This is expected as we did not integrate from $-\infty$ to $+\infty$ in our case, but only from -1.5 meV to +1.5 meV and thus do not take into account the infinitely far electronic states under the tail. The same situation is observed for the moiré spectrum, with a significantly higher difference. This could already be foreseen looking at the spectra plot. Indeed, the moiré spectrum presents a more pronounced hollow after the coherence peak (black arrow), indicating a lower number of states above the gap. This effect is even more pronounced in the amorphous C spectrum, which also presents abnormally high coherence peaks. For this latter spectrum, this results in $\mathcal{A}_{gap} < \mathcal{A}_{peaks}$, which means there are more additional electronic states available above the gap than the ones lost below the gap. In other words, the apparent DOS is not conserved in this case.

Before proposing possible interpretations accounting for this effect, we wanted to see if it was identical for the three presented CITS. To estimate the 'strength' of this non-conservation DOS effect, we calculated for each CITS the difference $\mathcal{A}_{peaks}$-$\mathcal{A}_{gap}$ for the average spectra measured on the moiré area and on the most remote amorphous carbon area. The results are summarized on Tab. 5.2. As a reference, we also indicate this difference for the BCS fit presented on Fig. 5.18 b. We see that:

- $\mathcal{A}_{peaks}$-$\mathcal{A}_{gap}$<0 for all the moiré spectra. Nevertheless, the difference values present strong discrepancies. In this respect, CITS 1 exhibits the behavior that is the closest to the BCS standard, although it could not be well-fitted by a BCS spectrum itself. This means its numerous sub-gap states are compensated by the low amplitude of its coherence peaks. As for CITS 3, it is far from the BCS standard, already for the moiré spectrum: its coherence peaks largely overcompensate the states lost in the gap.
- $\mathcal{A}_{peaks}$-$\mathcal{A}_{gap}$>0 for all the amorphous carbon spectra, which sets them far from the BCS standard.

If we look at the discrepancy between amorphous and moiré differences[11], we see that the CITS 2 shows the strongest effect, i.e. the larger area difference between the amorphous C spectrum and the moiré spectrum.

	BCS fit	CITS 1	CITS 2	CITS 3
moiré	-3.68	-4.95	-5.90	-0.67
amorphous C	/	1.21	2.10	5.22
Discrepancy	/	**6.16**	**8**	**5.89**

Table 5.2 $\mathcal{A}_{\mathbf{peaks}}$-$\mathcal{A}_{\mathbf{gap}}$ *for the moiré and amorphous C spectra of each CITS, in unit [0.01 mV]. The last row shows the effect amplitude.*

This proves that this lateral anomalous proximity effect does not depend on the presence of sub-gap states in the moiré region as it is stronger for CITS 2, which presents almost no sub-gap states.

As previously said, this proximity effect that affects the superconducting DOS is in contradiction with the existing models. Searching for its possible origin, we thought about two ways to interpret our observations:

- The tunneling conductance may not be strictly equal to the local DOS at the sample surface. This could come from a non-flat DOS of the tip itself, due for example to a non-metallic impurity attached to its apex. This hypothesis can be ruled out since this anomalous proximity effect has been observed systematically with different tips. Another possible explanation could be that the tunneling matrix is energy dependent. This is the case for example in the dynamical Coulomb blockade regime. We could imagine that the amorphous zone being more disordered the tunneling conductance consists there in the convolution of the local DOS and of a zero-bias anomaly (Aronov-Altshuler anomaly [4]). However, this would lead to an opposite effect, i.e. a decrease of the coherence peaks height.

[11] That is to say ($\mathcal{A}_{peaks}$-$\mathcal{A}_{gap}$)(amorphous C) - ($\mathcal{A}_{peaks}$-$\mathcal{A}_{gap}$)(moiré).

– Another possible scenario does consider that the tunneling conductance is still proportional to the local density of states but integrated in a specific region of the reciprocal space. It is indeed well known that there is a tunneling cone in a STM experiment, and that the tunneling current is dominated by states with wave-vectors perpendicular to the surface [108]. Since this is the total DOS integrated over all the **k**-directions that is conserved, we can imagine this conservation may not be respected in the STM tunneling cone.

These various options need to be further explored to propose a relevant explanation accounting for the observed phenomenon.

Conclusion

We have presented in this chapter our main results on the superconducting properties of our system made of epitaxial graphene grown on rhenium. Starting from transport measurements, we characterized the macroscopic and mesoscopic superconducting features such as the film transition temperature $T_c \sim 2\,K$ and the superconducting coherence length $\xi_s = 18\,nm$, which are consistent with values obtained on a bare Re film with similar thickness. The reduction of ξ_s was attributed to the presence of dissolved carbon atoms in the rhenium matrix that act as scattering centers. We then presented our local measurement by STS of the superconducting DOS and its temperature evolution. It shows a very good agreement with the BCS theory, and we extracted a superconducting gap $\Delta \simeq 330\mu eV$ and $\Delta/k_B T_c = 1.88$, which confirmed the highly transparent interface between graphene and rhenium. In line with the spatial study of the DOS at high-energy presented in the precedent chapter, we looked for possible variations of the superconducting DOS, and in particular the coherence peaks height, on a moiré scale. We have shown that, despite the careful filtering of noisy spectra and a quantitative statistic study, our STM measurements do not allow us to conclude as for a possible modulation of the superconducting features with the position on the moiré. We then presented a spectroscopic study carried out in the superconducting mixed state, when a perpendicular magnetic field is applied to our sample. We revealed the presence of a distorted Abrikosov vortex-lattice and a standard evolution of the vortex core DOS expected for a superconductor in the dirty limit. The last section was dedicated to the display of an anomalous lateral superconducting proximity effect we observed on a sample presenting various surface morphologies (moiré, detached moiré, amorphous carbon layer). It has been shown that this effect was reproducible and characterized by a decrease in the superconducting gap going along with an increase in the coherence peaks height. Its amplitude grows stronger while crossing surface areas from a regular moiré pattern to an amorphous carbon layer. Importantly, it does not depend on the peculiar shape of the superconducting spectrum in the moiré region. This effect is in contradiction with the existing models of the superconducting proximity effect and still needs to be understood.

Conclusion

We have introduced in chapter three of this manuscript the extraordinary physical properties of graphene that are responsible for the considerable enthusiasm of the scientific community. Its excellent electronic properties, high crystallographic quality and the fact that it is relatively easy to fabricate make it an ideal material for the study of physical phenomena in the ballistic regime. Its peculiar linear electronic dispersion promises even more new physical phenomena that could be revealed from its interplay with other states of matter. In this respect, the manifestation of superconductivity in graphene is a very exciting field of research.

We have seen that one way to induce superconducting properties in graphene can be realized by achieving a good contact between graphene and a superconductor, prerequisite that is often challenging.

In this manuscript, we have presented a new kind of hybrid system, where epitaxial graphene is grown directly on top of a superconductor, enabling to induce superconducting properties in graphene with a very high efficiency. Moreover, this technique ensures a very clean surface with a good crystalline quality of the graphene layer and presents the advantage to be easily studied by local probes such as STM.

We have exposed the fabrication process of our system, starting from superconducting rhenium thin films with high-crystallographic quality elaborated by Bruno Gilles in SIMAP, then transferred to the UHV setup of Johann Coraux in Institut Néel to proceed to the growth of a graphene monolayer by a segregation method.

We have shown that the lattice mismatch between graphene and rhenium results in a superstructure, a so-called moiré pattern, with hexagonal symmetry and about 2 nm periodicity. This moiré is a succession of 'hills' and 'valleys' corresponding to regions where the carbon atoms lie respectively further and closer to the rhenium film. The moiré corrugations have been estimated greater than 1Å. High-energy spectroscopy studies revealed a modulation of the density of states (DOS) features at the moiré scale, with a systematic enhancement of the DOS around the Fermi energy on the moiré hills as compared to the valleys. Nevertheless, the overall shape of the measured DOS highlights a strong coupling between rhenium and the graphene layer, as corroborated by density functional calculations performed by Laurence Magaud.

In the last chapter, we have reported the superconducting properties of the graphene-rhenium system. Transport measurements gave access to the superconducting critical temperature of the system estimated at 2 K and to the superconducting coherence length measured to be 18 nm. A comparison with measurements made on similar bare rhenium thin films has shown a limited influence of the dissolved carbon atoms (resulting from the segregation growth process) on the transition temperature but a strong one on the su-

perconducting coherence length (divided by two). From scanning tunneling spectroscopy measurements, we extracted the superconducting gap $\Delta \simeq 330\,\mu$eV. Its evolution with temperature gave access to the ratio Δ/k_BT_c=1.88, almost identical to the one measured on bare rhenium thin films. Referring to McMillan's model of a NS junction, we concluded that the interface between rhenium and graphene is highly transparent, in agreement with our previous conclusions.

Influenced by our high-energy spectroscopic data, we wondered if the superconducting DOS could also present a spatial modulation at the moiré scale. By doing a statistic spectroscopic study at low energy, we have shown that our STM measurements did not allow us to draw a conclusion on this question. In any case, if such a spatial inhomogeneity exists, it should be very small (<5%) and therefore difficult to detect.

Applying a perpendicular magnetic field to our sample, we have studied the superconducting mixed state and revealed the presence of magnetic vortices, organized in a distorted hexagonal Abrikosov vortex-lattice. A spectroscopic study in the vortex core has shown the expected DOS evolution for a superconductor in the dirty limit.

All these studies led to the conclusion that we achieved a very good coupling with a perfect interface between rhenium and graphene. Nevertheless, the annoying consequence soon became obvious: graphene is so strongly bond to rhenium that it lost its intrinsic peculiar electronic properties we are precisely interested in. Appeared then the necessity to locally decouple the graphene layer in some regions, while keeping a strongly bond graphene layer at others to ensure the good transmission of the superconducting correlations. Inspired by other studies on the graphene-ruthenium system, we have tried to grow a graphene bilayer on rhenium, as it had been showed that the second graphene top-layer would behave as free-standing graphene while the first one remains in strong interaction with the metal substrate. Our attempts to grow such a system led to a sample with a different morphology, presenting three kinds of surface. Some regions exhibit the regular moiré pattern previously observed and described but others presented a kind of 'detached' moiré with merging hills. Finally, the third surface type has been identified as an amorphous carbon layer. Although the origin and the exact structure of these regions are not well understood, spectroscopic measurements revealed an abnormal superconducting proximity effect with a large healing length. Indeed, when going from a regular moiré region to an amorphous carbon layer, the superconducting gap slightly decreases while the coherence peaks amplitude significantly increases, which is in total contradiction with the standard superconducting proximity effect. These results have been reproduced many times, on different areas, with different STM tips. No satisfying physical interpretation has been found yet and the analysis and modeling of this system is still in progress. They would require spectroscopic measurements above the critical temperature of the superconducting transition.

Conclusion en français

Nous avons introduit au chapitre 3 de ce manuscrit les propriétés physiques exceptionnelles du graphène, qui sont responsables de l'enthousiasme considérable de la communauté scientifique à son égard. Ses excellentes propriétés électroniques, sa haute qualité cristalline et sa facilité de fabrication en font un matériau idéal pour l'étude de phénomènes physiques dans le régime balistique. Sa dispersion électronique linéaire promet encore de nombreux autres phénomènes physiques nouveaux qui peuvent être mis à jour par son couplage avec d'autres états de la matière. A cet égard, la manifestation de la supraconductivité dans le graphène est un champ de recherche passionnant.
Nous avons vu qu'un moyen de rendre le graphène supraconducteur passe par la réalisation d'un bon contact entre le graphène et un supraconducteur, prérequis qui reste difficile.

Dans ce manuscrit, nous avons présenté un nouveau genre de système hybride, où le graphène est obtenu par épitaxie directement sur un supraconducteur, permettant ainsi d'induire des propriétés supraconductrices dans le graphène avec une très grande efficacité. De plus, cette technique garantit une surface très propre avec une bonne qualité cristalline de la couche de graphène et présente l'avantage d'être facilement accessible pour des sondes locales comme le STM.
Nous avons détaillé le procédé de fabrication de notre système, en commençant par les films minces de rhénium de haute qualité cristalline élaborés par Bruno Gilles au SIMAP, puis transférés dans le bâti UHV de Johann Coraux à l'Institut Néel pour procéder à la croissance d'une monocouche de graphène par ségrégation.
Nous avons montré que la différence de paramètre de maille entre le graphène et le rhénium induit une superstructure, appelée moiré, avec une symétrie hexagonale et de périodicité environ 2 nm. Ce moiré est un réseau périodique de 'collines' et de 'vallées' correspondant aux régions où les atomes de carbone se situent respectivement plus loin et plus près du film de rhénium. Les corrugations du moiré ont été estimées supérieures à l'angström. Des études spectroscopiques à haute énergie ont mis à jour une modulation de la densité d'états (DOS) à l'échelle du moiré, avec une augmentation systématique de la DOS autour de l'énergie de Fermi sur les collines du moiré comparativement aux vallées. Cependant, la forme globale de la DOS mesurée souligne un fort couplage entre le rhénium et la couche de graphène, corroboré par des calculs de la fonctionnelle de la densité réalisés par Laurence Magaud à l'Institut Néel.
Dans le dernier chapitre, nous avons présenté les propriétés supraconductrices du système graphène-rhénium. Des mesures de transport ont permis d'estimer à 2 K la température de transition supraconductrice du système et la longueur de cohérence supraconductrice à 18 nm. Une comparaison avec des mesures réalisées sur des films minces de rhénium similaires a montré une influence limitée des atomes de carbone dissouts dans le film (con-

séquence du procédé de croissance par ségrégation) sur la température de transition mais une forte influence sur la longueur de cohérence supraconductrice (divisée par deux). Nous avons extrait le gap supraconducteur $\Delta \simeq 330\,\mu$eV des mesures de spectroscopie tunnel. Son évolution avec la température a donné accès au rapport Δ/k_BT_c=1.88, quasiment identique à celui mesuré sur des films minces de rhénium sans graphène. En s'appuyant sur le modèle de McMillan pour une jonction NS, nous avons conclu que l'interface entre le rhénium et le graphène est hautement transparente, en accord avec nos conclusions précédentes.
Influencés par nos données spectroscopiques à haute énergie, nous nous sommes interrogés sur une possible modulation spatiale de la DOS supraconductrice à l'échelle du moiré. En réalisant une analyse statistique de nos données spectroscopiques à basse énergie, nous avons montré que nos mesures STM ne nous permettaient pas de conclure sur cette question. Dans tous les cas, si une telle inhomogénéité spatiale existe, elle devrait être très faible (<5%) et donc difficile à détecter.
Des mesures sous champ magnétique nous ont permis d'étudier l'état mixte supraconducteur et d'observer la présence de vortex magnétiques, organisés en un réseau d'Abrikosov déformé. Une étude spectroscopique dans le cœur de vortex a montré une évolution classique de la DOS pour un supraconducteur dans la limite sale.
Toutes ces études ont permis d'aboutir à la conclusion que nous avions atteint un très bon couplage avec une interface parfaite entre le rhénium et le graphène. Cependant, la conséquence fâcheuse est rapidement devenue évidente: le graphène est tellement bien couplé au rhénium qu'il a perdu ses propriétés électroniques intrinsèques si particulières qui sont précisément celles qui nous intéressent. Il est donc apparu nécessaire de découpler localement le graphène du substrat dans certaines zones de l'échantillon, tout en préservant un fort couplage de la couche de graphène dans d'autres afin de garantir la bonne transmission des corrélations supraconductrices. Nous avons essayé de faire croître une bicouche de graphène sur du rhénium car il a été montré, dans le cas du ruthénium, que la seconde couche de graphène supérieure se comporte comme du graphène suspendu tandis que la première couche reste en forte interaction avec le substrat métallique. Nos tentatives de croissance ont abouti à un échantillon de morphologie différente, présentant trois types de surface. Certaines régions présentent le moiré régulier préalablement observé et décrit mais d'autres montrent un moiré qui apparaît "décollé" avec des collines qui se rejoignent. Enfin, le troisième type de surface, très désordonné, est appelé couche de carbone amorphe dans le manuscrit, bien que l'origine et la structure exacte de ces régions ne soient pas bien comprises. Des mesures spectroscopiques ont révélé un effet de proximité supraconducteur spatial anormal sur des distances caractéristiques importantes. En effet, en se déplaçant d'une région de moiré régulier à une couche de carbone amorphe, le gap supraconducteur se ferme légèrement tandis que l'amplitude des pics de cohérence augmente de façon significative, ce qui est en apparente contradiction avec l'effet de proximité supraconducteur standard. Ces résultats ont été reproduits de nombreuses fois, sur différentes régions, avec différentes pointes STM. Aucune interprétation physique satisfaisante n'a encore été trouvée et l'analyse et la modélisation de ce système sont toujours en cours. Elles nécessiteront des mesures spectroscopiques au-dessus de la température de transition supraconductrice.

Perspectives

The graphene-rhenium system saw the light at the end of my first year of PhD. This project involving different teams in several laboratories, it took some time to define our objectives and priorities. As for every new system, we first did not know what would come out of it. When it became clear that it was adapted for the goal we had fixed in LaTEQS to study the superconducting proximity effect in graphene, a long phase of characterization, understanding and optimization of the system has begun. Delayed by several experimental set-up breakdowns, this project is now at the real beginning of the characterization step.

One of the priorities is to understand and master the growth process. This implies to understand the precise influence of the growth parameters on the final film morphology. Recent improvements of the UHV growth set-up will enable to monitor the graphene growth by in-situ live RHEED measurements. The achievement of a graphene submonolayer growth should also shed light on the exact growth process. This will also serve the low-temperature STM experiments focused on the superconducting properties of the system as we previously explained in this manuscript.

The goal defined for the spectroscopy study of superconductivity in graphene will be tackled in a second time, namely the **local decoupling** of the graphene layer from the rhenium substrate. Several directions should be explored:

- the growth of a **bilayer graphene**, where the top graphene layer is expected to be decoupled from the rhenium substrate and thus exhibit graphene-like electronic properties. This system could appear to be an interesting playground, coupling vertical and lateral superconducting proximity effect
- the decoupling of a graphene monolayer by **oxygen intercalation** (or other insulating materials) between graphene and rhenium. Indeed, it has been shown by micro-ARPES measurements that O_2 intercalation between Ru(0001) and as-grown monolayer graphene restored the linear π bands crossing the Fermi energy and results in a hole doping of the graphene layer [125] (see Fig. 5.21).

However, a third option could be considered to locally decouple graphene from rhenium, namely the **patterning of the rhenium substrate** either after or before the graphene growth. We could imagine etching the rhenium films to form pads separated by few dozens of nanometers and connected by free-standing graphene.

A fourth option is being explored only recently in the laboratory. Graphene can be grown on SiC substrates partially covered with Re. This would result in pristine graphene

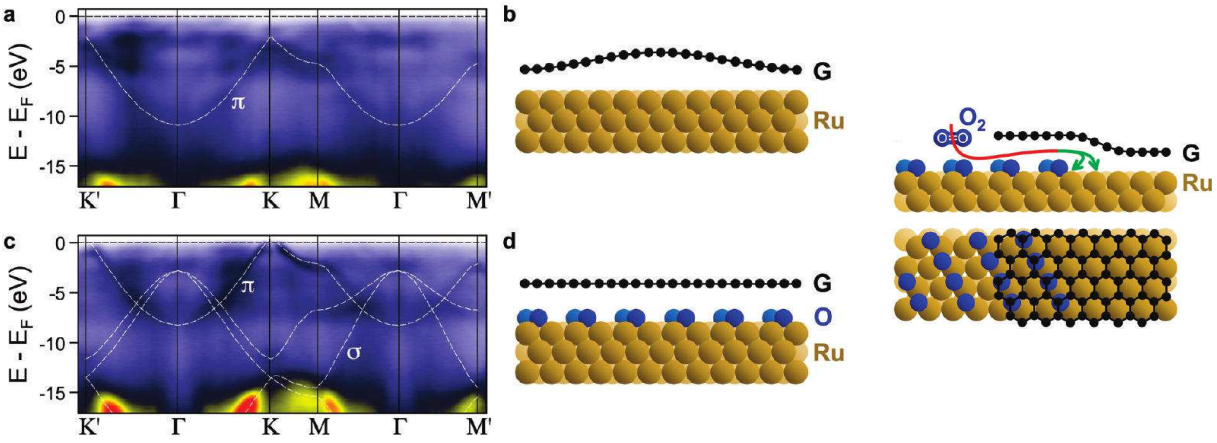

Figure 5.20 ***Decoupling of a monolayer graphene on Ru(0001) by intercalation of molecular oxygen (O_2)*** *- (a) Micro-ARPES map of the band structure of as-grown monolayer graphene on Ru(0001), reflecting the strong coupling to the metal d states. (b) Schematic of the corresponding moiré structure with alternating strong and weak coupling between graphene and Ru. (c) Micro-ARPES map after exposure to O_2, showing the restoration of linear π bands crossing the Fermi energy and hole doping with a charge-neutrality point 0.5 eV above E_F. (d) Schematic of the decoupled graphene sheet over an ordered Ru(0001)-(2×1)-O structure. Reproduced from [125].*

on the bare regions of SiC. However, this graphene would be superconducting thanks to the strong electronic coupling to Re at its edges.

All these experiments share one common goal, besides the study of the superconducting proximity effect in graphene: the realization of Andreev billiards, in which a ballistic metal surrounded by a superconductor exhibits DOS resonances at characteristic energies. The interplay of this phenomenon with the Dirac physics inherent to graphene also promises to be very exciting.

Perspectives en français

Le système graphène-rhénium a vu le jour à la fin de ma première année de thèse. Ce projet impliquant différentes équipes dans plusieurs laboratoires, la définition de nos objectifs et priorités a nécessité du temps. Comme pour tout nouveau système, nous ne savions pas ce qu'il en sortirait. Quand il est devenu clair qu'il était adapté à l'étude de l'effet de proximité supraconducteur dans le graphène, but que nous nous étions fixé au LaTEQS, une longue phase de caractérisation, compréhension et optimisation du système a commencé. Retardé par plusieurs pannes de montages expérimentaux, ce projet est maintenant au début effectif de l'étape de caractérisation.

Parmi les priorités de ce projet, la compréhension et la maîtrise du procédé de croissance sont capitales. Ceci implique de comprendre l'influence précise des paramètres de croissance sur la morphologie finale du film. Des améliorations récentes ont été apportées sur le bâti de croissance UHV et permettront de suivre en direct la croissance du graphene par des mesures RHEED in-situ. La réalisation de la croissance d'une monocouche partielle de graphène devrait également nous renseigner sur le procédé de croissance exact. Cela sera également utile pour les expériences STM à très basse température centrées sur l'étude des propriétés supraconductrices du système comme expliqué préalablement dans ce manuscrit.

La condition nécessaire à l'étude spectroscopique de la supraconductivité dans le graphène, à savoir le découplage local de la couche de graphène du substrat de rhénium, sera abordée dans un second temps. Plusieurs voies peuvent être explorées:

- la croissance d'une bicouche de graphène, système dans lequel on s'attend à ce que la couche supérieure soit découplée du substrat de rhénium et présente les propriétés électroniques intrinsèques au graphène. Ce système peut s'avérer être une aire de jeux intéressante, couplant un effet de proximité supraconducteur vertical et latéral
- le découplage de la monocouche de graphène par l'intercalation d'oxygène (ou autre matériau isolant) entre le graphène et le rhénium. En effet, il a été montré par des mesures micro-ARPES que l'intercalation d'O_2 entre Ru(0001) et une monocouche de graphène épitaxié restaurait les bandes linéaires π se croisant à l'énergie de Fermi et conduit à un dopage en trous de la couche de graphène [125] (cf Fig. 5.21).

Cependant, une troisième option peut être envisagée pour découpler localement le graphène du rhénium, à savoir la structuration du substrat de rhénium, soit avant, soit après la croissance de graphène. On pourrait imaginer graver les films de rhénium pour former des

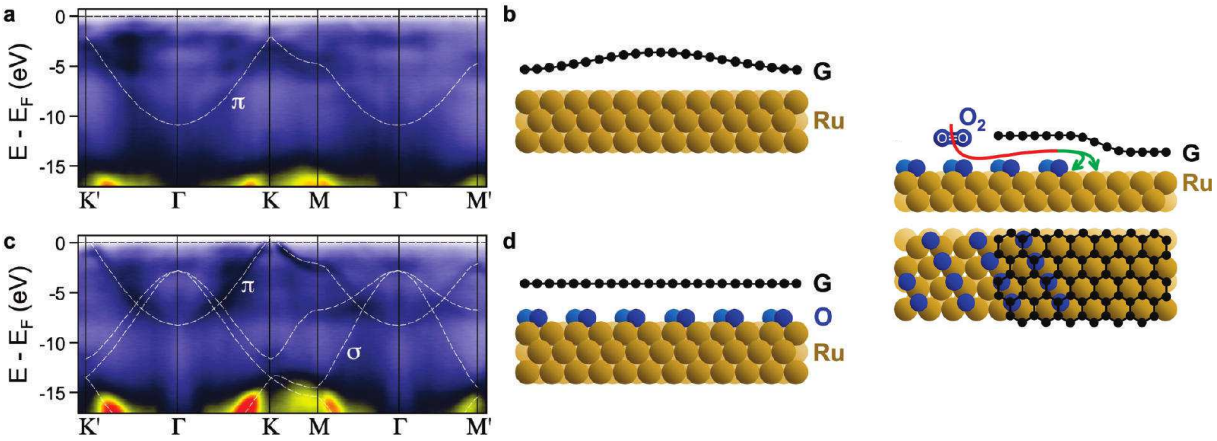

Figure 5.21 ***Découplage d'une monocouche de graphène sur Ru(0001) par intercalation de dioxygène (O_2)*** *- (a) Carte micro-ARPES de la structure de bande d'une monocouche de graphène épitaxié sur Ru(0001), montrant le fort couplage aux états d du métal. (b) Schéma de la structure de moiré correspondante avec un couplage alternativement fort et faible entre le graphène et le Ru. (c) Carte micro-ARPES après exposition à l'O_2 montrant la restauration des bandes π linéaires se croisant à l'énergie de Fermi et le dopage en trous avec un point de neutralité de charge à 0.5 eV au-dessus de E_F. (d) Schéma d'une couche de graphène découplée sur une structure Ru(0001)-(2×1)-O ordonnée. Reproduit de [125].*

blocs séparés de quelques dizaines de nanomètres et connectés par du graphène suspendu.

Une quatrième option est actuellement explorée depuis peu au laboratoire. Le graphène peut être fabriqué à partir de substrats de SiC partiellement couverts de rhénium. Cela aboutirait à du graphène idéal dans les zones découvertes du SiC et rendu supraconducteur grâce au fort couplage électronique au rhénium à ses extrémités.

Toutes ces expériences partagent un même objectif commun, en plus de l'étude de l'effet de proximité supraconducteur dans le graphène: la réalisation de billards d'Andreev, dans lesquels un métal balistique entouré d'un supraconducteur présente des résonnances dans sa DOS à des énergies caractéristiques. L'interaction de ce phénomène avec la physique de Dirac inhérente au graphène promet également d'être passionnante.

Bibliography

[1] The DFT calculations have been carried out with the code VASP. PAW approach, PBE functionnal and Grimme corrections to van der Waals interaction have been used. Calculations were performed with one k-point, the supercell K point to get a precise description of the graphene low energy states. After convergence, residual forces are lower than 0.025 eV/Å.

[2] Abrikosov, A. A. On the magnetic properties of superconductors of the second group. *Sov. Phys. JETP 5* (1957), 1174.

[3] Allain, A., Han, Z., and Bouchiat, V. Electrical control of the superconducting-to-insulating transition in graphene-metal hybrids. *Nat Mater 11*, 7 (July 2012), 590–594.

[4] Altshuler, B. L., and Aronov, A. G. *Electron-electron interaction in disordered conductors*. A.L. Efros and M. Pollak (Amsterdam : Elsevier Scientific Publishing), 1985.

[5] Andreev, A. *Sov. Phys. JETP 19* (1964), 1228.

[6] Andrei, E. Y., Li, G., and Du, X. Electronic properties of graphene: a perspective from scanning tunneling microscopy and magnetotransport. *Reports on Progress in Physics 75*, 5 (2012), 056501.

[7] Armbrust, N., Güdde, J., Jakob, P., and Höfer, U. Time-resolved two-photon photoemission of unoccupied electronic states of periodically rippled graphene on Ru(0001). *Phys. Rev. Lett. 108*, 5 (Jan. 2012), 056801.

[8] Arnoult, W. J., and McLellan, R. B. The solubility of carbon in rhodium ruthenium, iridium and rhenium. *Scripta Metallurgica 6*, 10 (Oct. 1962), 1013–1018.

[9] Ashcroft, N., and Mermin, N. *Solid State Physics*. CBC Publishing, 1975.

[10] Bae, S., Kim, H., Lee, Y., Xu, X., Park, J., Zheng, Y., Balakrishnan, J., Lei, T., Ri Kim, H., Song, Y., Kim, Y.-J., Kim, K., Ozyilmaz, B., Ahn, J.-H., Hong, B., and Iijima, S. Roll-to-roll production of 30-inch graphene films for transparent electrodes. *Nat Nano 5*, 8 (Aug. 2010), 574–578.

[11] Balandin, A. A. Thermal properties of graphene and nanostructured carbon materials. *Nat Mater 10*, 8 (Aug. 2011), 569–581.

[12] Banerjee, B. C., Hirt, T. J., and Walker, P. L. Pyrolytic carbon formation from carbon suboxide. *Nature 192*, 4801 (Nov. 1961), 450–451.

[13] Bardeen, J. Tunnelling from a many-particle point of view. *Phys. Rev. Lett. 6*, 2 (Jan. 1961), 57–59.

[14] Bardeen, J., Cooper, L. N., and Schrieffer, J. R. Theory of Superconductivity. *Phys. Rev. 108*, 5 (Dec. 1957), 1175–1204.

[15] Batzill, M. The surface science of graphene: metal interfaces, CVD synthesis, nanoribbons, chemical modifications, and defects. *Surface Science Reports 67*, 3–4 (Mar. 2012), 83–115.

[16] Beenakker, C. W. J. Specular Andreev Reflection in Graphene. *Phys. Rev. Lett. 97*, 6 (Aug. 2006), 067007.

[17] Beenakker, C. W. J. Colloquium: Andreev reflection and Klein tunneling in graphene. *Rev. Mod. Phys. 80*, 4 (Oct. 2008), 1337–1354.

[18] Benedict, L. X., Crespi, V. H., Louie, S. G., and Cohen, M. L. Static conductivity and superconductivity of carbon nanotubes: Relations between tubes and sheets. *Phys. Rev. B 52*, 20 (Nov. 1995), 14935–14940.

[19] Binnig, G., and Rohrer, H. Scanning tunneling microscopy: from birth to adolescence. *Rev. Mod. Phys. 59*, 3 (July 1987), 615–625.

[20] Binnig, G., Rohrer, H., Gerber, C., and Weibel, E. Surface Studies by Scanning Tunneling Microscopy. *Phys. Rev. Lett. 49*, 1 (July 1982), 57–61.

[21] Blase, X., Bustarret, E., Chapelier, C., Klein, T., and Marcenat, C. Superconducting group-IV semiconductors. *Nat Mater 8*, 5 (May 2009), 375–382.

[22] Blonder, G. E., and Tinkham, M. Metallic to tunneling transition in Cu-Nb point contacts. *Phys. Rev. B 27*, 1 (Jan. 1983), 112–118.

[23] Blonder, G. E., Tinkham, M., and Klapwijk, T. M. Transition from metallic to tunneling regimes in superconducting microconstrictions: Excess current, charge imbalance, and supercurrent conversion. *Phys. Rev. B 25*, 7 (Apr. 1982), 4515–4532.

[24] Bolotin, K., Sikes, K., Jiang, Z., Klima, M., Fudenberg, G., Hone, J., Kim, P., and Stormer, H. Ultrahigh electron mobility in suspended graphene. *Solid State Communications 146* (June 2008), 351–355.

[25] Brihuega, I., Mallet, P., Bena, C., Bose, S., Michaelis, C., Vitali, L., Varchon, F., Magaud, L., Kern, K., and Veuillen, J. Y. Quasiparticle chirality in epitaxial graphene probed at the nanometer scale. *Phys. Rev. Lett. 101*, 20 (Nov. 2008), 206802–.

[26] Brugger, T., Günther, S., Wang, B., Dil, J. H., Bocquet, M.-L., Osterwalder, J., Wintterlin, J., and Greber, T. Comparison of electronic structure and template function of single-layer graphene and a hexagonal boron nitride nanomesh on Ru(0001). *Phys. Rev. B 79*, 4 (Jan. 2009), 045407.

[27] Busse, C., Lazić, P., Djemour, R., Coraux, J., Gerber, T., Atodiresei, N., Caciuc, V., Brako, R., N'Diaye, A., Blügel, S., Zegenhagen, J., and Michely, T. Graphene on Ir(111): Physisorption with Chemical Modulation. *Phys. Rev. Lett. 107*, 3 (July 2011), 036101.

[28] Calandra, M., and Mauri, F. Theoretical Explanation of Superconductivity in C_6Ca. *Phys. Rev. Lett. 95*, 23 (Nov. 2005), 237002.

[29] Castro Neto, A. H., Guinea, F., Peres, N. M. R., Novoselov, K. S., and Geim, A. K. The electronic properties of graphene. *Rev. Mod. Phys. 81* (Jan 2009), 109–162.

[30] Cheianov, V. V., Falko, V. I., Altshuler, B. L., and Aleiner, I. L. Random resistor network model of minimal conductivity in graphene. *Phys. Rev. Lett. 99*, 17 (Oct. 2007), 176801.

[31] Chu, C. W., McMillan, W. L., and Luo, H. L. Superconductivity of Re-Os, Re-Ru, Ru-Os, and Re-W hcp Alloy Systems and Slightly Doped Re. *Phys. Rev. B 3*, 11 (June 1971), 3757–3762.

[32] Coraux, J. Lecture at Graphene School 2010 in Cargese: "Graphene preparation on metals", 2010.

[33] Coraux, J., N'Diaye, A., Busse, C., and Michely, T. Structural Coherency of Graphene on Ir(111). *Nano Lett. 8*, 2 (Jan. 2008), 565–570.

[34] Coraux, J., N'Diaye, A., Engler, M., Busse, C., Wall, D., Buckanie, N., zu Heringdorf, F.-J. M., van Gastel, R., Poelsema, B., and Michely, T. Growth of graphene on Ir(111). *New Journal of Physics 11*, 2 (2009), 023006.

[35] Courtois, H., Charlat, P., Gandit, P., Mailly, D., and Pannetier, B. The spectral conductance of a proximity superconductor and the reentrance effect. *Journal of Low Temperature Physics 116*, 3-4 (1999), 187–213.

[36] Crauste, O. *Etude de la transition de phase quantique supraconducteur-isolant, métal-isolant dans des matériaux amorphes désordonnés proches de la dimension 2.* PhD thesis, 2010.

[37] Crommie, M. F., Lutz, C. P., and Eigler, D. M. Confinement of electrons to quantum corrals on a metal surface. *Science 262*, 5131 (1993), 218–220.

[38] Daghero, D., and Gonnelli, R. S. Probing multiband superconductivity by point-contact spectroscopy. *Superconductor Science and Technology 23*, 4 (2010), 043001.

[39] Das, D., and Doniach, S. Existence of a Bose metal at T=0. *Phys. Rev. B 60*, 2 (July 1999), 1261–1275.

[40] De Gennes, P., and Saint-James, D. Elementary excitations in the vicinity of a normal metal-superconducting metal contact. *Physics Letters 4*, 2 (Mar. 1963), 151–152.

[41] Deutscher, G. Coherence and single-particle excitations in the high-temperature superconductors. *Nature 397*, 6718 (Feb. 1999), 410–412.

[42] Deutscher, G. Andreev-Saint-James reflections: A probe of cuprate superconductors. *Rev. Mod. Phys. 77*, 1 (Mar. 2005), 109–135.

[43] Deutscher, G., and Nozières, P. Cancellation of quasiparticle mass enhancement in the conductance of point contacts. *Phys. Rev. B 50*, 18 (Nov. 1994), 13557–13562.

[44] Ding, H., Yokoya, T., Campuzano, J. C., Takahashi, T., Randeria, M., Norman, M. R., Mochiku, T., Kadowaki, K., and Giapintzakis, J. Spectroscopic evidence for a pseudogap in the normal state of underdoped high-Tc superconductors. *Nature 382*, 6586 (July 1996), 51–54.

[45] Du, X., Skachko, I., and Andrei, E. Josephson current and multiple Andreev reflections in graphene SNS junctions. *Phys. Rev. B 77*, 18 (May 2008), 184507.

[46] Dubois, C., Santi, G., Cuttat, I., Berthod, C., Jenkins, N., Petrovic, A. P., Manuel, A. A., Fischer, O., Kazakov, S. M., Bukowski, Z., and Karpinski, J. Scanning Tunneling Spectroscopy in the Superconducting State and Vortex Cores of the β-Pyrochlore KOs_2O_6. *Phys. Rev. Lett. 101*, 5 (July 2008), 057004.

[47] Dubouchet, T. in preparation.

[48] Dubouchet, T. *Spectroscopie locale à basse température dans des systèmes supraconducteurs désordonnés*. PhD thesis, Université de Grenoble, 2010.

[49] Dynes, R. C., Narayanamurti, V., and Garno, J. P. Direct measurement of quasiparticle-lifetime broadening in a strong-coupled superconductor. *Phys. Rev. Lett. 41*, 21 (Nov. 1978), 1509–1512.

[50] Ekimov, E. A., Sidorov, V. A., Bauer, E. D., Mel'nik, N. N., Curro, N. J., Thompson, J. D., and Stishov, S. M. Superconductivity in diamond. *Nature 428*, 6982 (Apr. 2004), 542–545.

[51] Escoffier, W. *Etude de la cohérence quantique dans les systèmes supraconducteur-métal normal par microscopie et spectroscopie à effet tunnel*. PhD thesis, Université de Grenoble, 2004.

[52] Feigel'man, M. V., Ioffe, L., Kravtsov, V. E., and Cuevas, E. Fractal superconductivity near localization threshold. *Annals of Physics 325*, 7 (July 2010), 1390–1478.

[53] Feigel'man, M. V., Skvortsov, M. A., and Tikhonov, K. S. Proximity-induced superconductivity in graphene. *JETP 88* (2008), 747–751.

[54] Fischer, O., Kugler, M., Maggio-Aprile, I., Berthod, C., and Renner, C. Scanning tunneling spectroscopy of high-temperature superconductors. *Rev. Mod. Phys. 79*, 1 (Mar. 2007), 353–419.

[55] Gao, L., Guest, J. R., and Guisinger, N. P. Epitaxial Graphene on Cu(111). *Nano Lett. 10*, 9 (Aug. 2010), 3512–3516.

[56] Geim, A. K., and Novoselov, K. S. The rise of graphene. *Nat Mater 6*, 3 (Mar. 2007), 183–191.

[57] Gennes, P. G. D. *Superconductivity in Metals and Alloys*. W.A.Benjamin, New York, 1966.

[58] Girit, C., Bouchiat, V., Naaman, O., Zhang, Y., Crommie, M. F., Zettl, A., and Siddiqi, I. Tunable graphene dc superconducting quantum interference device. *Nano Lett. 9*, 1 (Dec. 2009), 198–199.

[59] Golubov, A. A. Abrikosov vortex core structure in a proximity-effect multilayer. 569–570.

[60] Golubov, A. A., and Hartmann, U. Electronic structure of the Abrikosov vortex core in arbitrary magnetic fields. *Phys. Rev. Lett. 72*, 22 (May 1994), 3602–3605.

[61] Guillamon, I., Suderow, H., Guinea, F., and Vieira, S. Intrinsic atomic-scale modulations of the superconducting gap of 2H-$NbSe_2$. *Phys. Rev. B 77*, 13 (Apr. 2008), 134505.

[62] Günther, S., Dänhardt, S., Ehrensperger, M., Zeller, P., Schmitt, S., and Wintterlin, J. High-Temperature Scanning Tunneling Microscopy Study of the Ordering Transition of an Amorphous Carbon Layer into Graphene on Ruthenium(0001). *ACS Nano 7*, 1 (Dec. 2012), 154–164.

[63] Gyamfi, M., Eelbo, T., Waśniowska, M., and Wiesendanger, R. Inhomogeneous electronic properties of monolayer graphene on Ru(0001). *Phys. Rev. B 83*, 15 (Apr. 2011), 153418.

[64] Hannay, N. B., Geballe, T. H., Matthias, B. T., Andres, K., Schmidt, P., and MacNair, D. Superconductivity in Graphitic Compounds. *Phys. Rev. Lett. 14*, 7 (Feb. 1965), 225–226.

[65] Hebard, A. F., Rosseinsky, M. J., Haddon, R. C., Murphy, D. W., Glarum, S. H., Palstra, T. T. M., Ramirez, A. P., and Kortan, A. R. Superconductivity at 18 K in potassium-doped C60. *Nature 350*, 6319 (Apr. 1991), 600–601.

[66] Heersche, H. B., Jarillo-Herrero, P., Oostinga, J. B., Vandersypen, L. M. K., and Morpurgo, A. F. Bipolar supercurrent in graphene. *Nature 446*, 7131 (Mar. 2007), 56–59.

[67] Hess, H. F., Robinson, R. B., Dynes, R. C., Valles, J. M., J., and Waszczak, J. V. Scanning-Tunneling-Microscope Observation of the Abrikosov Flux Lattice and the Density of States near and inside a Fluxoid. *Phys. Rev. Lett. 62*, 2 (Jan. 1989), 214–216.

[68] Hoogenboom, B. W., Kugler, M., Revaz, B., Maggio-Aprile, I., Fischer, O., and Renner, C. Shape and motion of vortex cores in $Bi_2Sr_2CaCu_2O_{8+\delta}$. *Phys. Rev. B 62*, 13 (Oct. 2000), 9179–9185.

[69] Hüfner, S., Hossain, M. A., Damascelli, A., and Sawatzky, G. A. Two gaps make a high-temperature superconductor ? *Reports on Progress in Physics 71*, 6 (2008), 062501.

[70] Hurd, M., Datta, S., and Bagwell, P. F. Current-voltage relation for asymmetric ballistic superconducting junctions. *Phys. Rev. B 54*, 9 (Sept. 1996), 6557–6567.

[71] Kasumov, A. Y., Deblock, R., Kociak, M., Reulet, B., Bouchiat, H., Khodos, I. I., Gorbatov, Y. B., Volkov, V. T., Journet, C., and Burghard, M. Supercurrents Through Single-Walled Carbon Nanotubes. *Science 284*, 5419 (1999), 1508–1511.

[72] Katsnelson, M. I., Novoselov, K. S., and Geim, A. K. Chiral tunnelling and the Klein paradox in graphene. *Nat Phys 2*, 9 (Sept. 2006), 620–625.

[73] Kessler, B. M., Girit, C., Zettl, A., and Bouchiat, V. Tunable Superconducting Phase Transition in Metal-Decorated Graphene Sheets. *Phys. Rev. Lett. 104*, 4 (Jan. 2010), 047001.

[74] Kim, K. S., Zhao, Y., Jang, H., Lee, S. Y., Kim, J. M., Kim, K. S., Ahn, J.-H., Kim, P., Choi, J.-Y., and Hong, B. H. Large-scale pattern growth of graphene films for stretchable transparent electrodes. *Nature 457*, 7230 (Feb. 2009), 706–710.

[75] Kociak, M., Kasumov, A. Y., Guéron, S., Reulet, B., Khodos, I. I., Gorbatov, Y. B., Volkov, V. T., Vaccarini, L., and Bouchiat, H. Superconductivity in Ropes of Single-Walled Carbon Nanotubes. *Phys. Rev. Lett. 86*, 11 (Mar. 2001), 2416–2419.

[76] Kohen, A., Proslier, T., Cren, T., Noat, Y., Sacks, W., Berger, H., and Roditchev, D. Probing the Superfluid Velocity with a Superconducting Tip: The Doppler Shift Effect. *Phys. Rev. Lett. 97*, 2 (July 2006), 027001.

[77] Komatsu, K., Li, C., Autier-Laurent, S., Bouchiat, H., and Guéron, S. Superconducting proximity effect in long superconductor/graphene/superconductor junctions: From specular Andreev reflection at zero field to the quantum Hall regime. *Phys. Rev. B 86*, 11 (Sept. 2012), 115412.

[78] Kopetskii, T. V., Myshlyaev, M. M., Novochatskai, N. I., Tulina, N. A., and Yukhanov, V. A. Critical temperature of superconducting transition in plastically deformed rhenium single crystals. *phys. stat. sol. (a) 16*, 1 (1973), 307–314.

[79] Kopnin, N. B., and Sonin, E. B. BCS Superconductivity of Dirac Electrons in Graphene Layers. *Phys. Rev. Lett. 100*, 24 (June 2008), 246808.

[80] Land, T. A., Michely, T., Behm, R. J., Hemminger, J. C., and Comsa, G. STM investigation of single layer graphite structures produced on Pt(111) by hydrocarbon decomposition. *Surface Science 264*, 3 (Mar. 1992), 261–270.

[81] Larkin, A., and Varlamov, A. *Theory of Fluctuations in Superconductors*. Oxford University Press, 2005.

[82] Lee, C., Wei, X., Kysar, J. W., and Hone, J. Measurement of the elastic properties and intrinsic strength of monolayer graphene. *Science 321*, 5887 (2008), 385–388.

[83] Li, X., Cai, W., An, J., Kim, S., Nah, J., Yang, D., Piner, R., Velamakanni, A., Jung, I., Tutuc, E., Banerjee, S. K., Colombo, L., and Ruoff, R. S. Large-area synthesis of high-quality and uniform graphene films on copper foils. *Science 324*, 5932 (2009), 1312–1314.

[84] Loeser, A. G., Shen, Z.-X., Dessau, D. S., Marshall, D. S., Park, C. H., Fournier, P., and Kapitulnik, A. Excitation Gap in the Normal State of Underdoped $Bi_2Sr_2CaCu_2O_{8+\delta}$. *Science 273*, 5273 (1996), 325–329.

[85] Magaud, L. Private communications.

[86] Marchini, S., Günther, S., and Wintterlin, J. Scanning tunneling microscopy of graphene on Ru(0001). *Phys. Rev. B 76*, 7 (Aug. 2007), 075429.

[87] Martin, J., Akerman, N., Ulbricht, G., Lohmann, T., Smet, J. H., von Klitzing, K., and Yacoby, A. Observation of electron-hole puddles in graphene using a scanning single-electron transistor. *Nat Phys 4*, 2 (Feb. 2008), 144–148.

[88] Mass, N., Ilzycer, D., Deutscher, G., Desgardin, G., Monot, I., and Weger, M. Sharp gap edge and determination of the fermi velocity in $YBa_2Cu_3O_{7-\delta}$ by point contact spectroscopy. *Journal of Superconductivity 5*, 2 (1992), 191–194.

[89] Mattheiss, L. F. Band Structure and Fermi Surface for Rhenium. *Phys. Rev. 151*, 2 (Nov. 1966), 450–464.

[90] May, J. W. Platinum surface LEED rings. *Surface Science 17*, 1 (Sept. 1969), 267–270.

[91] McChesney, J. L., Bostwick, A., Ohta, T., Seyller, T., Horn, K., Gonzalez, J., and Rotenberg, E. Extended van Hove Singularity and Superconducting Instability in Doped Graphene. *Phys. Rev. Lett. 104*, 13 (Apr. 2010), 136803.

[92] McMillan, W. L. Tunneling Model of the Superconducting Proximity Effect. *Phys. Rev. 175*, 2 (Nov. 1968), 537–542.

[93] Miniussi, E., Pozzo, M., Baraldi, A., Vesselli, E., Zhan, R. R., Comelli, G., Mentes, T. O., Niño, M. A., Locatelli, A., Lizzit, S., and Alfè, D. Thermal Stability of Corrugated Epitaxial Graphene Grown on Re(0001). *Phys. Rev. Lett. 106*, 21 (May 2011), 216101.

[94] Naaman, O., Teizer, W., and Dynes, R. C. Fluctuation Dominated Josephson Tunneling with a Scanning Tunneling Microscope. *Phys. Rev. Lett. 87*, 9 (Aug. 2001), 097004.

[95] Nandkishore, R., Levitov, L. S., and Chubukov, A. V. Chiral superconductivity from repulsive interactions in doped graphene. *Nat Phys 8*, 2 (Feb. 2012), 158–163.

[96] Naor, A., Eliaz, N., Gileadi, E., and Taylor, S. R. Properties and applications of rhenium and its alloys. *The AMMTIAC Quarterly 5*, 1.

[97] N'Diaye, A. T., Coraux, J., Plasa, T. N., Busse, C., and Michely, T. Structure of epitaxial graphene on Ir(111). *New Journal of Physics 10*, 4 (2008), 043033–.

[98] Noat, Y., Cherkez, V., Brun, C., Cren, T., Carbillet, C., Debontridder, F., Ilin, K., Siegel, M., Semenov, A., Hübers, H.-W., and Roditchev, D. Unconventional superconductivity in ultrathin superconducting NbN films studied by scanning tunneling spectroscopy. *Phys. Rev. B 88*, 1 (July 2013), 014503.

[99] Novoselov, K. S., Geim, A. K., Morozov, S. V., Jiang, D., Katsnelson, M. I., Grigorieva, I. V., Dubonos, S. V., and Firsov, A. A. Two-dimensional gas of massless dirac fermions in graphene. *Nature 438*, 7065 (Nov. 2005), 197–200.

[100] Ojeda-Aristizabal, C., Ferrier, M., Guéron, S., and Bouchiat, H. Tuning the proximity effect in a superconductor-graphene-superconductor junction. *Phys. Rev. B 79*, 16 (Apr. 2009), 165436.

[101] Pan, S. H., Hudson, E. W., and Davis, J. C. Vacuum tunneling of superconducting quasiparticles from atomically sharp scanning tunneling microscope tips. *Appl. Phys. Lett. 73*, 20 (Nov. 1998), 2992–2994.

[102] Pan, S. H., Hudson, E. W., and Davis, J. C. ^{3}He refrigerator based very low temperature scanning tunneling microscope. *Review of Scientific Instruments 70*, 2 (1999), 1459–1463.

[103] Pan, S. H., Hudson, E. W., Gupta, A. K., Ng, K.-W., Eisaki, H., Uchida, S., and Davis, J. C. STM Studies of the Electronic Structure of Vortex Cores in $Bi_2Sr_2CaCu_2O_{8+\delta}$. *Phys. Rev. Lett. 85*, 7 (Aug. 2000), 1536–1539.

[104] Pan, Y., Zhang, H., Shi, D., Sun, J., Du, S., Liu, F., and Gao, H.-J. Highly Ordered, Millimeter-Scale, Continuous, Single-Crystalline Graphene Monolayer Formed on Ru (0001). *Adv. Mater. 21*, 27 (2009), 2777–2780.

[105] Pekola, J. P., Maisi, V. F., Kafanov, S., Chekurov, N., Kemppinen, A., Pashkin, Y. A., Saira, O.-P., Möttönen, M., and Tsai, J. S. Environment-Assisted Tunneling as an Origin of the Dynes Density of States. *Phys. Rev. Lett. 105*, 2 (July 2010), 026803.

[106] Ponomarenko, L. A., Geim, A. K., Zhukov, A. A., Jalil, R., Morozov, S. V., Novoselov, K. S., Grigorieva, I. V., Hill, E. H., Cheianov, V. V., Falko, V. I., Watanabe, K., Taniguchi, T., and Gorbachev, R. V. Tunable metal-insulator transition in double-layer graphene heterostructures. *Nat Phys 7*, 12 (Dec. 2011), 958–961.

[107] Profeta, G., Calandra, M., and Mauri, F. Phonon-mediated superconductivity in graphene by lithium deposition. *Nat Phys 8*, 2 (Feb. 2012), 131–134.

[108] Proslier, T. *Spectroscopie tunnel à balayage avec une pointe supraconductrice.* PhD thesis, Université Paris 6, 2006.

[109] Proslier, T., Kohen, A., Noat, Y., Cren, T., Roditchev, D., and Sacks, W. Probing the superconducting condensate on a nanometer scale. *Europhys. Lett. 73*, 6 (2006), 962–968.

[110] Renner, C., Revaz, B., Genoud, J.-Y., Kadowaki, K., and Fischer, O. Pseudogap Precursor of the Superconducting Gap in Under- and Overdoped $Bi_2Sr_2CaCu_2O_{8+\delta}$. *Phys. Rev. Lett. 80*, 1 (Jan. 1998), 149–152.

[111] Renner, C., Revaz, B., Kadowaki, K., Maggio-Aprile, I., and Fischer, O. Observation of the Low Temperature Pseudogap in the Vortex Cores of $Bi_2Sr_2CaCu_2O_{8+\delta}$. *Phys. Rev. Lett. 80*, 16 (Apr. 1998), 3606–3609.

[112] Rodrigo, J., and Vieira, S. STM study of multiband superconductivity in $NbSe_2$ using a superconducting tip. *Physica C: Superconductivity 404* (May 2004), 306–310.

[113] Rodrigo, J. G., Suderow, H., and Vieira, S. Superconducting nanobridges under magnetic fields. *phys. stat. sol. (b) 237*, 1 (2003), 386–393.

[114] Rodrigo, J. G., Suderow, H., and Vieira, S. On the use of STM superconducting tips at very low temperatures. *Eur. Phys. J. B 40*, 4 (2004), 483–488.

[115] Sacépé, B. *Spectroscopie tunnel dans des films minces proches de la transition supraconducteur-isolant.* PhD thesis, Université de Grenoble, 2007.

[116] Sacépé, B., Chapelier, C., Baturina, T. I., Vinokur, V. M., Baklanov, M. R., and Sanquer, M. Disorder-Induced Inhomogeneities of the Superconducting State Close to the Superconductor-Insulator Transition. *Phys. Rev. Lett. 101*, 15 (Oct. 2008), 157006.

[117] Sacépé, B., Chapelier, C., Baturina, T. I., Vinokur, V. M., Baklanov, M. R., and Sanquer, M. Pseudogap in a thin film of a conventional superconductor. *Nat. Commun. 1* (Dec. 2010), 140.

[118] Sacépé, B., Dubouchet, T., Chapelier, C., Sanquer, M., Ovadia, M., Shahar, D., Feigel'man, M., and Ioffe, L. Localization of preformed Cooper pairs in disordered superconductors. *Nat. Phys. 7*, 3 (Mar. 2011), 239–244.

[119] Sharvin, Y. V. A possible methode for studying Fermi surfaces. *Sov. Phys. JETP 21* (1965), 655.

[120] Stander, N., Huard, B., and Goldhaber-Gordon, D. Evidence for Klein Tunneling in Graphene p-n Junctions. *Phys. Rev. Lett. 102*, 2 (Jan. 2009), 026807.

[121] Stradi, D., Barja, S., Díaz, C., Garnica, M., Borca, B., Hinarejos, J. J., Sánchez-Portal, D., Alcamí, M., Arnau, A., Vázquez de Parga, A. L., Miranda, R., and Martín, F. Role of Dispersion Forces in the Structure of Graphene Monolayers on Ru Surfaces. *Phys. Rev. Lett. 106*, 18 (May 2011), 186102.

[122] Stradi, D., Barja, S., Díaz, C., Garnica, M., Borca, B., Hinarejos, J. J., Sánchez-Portal, D., Alcamí, M., Arnau, A., Vázquez de Parga, A. L., Miranda, R., and Martín, F. Electron localization in epitaxial graphene on Ru(0001) determined by moiré corrugation. *Phys. Rev. B 85*, 12 (Mar. 2012), 121404.

[123] Sun, Q., and Wolkow, R. A. Three-dimensional displacement analysis of a piezoelectric tube scanner through finite element simulations of a tube assembly. *Review of Scientific Instruments 77*, 11 (2006), 113701.

[124] Sutter, E., Acharya, D. P., Sadowski, J. T., and Sutter, P. Scanning tunneling microscopy on epitaxial bilayer graphene on ruthenium (0001). *Applied Physics Letters 94*, 13 (2009).

[125] Sutter, P., Sadowski, J., and Sutter, E. Chemistry under Cover: Tuning Metal-Graphene Interaction by Reactive Intercalation. *J. Am. Chem. Soc. 132*, 23 (May 2010), 8175–8179.

[126] Sutter, P. W., Flege, J.-I., and Sutter, E. A. Epitaxial graphene on ruthenium. *Nat Mater 7*, 5 (May 2008), 406–411.

[127] Sutter, P. W., Sadowski, J. T., and Sutter, E. A. Graphene on Pt(111): Growth and substrate interaction. *Phys. Rev. B 80*, 24 (Dec. 2009), 245411.

[128] Tan, Y.-W., Zhang, Y., Bolotin, K., Zhao, Y., Adam, S., Hwang, E. H., Das Sarma, S., Stormer, H. L., and Kim, P. Measurement of Scattering Rate and Minimum Conductivity in Graphene. *Phys. Rev. Lett. 99*, 24 (Dec. 2007), 246803.

[129] Tang, Z. K., Zhang, L., Wang, N., Zhang, X. X., Wen, G. H., Li, G. D., Wang, J. N., Chan, C. T., and Sheng, P. Superconductivity in 4 Å Single-Walled Carbon Nanotubes. *Science 292*, 5526 (2001), 2462–2465.

[130] Tanigaki, K., Ebbesen, T. W., Saito, S., Mizuki, J., Tsai, J. S., Kubo, Y., and Kuroshima, S. Superconductivity at 33 K in Cs_xRb_yC60. *Nature 352*, 6332 (July 1991), 222–223.

[131] Ternes, M. *Scanning tunneling spectroscopy at the single atom scale*. PhD thesis, École Polytechnique Fédérale de Lausanne, 2006.

[132] Ternes, M., Schneider, W.-D., Cuevas, J.-C., Lutz, C. P., Hirjibehedin, C. F., and Heinrich, A. J. Subgap structure in asymmetric superconducting tunnel junctions. *Phys. Rev. B 74*, 13 (Oct. 2006), 132501.

[133] Tiedje, T., and Brown, A. Performance limits for the scanning tunneling microscope. *Journal of Applied Physics 68*, 2 (1990), 649–654.

[134] Titov, M., and Beenakker, C. W. J. Josephson effect in ballistic graphene. *Phys. Rev. B 74*, 4 (July 2006), 041401.

[135] Titov, M., Ossipov, A., and Beenakker, C. W. J. Excitation gap of a graphene channel with superconducting boundaries. *Phys. Rev. B 75*, 4 (Jan. 2007), 045417.

[136] Uchoa, B., and Castro Neto, A. H. Superconducting States of Pure and Doped Graphene. *Phys. Rev. Lett. 98*, 14 (Apr. 2007), 146801.

[137] Vázquez de Parga, A. L., Calleja, F., Borca, B., Passeggi, M. C. G., J., Hinarejos, J. J., Guinea, F., and Miranda, R. Periodically Rippled Graphene: Growth and Spatially Resolved Electronic Structure. *Phys. Rev. Lett. 100*, 5 (Feb. 2008), 056807.

[138] Vázquez de Parga, A. L., Calleja, F., Borca, B., Passeggi, M. C. G., J., Hinarejos, J. J., Guinea, F., and Miranda, R. Vázquez de Parga et al. Reply. *Phys. Rev. Lett. 101*, 9 (Aug. 2008), 099704.

[139] Vinogradov, N. A., Zakharov, A. A., Kocevski, V., Rusz, J., Simonov, K. A., Eriksson, O., Mikkelsen, A., Lundgren, E., Vinogradov, A. S., Martensson, N., and Preobrajenski, A. B. Formation and Structure of Graphene Waves on Fe(110). *Phys. Rev. Lett. 109*, 2 (July 2012), 026101.

[140] Wallace, P. R. The Band Theory of Graphite. *Phys. Rev. 71*, 9 (May 1947), 622–634.

[141] Wang, B., Bocquet, M.-L., Günther, S., and Wintterlin, J. Comment on Periodically Rippled Graphene: Growth and Spatially Resolved Electronic Structure. *Phys. Rev. Lett. 101*, 9 (Aug. 2008), 099703.

[142] Wang, B., Bocquet, M.-L., Marchini, S., Günther, S., and Wintterlin, J. Chemical origin of a graphene moiré overlayer on Ru(0001). *Phys. Chem. Chem. Phys. 10*, 24 (2008), 3530–3534.

[143] Wang, B., Günther, S., Wintterlin, J., and Bocquet, M.-L. Periodicity, work function and reactivity of graphene on Ru(0001) from first principles. *New Journal of Physics 12* (2010), 043041.

[144] Weller, T. E., Ellerby, M., Saxena, S. S., Smith, P., and Skipper, N. T. Superconductivity in the intercalated graphite compounds C_6Yb and C_6Ca. *Nat Phys 1*, 1 (Oct. 2005), 39–41.

[145] Wintterlin, J., and Bocquet, M.-L. Graphene on metal surfaces. *Surface Science 603* (June 2009), 1841–1852.

[146] Wolf, E. L. *Principles of electron tunneling spectroscopy.* Oxford University Press, 1985.

[147] Wu, X., Li, X., Song, Z., Berger, C., and de Heer, W. A. Weak Antilocalization in Epitaxial Graphene: Evidence for Chiral Electrons. *Phys. Rev. Lett. 98*, 13 (Mar. 2007), 136801.

[148] Xu, M., Takano, Y., Hatano, T., Kitahara, M., and Fujita, D. The fabrication of MgB_2 superconducting STM tips. *Physica C: Superconductivity 388–389*, 0 (May 2003), 117–118.

[149] Young, A. F., and Kim, P. Quantum interference and Klein tunnelling in graphene heterojunctions. *Nat Phys 5*, 3 (Mar. 2009), 222–226.

[150] Yu, Q., Lian, J., Siriponglert, S., Li, H., Chen, Y., and Pei, S.-S. Graphene segregated on Ni surfaces and transferred to insulators. *Appl. Phys. Lett. 93*, 11 (Sept. 2008), 113103.

[151] Zhang, Y., Brar, V. W., Girit, C., Zettl, A., and Crommie, M. F. Origin of spatial charge inhomogeneity in graphene. *Nat Phys 5*, 10 (Oct. 2009), 722–726.

[152] Zhang, Y., Brar, V. W., Wang, F., Girit, C., Yayon, Y., Panlasigui, M., Zettl, A., and Crommie, M. F. Giant phonon-induced conductance in scanning tunnelling spectroscopy of gate-tunable graphene. *Nat Phys 4*, 8 (Aug. 2008), 627–630.

[153] Zhang, Y., Tan, Y.-W., Stormer, H. L., and Kim, P. Experimental observation of the quantum Hall effect and Berry's phase in graphene. *Nature 438*, 7065 (Nov. 2005), 201–204.